TUM School of Computation, Information and Technology
Technische Universität München

# Perpendicular Nanomagnets: The Building Blocks of Field-Coupled Logic Devices

## Magnetization Reversal of Ion-Beam Engineering Single-Domain Nanomagnets with Perpendicular Magnetic Anisotropy

**Simon Mendisch**

Vollständiger Abdruck der von der TUM School of Computation, Information and Technology der Technischen Universität München zur Erlangung des akademischen Grades eines

**Doktors der Ingenieurwissenschaften (Dr.-Ing.)**

genehmigten Dissertation.

**Vorsitz:** **Prof. Dr. Bernhard Wolfrum**

**Prüfer der Dissertation:**

1. Priv.-Doz. Dr.-Ing. habil. Markus Becherer
2. Assoc. Prof. Gyorgy Csaba, Ph. D.

Die Dissertation wurde am 13.04.2022 bei der Technischen Universität München eingereicht und durch die Fakultät für Elektrotechnik und Informationstechnik am 26.09.2021 angenommen.

# Preface

> "The difference between theory and experiment is greater in theory than in experiment"
> (Unknown)

This work deals with tiny magnets, a few hundred nanometers in size, and only a couple of nanometers thick. Such nanoscale magnets can be utilized to perform logic operations employing their magnetic dipole fields. Based on these simple logic gates, digital non-volatile circuits can be realized. The corresponding technology is named *Perpendicular Nanomagnetic Logic* (pNML), owning its name to the perpendicular magnetization of its building blocks. Engineering the properties of these nanomagnets is the focus of this work.

# Abstract

Today, our lives depend entirely on the most complex technology ever created: integrated electronics. Despite this fact, most people are oblivious of the enormous research and development efforts driving this unparalleled development for more than half a century. From the beginning, ferromagnets, used as information carriers, played an integral part in this development. Magnets constituted the core of 20th-century memory technology and, even today, take up an irreparable role. Although the magnetic hard drive has almost vanished from consumer devices, it will remain the backbone of large scale data-storage for the foreseeable future. Using (Ferro-) magnets not only as information carriers but also as information processors was considered right from the start but quickly fell victim to the triumphal march of complementary metal-oxide-semiconductor (CMOS) technology.

However, at the beginning of the new millennia, advances in material science and sub-micron fabrication technology coincided with the first signs of an inevitable end to the exponential scaling of CMOS technology. This circumstance rewed interest in magnetic computing to offer low-power, scalable logic architectures. Perpendicular nanomagnetic logic (pNML) emerged as one of the most prospective magnetic logic technologies. It uses specifically engineered bistable magnets with out-of-plane magnetization (up/down) to represent the two digital states (1/0). Logic operations are performed via the stray fields emanating from the nanomagnets, acting on their neighbors. A complete set of digital logic gates was developed and experimentally demonstrated throughout the last decade. Furthermore, the viability of this technology was assessed via compact models and system-level simulations.

Today, the deciding topic for pNML is the performance of the fundamental building blocks, the nanomagnets. Both throughput and power consumption critically depend on the switching characteristics of the magnets. In order to feature perpendicular magnetization, these magnets need to consist of tailored, artificial materials with complex internal structures.

The present work addresses the search, assessment, and optimization of metallic multilayers for use in pNML systems. For that purpose, the focus is put on the sputter deposition of magnetic thin films, the characterization via magneto-optical methods, and the modeling of the time-dependent magnetization reversal process. Novel materials are introduced, the fabrication processes optimized, and the suitability for pNML assessed. The assessments span the entire pNML parameter space and cover the switching energies, reversal characteristics, and coupling strengths. The studies also include large numbers of magnets, thus allowing to determine significant variabilities for the first time. It is shown that the switching field distribution of the magnets can pose significant reliability risks.

A particular emphasis is put on the effects of local ion-beam irradiation, which is indispensable, modifying the magnetic energy landscape, controlling the switching energies, and reducing the variability. The material systems identified as most appealing for future generations of logic devices are low anisotropy cobalt-nickel superlattices and amorphous cobalt-iron-boron alloys.

By analyzing various magnetic materials, the present work can enable future research on perpendicular nanomagnetic logic or support research on related domain wall phenomena. Furthermore, the extensive studies of ion-beam engineered nanomagnets contribute to a better understanding of the magnetization reversal processes in these exotic systems.

# Kurzfassung

Unser tägliches Leben hängt heutzutage fast vollständig von der komplexesten Technologie ab, die je entwickelt wurde: der integrierten Elektronik. Trotz dieser Tatsache ist den meisten Menschen nicht bewusst, welche enormen Forschungs- und Entwicklungsanstrengungen diese beispiellose Entwicklung seit mehr als einem halben Jahrhundert vorantreiben. Von Anfang an spielten Ferromagnete, die als Informationsträger verwendet wurden, eine wesentliche Rolle bei dieser Entwicklung. Magnete bildeten das Herzstück der Speichertechnologie des 20. Jahrhunderts und nehmen auch heute noch eine essenzielle Rolle ein. Der Einsatz von (Ferro-) Magneten nicht nur als Informationsträger, sondern auch als Informationsverarbeiter wurde von Anfang an erwogen, fiel aber alsbald dem Siegeszug der komplementären Metall-Oxid-Halbleiter-Technologie (CMOS) zum Opfer.

Zu Beginn des neuen Jahrtausends jedoch trafen Fortschritte in der Materialwissenschaft und der Fertigungstechnologie mit den ersten Anzeichen für das unvermeidliche Ende der exponentiellen Skalierung der CMOS-Technologie zusammen. Dieser Umstand erneuerte das Interesse an magnetischen Technologien, die skalierbare Logikarchitekturen mit gleichzeitig geringem Stromverbrauch realisieren könnten.

Die senkrechte nanomagnetische Logik (Englisch: Perpendicular Nanomagnetic Logic (pNML)) hat sich dabei als eine der vielversprechendsten magnetischen Logiktechnologien etabliert. Sie verwendet speziell entwickelte bistabile Magnete mit aus der Ebene (oben/unten) zeigender Magnetisierung, um die digitalen Zustände (1/0) zu repräsentieren. Logikoperation werden über die von den Nanomagneten ausgehenden Streufelder ermöglicht, indem sie auf ihre Nachbarn wirken. In den letzten zehn Jahren wurde ein vollständiger Satz digitaler Logikgatter entwickelt und experimentell demonstriert. Darüber hinaus wurde die prinzipielle Realisierbarkeit der Technologie mittels Kompakt-Modellen und Simulationen auf Systemebene gezeigt. Heute ist das entscheidende Thema für pNML die Leistung der grundlegenden Bausteine, der Nanomagnete. Sowohl der Durchsatz als auch die Leistungsaufnahme hängen entscheidend von den Schalteigenschaften dieser Magnete ab. Um die senkrechte Magnetisierung zu realisieren, bestehen die Magnete aus maßgeschneiderten Materialien mit komplexen inneren Strukturen. Die vorliegende Arbeit befasst sich mit der Suche, Bewertung und Optimierung neuartiger metallischer Mehrlagenschichten für den Einsatz in pNML-Systemen. Zu diesem Zweck wird der Schwerpunkt auf die Sputterabscheidung magnetischer Dünnschichten, die Charakterisierung mittels magneto-optischer Methoden und die Modellierung des zeitabhängigen Schaltverhaltens gelegt. Neuartige Materialien werden vorgestellt, die Herstellungsprozesse optimiert und die Eignung für pNML bewertet. Die Bewertungen umfassen den gesamten pNML-Parameterraum und decken die Schaltenergien, Schaltcharakteristika und Kopplungsstärken ab. Die Untersuchungen umfassen auch eine große Anzahl von Magneten, so dass erstmalig signifikante Variabilitäten ermittelt werden können. Es wird gezeigt, dass die Schaltfeldverteilung der Magnete ein erhebliches Zuverlässigkeitsrisiko darstellen kann.

Ein besonderer Fokus liegt zudem auf den Effekten lokaler Ionenbestrahlung auf die Magneten. Diese ist unverzichtbar, um die magnetische Energielandschaft zu modifizieren, die Schaltenergien zu kontrollieren und die Variabilität zu reduzieren. Die Materialsysteme, welche für künftige Generationen von logischen Bauelementen am attraktivsten herausstellen, sind Kobalt-Nickel-Mehrlagen mit geringer Anisotropie und amorphe Kobalt-Eisen-Bor-Legierungen.

Die gewonnen Erkenntnisse über die verschiedene Materialien können künftige Forschung auf dem Gebiet der senkrechte nanomagnetische Logik oder verwandter Gebiete unterstürzen. Darüber hinaus tragen die umfangreichen Untersuchungen von Ionenstrahl-modifizierten Nanomagneten zu einem besseren Verständnis der Schaltprozesse in diesen exotischen Systemen bei.

# Contents

# List of Figures

# List of Tables

# 1 Introduction

Magnetic domains in atomically thin films, which are the focus of the work, were first observed in 1990 in perpendicularly magnetized cobalt/gold films shortly after the discovery of the giant magnetoresistance in 1988 [1]–[3]. This timing was no coincidence; both discoveries were driven by the continuous scaling of magnetic hard disk drives, requiring massive investments in research and technology. The history of magnetic data storage dates back to the first random-access core-memories and data tapes in the 1950s [4], [5]. Data storage, using out-of-plane magnetization, followed in the 1970s in the form of magnetic bubble memory using circular out-of-plane domains (bubbles) as information carriers in a shift-register design (up to 4 Mbit storage with an average access time of 40 ms and data rates up to 400 $\mathrm{kbit\,s^{-1}}$) [6]–[8]. These times also saw the implementations of magnetic bubble logic, using the dipolar repulsion of adjacent magnetic bubbles for complex logic operations [8], [9]. The bubble memory, suffering from the drawbacks of a shift-register design, complex clocking, and limited speeds, was eventually replaced by the above-mentioned hard disk drives and the first flash memories in the early 1980s. This also ended the first serious attempts at magnetic computing. At the same time, complementary metal-oxide-semiconductor technology (CMOS) replaced the established p- and n-type MOS logic families. Today, the economic pressure is still driving miniaturization and integration of both logic and memory. Now, hard disk drives are running the risk of suffering a similar fate as the bubble memories half a century ago, while CMOS technology is still the only relevant form of logic with no contender in sight.

CMOS technology has fueled economic growth and progress in virtually all research fields for half a century by offering ever-growing computation capacities with decreasing costs. The challenges and implications of this continuous device scaling, summarized under the term Moore's law, have always been at the center of the academic debate. However, this discourse, naturally involving projections and fears of a looming end of CMOS scaling, has entered the public discussion throughout the last two decades [10]–[12]. Huge resources have since, and still are being invested in identifying and developing viable and competitive alternatives [13]. However, until now, with little to no success.

In the meantime, CMOS is going strong, and there seems to be still "*plenty of room at the bottom*" for further scaling, although getting there is becoming increasingly more costly [14], [15]. This became especially evident by the drastic increase in design and manufacturing costs caused by the necessary move from planar to three-dimensional transistor designs in the second part of the 2010s [16]. The adoption of extreme ultraviolet lithography ($\lambda = 13.5\,\mathrm{nm}$) in the early 2020s will, in contrast to initial predictions, only accelerate the cost increase of the most advanced technology nodes [16], [17]. In order to cope with that increase, it will soon be necessary to fabricate only the critical and best scalable parts of a design in the most advanced nodes and integrate those parts together with other chiplets, realized in less expensive technologies, using interposers or through-silicon-vias. The ongoing development of these highly advanced assembly, 3D-packaging, and integration technologies has already opened the perspective for task-dedicated co-processors, hardware accelerators, and on-site memory. Today, distinct hardware accelerators have already found their way into virtually all, still monolithic, systems-on-a-chip designs. Thus, the 2020s will likely see the monolithic and three-dimensional integration of heterogeneous logic and memory blocks based on highly diversified fabrication technologies.

These advances in device stacking, packaging, and heterogeneous integration will yield significantly reduced integration costs and thus open a window for emerging beyond CMOS technologies, offering niche advantages.

### 1.0.1 Emerging Magnetic Technologies

The most prospective magnetic technology which might play a relevant part in future highly integrated systems is, at this point, without a doubt, the magnetoresistive random-access memory (MRAM). However, although available for several years, STT-MRAM has yet to prove that it can be a widespread commercial success. More advanced technologies employing the Spin-Hall effect (SOT-MRAM) or voltage-controlled magnetic anisotropy (VCMA) exist, as of 2021, only as prototypes [18], [19]. Beyond that, there are magnetic domain wall devices for multi-bit MRAM storage or even a revival of the above mentioned bubble-memory with new materials and a catchier name. The so-called racetrack-memory aims to store and move magnetic domains or bubbles along nanowires (made from synthetic antiferromagnets) via spin-transfer (STT) and spin-orbit torques (SOT) and readout the information encoded into the magnetization direction via TMR-effect sensors [20]. However, after significant investments and more than a decade of research, there are still significant technological, architectural, and design challenges to be overcome before a valid assessment of its competitive prospects can be made [21]. The racetrack memory lies in the future and will probably stay there.

Aside from memory, there have been various proposals for charge-based as well as non-charge-based magnetic computing technologies. Nevertheless, thus far, no concept has moved beyond the point of limited proof-of-concept studies. In the case of charge-based technologies today, there are interesting concepts for magneto-electric transistors (MEFET), where ferromagnetic source and drain regions act as spin-polarizer/analyzer and a voltage-controlled magneto-electric gate is used to modulate the spin-orbit-coupling of a semiconducting transistor channel [22]. Another concept, the nonvolatile magneto-electric spin-orbit (MESO) logic, proposed by Intel in 2019, uses still fictional materials with extremely high spin-to-charge conversion efficiencies to switch nanomagnets and generate charge currents vice versa [23]. Nevertheless, no proof of concept has been shown for either technology. Since most of the proposed charge-based technologies utilize recently discovered phenomena like the Spin-Hall effect or novel advances in spin-orbit torques, the lack of experimental work is to be expected at this point.

Thus, there have been significantly more purely magnetic (non-charge-based) proposals for novel computing technologies. Out of those, different approaches focus on utilizing magnetic fringing fields, domain walls, or even spin-waves (SW) for data processing. Spin-waves, generally described as wave-like excitations in magnetic materials propagating via the coupling between the individual precessing spins, have been proposed for digital logic as well as for analog signal processing [24], [25]. With frequencies in the low to high GHz range and adjustable wavelengths, they would be ideally suited to realize optically inspired signal processing on-chip [26], [27]. Furthermore, the non-linear effects in magnetic materials can be exploited to achieve highly sophisticated logic functions [28]. Though, efforts using spin waves and their complex interactions purely for digital means seem somewhat misguided. Today, spin-wave technology mainly suffers from insufficient SW propagation lengths, huge insertion, and even huger detection losses [29]–[31]. For a successful implementation, the development of efficient spin-wave transducers will be a deciding challenge. Furthermore, significant advances in the magnetic damping and thermal stability of the propagation media will be required.

The above-mentioned magnetic domain walls (DW) have not only been proposed for data storage but also for computation. First concepts, using domain walls for computing, date back to the 1960s, even before the advent of magnetic bubble technology [32]–[34]. Then, the technology used highly mobile DWs in soft magnetic media with in-plane magnetization (e.g., Permalloy) and rotating magnetic fields to drive DWs through zigzag structures (realizing shift-register functionalities) or used the magneto-static interactions between so-called domain-tips for digital logic operations (domain-tip propagation logic) [35]. In the early 2000s, this technology briefly gained renewed interest when advances in fabrication technologies allowed the realization of sub-µm structures [36]. Today, the advances in spin-transfer and spin-orbit torques enable new concepts for DW-logic, involving DWs propagating via electric currents through nanowires with out-of-plane magnetization. Logic operations are thereby archived by different means, either by the careful placement of so-called DW-injectors and readout elements or, for example, by the current-driven DW inversion across artificial, in-plane magnetized barriers [37], [38]. The overall prospects of these current-driven DW-logic technologies are closely coupled to the maximum achievable DW velocities in magnetic nanowires and the required current densities. Recent results of 180 nm wide DW-tracks, fabricated using a state-of-the-art MRAM process on 300-mm wafers, indicate that there are still significant technological challenges to overcome before sound assessments can be made [39].

Using individual magnets and their magnetostatic interactions for computation was for a long time effectively prohibited by the lack of sufficient (sub-µm) fabrication technologies. However, in the early 2000s, a ferromagnetic logic architecture using in-plane magnetized nanomagnets was proposed and, later on, experimentally demonstrated [40]–[42]. The so-called in-plane nanomagnetic logic (iNML) uses small (< 100 nm) nanomagnets, made from soft magnetic materials (e.g., Permalloy), with large aspect ratios (large shape anisotropy) to encode the binary states "0" and "1" into the magnetization directions of the magnetic easy-axis. The technology builds on majority-gate logic, which is realized via the antiferromagnetic coupling between closely packed magnets combined with a clock-field along the magnetic hard-axis, driving the so-called reevaluation of the magnets towards the input-dependent lowest energy state, thus performing logic operations. Compared to CMOS, ferromagnetic logic technologies can have numerous advantages. The first is the nonvolatile nature of ferromagnetic building blocks, which keep their information even without a power supply. Second is the interaction between magnets, which can be ferromagnetic as well as antiferromagnetic, thus allowing complex logic functions with a minimum amount of building blocks. Using magnetic fields for clocking furthermore alleviates the need for complex clock-distribution networks. Finally, there is no leakage current resulting in virtually no static power consumption. The prospective power–delay products of iNML compered well with CMOS technology at the time [43]–[45]. Thus, the technology received substantial support from DARPA's Non-Volatile Logic (NVL) program in 2010 [43].

However, the reliance on a pronounced shape anisotropy for easy-axis control turned out to be a significant reliability concern for the small nanomagnets and prohibited further device scaling [46]–[48]. Additionally, device integration on-chip was hampered by the necessity for complex multiphasic field clocks. In iNML, the propagation axis of the information is constrained along the magnetic field direction of the hard-axis clock, realized by buried metal coils. Thus, driving information through the circuit requires the synchronized clocking of adjacent logic stages as part of an intrinsically pipelined architecture [49].

However, by shifting the magnetic easy axis out-of-plane, a ferromagnetic logic architecture can be designed, which is not affected by the mentioned design and scaling constraints. This so-called perpendicular nanomagnetic logic (pNML) was first proposed by Csaba et al. in 2002 and subsequently pursued actively from 2008 onward by Becherer and colleagues at the Chair of Technical Electronics at the Technical University of Munich (TUM).

### Perpendicular Nanomagnetic Logic

Perpendicular Nanomagnetic Logic (pNML) enables non-volatile, boolean as well as majority-logic via the magnetic dipole-coupling between adjacent nanomagnets with out-of-plane (OOP) magnetization (magnet size ideally $< 100\,\mathrm{nm}$) [50]. Although bearing a similar name as the above introduced in-plane nanomagnetic logic, pNML is a radically different technology. In the case of pNML, the digital states are encoded into the OOP magnetization direction (1 as "up" and 0 as "down"). The working principles of pNML are based on the overlapping stray fields of multiple (input) magnets, acting in superposition on one (output) magnet, resulting in a majority decision. The output magnet switches antiparallel to the majority of the input magnets. The antiferromagnetic nature of the dipole coupling allows for complex logic function together with a minimum amount of devices (e.g., five magnets for a 1-bit full-adder)[51].

The flow of information is achieved via domain wall propagation inside the nanomagnets and the chained magnetization reversal of concatenated magnets, driven by an external alternating magnetic field along the magnetic easy-axis and initiated by the stray fields of the preceding magnet. This clock field acts as a global system clock and power supply, thus making complex clock trees superfluous. As nonvolatile nanomagnets carry the information, it represents a paradigm change in architecture, circuit design, and manufacturing.

This new paradigm involves a three-dimensional approach to data processing and computing, combining logic circuits with memory. Nanomagnets can be fabricated via sputter deposition and subsequent pattering on all planarized surfaces with a minimal thermal budget. Thus, individual pNML layers (each only between 10 and $50\,\mathrm{nm}$ thick) can be stacked to realize unrivaled computational densities. It is even possible to realize logic gates and memories across functional layers [52]–[55]. The marginal energy dissipation during switching ($\approx 1\,\mathrm{aJ}$) allows an unmatched degree of monolithic three-dimensional integration, only limited by the effective width of the computer architecture[52], [56]. The interface between pNML and electronic systems can be realized via dedicated input and readout elements. A simple conductor generating a small magnetic field can already act as an input, while more efficient solutions would probably employ sophisticated STT- or SOT-based domain wall injectors [39], [57], [58]. The same holds for the readout elements, where magnetoresistive sensors using the GMR or TMR effect are becoming the most practical solution compared to simpler designs building, for example, on the anomalous Hall effect [39], [59].

However, in order to be able to complement or potentially replace current information technologies successfully, an emerging logic technology must at least satisfy the so-called five "tenets" of logic [60]. Perpendicular Nanomagnetic Logic complies with all five of these principles, which are,

- Nonlinearity: Due to the magnetic hysteresis, pNML devices have nonlinear characteristics.
- Concatenation: Output magnets can act as inputs [61], [62].
- Signal amplification (gain $> 1$): Output magnets can drive multiple inputs via fan-outs (energy is supplied by the clock-field) [63].
- Unidirectionality: Unidirectional signal flow is achieved and guaranteed via artificial domain wall nucleation centers [61]–[63].
- Functional completeness: Perpendicular Nanomagnetic Logic features a complete set of logic gates implemented via majority gates with different numbers of inputs [51], [64].

However, these principles only define the prerequisites to building a functional logic system. They do not predict any important figure of merits like performance, power consumption, or reliability. It is nevertheless important to emphasize them, as these days, novel technologies tend to claim fabulous device performances while not even fulfilling the basic criteria for a functional logic architecture.

To assess the potential of pNML, one must first consider the physical properties and limitations of magnets with perpendicular magnetic anisotropy and combine them with the possible and desirable system architectures and clocking infrastructure. As already established, the switching energy of the individual magnets is with $\approx 1$ aJ highly competitive, even when considering future transistor designs [65]–[67]. Furthermore, the switching energy scales with the magnet volume, which is ultimately only limited by the superparamagnetic limit of the used materials.

Aside from the minimum features size, the general characteristics of pNML are also dominated by the magnet material and its properties, which are the main focus of this work. Identifying and optimizing suitable thin-film materials will decisively shape the future prospects of pNML.

### 1.0.2 Contribution of this work

This project started in mid of 2017 at the Chair of Nanoelectronics (later succeeded by Chair of Nano- and Quantum Sensors), continuing and extending the works of the nanomagnetic logic group, founded by Becherer and colleges at the former Chair of Technical Electronics at the Technical University of Munich.

With the proof-of-concept phase for pNML already competed, the focus was shifted towards on-chip demonstrators. However, for that purpose, new magnetic materials were essential, allowing for lower coercive fields and narrower switching field distribution. Consequently, the goal of this project was to identify and optimize promising materials for pNML, thereby addressing the critical magnetic parameters (e.g., switching fields, switching field distribution, magnetic coupling). In order to achieve this goal, new methodologies and techniques had to be developed and implemented to allow the analysis of large numbers of nanomagnets. In this context, several relevant contributions were made to reduce the switching fields and extend the understanding of ion-beam engineered nanomagnets for pNML. The most relevant of which are the:

- Extension of an existing Wide-field magneto-optical Kerr-effect microscope for semi-automatic and remote operation. Development of complementary software components for automated tests and image analysis.
- Process development and optimization for various magnetic thin-film technologies, aiming for low coercive and domain wall depinning fields (e.g., Pt/Co/W, Co/Ni, Ta/CoFeB/MgO, W/CoFeB/MgO). Trilayers, superlattices, and synthetic-antiferromagnets.
- Development of a focused-ion-beam lithography process with sub-micron resolution using a negative tone double-layer resist (with generous support from Allresist GmbH). Further optimization of well-established fabrication processes for thin-film patterning and metallization.
- Experimental demonstration of the first Pt/Co/W based pNML inverter.
- First statistical analysis of the magnetization reversal process of nanomagnets with ion-beam created artificial nucleation centers.
- Demonstration of bi-directional anisotropy control in Ta/CoFeB/MgO films via $\mathrm{Ga}^{+}$ ion-beam irradiation
- First experimental demonstration and analysis of ion-beam created artificial nucleation centers in Ta/CoFeB/MgO nanomagnets.

The listed contributions underline the focus on process development, material engineering, and extending the characterization capabilities of the research group. Additionally, it has to be noted that relevant contributions were made supporting other research projects at the Chair of Nano- and Quantum Sensors throughout the duration of this work. The list of notable contributions contains the

- Design and automation of a vector network analyzer (VNA) based ferromagnetic resonance setup for ferrimagnetic-thin-films with associated data analysis software (implemented in LabView). [27]

- Development of a sputtering process for the epitaxial growth of Yttrium-Iron-Garnet (YIG) thin-films on Gadolinium Gallium Garnet (GGG) substrates for spin-wave applications. [27]
- Thermal growth and physical vapor deposition of silicon-oxide layers for photocatalytic applications. [68]
- Extension of the Wide-field magneto-optical Kerr-effect microscope software to support automated STT & SOT pulse tests [69]

### 1.0.3 Thesis Outline

This work introduces and discusses different magnetic materials for use in perpendicular nanomagnetic logic. In order to achieve that, it is structured into nine parts.

In chapter 2, the theoretical framework needed for the intended discussions is laid out. It introduces the fundamentals of micro-magnetism and magnetic domain wall theory from the perspective of an electrical engineer. Thereby, an emphasis is put on media with out-of-plane magnetization and related phenomena. Readers with a sound background in the field of magnetism are encouraged to skip this chapter and directly continue to the third chapter.

In chapter 3, the state-of-the-art in perpendicular nanomagnetic logic is presented and discussed in detail. Thereby, the fundamental working principles and designs of the individual magnets and logic gates are discussed, together with the concepts of on-chip clocking for information propagation. Electrical inputs and outputs, together with system design and envisioned architectures, are addressed thereafter. Finally, the material systems analyzed during this work are introduced, and their fundamental physical properties are discussed.

Chapter 4 describes and discusses the fabrication processes used and developed during this work. Thereby, an emphasis is put on the sputter deposition of different magnetic thin-film systems and the subsequent patterning by means of ion-beam lithography. The chapter also gives a general overview of the available fabrication, capabilities, and limitations thereof.

Chapter 5 covers all relevant magnetic metrology methods and techniques used and developed throughout this work. Special attention is given to the magneto-optical characterization of ensembles of magnets via wide-field imaging. The following chapters 6, 7, and 8 discuss the materials systems, analyzed and evaluated for use in pNML. The chapters each focus on a specific material system, present different analyses, and discuss the obtained findings in the context of pNML.

The final chapter, chapter 9, attempts a summary of the different materials and obtained findings but also presents a review of one decade of pNML research.

# 2 Theoretical Framework

This chapter aims to build the necessary theoretical framework to understand the underlying physical effects and mechanisms relevant to nanomagnetic logic and related magnetic domain and domain wall phenomena. This work does not aim to provide a comprehensive mathematical formulation of every relevant topic but instead attempts descriptive and vivid explanations supported and complemented by the necessary mathematical background. The chapter targets an audience with an electrical engineering background, thus presuming basic knowledge of solid-state physics. Readers well versed in the topics of micro magnetism are encouraged to skip this chapter.

## 2.1 The Quantized Magnetic Moment

Phenomenologically speaking, we can describe the magnetic moment $\mu$ via the Bohr model, imagining $\mu$ as a circular current of an electron in its shell surrounding the core of the atom, covering the circular area $A = \pi r^2$, with $r$ as the radius of the orbital. From electrodynamics, we know that the magnetic moment $\mu = I \cdot A$.

The current equals the electron charge $-e$, times the frequency $\omega/2\pi$ (with the angular frequency $\omega = v_\mathrm{e}/r$, and $v_\mathrm{e}$ as the electron velocity). The current then amounts to $I = -e\omega/2\pi$, and the magnetic moment calculates as

$$\mu = -\frac{1}{2} e \omega r^2 \,. \tag{2.1}$$

Subsequently, when considering the angular momentum $J = m_\mathrm{e} \omega r^2$, we can write $\mu$ as

$$\mu = -\frac{e}{2m_\mathrm{e}} J \,, \tag{2.2}$$

with $m_\mathrm{e}$ as the electron mass [70], [71]. This relation between the angular momentum and the magnetic moment was first demonstrated by the *Einstein–de Haas* experiment [72]. The factor, relating the magnetic moment to the orbital angular momentum is called the *gyromagnetic ratio* ($\gamma$). In the case of the simplified orbital motion $\gamma = -\frac{e}{2m_\mathrm{e}}$.

Since the orbital angular momentum of an electron is quantized in multiples of $\hbar$, we can define the smallest non-dividable magnetic moment as the Bohr magneton $\mu_\mathrm{B}$ to be equal to

$$\mu_\mathrm{B} = -\frac{e\hbar}{2m_\mathrm{e}} = 9.27 \times 10^{-24}\,\mathrm{J\,T^{-1}} = 9.27 \times 10^{-24}\,\mathrm{A\,m^{-2}} \,. \tag{2.3}$$

However, the Bohr model is far too simplistic to accurately describe the magnetism of the electron. From quantum mechanics, we know that the individual electrons also possess an intrinsic spin angular momentum $s = \pm\frac{1}{2}\hbar$. The resulting magnetic moment of the electron spin $\mu_\mathrm{s}$ amounts to almost exactly $\mu_\mathrm{B}$ and calculates as

$$\mu_\mathrm{s} = -g \frac{e}{2m_\mathrm{e}} s = 1.00116 \mu_\mathrm{B} \,, \tag{2.4}$$

with $g = 2.0023$ as the so-called g-factor relating the spin angular momentum $s$ to the Bohr magneton $\mu_\mathrm{B}$. The spin angular momentum is coupled to the orbital angular momentum via so-called spin-orbit interactions to form a combined total angular momentum [70], [71].

## 2.2 Magnetic Order on the Atomic Scale

After establishing that every electron carries a magnetic moment, the question arises as to why only very few elements possess a net magnetic moment. The answer to this question lies in the intricate interplay between the shell electrons, almost completely canceling out the individual moments. In this section, we now address the coupling between these moments on the angstrom and nanometer scale. The mechanisms and forces at play are summarized under the term magnetic exchange interaction. Initially, one would assume that the dipole coupling is the dominant force governing the orientation of neighboring magnetic moments. However, when calculating the dipole coupling between two adjacent spins, one quickly realizes that the coupling energy between two moments of $\mu_B$, several angstroms apart is only in the range of $\approx 100\,\mu\text{eV}$ . This in turn means, that the critical disorder temperature, above which the moments are no longer effectively coupled, is only in the range of $\approx 1\,\text{K}$ ($E \approx k_\text{B} \cdot 1\,\text{K}$) [71], [73]. Therefore, the dipole-dipole coupling can not be the dominant force here.
The magnetic exchange interaction is a quantum-mechanical phenomenon with no classical analogon. It originates from the Pauli exclusion principle struggling with the Coulomb repulsion of electrons and enables ferro - as well as antiferromagnetic order on the atomic scale. These interactions are highly complex and, are not very well understood for many systems up to this date. Therefore, we use a dangerously simplified model to attempt a satisfying explanation within the scope of this work. In doing so, only the simplest form of interaction, the direct exchange interaction (between neighboring atoms or orbitals), is considered.

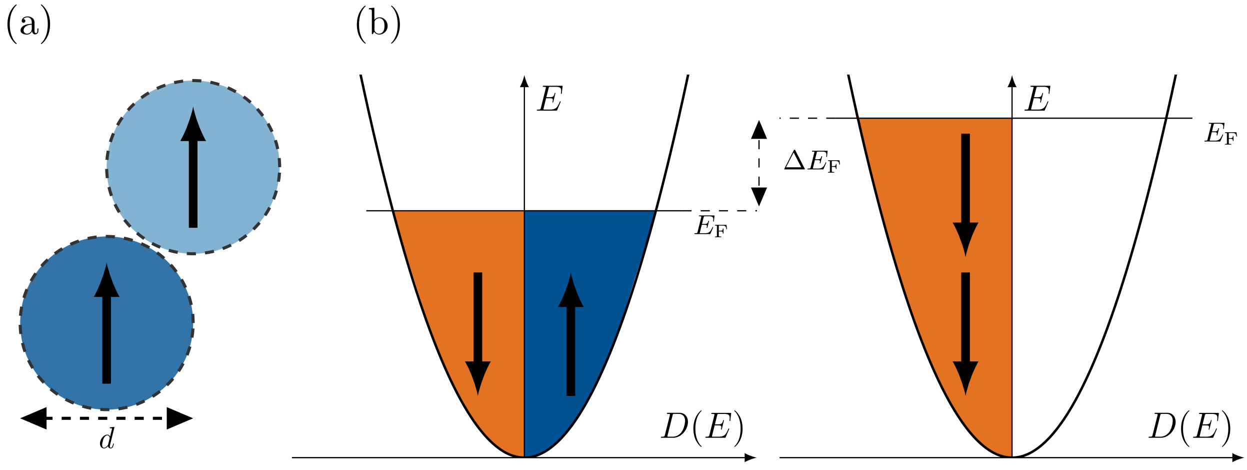

**Figure 2.1** In (a), the Pauli exclusion principle is symbolically illustrated, defining a minimal distance between particles with parallel spins. In (b), the density of states (DOS) $D(E)$ of a free electron gas depending on the energy, with either an anti-parallel (left) or a parallel (right) spin-alignment is depicted schematically. In case of parallel alignment, the Coulomb repulsion $\Delta E_\text{C} \propto \Delta E_\text{pot}$ is reduced as the electron distance increases. However, the *Fermi* energy is increased by $\Delta E_\text{F} \propto \Delta E_\text{kin}$ to allow the occupation of higher orbitals.

### Direct Exchange

The interaction (e.g., direct exchange) of two fermions demands an asymmetric two-body wave function [70], [71], [74]. In other words, this means that two electrons occupying the same orbital must have different spin quantum numbers ($\pm\frac{1}{2}$), and in turn, if they have the same spin quantum numbers or spins, they cannot occupy the same orbital. Due to this Pauli exclusion principle, electrons effectively repel other electrons (or fermions) with the same spin within a specific "shell" with diameter $d$ surrounding them, as illustrated in Figure 2.1 (a). The second force at play is the Coulomb repulsion, which generally favors a maximum distance between the electrons regardless of spin. However, distance in this context means higher a molecular orbital, which comes at an energy cost (The *Fermi* energy $E_\mathrm{F}$ needs to be increased in order to allow higher orbitals to be occupied). When considering two neighboring spins, there effectively exist two configurations, parallel and antiparallel alignment, both of which are described in the following.

- ↑↓ /↓↑ In case of an anti-parallel spin alignment (↑↓), the electrons stay "closer" together. This leads to higher potential energies ($E_\mathrm{Pot}$) due to the increased Coulomb repulsion. However, at the same time, the *Fermi* energy $E_\mathrm{F}$ (and thus the kinetic energy $E_\mathrm{kin}$ of the electrons) is reduced compared to a parallel spin alignment as illustrated in Figure 2.1 (b).
- ↑↑ /↓↓ In case of an parallel alignment (↑↑), the potential energy from Coulomb repulsion is reduced by $\Delta E_\mathrm{Pot}$ as the electrons are placed further apart. However, the kinetic energy is increased by $\Delta E_\mathrm{kin}$, as the *Fermi*-level rises to accommodate the electrons with parallel spin in higher orbitals (Figure 2.1 (b)).

To summarize, we can state that the energy difference between both states equals to

$$\Delta E_\mathrm{tot} = \Delta E_\mathrm{Kin} - \Delta E_\mathrm{Pot}\,. \tag{2.5}$$

Therefore, a parallel alignment of spins is favored if the distance between the electrons is large enough (not too large) and $\Delta E_\mathrm{F}$ thus comparatively small. If $\Delta E_\mathrm{F}$ on the other hand is very large and the particles therefore closer together, anti-parallel alignment is preferred. Figure. 2.2 depicts a schematic of this relation.

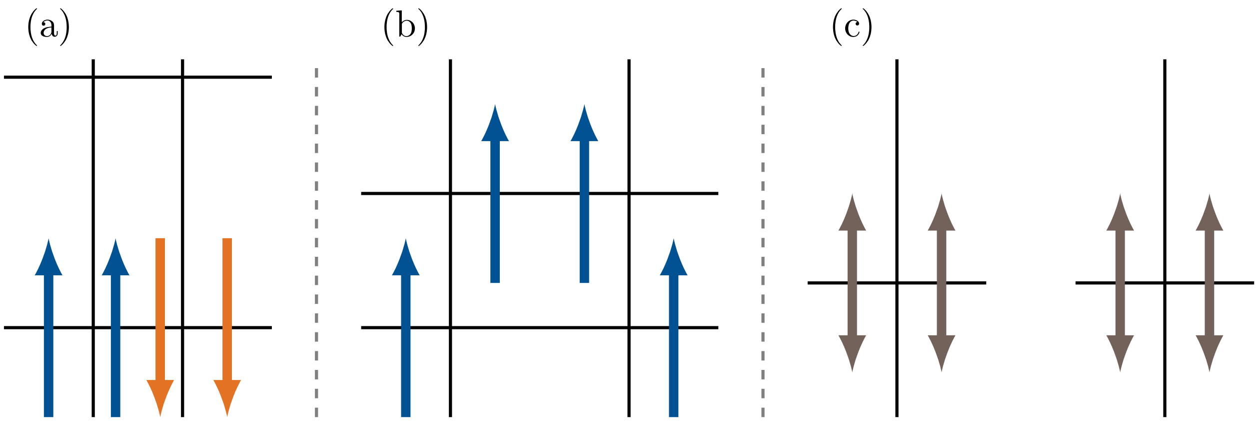

**Figure 2.2** The image shows schematic energy diagrams of the distance-dependent magnetic coupling of spins. In (a), the small distance leads to anti-ferromagnetic coupling. In (b), the smaller energy gap allows for redistribution of electrons into the upper level and thus ferromagnetic coupling. Finally, in (c), the distance is too large, and no coupling occurs.

### 2.2.1 Ferromagnetism of the 3d-Transition Metals

Ferromagnetism in metals, the main subject of this work, is caused by the exchange interaction between the delocalized (itinerant) conduction electrons. Using a simple electron gas model allows describing ferromagnetic coupling in such systems up to a certain degree. We know from the direct exchange interaction (section 2.2) that the *Fermi* energy and thus the kinetic energy of the system is higher for parallel (ferromagnetic) alignment. Ferromagnetic coupling is, therefore, most likely to be found in systems where this increase in *Fermi* energy $\Delta E_\mathrm{F}$ is comparatively small. This is the case for systems with a high density of states near the *Fermi*-level (the so-called Fermi edge). The high number of vacant states near the *Fermi*-level allows for a relatively cheap (energetically speaking) rearrangement of the anti-parallel (double occupied) states to the parallel (single occupied) states [71]. This situation is typically found in systems with conduction electrons in the highly localized 3d, 4f, and 5f orbitals [73], [75]. Especially interesting are the 3d transition metals (e.g., Cr, Fe, Co, Ni, Cu), which, depending on the number of electrons in their 3d-shell, show different magnetic behavior. Parallel spin alignment for a given element now depends on the sum of the changes in Coulomb and *Fermi* energy $\Delta E_\mathrm{tot} = \Delta E_\mathrm{kin} - \Delta E_\mathrm{pot}$. A system will, therefore, exhibit spontaneous spin alignment only if the net energy difference becomes smaller than zero, and the spin-up and down bands split (indicated in Figure 2.3). This is only the case for Fe, Co, and Ni which fulfill this so-called *Stoner*-criterion ($\Delta E_\mathrm{tot} < 0$). Without going into the details of the *Stoner*-model of ferromagnetism, we can approximate $\Delta E_\mathrm{kin}$ and $\Delta E_\mathrm{pot}$ to derive a more refined version of the *Stoner*-criterion. The number of dislocated electrons before and after the band splitting depends on the density of states at the *Fermi*-level [70], [74]. The kinetic energy can therefore be calculated as

$$\Delta E_\mathrm{kin} = \frac{1}{2} D(E_\mathrm{F}) \Delta E^2 \,, \tag{2.6}$$

with $D(E_\mathrm{F})$ as the density of states at the *Fermi* edge and $\Delta E^2$ as the increase in *Fermi* energy depicted in Figure 2.3 (b) [73]. The $\frac{1}{2}$ bstemms from the fact that only the spin-up or spin-down side is considered. The potential energy is calculated by considering the Coulomb potential of the displaced electrons via

$$\Delta E_\mathrm{pot} = \frac{1}{2} U (D(E_\mathrm{F}) \Delta E)^2 \,, \tag{2.7}$$

with $U$ as a measure of the Coulomb energy (which scales $\propto \frac{1}{r^2}$) [73]. The total energy is then defined as

$$\Delta E_\mathrm{tot} = \frac{1}{2} D(E_\mathrm{F}) \triangle E^2 (1 - U(D(E_\mathrm{F}))) \,, \tag{2.8}$$

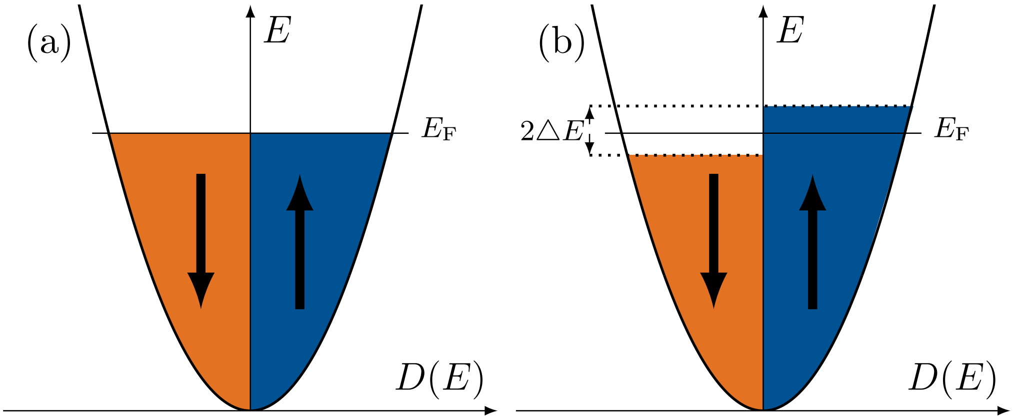

**Figure 2.3** Schematic plots of the density of states ($D(E)$) of a free-electron gas depending on the energy. In (a) both, spin-up and spin-down electrons are distributed equally up to the *Fermi*-level. In (b), the energy bands are split with a majority of spin-up electrons.

which leads to the refined *Stoner*-criterion

$$UD(E_\mathrm{F}) \overset{!}{>} 1\,. \tag{2.9}$$

This, again, means that the probability of finding ferromagnetic behavior in a material is highest in systems with a high density of states at the *Fermi* edge [70], [71]. This is only the case for the 3d metals Iron, Cobalt, and Nickel as shown by their respective DOS in Figure 2.4. The respective *Stoner*-parameters ($UD(E_\mathrm{F})$) are depicted in Table 2.1. The magnetic moment per atom is then calculated as a multiple of $\mu_\mathrm{B}$, depending on the effective number of majority spin electrons in the 3d band ($n_\mathrm{eff} = |n_\uparrow - n_\downarrow|$). In other words, $n_\mathrm{eff}$ describes the number of magnetic moments (in $\mu_\mathrm{B}$) that are not canceled out. The $n_\mathrm{eff}$ values listed in Table 2.1 range between 0.5 and 2.2 underlining the fact that only a small fraction of the overall electrons contribute to the net magnetic moment of the elements. One of the most essential material parameter, the spontaneous or saturation magnetization $M_\mathrm{s}$ can be calculated from the magnetic moment of the individual atoms and the number of atoms per cubic meter via

$$M_\mathrm{s} \approx n_\mathrm{eff}\mu_\mathrm{b}N_\mathrm{atoms} = n_\mathrm{eff}\mu_\mathrm{b}\frac{\rho N_\mathrm{A}}{m}\,, \tag{2.10}$$

with $\rho$ as the material density per cubic meter, $N_\mathrm{A}$ as the *Avogadro* number and $m$ as the atomic mass of the element [70]. An overview of the element specific atomic moments and associated saturation magnetization is illustrated in Table 2.1. Some material systems come very close to the *Stoner*-criterion. Although they cannot be considered ferromagnets, they will adapt ferromagnetic behavior when brought in contact with ferromagnets. This phenomenon is often called spin-polarization, *Stoner*-enhancement or proximity magnetism. Known elements being close to the *Stoner*-criterion are, for example, the noble metals Pt, Ir, and Pd [70], [75]. Primarily Pt is also used in applications, most notably as part of the pinned-layer (Pt/Co) in MRAMs and other MTJ applications, contributing to a higher total magnetization [76], [77]. However, how far this effect propagates into the nonmagnetic materials is not known precisely (for Pt, it is sometimes defined as half an atomic layer). However, estimations put it at the lower end of the spin-diffusion length, which itself is a debated parameter for these materials, usually set between a few Å and < 5 nm [70], [75], [78].

**Table 2.1** Table showing the magnetic properties of the ferromagnetic 3d-transition metals. Comparison of the *Stoner* parameter ($UD(E_\mathrm{F})$), the magnetic moments (in multiples of $\mu_\mathrm{b}$), and the saturation magnetization ($M_\mathrm{s}$). Data taken from [70].

| **Element** | $UD(E_\mathrm{F})$ | Magnetic Moment ($n_\mathrm{eff}\mu_\mathrm{b}$) | Saturation Magnetization |
|---|---|---|---|
| Iron (Fe) | 1.54 | $2.15\,\mu_\mathrm{b}$ | $\approx 1.7\times10^{6}\,\mathrm{A\,m^{-1}}$ |
| Cobalt (Co) | 1.72 | $1.71\mu_\mathrm{b}$ | $\approx 1.4\times10^{6}\,\mathrm{A\,m^{-1}}$ |
| Nickel (Ni) | 2.02 | $0.61\mu_\mathrm{b}$ | $\approx 0.48\times10^{6}\,\mathrm{A\,m^{-1}}$ |

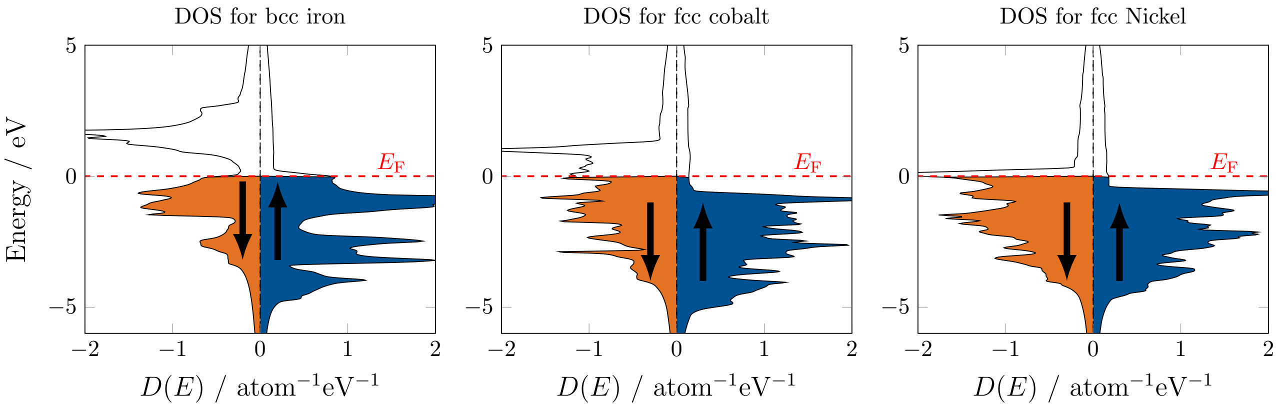

**Figure 2.4** The three plots show the electron density of states (DOS) for Iron, Cobalt, and Nickel. The density of states for the spin-up electrons is plotted on the positive x-axis, the density of states for spin-down electrons, respectively, on the negative x-axis. Density of states data reused with permission [79].

## 2.2.2 Ruderman–Kittel–Kasuya–Yosida Interaction

The so-called *Ruderman–Kittel–Kasuya–Yosida* (RKKY) interaction is a form of long-range magnetic exchange interaction especially relevant for applications. The coupling is again mediated by the conduction electrons, but in contrast to before, it describes the interaction between ferromagnets across a non-magnetic (but conductive) spacer layer or impurity. It is, therefore, considered as a form of indirect exchange interaction. The origins of this form of coupling are modulations in the electron density, the so-called *Friedel*-oscillations, which are the quantum mechanical analog to the electric charge screening effect occurring, for example, in liquids [70], [71], [73]. In their simplest form, these oscillations or modulations are described as the result of scattering processes at impurities (e.g., at a non-magnetic spacer layer) involving the electrons at the *Fermi* edge. Only electrons with high enough energies near the *Fermi*-level can scatter and find unoccupied states. These scattering processes result in the above mentioned, dampened oscillating electron density in the vicinity of an impurity with a wavelength of $\frac{\pi}{k_f}$ ($k_f$ thereby denotes the *Fermi* wave-vector with a length of $\approx 1$ Å). Since we already know that in these materials, the magnetic order is mediated via the itinerant conduction electrons, we

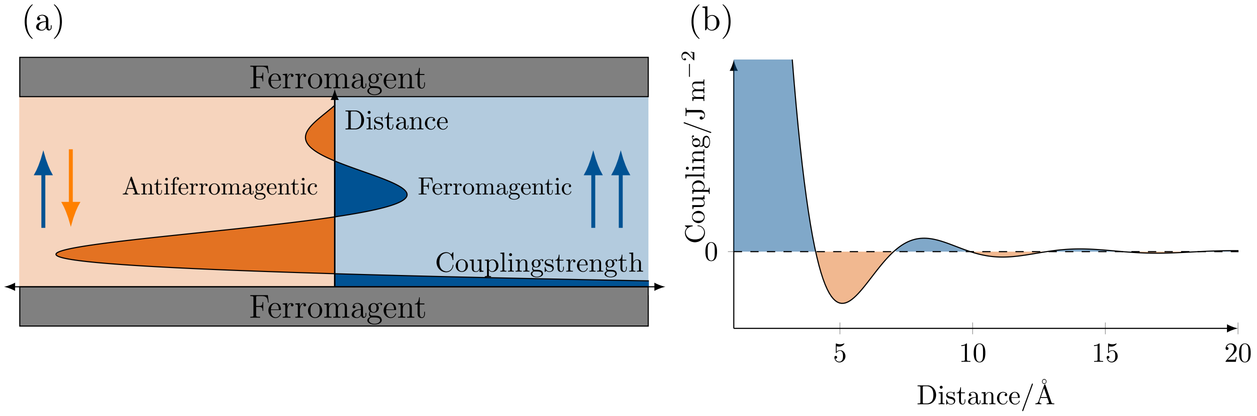

**Figure 2.5** In (a), a schematic illustration of the oscillatory nature of the RKKY coupling is illustrated. Depending on the thickness of the non-magnetic conductive spacer layer between the two ferromagnetic layers, the coupling is either ferro or antiferromagnetic. The plot in (b), shows a detailed evolution of the coupling strength versus the distance between the two magnetic layers.

find that the modulation of the electron density translates into a distance-dependent spin polarization according to

$$P_{\text{spin}}(x) = \frac{\sin(x) - x\cos(x)}{x^4}\,, \tag{2.11}$$

where $x = 2k_\text{f}r$ and $r$ is the distance between the ferromagnets. In Figure 2.5 (a), the oscillatory nature of the RKKY interaction is illustrated[70], [73]. The sign of the coupling thereby solely depends on the distance between the two ferromagnetic layers. The plot in Figure 2.5 (b) furthermore depicts a plot according to Equation (2.11) underlining the relative strength of the first three oscillations and the approximate length of the individual oscillation, which is roughly two atomic layers. It has to be noted, though, that Equation (2.11) only describes the qualitative evolution of the coupling between two layers. In experiments, the measured coupling not only depends on the distance $r$ but also on the non-magnetic spacer material. Iridium and Ru, for example, are known for their strong anti-ferromagnetic coupling, whereas other materials like Pt never cross the threshold and always promote ferromagnetic alignment. The RKKY interaction is critically relevant for the design of synthetic anti-ferromagnets in GMR/TMR sensors as well as magnetic random-access memories [80], [81]. However, the interaction also plays a relevant role in many magnetic multilayer systems, which are being investigated for potential use in future applications (e.g., spin-valves, nanomagnetic logic, or DW-logic/memory) [38], [80], [82].

### 2.2.3 Dzyaloshinskii–Moriya Interaction

The Dzyaloshinskii-Moriya interaction (DMI), sometimes also called antisymmetric exchange interaction or anisotropic superexchange, occurs in some crystalline antiferromagnets (giving them a small magnetic moment) and other bulk materials. More notably though, it also occurs at the interfaces between a ferromagnet and a heavy metal (HM) with large spin-orbit coupling in multilayer systems with broken inversion symmetry [83], [84]. This interfacial Dzyaloshinskii-Moriya interaction iDMI gained much attraction in the last decade as it plays a vital role in the stabilization of magnetic skyrmions in thin films [85]. The DMI is a form of indirect exchange between two spins mediated via a third non-magnetic heavy metal atom favoring perpendicular or canted spin alignment as depicted in Figure 2.6. Vividly speaking, this can be interpreted as an effective field running along with the interface. The Hamiltonian describing the iDMI can be expressed as

$$\mathcal{H}_{\text{DMI}} = \boldsymbol{D}(\boldsymbol{S}_i \times \boldsymbol{S}_j)\,, \tag{2.12}$$

with $\boldsymbol{S}_i$ and $\boldsymbol{S}_j$ as the two interacting spins and $\boldsymbol{D} = D_{i,j}(\hat{r}_{i,j} \times \hat{n})$ as the DMI vector consisting of the DMI constant $D_{i,j}$, the unit vector $\hat{r}_{i,j}$ linking the two spins and the vector $\hat{n}$ perpendicular to the

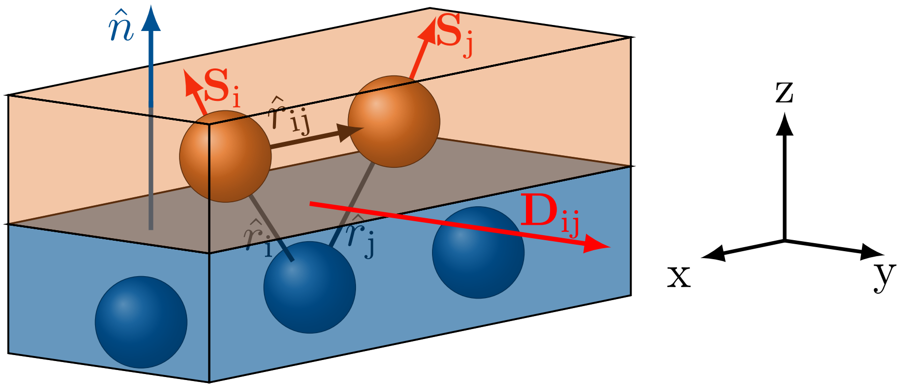

**Figure 2.6** Sketch of the interfacial Dzyaloshinskii-Moriya interaction showing the two spins $\boldsymbol{S}_\text{i}$ and $\boldsymbol{S}_\text{j}$ interacting via an atom with strong spin-orbit coupling from the heavy metal layer beneath.

interface [83], [84]. The sign of $D_{\mathrm{ij}}$ defines the direction of canting, and thus whether right-handed or left-handed, rotation is energetically favored. The top and bottom interfaces of the ferromagnet must be different in order to prevent cancellation of the effect and achieve a net iDMI (hence the broken inversion symmetry). For a comprehensive review of the Dzyaloshinskii–Moriya interaction in thin films, it is referred to [70], [83], [84].

## 2.3 Magnetic Moments & Dipole Fields

The magnetic moment of a small ferromagnetic particle with homogeneous magnetization is given as

$$\boldsymbol{m}_i = M_{\mathrm{s}} \cdot V_i \cdot \boldsymbol{e}_i \,, \tag{2.13}$$

where $M_{\mathrm{s}}$ is the saturation magnetization per unit volume, $V_i$ is the unit volume ($V_i = \frac{4}{3}\pi r^3$), and $\boldsymbol{e}_i$ the vector of the magnetization direction [70]. From *Amperes* law we know that the magnetic moment is equivalent to a current loop covering the area $A$. Thus $\boldsymbol{m} = IA$, where $I$ is the (DC) current and $A$ the covered area. The unit of the magnetic moment is $\mathrm{A\,m^2}$, giving $\mathrm{A\,m^{-1}}$ for the magnetization $M$ [70]. The generalized expression of the magnetic-moment generated by the current at the point $\boldsymbol{r} = r \cdot \boldsymbol{e}_{\mathrm{r}}$ is

$$\boldsymbol{m} = \frac{1}{2}\int \boldsymbol{r} \times \boldsymbol{j}(\boldsymbol{r})\mathrm{d}^3 r = \frac{1}{2}\int \boldsymbol{r} \times \boldsymbol{j}(\boldsymbol{r})\mathrm{d}V \,, \tag{2.14}$$

with the current density $\boldsymbol{j} = j \cdot \boldsymbol{e}_j$ and $j = \frac{I}{A}$[70]. The resulting magnetic field $\delta\boldsymbol{H}$ created by the current loop at a point $\boldsymbol{X}$ (depicted in Figure 2.7) away from the magnetic moment (or current loop) can then be calculated via the *Biot-Savart* law [70]. It calculates as

$$\delta\boldsymbol{H} = -\frac{1}{4\pi}\frac{\boldsymbol{r} \times \boldsymbol{j}}{r^3}\delta V \,. \tag{2.15}$$

The vector $\boldsymbol{r}$, thereby describes the distance between $\boldsymbol{X}$ and the current loop. By integrating Equation (2.15) it is possible to constitute a formalism describing the magnetic field at the receptor point $\boldsymbol{X}$ [70]. The resulting magnetic field is given by

$$\boldsymbol{H}(\boldsymbol{r},\boldsymbol{m}) = \frac{1}{4\pi r^3}\left[3\frac{(\boldsymbol{r}\cdot\boldsymbol{m})\boldsymbol{r}}{r^2} - \boldsymbol{m}\right] \,. \tag{2.16}$$

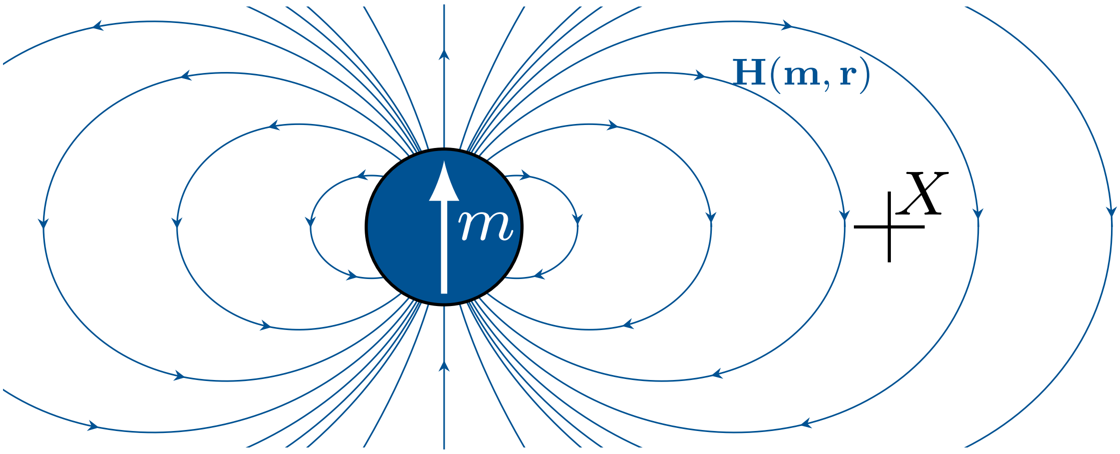

**Figure 2.7** Schematic illustration of a magnetic moment $m$ with the corresponding dipole fields illustrated as lines of force, acting on the point $\boldsymbol{X}$.

With this, it is possible to describe entire ensembles of moments, acting in superposition on $\boldsymbol{X}$.

## 2.4 Magnetic Energies

Before discussing magnetic ordering on larger scales, we first have to better understand the different forces and their interplay in magnetic materials. We have already discussed the ferromagnetic exchange as well as the anti-ferromagnetic dipole coupling qualitatively. The overall spin-arrangement inside materials is generally modeled as the result of an ongoing minimizing of the total free energy of the system. We can thus express the different interactions quantitatively as magnetic energies. The total energy is thereby expressed as the sum of multiple magnetic energy components with different signs. It can be written as

$$E_{\text{tot}} \approx E_{\text{Exchange}} + E_{\text{Anis}} + E_{\text{Demag}} + E_{\text{Zeeman}} + E_{\text{Stress}}\,, \tag{2.17}$$

where $E_{\text{Exchange}}$ denotes the energy of the ferromagnetic exchange interaction and $E_{\text{Anis}}$ describes the energies associated with a preferential magnetization axis (e.g., out-of-plane). The components $E_{\text{Demag}}$ and $E_{\text{Zeeman}}$ summarize the contributions arising from the dipolar energy of the magnetization and optionally from an external magnetic field interacting with the magnetization. The final term $E_{\text{Stress}}$ is usually used to describe ambiguous effects from mechanical stresses. In the following section, we will discuss the individual energy terms in more detail.

### 2.4.1 Exchange Energy

The exchange energy describes the coupling between adjacent spins ($\boldsymbol{S}_{\text{i}}$ and $\boldsymbol{S}_{\text{j}}$), depending on their angular alignment. The energy of two spins can be written as

$$E^{\text{pair}}_{\text{exchange}} = -2J_0 \boldsymbol{S}_i \cdot \boldsymbol{S}_j = -2J_0 S^2 \cos(\phi)\,, \tag{2.18}$$

with $J_0$ as the material dependent exchange constant and $\phi$ as the angle between the two spins [70], [71], [75]. The spins $\boldsymbol{S}_i$ and $\boldsymbol{S}_j$ are thereby described as the products of the amplitude $S$ and the respective unit vectors $\boldsymbol{e}_{i,j}$ ($\boldsymbol{S}_{i,j} = S\boldsymbol{e}_{\text{s}_{i,j}}$). The energy of the two spins is best minimized with an angle $\phi = 0$ leading to a "negative" energy of $E^{\text{pair}}_{\text{exchange}} = -2J_0S^2$. From Equation (2.18) it is possible to derive the so-called exchange stiffness $A_{\text{ex}}$, an expression for the mean exchange energy given in a unit cell of the material, assuming parallel alignment [70]. It calculates as

$$A_{\text{ex}} \approx \frac{J_0 S^2 N_{\text{u}}}{a_0}\,, \tag{2.19}$$

with $N_{\text{u}}$ as the number of atoms in a unit cell of the material and $a_0$ as the lattice constant. The exchange stiffness is also closely related to the *Curie*-temperature via the expression $A_{\text{ex}} \approx \frac{k_{\text{b}}T_{\text{c}}}{2a_0}$ [70]. The exchange stiffness is seldomly determined in experiments and amounts to $\approx 2 \times 10^{-11}\,\text{J}\,\text{m}^{-1}$ for 3d transition-metal ferromagnets.
At his point, it is furthermore useful to introduce another characteristic material parameter, the so-called exchange length $l_{\text{ex}}$. It describes a distance below which the exchange interaction dominates totally, or in other words, it denotes the shortest distance over which the dipole energy can be minimized by reorienting the spins. It is defined as $l_{\text{ex}} = \sqrt{\frac{A_{\text{ex}}}{\mu_0 M_{\text{s}}^2}} \approx 2 - 5\,\text{nm}$ [70], [75].

### 2.4.2 Magnetostatic Energies

Magnetostatic energies generally summarize energies from magnetic fields. These can originate from the uncompensated magnetic moments at the surface of a magnet (stray fields) or external fields interacting with the magnetization $\boldsymbol{M}$.

#### Demagnetizing Energy

The so-called demagnetizing or stray fields are caused by the uncompensated magnetic moments at the surface of a magnet. Or, in other words, by the diverging magnetization outside the magnet. From electromagnetism, we know that

$$\nabla \cdot \boldsymbol{B} = \nabla \cdot \mu_0(\boldsymbol{H}_{\text{Demag}} + \boldsymbol{M}) = 0\,, \tag{2.20}$$

with $\boldsymbol{H}_{\text{Demag}}$ as the demagnetizing field and $\boldsymbol{B}$ as the flux density [70]. Subsequently we can write

$$\nabla \cdot \boldsymbol{H}_{\text{Demag}} = -\nabla \cdot \boldsymbol{M}\,. \tag{2.21}$$

Furthermore, if there is no external magnetic field, we can state that

$$\int_{\text{all space}} \boldsymbol{B} \cdot \boldsymbol{H}_{\text{Demag}}\, \mathrm{d}V = 0\,, \tag{2.22}$$

and use this result to express the demagnetizing energy as

$$E_{\text{Demag}} = \frac{1}{2} \int_{\text{all space}} \mu_0 \boldsymbol{H}_{\text{Demag}}^2\, \mathrm{d}V\,, \tag{2.23}$$

or

$$E_{\text{Demag}} = -\frac{1}{2} \int_{\text{magnet}} \mu_0 \boldsymbol{H}_{\text{Demag}} \cdot \boldsymbol{M}\, \mathrm{d}V\,. \tag{2.24}$$

From Equation (2.23) we can now directly infer, that the demagnetizing energy is minimized for the lowest amount of stray fields $\boldsymbol{H}_{\textbf{Demag}}$[70].
Additionally, we can now derive a characteristic expression for the demagnetization field of a unit volume of magnetization, assuming a homogeneously magnetized film with out-of-plane magnetization amounting to $-\frac{1}{2}\mu_0 M_{\text{s}}^2$ [70].

#### Zeeman Energy

The *Zeeman*-energy describes the interaction between the apparent magnetization $\boldsymbol{M}$ and an external magnetic field $\boldsymbol{H}_{\text{ext}}$ [70], [75]. It is best minimized for a parallel alignment of the spins with the external field. The energy can be written as

$$E_{\text{Zeeman}} = -M_{\text{s}} \int_{\text{magnet}} \boldsymbol{H}_{\text{ext}} \cdot \vec{e}_m\, dV\,, \tag{2.25}$$

using $\boldsymbol{M} = M_{\text{s}} \cdot \vec{e}_{\text{m}}$. In discussions, and calculations, the so-called *Zeeman* term is often used as a direct replacement for the external field.

### 2.4.3 Magnetic Anisotropies

Magnetic anisotropy is, in the beginning, a difficult concept to grasp. It acknowledges the fact that the magnetic properties of a particle are direction-dependent. In other words, the magnetic properties are different along the x, y, and z-axis. Magnetic anisotropy is a fundamental property of ferromagnetic particles and the origin of the of the hysteresis behavior associated with ferromagnetism. Without anisotropy, the particles would be superparamagnetic, following the external field in order to minimize the *Zeeman*-energy [70].

### Shape-Anisotropy

The shape anisotropy is closely related to the aforementioned demagnetizing fields and their minimization. The magnetization will always tend towards the direction resulting in the lowest amount of uncompensated surface moments and thus stray fields. The shape of a particle is, thus, the most plausible cause of magnetic anisotropy. Figure 2.8 schematically illustrates the direction-dependent stray fields of a bar magnet with a height to width ratio of $\frac{1}{4}$. When comparing Figure 2.8 (a) and (b), it becomes directly apparent that the number of uncompensated surface moments and thus the stray-field energy is much lower in the case of a horizontal magnetization, running along the dominant magnet dimension. The resulting magnetostatic energy arising from the shape, per unit volume of magnetization, can be expressed as

$$E_{\mathrm{shape}} = \frac{1}{2}\mu_0 N_{\mathrm{x,y,z}} M_{\mathrm{s}}^2 \,, \tag{2.26}$$

with $N_{\mathrm{x,y,z}}$ as the direction dependent demagnetizing factors. These factors are very difficult to calculate in detail for complex shapes. However, for most cases, simplified approximations give satisfying results [71], [86]–[88]. The direction dependent demagnetization field can be written as

$$\vec{\boldsymbol{H}}_{\mathrm{demag}} = -4\pi \begin{pmatrix} N_{\mathrm{x}} & 0 & 0 \\ 0 & N_{\mathrm{y}} & 0 \\ 0 & 0 & N_{\mathrm{z}} \end{pmatrix} \vec{\boldsymbol{M}} \,, \tag{2.27}$$

with $N_{\mathrm{x,y,z}}$ as the axis specific prefactors. It furthermore holds, that $N_{\mathrm{x}} + N_{\mathrm{y}} + N_{\mathrm{z}} = 1$ [71], [89]. For the quasi-two-dimensional thin-films (or structures) with out-of-plane magnetization considered in this work, we can reasonably approximate $N_{\mathrm{x}}$ and $N_{\mathrm{y}}$ with zero, leading to a shape anisotropy of

$$E_{\mathrm{shape}}^{\mathrm{thin\,film}} = \frac{1}{2}\mu_0 N_{\mathrm{z}} M_{\mathrm{s}}^2 \approx \frac{1}{2}\mu_0 M_{\mathrm{s}}^2 \,. \tag{2.28}$$

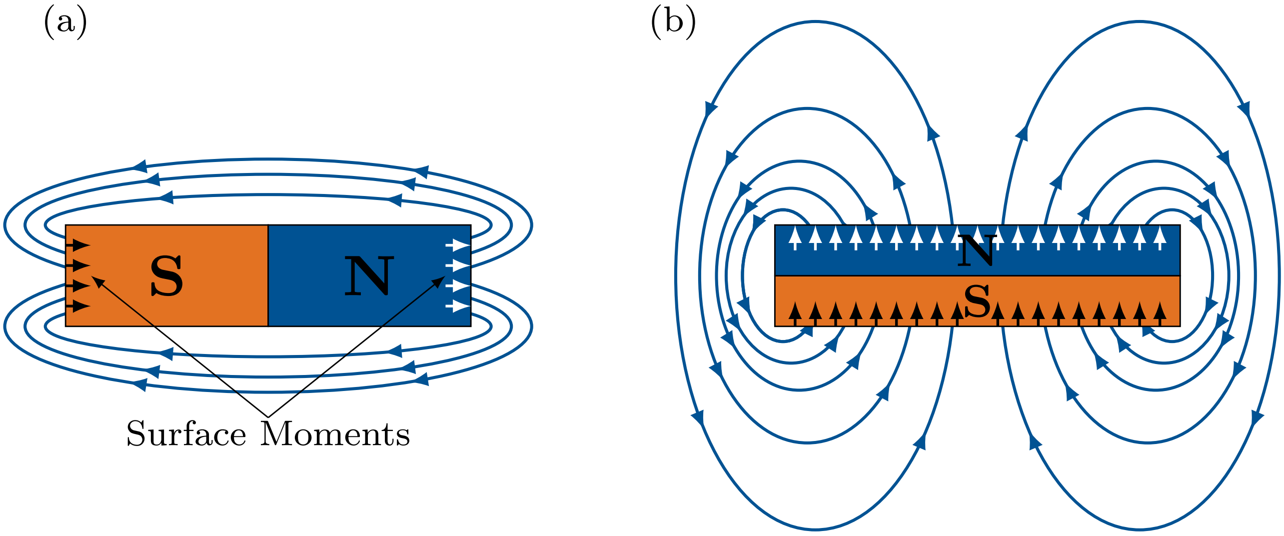

**Figure 2.8** Sketch of the stray field distribution of a bar-magnet. In (a), the magnetization points along the dominant axis of the bar, resulting in a small number of uncompensated surface poles and reduced stray-field energies, compared to (b) where the magnetization points normal the surface.

### Magnetocrystalline Anisotropy

The Magnetocrystalline anisotropy (also often described as uniaxial anisotropy) arises from spin-orbit interactions and is especially relevant for crystalline systems. The electron orbital angular momenta in the unit-cells are coupled to the respective electron spins and therefore experience a torque upon the reorientation of the magnetization. This torque results in preferential magnetization axis (easy-axis) depending on the structure of the unit cell [71]. The preferential axes can be derived from *ab-initio* calculations, however, with varying degrees of success [71]. The magnetocrystalline anisotropy is especially pronounced for hexagonal lattices [70]. Without an external field, the magnetization will always align along this magnetocrystalline easy axis. The uniaxial anisotropy energy $K_\mathrm{u}$ is therefore best minimized for an angle $\theta$ between easy-axis and magnetization of $\theta = 0 \,\mathrm{or}\, \pi$. The angle dependent energy is often described as a simplified power series, integrating over the entire sample volume $V$ according to [70]

$$E_\mathrm{u} = \int (K_{\mathrm{u}_1} \sin^2\theta + K_{\mathrm{u}_2} \sin^4\theta + K_{\mathrm{u}_3} \sin^6\theta + \ldots)\,\mathrm{d}V \approx V(K_{\mathrm{u}_1} \sin^2\theta + K_{\mathrm{u}_2} \sin^4\theta)\,. \tag{2.29}$$

The anisotropy energy per unit volume is then given as

$$K_\mathrm{u} \approx K_{\mathrm{u}_1} \sin^2\theta + K_{\mathrm{u}_2} \sin^4\theta\,, \tag{2.30}$$

with the sign of $K_\mathrm{u}$ giving the direction of the easy axis (in-plane anisotropy for $K_\mathrm{u} < 0$ and out-of-plane anisotropy for $K_\mathrm{u} > 0$) [90]. For many systems it furthermore holds that $K_{\mathrm{u}_2} \ll K_{\mathrm{u}_1}$, leading to the fact that $K_{\mathrm{u}_2}$ is often neglected [70], [90].

### Interface Anisotropy

Magnetic materials exhibit a magnetic anisotropy component at their surfaces, originating from broken translational symmetry at the discontinuity formed by the interface [71], [75]. The crystal either stops abruptly, or the lattice is disturbed by the abrupt transition to another material. This circumstance has profound consequences for the local anisotropies, usually leading to an anisotropy component normal to the surface plane (in-plane anisotropies may also occur in exceptional cases, e.g., Ni/Cu). The energy per unit area calculates as

$$E_\mathrm{s} = N K_\mathrm{s} \sin^2\varphi\,, \tag{2.31}$$

where $N$ is the number of interfaces with the mean interface anisotropy $K_\mathrm{s}$ and $\varphi$ is the angle between the magnetization and the surface normal. In bulk materials, the interface anisotropy is of no relevance, as the surface to volume ratio is too small [70], [90]. However, in the case of superlattices or atomically thin-layers, the interface anisotropy is the dominant contributor to the perpendicular magnetic anisotropy. Typical values of $K_\mathrm{s}$ range between $0.1\,\mathrm{mJ\,m^{-2}}$ and $1\,\mathrm{mJ\,m^{-2}}$ [70], [82], [90], [91].

### Additional Magnetic Energies

Additional but within the context of this work less relevant energy contributions, arise for example from magnetoelastic ($E_\mathrm{me}$) or magnetostrictive ($E_\mathrm{ms}$) effects. The magnetoelastic anisotropy is closely related to the magneto-crystalline anisotropy but describes the effects of lattice strain or stress on the magnetization. On the other hand, magnetostriction describes the slight change in lattice spacing (translating into volume) upon the occurrence of magnetic order. Individual iron-rich alloys, for example, possess the ability to minimize their magnetic energy by expanding ($\approx 1\,\%$) and thus increasing their exchange coupling [70].

### Temperature

Temperature, although not a magnetic energy per se, needs to be considered at this point, as it is a vital but often neglected parameter, affecting all aforementioned magnetic interaction and energies. The most notable effect is without a doubt on the saturation magnetization, which generally decreases with increasing thermal energy up to the curie temperature, beyond which thermal fluctuations completely overcome the ferromagnetic order. In broader terms, increasing temperatures come with increasing disorder and increased probabilities to overcome existing energy barriers by thermal fluctuations alone. Therefore, most of the considerations and arguments here are done assuming the material parameters at room temperature, thus not considering temperature directly. In micromagnetic simulations, temperatures are usually modeled as an additional stochastic field term [92], [93]

### Combined Magnetic Energies

Via combining the primary magnetic energies it is possible to calculate the effective anisotropy ($K_\mathrm{eff}$) of a magnet and predict whether the easy axis of the magnetization points in or out of the sample plane. The total effective anisotropy per unit area calculates as

$$K_\mathrm{eff} t_\mathrm{film} \approx \underbrace{K_\mathrm{u} t_\mathrm{film}}_{\text{Uniaxial term}} \underbrace{-\frac{1}{2}\mu_0 M_\mathrm{s}^2 t_\mathrm{film}}_{\text{Demag term}} + \underbrace{N K_\mathrm{s}}_{\text{Surface term}} , \tag{2.32}$$

with the respective uniaxial, demagnetizing and surface terms ($N$ being the number of surfaces) and $t_\mathrm{film}$ as the film thickness [90]. In many cases, not the areal but the volume density is used, it amounts to

$$K_\mathrm{eff} \approx K_\mathrm{u} - \frac{1}{2}\mu_0 M_\mathrm{s}^2 + \frac{N K_\mathrm{s}}{t_\mathrm{film}} \tag{2.33}$$

The easy axis of the system will point out-of-plane for $K_\mathrm{eff} > 0$. Both the uniaxial and the demagnetizing components scale with the film thickness. Thus, they are often summarized under the term volume anisotropy ($K_\mathrm{v} = K_\mathrm{u} - \frac{1}{2}\mu_0 M_\mathrm{s}^2$). Since interface effects do not scale with the film thickness, and $K_\mathrm{v}$ is found to be negative in almost all cases, a steady decline in the out-of-plane anisotropy for increasing film thicknesses is observed. Via Equation (2.32) it is possible to formulate a simple relation, defining the transition thickness $t_\mathrm{crit}$ at which the easy axis turns from the film normal, into the plane [90]. It calculates as

$$t_\mathrm{crit} \approx -\frac{N K_\mathrm{s}}{K_\mathrm{u} - \frac{1}{2}\mu_0 M_\mathrm{s}^2} . \tag{2.34}$$

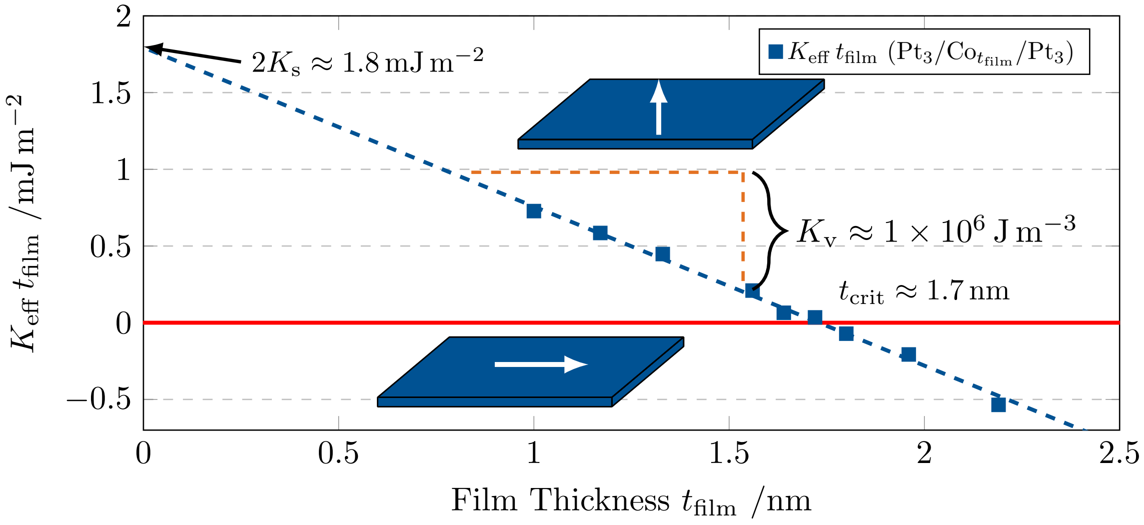

**Figure 2.9** A plot of the thickness-dependent effective anisotropy per unit area $K_\mathrm{eff} \cdot t_\mathrm{film}$ of a series of Pt/Co/Pt trilayer with increasing cobalt thickness. A liner fit to the data points is used to determine the volume anisotropy $K_\mathrm{v}$ as the slope, and the $2K_\mathrm{s}$ interface anisotropy as the y-intercept of the function.

In order to extract the individual anisotropy components from experiments, the linearity of Equation (2.32) is used. The areal anisotropy density $K_{\mathrm{eff}} t_{\mathrm{film}}$ is thereby plotted against the increasing film thickness. The volume anisotropy is then given as the slope of a linear fit to the data. The interface anisotropy is given as the intersection with the y-axis, respectively [90]. Figure 2.9 illustrates this relation as an example, showing the thickness-dependent anisotropy evolution of a Pt/Co/Pt trilayer system. However, the simple linear model of Equation (2.32) and (2.34) only holds, assuming a constant $K_{\mathrm{u}}$ and $M_{\mathrm{s}}$ which, for atomically thin layers is often not the case.

## 2.5 Magnetization Dynamics

Now that we have developed a rough understanding of magnetic order on atomic and inter-atomic scales, we can zoom out and look at magnetic order on a larger scale. Here, a comprehensive model for the dynamics of large ensembles of neighboring spins was developed, considering the different forms of coupling (e.g., exchange or dipole coupling) in combination with the different magnetic energies (modeled as effective fields). This model was modified and improved upon several times and is, in its current form, best known as the *Landau-Lifshitz-Gilbert* (LLG) Equation [94]–[97]. It has to be noted though, that *Slonczewski* made further contributions to incorporate spin-transfer torques (STT) [98], [99]. Since STT experiments are not part of this work, we neglect these contributions at this point. The LLG equation describes the magnetic moment of a unit volume of magnetization as the rotation of a rigid body (the magnetization vector $\boldsymbol{m}$) around an effective field vector $\boldsymbol{H}_{\mathrm{eff}}$. This motion is schematically illustrated in Figure 2.10 and can be mathematically expressed as

$$\frac{\mathrm{d}\boldsymbol{m}(t)}{\mathrm{d}t} = -\gamma\mu_0 \boldsymbol{m} \times \boldsymbol{H}_{\mathrm{eff}} + \alpha \boldsymbol{m} \times \frac{\mathrm{d}\boldsymbol{m}(t)}{\mathrm{d}t}\,, \tag{2.35}$$

where $\boldsymbol{m} = \frac{\boldsymbol{M}}{M_{\mathrm{s}}}$ describes the normalized magnetization vector, $\gamma$ denotes the gyromagnetic ratio of the electrons ($\frac{\gamma}{2\pi} \approx 2.80 \times 10^{10}\,\mathrm{Hz\,T^{-1}}$ or $\gamma \approx 1.760 \times 10^{11}\,\mathrm{rad\,s^{-1}\,T^{-1}}$) and $\alpha$ the material specific damping constant [70], [75]. As depicted in Figure 2.10, the equation consists of two distinct terms, a precession

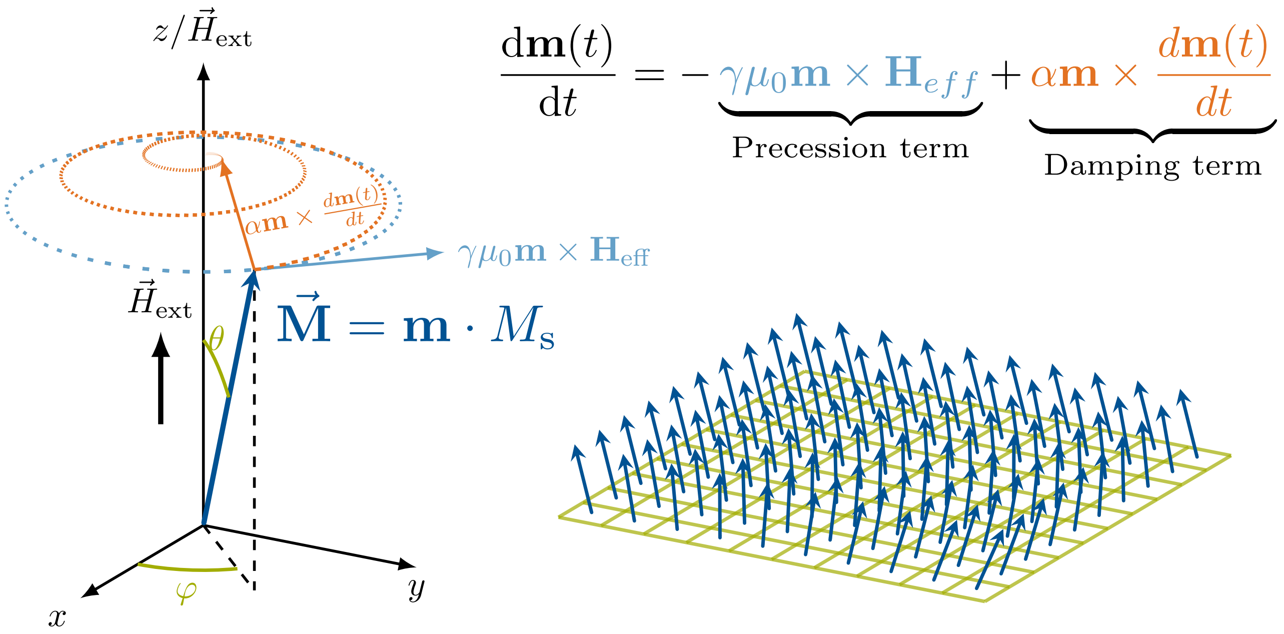

**Figure 2.10** Overview of the Landau-Lifshitz-Gilbert equation. The sketch on the left, draws a vivid picture of the equation on the top right. The normalized magnetization vector $\vec{\boldsymbol{M}}$ spiralizes around $\vec{H}_{\mathrm{ext}}$ eventually aligning with $\vec{H}_{\mathrm{ext}}$. The sketch on the bottom right illustrates an ensemble of interacting spin on a unit grid, all described individually by the LLG equation.

term, and a damping term. Without damping, the magnetization vector $\vec{M}$ would precesses around $\boldsymbol{H}_{\text{eff}}$ with a constant angle $\theta$. With damping, the magnetization asymptotically spirals towards $\boldsymbol{H}_{\text{eff}}$ continuously reducing $\theta$. The precession term is dominated by the effective field vector $\boldsymbol{H}_{\text{eff}}$, which summarizes all aforementioned magnetic energies and coupling terms, translated into one local field according to

$$\boldsymbol{H}_{\text{eff}} = \boldsymbol{H}_{\text{External}} + \boldsymbol{H}_{\text{Demag}} + \boldsymbol{H}_{\text{Exchange}} + \boldsymbol{H}_{\text{Anis}} + \boldsymbol{H}_{\text{Thermal}} \, . \tag{2.36}$$

This creates a simplistic though practical perspective, from which most parameters and interactions are expressed via an appropriate magnetic field. The thermal field can thereby be used to introduce characteristic temperature effects via a stochastic field vector, modeled as

$$\boldsymbol{H}_{\text{Thermal}} = \boldsymbol{\eta}\sqrt{\frac{2k_{\text{B}}T\alpha}{\mu_0\gamma M_{\text{s}}V\Delta t}} \, , \tag{2.37}$$

with $k_{\text{B}}T$ as the characteristic *Boltzmann* term, $\Delta t$ as the time step, and $V$ as the volume of the unit cell [94], [100]. The randomly (Gaussian distributed) oriented vector $\boldsymbol{\eta}$ is furthermore redetermined for every time step. Today, the LLG equation is applied very successfully in the description of the dynamics of small and large spin ensembles. Applied in micromagnetic simulations, it allows the modeling of most magnetic phenomena with very high accuracy. However, the accurate simulation of larger structures still results in extreme computation requirements, which to this date cannot be met for all relevant cases [92], [100], [101].

## 2.6 Stoner–Wohlfarth Model

The *Stoner-Wolfarth* (SW) model is one of the simplest but also one of the most successful models, describing the magnetization of small magnetic particles under the influence of various magnetic forces and energies. In 1948 *E. Stoner* and *E. Wohlfarth* published this model, based on geometric considerations [102]. The model describes the magnetiztaion of the particle as one macro spin and sums up all relevant and mostly angle-dependent magnetic energies to find the energetically most favorable magnetization direction. The most straightforward example of an angle-dependent magnetic energy is the uniaxial anisotropy. Its energy is $\propto \sin^2(\theta)$, with $\theta$ being the angle between the anisotropy axis and the magnetization vector in a three-dimensional space. This is schematically illustrated in Figure 2.11 (a) with an anisotropy component running along the dominant extension of the SW particle, an ellipsoid with a homogeneous magnetization $\vec{M}$. In its simplest form, the SW model of a magnetic particle only considers the anisotropies and the respective *Zeeman* energy originating from the interaction between the magnetization and an externally applied magnetic field. The total magnetic energy $E_{\text{tot}}$ of such a SW particle calculates as,

$$E_{\text{tot}} = E_{\text{anis}} + E_{\text{Zeeman}} = K_{\text{eff}}V_{\text{sw}}\sin^2(\theta) + \mu_0 M_{\text{s}} V_{\text{sw}} H_{\text{ext}} \cos(\varphi - \theta) \, , \tag{2.38}$$

where $V_{\text{sw}}$ is the volume of the *Stoner–Wohlfarth* particle, $E_{\text{anis}}$ describes the anisotropy, $H_{\text{ext}}$ the external field, and the angles $\theta$ and $\varphi$ describe the respective angles between the magnetization/external field and the easy axis [75], [102], [103]. Additional energy components (e.g., exchange bias or RKKY interaction) can be added, provided the $\theta$ and $\varphi$ angle dependencies are known. Minimizing $E_{\text{tot}}$ for the given input parameter then allows determining the preferred magnetization direction of the particle. This allows to precisely calculate the response of the magnetization to different magnetic fields. Figure 2.11 (b) depicts the normalized magnitude of the magnetization component along the x-axis versus the external magnetic field strength at different angles $\varphi$. In other words, the plot shows the magnetic hysteresis of the *Stoner–Wohlfarth* particle. The shape of the hysteresis critically depends on the field angle $\varphi$, as the magnetization rotates to find the respective energy minima. At $\varphi = 180°$ (external field along the easy axis), the field necessary to reverse the magnetization is equal to $2K_{\text{eff}}/\mu_0 M_{\text{s}}$, the so-called anisotropy field $H_{\text{k}}$. At this field, a coherent rotation of the magnetization by $\varphi = 180°$ occurs. This is not the case for angles $\varphi \neq 180°$ or 0°, as the energy minimum and thus the magnetization coherently rotates with $H_{\text{ext}}$. This is especially apparent for $\varphi = \pm 90°$, showing a continuous and linear tilting of the magnetization off the easy axis until $H_k$ where the magnetization aligns perpendicular to the easy axis [75].

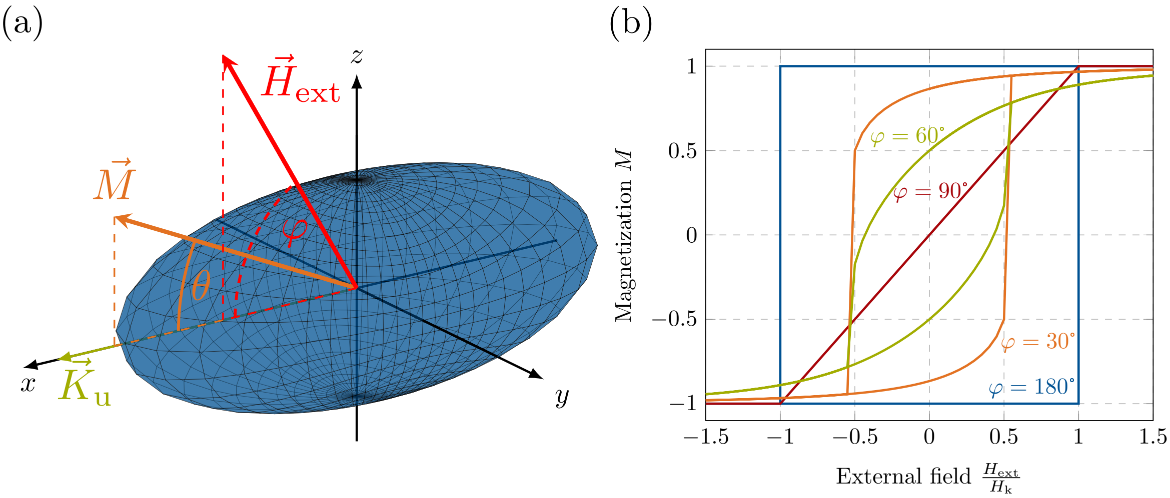

**Figure 2.11** In (a), an ellipsoidal *Stoner-Wolfarth* particle with a uniaxial shape anisotropy component $\vec{K}_{\text{u}}$ along the x-axis is displayed under the influence of the external magnetic field $\vec{H}_{\text{ext}}$. In (b), the magnetic hysteresis of the particle for various field angles $\varphi$ is shown. The shape of the hysteresis depends on the field angle $\varphi$, as the magnetization rotates to find the respective energy minima.

## 2.7 Magnetic Domain Theory

The Magnetic domain theory is a description of small to long-range magnetic order. The order arises from the delicate interplay between the long-range dipole interaction and the short-range exchange coupling on these scales. Although we were able to almost neglect the dipole interaction in the earlier sections due to the comparatively small magnetic moments of the individual atoms, it now becomes the driving force due to its long-range and the sheer number of magnetic moments in a given material. Magnetic domain theory, generally speaking, describes the arising ordering of spins in the range from $\approx 50$ nm to hundreds of µm or even mm. A magnetic domain is thereby defined as an area within a magnetic media that exhibits a uniform magnetization in one direction. In case that there is more than one domain, it is bordered by another domain showing a magnetization in the opposite direction (only in the case of materials with out-of-plane magnetization). The transition regions between individual domains are called domain walls (DW). They comprise a smooth transition from one magnetization direction to the other. The dimensions and wall geometries critically depend on the aforementioned material parameters and interacting forces. Nevertheless, the formation of domains can be attributed to a simple fact. The energies of the demagnetizing fields grow proportional to the domain area. However, the energy cost of creating a domain wall only scales with the circumference of the domain, thus always leading to multi-domain formation beyond a critical domain size. A variety of different OOP domain patterns is depicted in Figure 2.12 as an example. To stay within the framework of this work, we will only cover this theory briefly and constrain all consideration to magnetic media with an out-of-plane easy axis and the mechanisms most relevant for nanomagnetic logic and DW dynamics.

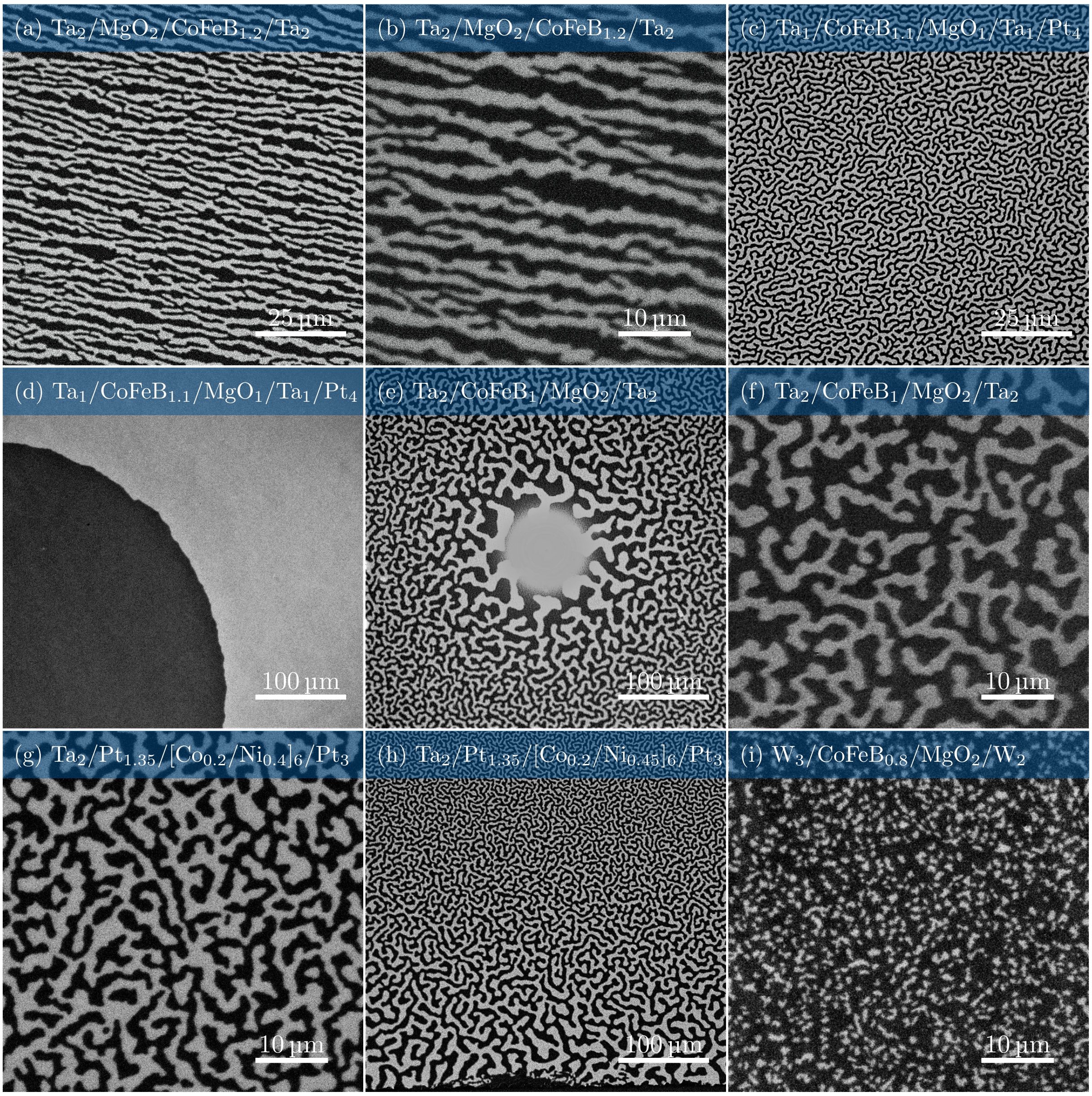

**Figure 2.12** Images of different magnetic domain patterns. The bright and dark areas indicate the opposing magnetization directions (up/down). In (a) and (b), the stripe domains of a $Ta_2/MgO_2/CoFeB_{1.2}/Ta_2$ stack are displayed at different magnifications. After deposition, the stack is annealed at 250 °C for 10 min. In (c), the labyrinthine domains of an as-grown $Ta_1/CoFeB_{1.1}/MgO_1/Ta_1/Pt_4$ stack are shown. The same stack is shown after annealing (275 °C for 5 min) in (d). In (e), a domain size gradient around a large central particle (bright spot) is shown (the sputtered $Ta_2/CoFeB_1/MgO_2/Ta_2$ film was annealed at 275 °C for 5 min). The gradient is the result of shadowing effects during film growth. The image in (f) shows the domain configuration of the same stack with higher magnification. In (g) and (h), a $Ta_2/Pt_{1.35}/[Co_{0.2}/Ni_{0.4}]_6/Pt_3$ stack is shown (not annealed). In (h), the domain configuration at the edge of the sample is shown, depicting a size gradient due to shadowing effects. In (i), the naturally forming bubble domains of a $W_3/CoFeB_{0.8}/MgO_2/W_2$ stack are displayed (annealed at 250 °C for 15 min). The respective film thicknesses are given in nm.

### 2.7.1 Domain Configuration & Size

The domain configuration in equilibrium is the result of the intricate interplay between all the aforementioned magnetic energies. Most notably, the dipole coupling, the exchange interaction, and the uni-axial OOP anisotropy, present in the described systems. Accurately modeling the domain configuration is no simple task. Today, the best results are obtained via micromagnetic simulations, taking into account and minimizing all relevant energy therms [92], [93], [101]. Nevertheless, analytical models have been developed from the early 1990s to the mid-2000s after the discovery of magnetic domains in ultra-thin films in the late 1980s [1].
It is essential to stress the fact that this section only considers atomically thin layers with strong PMA, where the domain size $D$ is always much larger than the film thickness $t_{\mathrm{film}}$ ($D \gg t_{\mathrm{film}}$). Important contributions in modeling and understanding the domain configurations in these films were made by *B. Kablan*, *A. Sukstanskii*, and others [104]–[107]. The following discussion is based on their works.

#### Analytic Domain Size Model

As we have already established, the magnetic system tries to reduce its dipole energy by creating magnetic domains with their respective magnetizations pointing in opposing directions. However, this process is offset by the energy "price" required to create the necessary domain walls. The number (and thus the size) of domains is therefore in first approximation determined by a trade-off between the DW energy and the dipole energy of the system. We can thus define a characteristic domain size $D_0$ also called "*characteristic dipolar length*" by dividing the DW energy density by the dipole energy and derive the term,

$$D_0 = \frac{\sigma_{\mathrm{DW}}}{\mu_0 M_{\mathrm{s}}^2} \approx 5 - 20\,\mathrm{nm}, \tag{2.39}$$

with $\sigma_{DW}$[1] as the energy density of the domain wall (later discussed in detail in section 2.8) [104], [108]. For a simple labyrinthine domain model at 0 K, and a film thickness smaller than $D_0$, the model developed by *B. Kablan* predicts a scaling of the domain sizes according to

$$D_{\mathrm{size}} \approx C \cdot t_{\mathrm{film}} e^{\pi D_0 / t_{\mathrm{film}}} \approx C \cdot t_{\mathrm{film}} \exp\left[\frac{\pi \sigma_{\mathrm{w}}}{t_{\mathrm{film}} \mu_0 M_{\mathrm{s}}^2}\right], \tag{2.40}$$

with $t_{\mathrm{film}}$ as the film thickness and $C$ as a fitting prefactor [104]. Figure 2.13 (a) depicts the calculated domain size evolution with the film thickness $t_{\mathrm{film}}$ according to the described model for a thin film with out-of-plane magnetization. The model gives satisfying results within thicknesses roughly ranging from 1 to 5 atomic layers. However, the model does not take thickness-dependent changes in the material parameter into account, which are common for atomically thin layers, and must therefore be used very carefully. Furthermore, the model can not only be used to show the thickness dependencies but also to visualize the anisotropy and saturation magnetization dependencies. Figure 2.13 (b) displays the calculated domain size at a fixed film thickness of 1 nm with changing material parameters. Thereby only one parameter is changed ($K_{\mathrm{u}}$ or $M_{\mathrm{s}}$) while the other is kept constant. Both plots underline the extreme sensitivity of the domain size towards changes in the film thickness and the individual material parameter.

---

[1] The energy density of a DW in thin-films with OOP magnetization amounts to $\sigma_{\mathrm{DW}} \approx \pi\sqrt{A_{\mathrm{ex}} K_{\mathrm{eff}}} \approx \pi\sqrt{A_{\mathrm{ex}}(K_{\mathrm{u}} - 0.5\mu_0 {M_{\mathrm{s}}}^2)}$

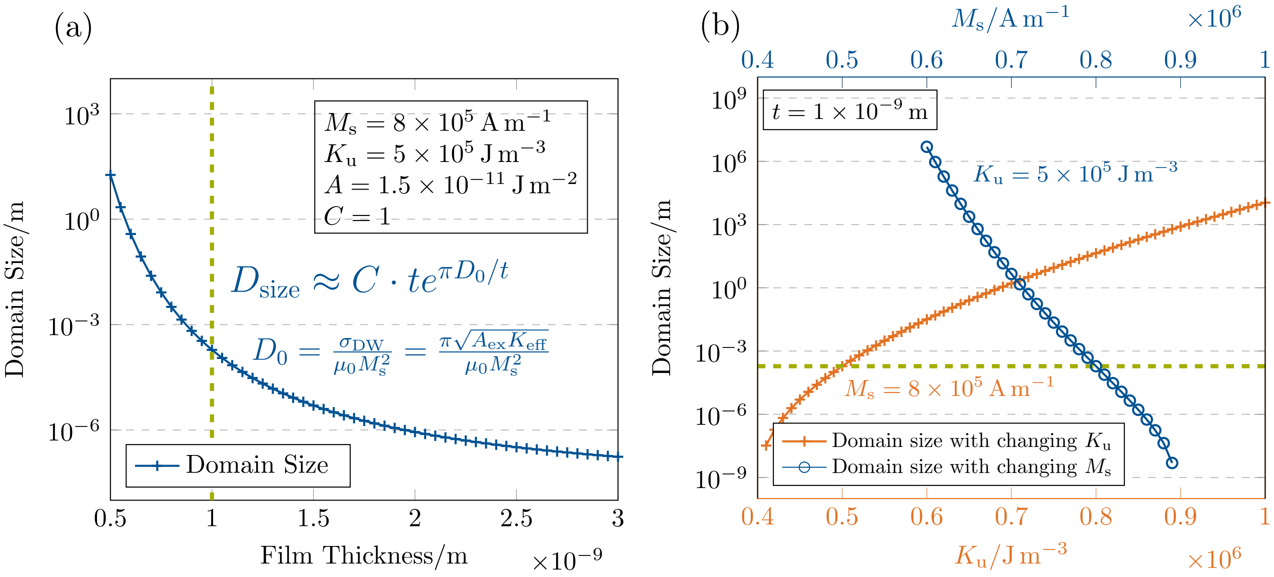

**Figure 2.13** Calculated domain sizes according to the model developed by *B. Kablan*. In (a), the film thickness dependent domain size is depicted. The inlet shows the used material parameters. The dotted green line shows the constant film thickness used for (b). In (b), the domain size evolution with changing material parameters is shown. The orange plot corresponds to changes in the uniaxial anisotropy constant $K_u$ while keeping the saturation magnetization $M_s$ and film thickness constant. The blue plot shows changes depending on $M_s$ respectively.

#### Single Domain Limit

Important for technological applications is the so-called single-domain limit. It defines a size threshold over which it is more energetically favorable for a magnetic particle to form domains rather than feature a homogeneous magnetization. This threshold limits the design choices for the used materials and the overall magnetic volume and geometry of the magnets, since most applications necessitate single domain states. An estimate for this critical parameter can be derived from the characteristic dipolar length ($D_0$) by adding a shape-dependent demagnetizing factor $N_{\mathrm{xyz}}$. For a simple ellipsoid, this value is usually given as ≈ 72 [75].

$$D_{\mathrm{crit}} = N_{\mathrm{xyz}} \frac{\sigma_{\mathrm{DW}}}{\mu_0 M_s^2} \approx 72 \frac{\sigma_{\mathrm{DW}}}{\mu_0 M_s^2}\,. \tag{2.41}$$

When analyzing Equation 2.41, a clear picture emerges, while the domain wall energy density $\sigma_{\mathrm{DW}}$ is, of course, a relevant term, the dominating variable is the saturation magnetization. The saturation magnetization has, thus, profound consequences for the magnet design. In order to achieve large total magnetic moments (essential for field-coupled devices), a high saturation magnetization is desired, which in turn necessitates device scaling to retain a single-domain state. However, this circumstance heavily limits the parameter space for university research in its current state, as the widely used optical detection schemes require magnet sizes above the diffraction limit (≈ 200 nm).

## 2.8 Domain Walls in Atomically Thin Layers

The term domain wall (DW) describes the naturally occurring magnetic discontinuity that separates the individual domains with opposing magnetization directions. They constitute a continuous transition from one magnetization direction to the other and are thus essential in understanding the complex phenomena involved in the magnetization reversal of out-of-plane magnets. For the following discussion, we use the picture of a magnetic nanowire with a width much larger than the domain wall width ($\Delta_{\mathrm{DW}}$) as depicted in Figure 2.14 (b). In order to better understand the different

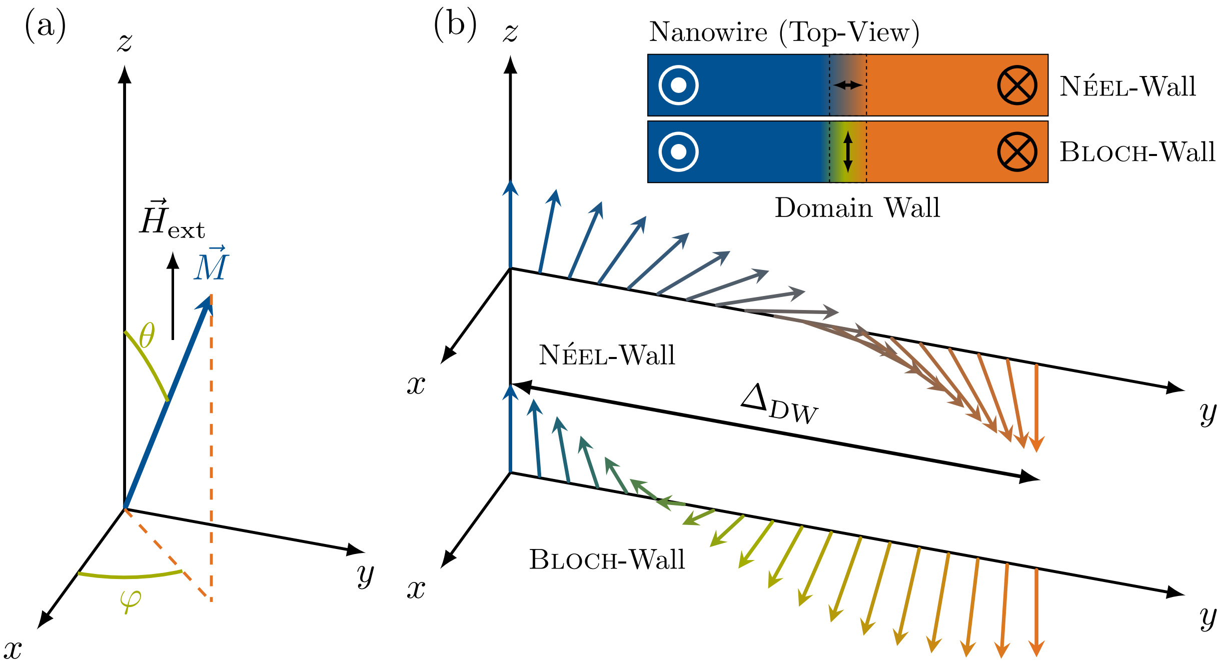

**Figure 2.14** In (a), the three-dimensional magnetization vector $\boldsymbol{M}$ is illustrated. In (b), a pure *Bloch*-type as well as a *Néel*-type domain wall is illustrated with its respective rotation profile. While in the case of a *Néel*-wall, the spin transition occurs only in the *yz*-plane, different behavior is observed for a *Bloch*-wall. Here, the transition takes place solely in the *xz*-plane. In the upper right corner, a top view of the wall areas highlighting the axis of the respective DW-cores is provided.

wall geometries, we again consider the magnetization vector $\vec{M}$ as depicted in Figure 2.14 (a) with its distinct $x$, $y$, and $z$ components together with the angles $\theta$ and $\varphi$. There are, generally speaking, two ways for the magnetization to rotate by ±180° ($\theta$) within the width of the wall. The first and simplest DW profile is a coherent spin-rotation along the nano-wire and strictly within the easy axis of the material (rotation only within the z and y-axis with $\varphi = \pm 90°$). This configuration, depicted in the upper part of Figure 2.14 (b) is called a *Néel*-wall. However, there exists a second wall configuration, called a *Bloch*-wall, in which the spins only rotate in the $x$ and $z$ plane, thus perpendicular to the nano-wire ($\varphi = 0°$ or $180°$). In both cases, the magnetization can either rotate clock-wise (CW) or counter clock-wise (CCW) through the extension of the DW with the width $\Delta_{\text{DW}}$. Clock-wise, as well as CCW *Bloch* walls, usually exist simultaneously within a structure. This is beneficial to reduce the stray field energy of the walls [75]. In reality, both wall configurations are usually found in superposition, with one of the two configurations being more pronounced. The final DW configuration will then lean towards the wall type featuring the lower energy cost, which in turn depends on the material parameters, the crystal structure, and the thickness of the ferromagnetic layer.

### 2.8.1 Domain Wall Widths and Energies

To calculate the individual wall energies, we first have to find estimates for the respective wall widths and corresponding energy densities. The actual domain wall width $\Delta_{\text{DW}}$ can, due to its asymptotic nature, only be approximated [70], [89], [109]. This is usually done by a tangential approach with varying criteria, leading to slightly different prefactors (e.g., 4 or $\pi$). The characteristic width of a domain wall depends on the exchange stiffness, the anisotropy terms, and the acting magnetostatic forces. The exchange energy is best minimized by infinitely wide walls, while the opposite is true for the anisotropy energy. The magnetostatic demagnetizing energy acts directly on the anisotropy and depends on wall type as well as geometry. The characteristic DW width is therefore given as

$$\Delta_{\mathrm{DW}} = \pi\sqrt{\frac{A_{\mathrm{ex}}}{K_{\mathrm{u}} + \frac{1}{2}\mu_0 M_{\mathrm{s}}^2(N_{\mathrm{x}}\cos^2\varphi + N_{\mathrm{y}}\sin^2\varphi - N_{\mathrm{z}})}}\,, \tag{2.42}$$

with $A_{\mathrm{ex}}$ as the exchange constant and $K_{\mathrm{u}}$ as the sum of all anisotropy terms (not to be confused with $K_{\mathrm{eff}}$)[89]. The pre-factors $N_{\mathrm{x}}$, $N_{\mathrm{y}}$, and $N_{\mathrm{z}}$ denote the axis specific demagnetizing components, basically a relative measure of the axis specific demagnetizing energy [89], [109]. They are very difficult to calculate precisely, but can be approximated for simple shapes. For an uniform ellipsoid it generally holds , that $N_{\mathrm{x}} + N_{\mathrm{y}} + N_{\mathrm{z}} = 1$ [89]. For an infinite layer with OOP magnetization we can therefore write $N_{\mathrm{x}} = N_{\mathrm{y}} \approx 0$, and $N_{\mathrm{z}} \approx 1$. The DW specific components, now depend on the geometry of the investigated object. We fist consider a *Bloch*-wall in an infinite and thick layer, in this case we can write $N_{\mathrm{x}} \approx N_{\mathrm{y}} \approx N_{\mathrm{z}}$. If we now consider $\varphi = 0$ or $\pi$ for a pure *Bloch*-wall, then Equation (2.42) simplifies to

$$\Delta_{\mathrm{DW}}^{Bloch_{\mathrm{thick}}} = \pi\sqrt{\frac{A_{\mathrm{ex}}}{K_{\mathrm{u}} + \frac{1}{2}\mu_0 M_{\mathrm{s}}^2(N_{\mathrm{x}} - N_{\mathrm{z}})}} \approx \pi\sqrt{A_{\mathrm{ex}}/K_{\mathrm{u}}}\,, \tag{2.43}$$

which is the often cited characteristic width of a pure *Bloch*-wall. The wall width is therefore directly proportional to the square root of $A_{\mathrm{ex}}$ and inversely proportional to the square root of $K_{\mathrm{u}}$ [75], [89]. However, if we now look at atomically thin layers we have to consider that $N_{\mathrm{x}} \ll N_{\mathrm{z}}$, which changes equation Equation (2.43) to

$$\Delta_{\mathrm{DW}}^{Bloch_{\mathrm{thin}}} = \pi\sqrt{\frac{A_{\mathrm{ex}}}{K_{\mathrm{u}} - \frac{1}{2}\mu_0 M_{\mathrm{s}}^2 N_{\mathrm{z}}}} \approx \pi\sqrt{A_{\mathrm{ex}}/K_{\mathrm{eff}}}\,. \tag{2.44}$$

In contrast to pure *Bloch*-walls, which have an effective magnetic moment pointing perpendicular to the propagation axis of the DW ($\varphi = 0$ or $\pi$), pure *Néel*-walls rotate along the propagation axis ($\varphi = \pm\frac{\pi}{2}$) as depcited in Figure 2.14 (b). The demagnetizing energy along the y-axis therefore mainly depends on the film thickness. Equation (2.42) therefore simplifies to

$$\Delta_{\mathrm{DW}}^{N\acute{e}el} = \pi\sqrt{\frac{A_{\mathrm{ex}}}{K_{\mathrm{u}} + \frac{1}{2}\mu_0 M_{\mathrm{s}}^2(N_{\mathrm{y}} - N_{\mathrm{z}})}} = \pi\sqrt{\frac{A_{\mathrm{ex}}}{K_{\mathrm{u}} - \frac{1}{2}\mu_0 M_{\mathrm{s}}^2 N_{\mathrm{z}}}} \approx \pi\sqrt{A_{\mathrm{ex}}/K_{\mathrm{eff}}}\,, \tag{2.45}$$

with $N_{\mathrm{y}}$ again much smaller than $N_{\mathrm{z}}$ ($N_{\mathrm{y}} \ll N_{\mathrm{z}}$). To summarize this section, we can state, that for atomically thin layers, where $t_{\mathrm{film}}$ is generally smaller than $\Delta_{\mathrm{DW}}$, it holds that $\Delta_{\mathrm{DW}}^{Bloch} \approx \Delta_{\mathrm{DW}}^{N\acute{e}el} \approx \pi\sqrt{A_{\mathrm{ex}}/K_{\mathrm{eff}}}$ [109]. However, we have to stress the fact, that approximately does not necessarily mean equal ($N_{\mathrm{y}} \ll N_{\mathrm{z}}, N_{\mathrm{x}} \ll N_{\mathrm{z}}, N_{\mathrm{y}} \approx N_{\mathrm{x}}$).

Subsequently we can look at the energy densities of both wall configurations and find, that the same considerations as for the widths hold true here as well. The energy density of a DW is generally described as

$$\sigma_{\mathrm{DW}} \approx \pi\sqrt{A_{\mathrm{ex}} \cdot K}\,, \tag{2.46}$$

which, considering the simple approximations discussed above, results in respective DW energy densities of

$$\sigma_{\mathrm{DW}}^{Bloch} = \pi\sqrt{A_{\mathrm{ex}}(K_{\mathrm{u}} + \frac{1}{2}\mu_0 M_{\mathrm{s}}^2(N_{\mathrm{x}} - N_{\mathrm{z}}))} \approx \pi\sqrt{A_{\mathrm{ex}} K_{\mathrm{eff}}}\,, \tag{2.47}$$

for a pure *Bloch*-wall and

$$\sigma_{\mathrm{DW}}^{N\acute{e}el} = \pi\sqrt{A_{\mathrm{ex}}(K_{\mathrm{u}} + \frac{1}{2}\mu_0 M_{\mathrm{s}}^2(N_{\mathrm{y}} - N_{\mathrm{z}}))} \approx \pi\sqrt{A_{\mathrm{ex}} K_{\mathrm{eff}}} \tag{2.48}$$

for a pure *Néel*-wall [70], [75]. The energy cost creating a domain wall, therefore, increases with both anisotropy and exchange stiffness.
It is important to note, that in systems with strong net interfacial *Dzyaloshinskii–Moriya* interaction (e.g. Pt/Co/HM, HM/CoFeB/Ox), the energy density of *Néel*-walls is further reduced, as the iDMI favors perpendicular alignment of neighboring spins. This leads to a modified equation for the DW energy density according to

$$\sigma_{\mathrm{DW}_{iDMI}}^{N\acute{e}el} \approx \pi\sqrt{A_{\mathrm{ex}} \cdot K_{\mathrm{eff}}} - \pi|D|\,, \tag{2.49}$$

with $D$ as the net iDMI constant in $\mathrm{mJ\,m^{-2}}$ [75].
Finally we have to stress the fact, that the above described derivations are strongly simplified, they assume a homogeneous magnetization inside the wall and do not take dipole energies from magnetization gradients into account. In particular, they fail to explain the transitions between *Bloch* and *Néel* walls occurring at certain geometries and material parameter. For a more comprehensive discussion of DWs in thin films and nanowires it is referred to [89], [109], [110].
Furthermore, for a discussion of DWs in in-plane magnetized thin-films, it is referred to Appendix 9.4.

## 2.9 Domain Wall Dynamics

The magnetization reversal process in magnets with out-of-plane anisotropy usually occurs via domain wall nucleation and subsequent rapid propagation of one or many DWs through the magnet. The dynamics of this process are the subject of this section. First, we will discuss the DW nucleation process and its time, temperature, and field dependencies described by an Arrhenius equation. The second part focuses on field-driven DW motion. The concepts of DW pinning at anisotropy gradients and notches will be introduced before the probabilistic depinning process is explained. Finally, steady as well as precessional DW propagation is discussed, also factoring in the earlier introduced concepts of DW pinning.

### 2.9.1 Domain Wall nucleation

The creation, or in other words, the nucleation of a domain wall, is the starting point of almost all magnetization reversal processes (coherent rotations excluded). We already know that domain walls come at an energy cost. Their existence in the ground state depends on the trade-off between the demagnetizing dipole energies and the counteracting anisotropy and exchange energies. Since we are considering single-domain nanostructures, there are no DWs in the ground state, and the energies are best minimized by a homogeneous magnetization pointing along the easy axis. Having that in mind, the question arises, how does the reversal of the magnetization under external fields take place. The reversal of single domain nanostructures is commonly modeled via the in section 2.6 already introduced *Stoner-Wohlfarth* (SW) model, describing the reversal as a coherent process [102]. However, this seemingly contradicts the premise of this section, explicitly addressing non-coherent, DW-mediated reversal processes. Indeed, the model is only used to describe the coherent spin-rotation of the smallest possible nucleation volume, neglecting the subsequent DW propagation. In most cases, this DW propagation occurs at much smaller driving energies compared to the initial DW nucleation. Thus, the model, although limited in its application to nucleation-dominated systems, still gives valuable insights into the reversal process. The SW model allows to estimate the energy needed to reverse the magnetization in a given volume $V_{\mathrm{nuc}}$ at $0\,\mathrm{K}$. This energy depends on the anisotropy landscape of the material as well as the externally applied magnetic field and can be expressed as

$$E_{\mathrm{nuc}} = K_{\mathrm{eff}} V_{\mathrm{nuc}} (1 - \frac{H_{\mathrm{ext}}}{H_{\mathrm{anis}}})^2\,, \tag{2.50}$$

with $H_{\mathrm{ext}}$ as the applied field and $H_{\mathrm{anis}}$ as the intrinsic anisotropy field $H_{\mathrm{anis}} = \frac{2K_{\mathrm{eff}}}{\mu_0 M_{\mathrm{s}}}$. Since DW nucleation is a thermally activated process, it obeys Arrhenius statistics with the nucleation energy

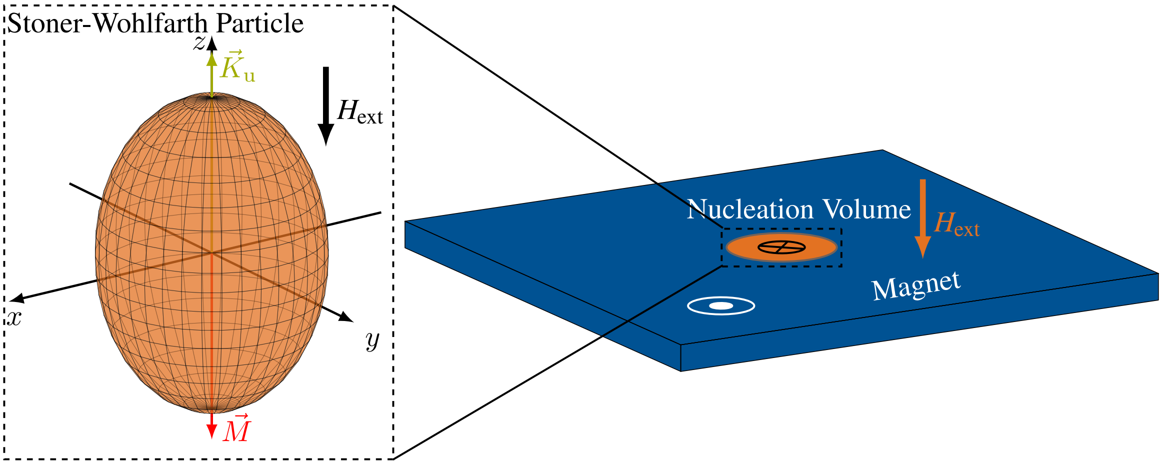

**Figure 2.15** Illustration of the domain wall nucleation process inside a nanomagent. The nucleating volume is thereby modeled as a *Stoner-Wohlfarth* particle with strong out-of-plane anisotropy.

as the barrier to overcome [111], [112]. It is therefore possible to model the time and temperature dependence of the nucleation process with a simple exponential function and derive the nucleation rate $r_\mathrm{nuc}$ to be

$$r_\mathrm{nuc} = f_0 \exp\left[-\frac{E_\mathrm{nuc}}{k_\mathrm{B}T}\right] = f_0 \exp\left[-\frac{K_\mathrm{eff}V_\mathrm{nuc}(1-\frac{H_\mathrm{ext}\mu_0 M_\mathrm{s}}{2K_\mathrm{eff}})^2}{k_\mathrm{B}T}\right], \tag{2.51}$$

with $f_0$ as the so-called attempt frequency of the material (usually in the range of 1 GHz for ferromagnetic thin films). This expression is closely related to the *Néel* relaxation time arising from the *Néel–Arrhenius* model [113]–[115]. From the switching rate, it is possible to derive the switching probability at a given external field $H_\mathrm{ext}$ and pulse width. It amounts to

$$P_\mathrm{nuc} = 1 - \exp\left[\frac{-t_\mathrm{pulse}}{\tau_\mathrm{nuc}}\right], \tag{2.52}$$

with $\tau_\mathrm{nuc}$ as the inverse of the switching rate $r_\mathrm{nuc}$ and $t_\mathrm{pulse}$ as the width of the applied magnetic field pulse in seconds. However, the usage of the macroscopic anisotropy field, describing the energy barrier in Equation (2.51) is only valid at 0 K and ideal materials. Furthermore, the nucleation volume is not know precisely. In experiments $K_\mathrm{eff}$, $V_\mathrm{nuc}$ and $H_\mathrm{anis}$ are therefore substituted by fitting parameters to fit the inverse of the switching rate as

$$\tau_\mathrm{nuc} = f_0^{-1} \exp\left[-\frac{E_0(1-\frac{H_\mathrm{ext}}{H_0})^2}{k_\mathrm{B}T}\right], \tag{2.53}$$

with $E_0$ and $H_0$ as the aforementioned fitting parameter, determined from experiment [56], [116]. Figure. 2.16 (a) depicts the calculated field and time dependent nucleation probability, assuming an energy barrier $E_0 = 28\,k_\mathrm{B}T$, a nucleation field $H_0 = 38\,\mathrm{mT}$ and an attempt frequency $f_0 = 1\,\mathrm{GHz}$. To better express the time and temperature dependence of the switching process, *Michael P. Sharrock* proposed an expression for a characteristic switching field $H_\mathrm{sw}$, defined as the threshold with a switching probability of 50 %. This switching field, according to the above described model calculates as

$$H_\mathrm{sw} = H_\mathrm{s0}\left[1-\left(\frac{k_\mathrm{B}T}{E_0} ln\left(\frac{f_0 t_\mathrm{p}}{ln(2)}\right)\right)^{(1/2)}\right], \tag{2.54}$$

with $H_0$ as the switching field at 0 K and $E_0$ as the energy barrier without field [102], [117]. The energy barrier can be modeled as the product of anisotropy and nucleation volume ($E_0 \approx K_\mathrm{eff}V_\mathrm{nuc}$)

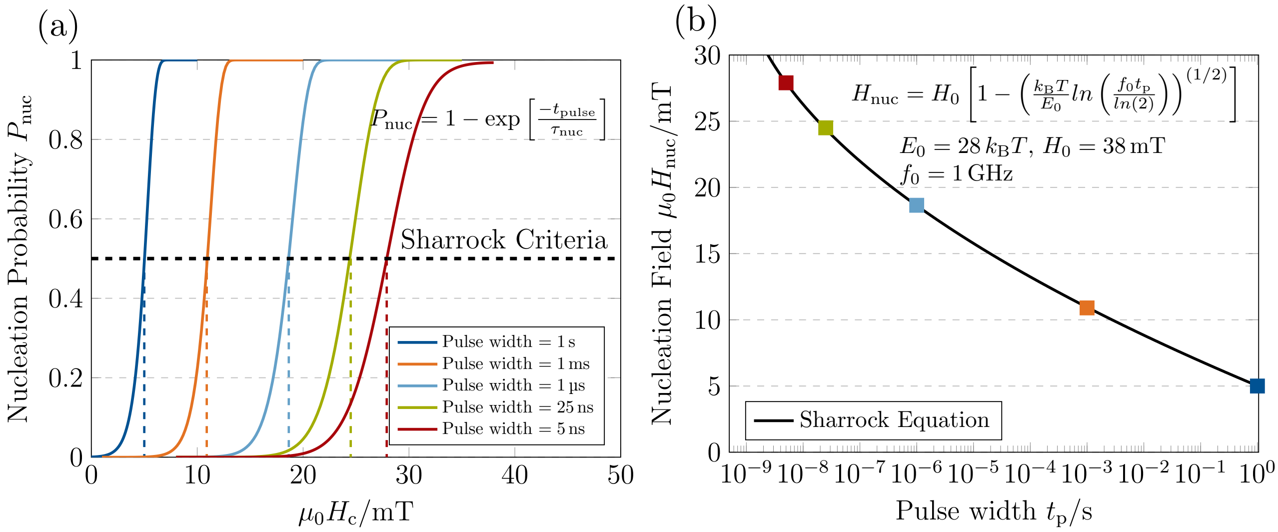

**Figure 2.16** In (a), the domain wall nucleation probability $P_{\text{nuc}}$ as a function of the external field and magnetic field pulse-width. The Sharrock criteria marks $P_{\text{nuc}} = 0.5$. In (b), the external field and pulse-width dependent characteristic nucleation fields according to the Sharrock equation are plotted against the pulse-width.

[111], [112]. There have been various, mostly unsatisfying approaches describing and predicting the nucleation volume. Therefore, it is usually only used as a fitting parameter [111]. However, from geometrical considerations it is possible to define the smallest possible domain wall area $\Delta^2_{\text{DW}}$ as a lower bound for $V_{\text{nuc}}$ [112]. Figure 2.16 (a) and (b) depict the characteristic switching field determined at $P_{\text{nuc}} = 0.5$ plotted against the magnetic field pulse-width.

### 2.9.2 Domain Wall Motion

The motion of domain walls is affected by most of the aforementioned magnetic energy terms. Therefore, the net force acting on the individual DWs is the result of the different magnetic energy components trying to minimize the total energy of the system. In an ideal system, the DWs will therefore converge towards positions resembling the lowest energy state. For example, in the case of a one-dimensional wire, the DW will tend towards the center to best minimize the dipole energy. On the other hand, if the DW is created in a single domain particle, the exchange and anisotropy contributions outweigh the demagnetizing energy. Therefore, the DW will try to minimize its energy

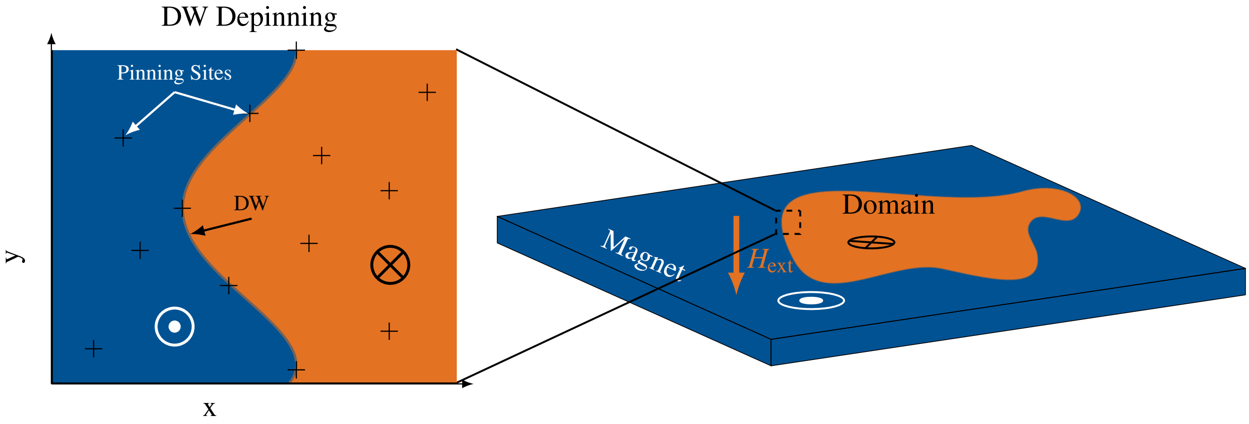

**Figure 2.17** Schematic illustration of the domain expansion via DW propagation, driven by the *Zeeman* pressure from an external magnetic field. The DW propagation occurs via jumps from pinning-site to pinning-site. The DW stays pinned until the energy barrier is overcome, either by the driving field or thermal excitation.

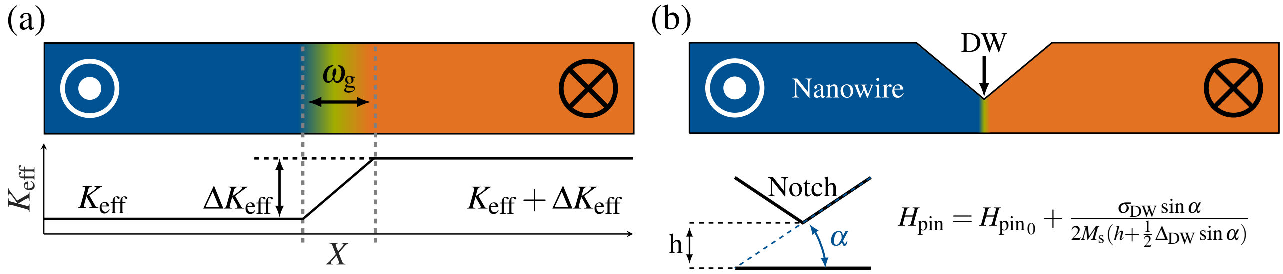

**Figure 2.18** Overview of the two domain wall pinning models. In (a), the pinning at an anisotropy gradient is depicted, the key parameter in this model are the gradient $\Delta K_{eff}$ and its length $\omega_g$. In (b), DW pinning at a notch is used to introduce the concept of pinning due to geometrical constrictions.

by reducing its length until it is annihilated. Furthermore, if an external field is applied to such a system, the introduced Zeeman energy term, which favors spin alignment with the external field, must be added to the minimization problem, shifting the global energy minimum. However, in experiments, the forces driving DW motion in ideal systems are often superseded by the pinning of domain walls at anisotropy gradients. These pinning sites interrupt DW propagation and require gradient-dependent activation energies to be overcome. Therefore, DW motion can be described as a kind of "hopping" process, in which the DW moves from pinning site to pinning site, with a pinning site being any significant anisotropy gradient (defects or geometrical constrictions). A schematic of this process is depicted in Figure 2.17, using a simple two-dimensional model.

### Pinning at Anisotropy Gradients

Domain wall pinning is usually described based on anisotropy discontinuities or geometrical constrictions. Both cases occur naturally but can also be of artificial origin. We will first consider DW-pinning at anisotropy gradients as they occur in nature, at defects, or crystal boundaries. The term anisotropy, in this context, denotes the effective anisotropy $K_{eff}$ which engulfs all anisotropy constants and demagnetizing contribution. The model is therefore also applicable to changes in the saturation magnetization. Figure 2.18 (a) depicts the simplified one-dimensional model of such a gradient with a gradient height of $\Delta K_{eff}$ and a gradient length of $\omega_g$ [118]. For such cases, the field necessary to depin a DW, stuck at the gradient amounts to

$$H_{pin} = \frac{\Delta K_{eff}}{2\mu_0 M_s} \frac{2\Delta_{DW}}{\omega_g} \tanh \frac{\omega_g}{2\Delta_{DW}} , \tag{2.55}$$

where $\Delta_{DW}$ is the width of the pinned domain wall [119], [120]. This expression can further be simplified for very short and very extended anisotropy gradients. In case the $\omega_g$ is much smaller than the DW width (for example, at a grain boundary), the equation reduces to

$$\lim_{\omega_g \to 0} H_{pin} = \frac{\Delta K_{eff}}{2\mu_0 M_s} , \tag{2.56}$$

or vice versa to

$$\lim_{\omega_g \to \infty} H_{pin} = 0 . \tag{2.57}$$

### Pinning at Geometrical Constrictions

The second form of domain wall pinning originates in the fact that in order to pass geometrical constrictions (e.g., notches or corners), the DW must increase its length. The total energy, needed to lengthen the domain wall amounts to

$$\Delta E_{DW} \approx \sigma_{DW} \cdot t_{film} \cdot \Delta l_{DW} , \tag{2.58}$$

with $\Delta l_{\mathrm{DW}}$ as the change in DW length, $\sigma_{\mathrm{DW}}$ as the wall energy density and $t_{\mathrm{film}}$ as the thickness of the magnetic layer [121], [122]. Thus, we can define a $\Delta E_{\mathrm{DW}}$ according the necessary change in DW length $\Delta l_{\mathrm{DW}}$. The depinning field is then defined as the sum of the intrinsic propagation field ($H_{\mathrm{int}}$) and the field necessary to reduce $\Delta l_{\mathrm{DW}}$ to zero and lengthen the DW. For the exemplary case of a one-sided notch as illustrated in Figure 2.18 (b) it holds that $\Delta E_{\mathrm{DW}} \propto \Delta l_{\mathrm{DW}} \propto \sin(\alpha)$ and the depinning field can be expressed as

$$H_{\mathrm{pin}} = H_{\mathrm{int}} + \frac{\sigma_{\mathrm{DW}} \sin(\alpha)}{2M_{\mathrm{s}}(h + \frac{1}{2}\Delta_{\mathrm{DW}} \sin(\alpha))}\,, \tag{2.59}$$

with $h$ as the width and $\alpha$ as the angle of the notch [122]–[124]. This expression can be further simplified for the case of a very wide notch ($h \gg \Delta_{\mathrm{DW}}$) to

$$H_{\mathrm{pin}} \approx H_{\mathrm{int}} + \frac{\sigma_{\mathrm{DW}} \sin(\alpha)}{2M_{\mathrm{s}} h}\,. \tag{2.60}$$

### Domain Wall Depinnig

The described pinning models and the resulting pinning fields are, strictly speaking, only valid at a temperature of 0 K. At temperatures > 0 K we know that energy barriers can be overcome by thermal fluctuations, given enough time. Therefore, we can again formulate an exponential model to estimate the time necessary to depin a DW even if $H_{\mathrm{depin}} > H_{\mathrm{ext}}$. The time $\tau$ to overcome this energy barrier is given by the *Néel–Brown* theory and can be expressed as an exponential function according to

$$\tau_{\mathrm{pin}} = \tau_0 \exp\left[\frac{M_{\mathrm{s}} V_{\mathrm{a}}}{k_{\mathrm{B}} T}(H_{\mathrm{pin}} - H_{\mathrm{ext}})\right]\,, \tag{2.61}$$

with $\tau_0$ as the inverse of the attempt frequency ($f_0^{-1} \approx 1\,\mathrm{ns}$), $H_{\mathrm{pin}}$ as the energy barrier translated into field [113]–[115]. The activation volume $V_{\mathrm{a}}$ refers to the effective magnetic volume at the pining site that is depinned. Figure 2.19 illustrates the measured depinning fields from an anisotropy gradient surrounding a circular area at the center of a nanomagnet. The measurements are complemented by a fit according to Equation (2.61). The logarithmic scale of the x-axis allows linearizing Equation (2.61), where $H_{\mathrm{pin}}$ equals a depinning field at $\tau_0$ and $\frac{M_{\mathrm{s}} V_{\mathrm{a}}}{k_{\mathrm{B}} T}$ indicates the slope of the function.

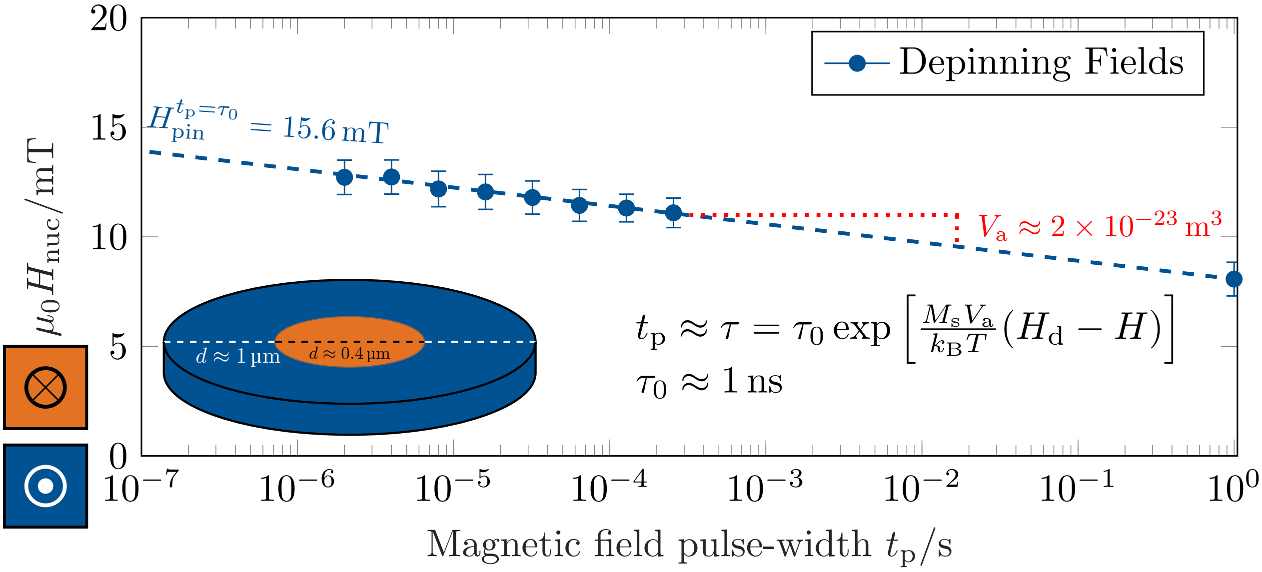

**Figure 2.19** Plot of the measured, time-dependent depinning fields of nanodiscs with a diameter of 1 µm. The DWs are depinned from a circular area with opposing magnetization and a diameter of 400 nm. The data points display the mean magnetic field strength necessary to depin the DW.

### Domain Wall Propagation

To understand domain wall propagation under applied magnetic fields, it is necessary to distinguish between two different kinds of motion and subsequently factor in the above introduced concepts of DW pinning. First, lets consider a simple one-dimensional model of an ideal *Bloch* wall in an ideal medium, with the center-spin pointing in-plane and perpendicular to the propagation axis (running along the y-axis), as depicted in Figure 2.20 (b) and (c). Upon the application of an external magnetic field in $z$-direction, the equilibrium is disturbed and the wall starts moving on order minimize the Zeeman term and find the new energy minimum of the system. The wall mobility during this steady motion is then given by

$$m_{\mathrm{st}} = \frac{\gamma_0 \Delta_{\mathrm{DW}}}{\alpha}\,, \tag{2.62}$$

with $\gamma_0$ as the gyromagnetic ratio of the material, $\alpha$ as the damping factor and $\Delta_{\mathrm{DW}}$ as the width of the DW [125], [126]. Together with the external field, this leads to a field dependent velocity according to

$$v_{\mathrm{st}} = m_{\mathrm{st}} H_{\mathrm{ext}} = \frac{\gamma_0 \Delta_{\mathrm{DW}}}{\alpha} H_{\mathrm{ext}}\,. \tag{2.63}$$

From the equation follows that both, the damping constant $\alpha$, as well as the DW width $\Delta_{\mathrm{DW}}$ affect the velocity [125], [126]. However, this simple model is flawed, as it fails to take the torque of the external field on the DW core into account. The enacted torque per unit volume is calculated as

$$\vec{\Gamma}_H = \mu_0 \vec{\boldsymbol{M}} \times \vec{\boldsymbol{H}}\,, \tag{2.64}$$

where $\vec{\boldsymbol{M}}$ bis the magnetization vector as illustrated in Figure 2.20 (a) and $\vec{\boldsymbol{H}}$ is the external field. This torque results in a precession of the magnetization around $\vec{H}_{\mathrm{ext}}$ (already introduced in section 2.5) [70]. For small fields, this is negligible and the aforementioned model holds, at larger fields however it becomes a relevant factor, as the in-plane magnetized core of the DW is slightly tilted out-of-plane ($\theta \neq 90°$) and the DW starts to deform, breaking its symmetry. Above a critical field strength, called the *Walker*-field, the DW core eventually starts to precess in the x-plane ($\varphi \neq 0$ and time-dependent).

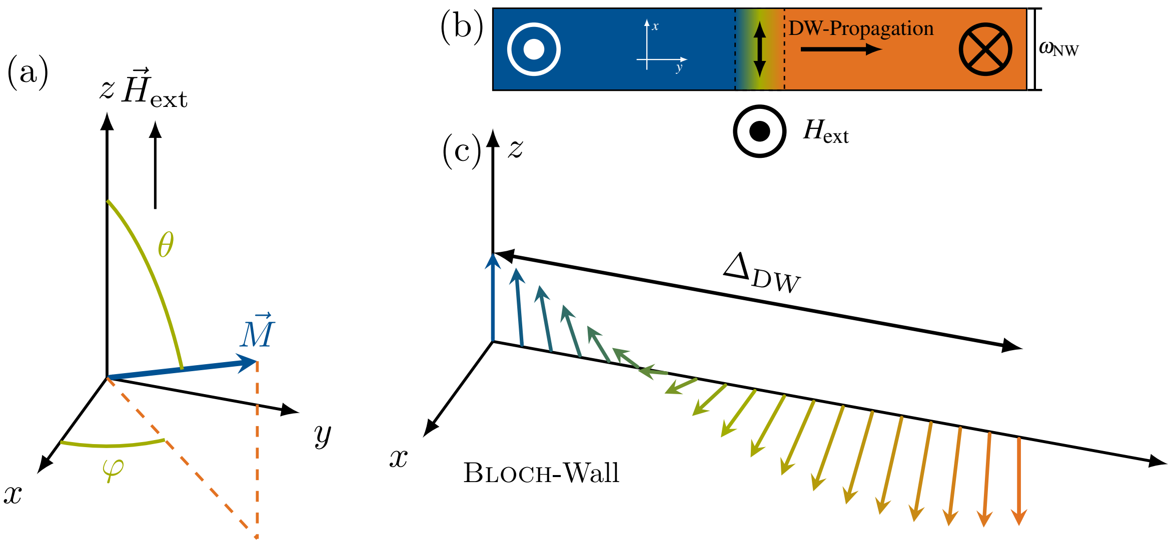

**Figure 2.20** The image in (a), displays the magnetization vector $\vec{\boldsymbol{M}}$ with the angles $\theta$ and $\varphi$ defining its direction in three-dimensional space. In (b), a top view of a pure *Bloch* type DW is shown. The DW propagates to the right under the *Zeeman* pressure of the external field. In (c), the wall profile of the *Bloch*-wall is depicted. The Magnetization $\vec{\boldsymbol{M}}$ rotates by 180° with $\varphi = 0$ or 180°.

This DW "wobble" dissipates relevant parts of the driving field energy, leading to reduced DW mobilities and propagation velocities above the so-called *Walker*-breakdown. The critical *Walker*-field is, besides by material parameter, also defined by the geometry of the system. This becomes apparent when considering the demagnetizing fields of the DW with its distinct $x$ and $y$ components, counteracting $H_{\mathrm{ext}}$. The different magnetostatic demagnetizing factors for the x, y and z-plane are very difficult to calculate for complex shapes. However, for the constricted case of a nanowire, they can be approximated as

$$N_{\mathrm{x}} \simeq \frac{t}{t+\omega_{\mathrm{NW}}}\,, \tag{2.65}$$

$$N_{\mathrm{y}} \simeq \frac{t}{t+\Delta_{\mathrm{DW}}}\,, \tag{2.66}$$

where $\omega_{\mathrm{NW}}$ is the width of the nanowire in the x-axis and $\Delta_{\mathrm{DW}}$ is the width of the domain wall along the y-axis [89], [125], [127]. For a pure *Bloch*-wall ($\varphi = 0$ or $\pi$) there is no $y$ component of $\vec{M}$ and $N_{\mathrm{y}}$ equals zero. In the case of intermediate DWs $\Delta_{\mathrm{DW}}$ depends on $\varphi$, as discussed in section 2.8.1). The $N_{\mathrm{x}}$ prefactor mainly depends on the length of the entire DW which is in first approximation equal to the width of the nanowire [89], [125], [127]. The difference between both demagnetizing components is then used to complement the demagnetizing term and formulate the expression

$$H_{\mathrm{walker}} = 2\pi\alpha M_{\mathrm{s}}|N_{\mathrm{x}} - N_{\mathrm{y}}|\,. \tag{2.67}$$

Above the *Walker*-breakdown, the DW motion is characterized as precessional-flow with a reduced DW mobility as parts of the driving energy are dissipated by the precessing domain wall core [125], [126]. The adapted mobility amounts to

$$m_{\mathrm{prec}} = \frac{\gamma_0 \Delta_{\mathrm{DW}}}{\alpha + \alpha^{-1}}\,, \tag{2.68}$$

leading to a velocity expression, changed accordingly to

$$v_{\mathrm{prec}} = m_{\mathrm{prec}} H_{\mathrm{ext}} = \frac{\gamma_0 \Delta_{\mathrm{DW}}}{\alpha + \alpha^{-1}} H_{\mathrm{ext}}\,. \tag{2.69}$$

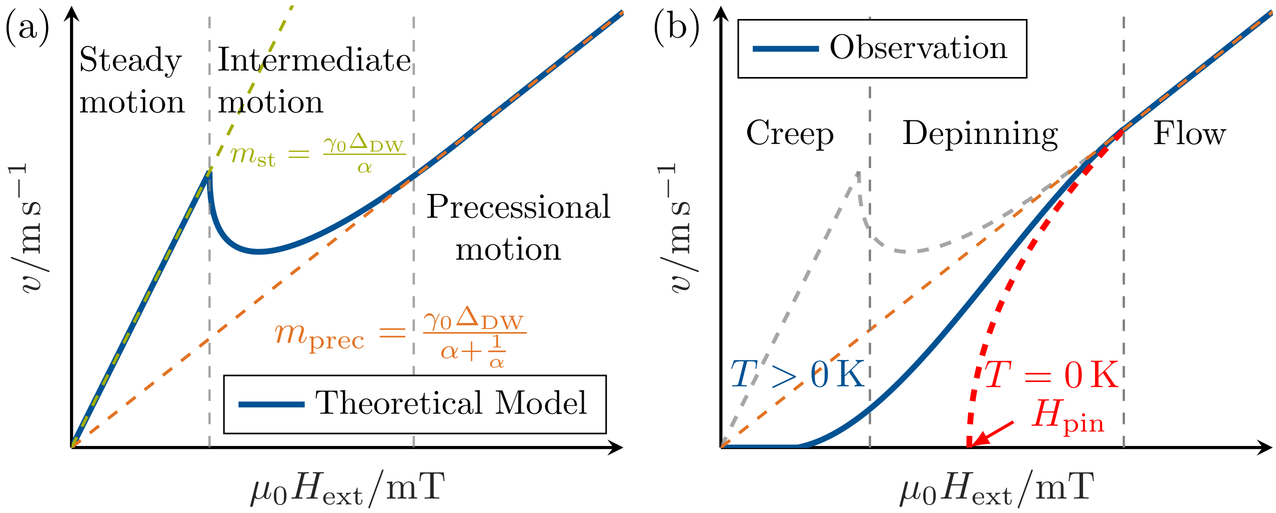

**Figure 2.21** The two graphs describe the theoretical (a) and experimentally observed (b) domain wall velocity evolution under increasing external fields. Theory predicts an initial steady motion regime with high DW mobility, followed by a transition region, before entering the precessional motion regime. It has to be stressed, that $m_{\mathrm{st}}$ can be orders of magnitude larger than $m_{\mathrm{prec}}$. In experiments, the steady motion regime is usually completely covered by the creep and depinning regime, with distinct exponential slopes.

The different flow regimes are, however, not separated by a sharp phase-transition at the *Walker*-field [89], [109], [125]. The change rather happens via a large intermediate regime with fluctuating (or even oscillating) DW mobilities, as depicted in Figure 2.21 (a) [127]. With a basic understanding of the theoretical models, we can now factor in the aforementioned domain wall pinning. At small fields, the energy of the driving field is not sufficient to overcome even the lowest energy barriers imposed by the pinning sites. If we assume a temperature of 0 K, the DW will stay pinned until the driving fields cross the threshold defined by the "weakest" pinning sites. This field, defined as $H_\text{pin}$ is depicted in Figure 2.21 (b). Beyond this field, increasingly more pinning sites can be overcome, which considering an infinitely long DW is equivalent to an increase in velocity, which will eventually converge with the theoretical models.

At Temperatures $> 0\,\text{K}$, however, there exists, according to Equation (2.61), a finite time to overcome these energy barriers regardless of $H_\text{ext}$. The DW velocity will, therefore, be $> 0$ even for $H_\text{ext} < H_\text{pin}$. Figure 2.21 (b) illustrates this creep and depinning regime, in which DW propagation is probabilistic and must rely on thermal activation. Both regimes are not strictly separated, nor are they governed by different physical phenomena. A distinction should nevertheless be made to acknowledge the fact that in the depinning regime, the driving fields start to overcome more and more energy barriers, increasingly mimicking flow-like motion. In other words, the mean time to depin ($\tau_\text{depin}$) becomes minimal. The exponential function, describing the average velocities below the flow regime, is expressed as

$$v_{DW} \approx v_0 \exp\left[-\left(\frac{E_\text{pin}}{k_\text{B}T}\right)\left(\frac{H_\text{pin}}{H_\text{ext}}\right)^{1/4}\right], \tag{2.70}$$

where $E_\text{pin}$ describes the activation barrier height, $H_\text{pin}$ the depinning field at 0 K, and $v_0$ is used as a simple pre-factor [125], [128], [129]. With increasing external fields, more and more pinning sites can be overcome easily, and the velocity approaches the theoretical flow models. As a summary, Figure 2.22 displays the combined DW propagation models. It is important to emphasize that the flow regime does not require precessional DW motion. However, as the *Walker*-breakdown usually occurs well below 10 mT, steady flow is seldomly observed [89], [109], [130]. In systems with very low depinning fields, it is, however, possible to observe the tail of the transition region [131]. In general, it has to be stressed that the topic of DW propagation is highly complex. Even without considering current-driven DW motions or the effects of iDMI, we could only sketch a rough overview of the topic and introduce the most simple analytical models. For a more comprehensive discussion, it is referred to [127], [132]–[135].

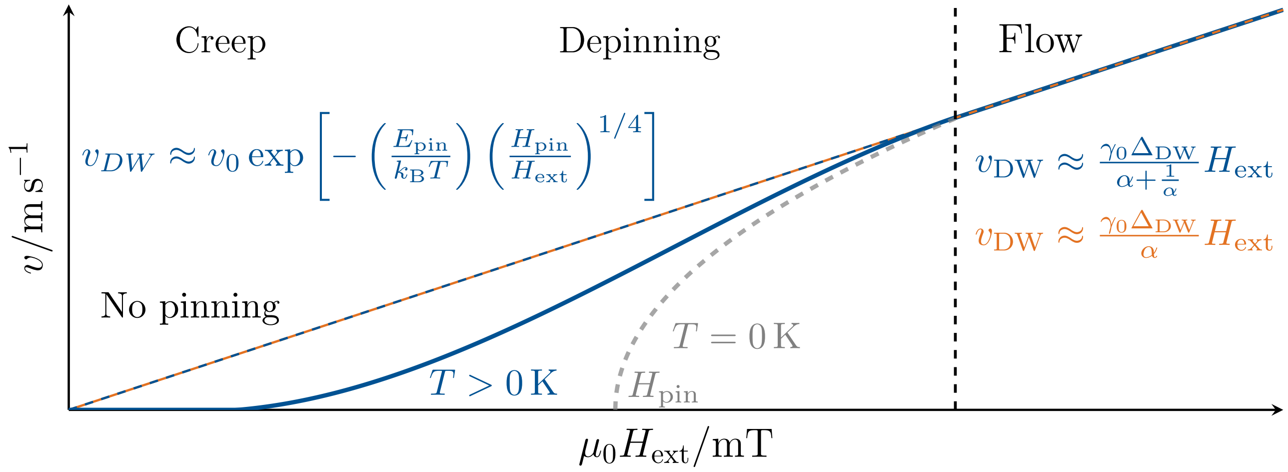

**Figure 2.22** The plot displays the typical field-dependent domain wall velocity. The velocity exhibits an initial exponential dependency in the creep and depinning regime, followed by a linear flow regime with a slope defined by the materiel parameter.

## 2.10 Hysteresis of PMA Magnets

The term hysteresis generally describes a history dependency in the state of a physical system. Meaning, the states of the system will depend not only on external inputs and material properties but also on the previous states [70], [75]. Therefore, we can define the magnetic hysteresis as the evolution of the total magnetic moment $M$ of a magnet under the influence of an external magnetic field $H_{\mathrm{ext}}$. This evolution is usually expressed in graphs, plotting the cumulative magnetic moment $M$ of the magnet versus the external field $H_{\mathrm{ext}}$. In section 2.6 we have already introduced the magnetic hysteresis of a single domain Stone-Wolfarth particle. Thus, we know that the shape of the hysteresis curve is strongly dependent on the angle of the applied field with respect to the anisotropy axis. Since magnets with out-of-plane magnetization and their reversals are the focus of this work, we will only discuss the hysteresis considering out-of-plane magnet fields along the easy axis of the PMA magnets. In contrast to a Stone-Wolfarth particle, which exhibits coherent rotation of the spins in an external field, we know from section 2.7 that the magnetization reversal in PMA magnets occurs via DW nucleation and propagation. Therefore, domain wall dynamics and related phenomena need to be taken into consideration when discussing hysteresis curves [70], [75]. Figure 2.23 depicts the hysteresis of a single-domain, a multi-domain, and a thin film magnet. It can be difficult to separate the three in experiments, leading to mistakes or misjudgments. However, before discussing differences and similarities, we first introduce the general characteristic of a magnetic hysteresis curve. First, we define the maximum attainable magnetic moment at high fields as the saturation magnetization $M_{\mathrm{s}}$ and the remaining magnetic moment at zero fields after saturation as the remanent magnetization $M_{\mathrm{r}}$, both are indicated in Figure 2.23. The saturation field $H_{\mathrm{s}}$ defines the field necessary to saturate the magnet and achieve $M_{\mathrm{s}}$. During the magnetization reversal, $H_{\mathrm{nuc}}$, $H_{\mathrm{c}}$, and $H_{\mathrm{pin}}$ define the nucleation, the coercive ($M = 0$) and DW pinning fields of the individual magnets [70], [75].

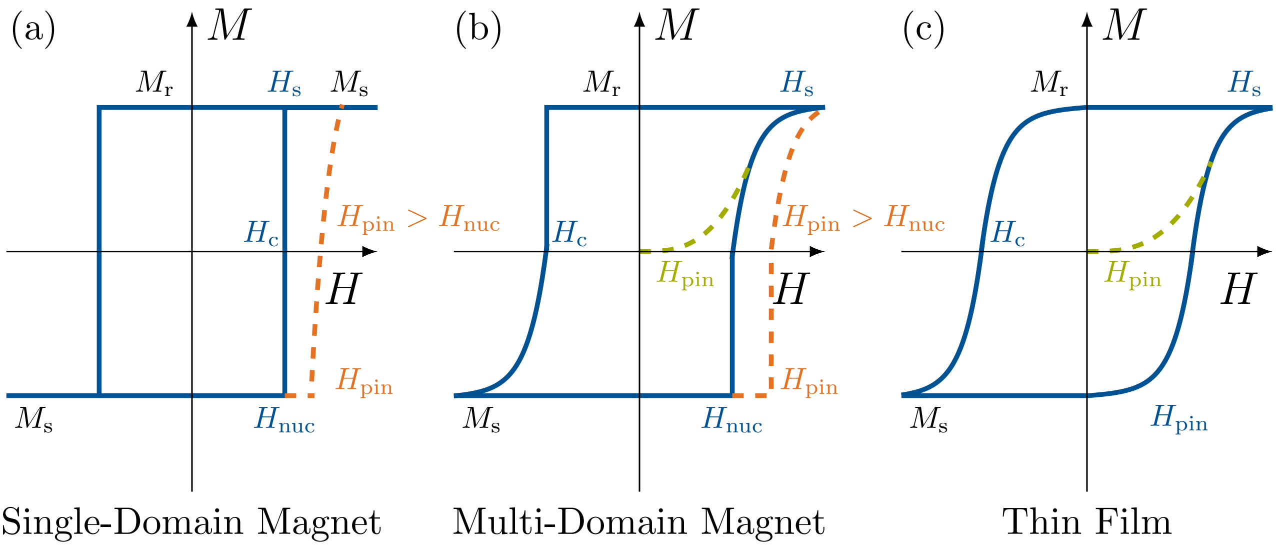

**Figure 2.23** Sketched out-of-plane hysteresis curves of different PMA magnets. In (a), the hysteresis of a single-domain magnet with its characteristic square shape is depicted ($H_{\mathrm{nuc}} = H_{\mathrm{s}}$). Only in the case of dominating pinning fields is the squareness reduced. The hysteresis of a multi-domain magnet is shown in (b). Domain formation leads to a smeared out hysteresis ($H_{\mathrm{nuc}} < H_{\mathrm{s}}$). In (c), a thin-film hysteresis is depicted. Due to a large number of defects in the system, it is difficult to distinguish nucleation from DW depinning. The dashed orange plot describes the case of a depinning field larger than the nucleation field, while the green plot shows the case of an initial multi-domain state.

### Single-Domain Magnets

The typical hysteresis of single-domain magnets is sketched in Figure 2.23 (a), it can be split into two cases. Either the nucleation field is above the DW depinning fields, or it is not. If nucleation occurs above the depinning fields, the DW depinns from the nucleation site and propagates through the entire magnet at $H_{\mathrm{nuc}}$. It can, therefore, be stated that the saturation field is equal to the nucleation field ($H_{\mathrm{nuc}} = H_{\mathrm{c}} = H_{\mathrm{s}}$). This is usually the case for SD nanostructures with low defect densities. The hidden, underlying depinning fields can be made visible by nucleating a DW without propagating it (done via short magnetic field pulses). In this case, the DW would already start to propagate at a lower $H_{\mathrm{pin}}$. However, the pining fields would increase marginally with $M$ as the balance of the demagnetizing fields is slowly shifted towards the opposing domain. Though, it has to be stressed that this increase is minimal and usually not observed in experiments. On the other hand, if the depinning fields are higher than the nucleation field, the DW will nucleate but stay pinned until the depinning field is reached. At $H_{\mathrm{pin}}$ the DW will depin from the nucleation site and propagate through the magnet, provided it does not encounter other significant pinning sites.

### Multi-Domain Magnets

Before discussing the hysteresis of multi-domain magnets, it is important to stress that only magnets with a remnant magnetization equal to the saturation magnetization are considered here ($M_{\mathrm{r}} = M_{\mathrm{s}}$). The hysteresis of such magnets can be very similar to those of single-domain magnets. However, the underlying magnetization reversal process is fundamentally different. First, we again consider the case of a nucleation field larger than the depinning fields. After nucleation, the DW depinns and propagates through the magnet. However, due to the stronger demagnetizing fields, multiple domains start to form in order to minimize the stray field energy. This continues until the magnet reaches its ground state at $M = 0$ ($H_{\mathrm{nuc}} = H_{\mathrm{c}}$). From this point onward, additional energy is required to compress and annihilate the created domains, thus leading to a smeared-out hysteresis curve ($H_{\mathrm{c}} < H_{\mathrm{s}}$). A similar picture evolves if the depinning fields are larger than $H_{\mathrm{nuc}}$, after depinning, the stray field energy will support the domain formation until $M$ reaches zero. After that, the same smearing effect as in the case of nucleation-dominated reversal is observed. If the field is ramped, started from a demagnetized state ($M = 0$), the DWs start to move and compress the opposing domains from $H_{\mathrm{pin}}$ onward until an equilibrium state between the *Zeeman* energy and the demagnetizing fields is reached. This continues until $H_{\mathrm{s}}$ when all domains are annihilated.

### Thin-Films

Thin-film magnets are multi-domain magnets, only on a larger scale. The macroscopic nature of a film leads to a high number of defects which in turn leads to DW nucleation at very low fields. However, depending on the anisotropy gradients, the DWs might stay pinned for a considerable field range. Depinning will then occur from those nucleation sites which have the lowest anisotropy gradient. Depending on the overall anisotropy of the film, these initial depinning fields can be much higher than the intrinsic pining a DW would exhibit. The intrinsic pinning fields can again be revealed by starting the field ramp from a demagnetized state.

## 2.11 Summary of Material Relevant Parameter

The magnetism research community uses a variety of different material parameter and constants. The large number of parameter together with an inconsistent or sometimes even mixed use of SI and GSI units makes this very confusing. In the following we provide a condensed overview of the most important parameter, relations and unit transformations.

$-\mu$ in $\mathrm{H\,m^{-1}}$ Magnetic permeability ($\mu_0 = 4\pi \times 10^7 \mathrm{H\,m^{-1}} \approx 1.256\,\mathrm{H\,m^{-1}}$).

$-B$ in T Magnetic flux density, also expressed in oersted. $1\,\mathrm{T} = 1 \times 10^4\,\mathrm{G}$

$-H$ in $\mathrm{A\,m^{-1}}$ Magnetic field strength, also expressed in gauss. $1\,\mathrm{Oe} = 1 \times 10^3/4\pi\,\mathrm{A\,m^{-1}}$

$-M$ in $\mathrm{A\,m^2}$ Magnetic moment, also expressed in $\mathrm{J\,T^{-1}}$ or with the prefactor $1 \times 10^3$ as emu or erg $\mathrm{G^{-1}}$ ($1\,\mathrm{emu} = 1 \times 10^{-3}\,\mathrm{A\,m^2}$)

$-M_\mathrm{s}$ in $\mathrm{A\,m^{-1}}$ The saturation magnetization per a unit volume of magnetization, also expressed in T ($1\,\mathrm{T} = \frac{1}{\mu_0}\,\mathrm{A\,m^{-1}} \approx 7.96 \times 10^5\,\mathrm{A\,m^{-1}}$)

$-K_\mathrm{u}$ in $\mathrm{J\,m^{-3}}$ Uniaxial anisotropy energy density, also expressed as $\mathrm{erg\,cm^{-3}}$ ($1\,\mathrm{erg\,cm^{-3}} = 1{\times}10^{-1}\,\mathrm{J\,m^{-3}}$)

$-K_\mathrm{eff}$ in $\mathrm{J\,m^{-3}}$ Effective anisotropy. Positive for materials with out-of-plane magnetization. Also expressed as $\mathrm{erg\,cm^{-3}}$ ($1\,\mathrm{erg\,cm^{-3}} = 1 \times 10^{-1}\,\mathrm{J\,m^{-3}}$)

$-H_\mathrm{K}$ in T Anisotropy equivalent field, equal to the switching field at 0 K. $H_\mathrm{anis} \approx 2K_\mathrm{K}^\mathrm{nuc}/M_\mathrm{s}$

$-M_\mathrm{eff}$ in T Effective magnetization, taking also the anisotropies into account ($M_\mathrm{eff} = M_\mathrm{s} - H_\mathrm{K}$ ). Negative for materials with out-of-plane magnetization.

$-A_\mathrm{ex}$ in $\mathrm{J\,m^{-1}}$: The exchange stiffness of the magnetic material ($\approx 2 \times 10^{-11}\,\mathrm{J\,m^{-1}}$ for 3d-transition metals like Co, Ni, Fe)

$-\alpha$: Damping factor $\approx 0.3$ for Pt/Co multilayer and $\approx 0.02$ for CoFeB

$-\gamma/\mathrm{Hz\,T^{-1}}$ Gyromagnetic ratio in $\mathrm{rad\,s^{-1}\,T^{-1}}$ ( $\gamma \approx 1.760 \times 10^{11}\,\mathrm{rad\,s^{-1}\,T^{-1}}$ )

# 3 Perpendicular Nanomagnetic Logic

After introducing the relevant physical mechanisms of magnetism and sketching a rough image of the physics needed to be taken into consideration, we can now discuss the designs and architectures necessary to develop and realize logic operations in media with perpendicular magnetic anisotropy. Perpendicular nanomagnetic logic uses the magnetization direction of nanomagnets to represent the digital values one and zero. Therefore, the used magnets must be single-domain (SD), meaning that the magnetic energies are best minimized for a homogeneous magnetization pointing either ’up’ or ’down’. This is schematically illustrated in Figure 3.1 (a), with both energy minima separated by a distinct energy barrier. To transform or switch the magnetization direction from one state to the other requires energy, commonly supplied by an external magnetic field or spin-current. To allow for efficient logic operations, the magnetization (or magnetic state) must be easily reversible at particular frequencies or within specific times (similar to the threshold voltage and turn-on time of a transistor) but also stable enough (at operation temperature) to prohibit random (thermal) switching. Logic operations and signal propagation are realized via the magnetic dipole interaction between adjacent SD nanomagnets. This antiferromagnetic dipole coupling, illustrated in Figure 3.1 (b), allows for simple boolean as well as more complex threshold logic operations with multiple inputs. The required energy for such a logic operation is the energy needed to reverse the magnetization of the output magnet ($E_\mathrm{sw}$). This energy scales with the total magnetic moment of the magnet and its switching field. It can be approximated from the absolute hysteresis curve and roughly amounts to

$$E_\mathrm{sw} \approx 4M_\mathrm{s}V_\mathrm{M}H_\mathrm{c} = 4\cdot 1\times 10^{6}\,\mathrm{A\,m^{-1}}\cdot 1.5\times 10^{-23}\,\mathrm{m^{3}}\cdot 0.02\,\mathrm{T} = 1.2\times 10^{-18}\,\mathrm{J}\,, \tag{3.1}$$

considering a magnet volume ($V_\mathrm{M}$) of 50 nm × 100 nm × 3 nm and a coercive field of 20 mT. Energies in the single-digit atto-joule regime are otherwise only imaginable by end of the road-map CMOS devices, thus making pNML especially attractive for ultra-low power applications [56], [136].

Developing a computation technology based on the dipolar coupling of out-of-plane magnets has been the focus of the pNML research group at TUM for the past ten years. Within this time, the main objective was to show the functionality and the underlying physics of basic logic elements (NOT/NAND/NOR-gates, vias, interconnects) in proof-of-concept studies and benchmark the performance characteristics against advanced CMOS designs [52], [137]. Since there already exist multiple works on pNML, the following chapter aims to provide a compact description focusing on the

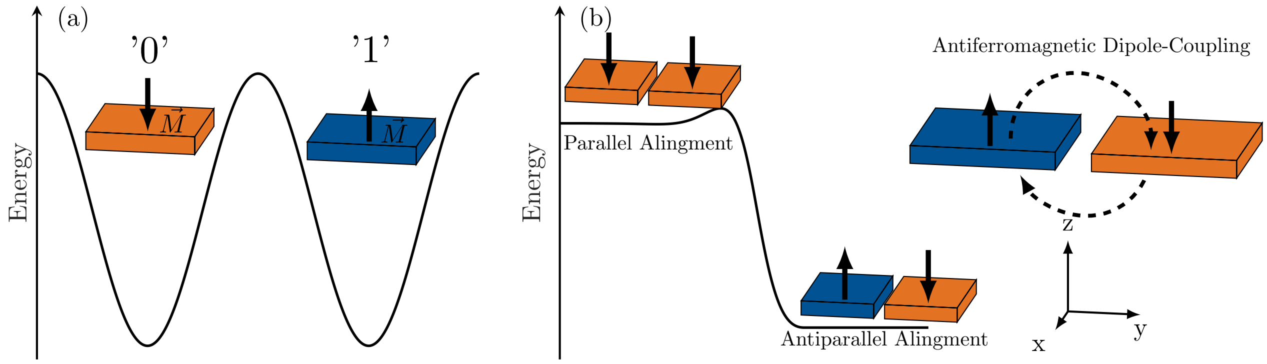

**Figure 3.1** The energy diagram in (a) illustrates the bi-stable magnetization of single-domain magnets, showing global energy minima for homogeneous magnetizations pointing either up or down. In (b), the antiferromagnetic nature of the dipole coupling between magnets is depicted.

individual magnets made from different materials. Additional introductions into pNML can be found in [50], [138]–[140].

## 3.1 Magnets and Logic Gates

The working principle of pNML logic gates can be broken down into two elements. The magnetic dipole-coupling between magnets and the magnetization reversal of the individual magnets under the influence of this coupling and the external clock field. We will first discuss the means necessary to ensure non-reciprocal coupling and guided signal flow before focusing on the magnetization reversal in greater detail.

### 3.1.1 Logic Operations via Non-Reciprocal Dipole Coupling

As with any binary logic architecture, pNML performs logic operations to a set of binary inputs resulting in deterministic outputs. Both inputs and outputs are thereby realized as bi-stable nanomagnets. The logic operations are performed by the overlapping stray or dipole fields of the input magnets, acting in superposition on the output magnets. With this picture, the simplest logic element, an inverter (NOT-gate), can be realized with just two magnets, one input, and one output magnet. In the case of parallel alignment (both magnetizations point in the same direction), the stray fields of the input magnet will lower the coercive field of the output magnet and support its transition into the energetically favored state with antiparallel alignment. This is expressed in terms of an energy diagram in Figure 3.1 (b). An oscillating magnetic field (called clock-field) is subsequently used to overcome the activation energy and drive the switching of the output magnet. On the other hand, antiparallel alignment can also be achieved by switching the input magnet. Directed signal flow, indispensable for computation, is thus not guaranteed. However, the reciprocity of the dipole interaction can effectively be broken by locally changing the anisotropy landscape within the individual magnets. As introduced in chapter 2, the dipole fields emanated by a magnet fall off with the third power of the distance ($\propto 1/d^3$). Therefore, the coupling fields across the magnets will be strongest at the side of the closest approach. By locally reducing the effective anisotropy $K_{\mathrm{eff}}$ it is possible to create a so-called artificial nucleation center (ANC) on one side of each magnet (depicted in Figure 3.2 (a)). This ANC not only defines the point of DW nucleation but also lowers the overall coercivity of the magnet significantly; this is illustrated by comparing the hysteresis curve of magnets with and without ANC in Figure 3.2 (b). With the ANC on one side of the magnets (the left in the examples),

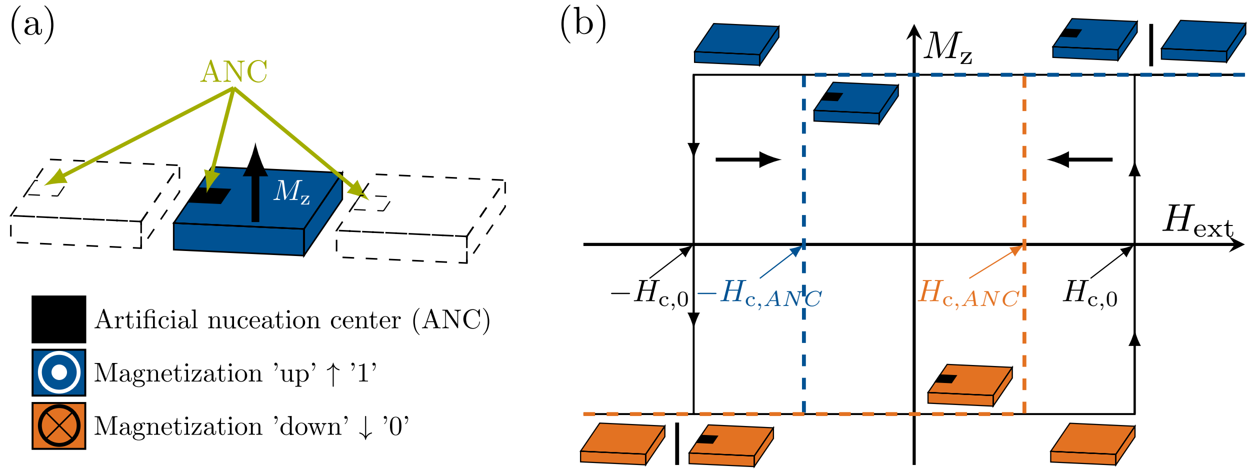

**Figure 3.2** In (a), a sketch of the typical magnet arrangements with ANC positions on one side of every magnet is displayed. In (b), the hysteresis of a pNML magnet is displayed, showing the reduction in coercivity upon the introduction of the ANC.

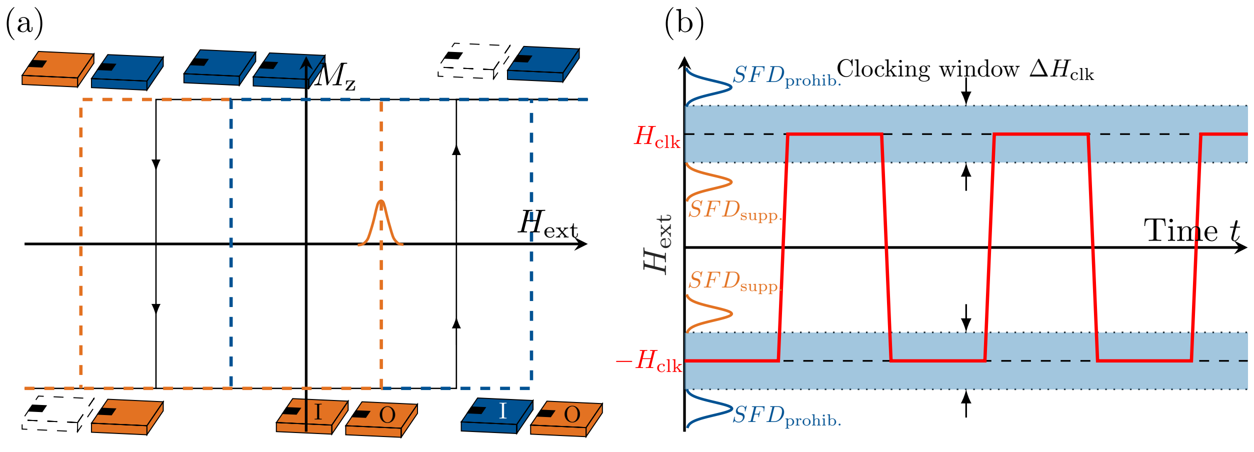

**Figure 3.3** In (a), the magnetic hysteresis of the output magnet (**O**) of a NOT-gate with varying input states (**I**) is displayed. For a parallel input, the switching field distribution of the output magnet is shifted by the dipole field $H_{\rm dip}$ to lower fields and vice versa. In (b), the clock-field is plotted, illustrating the magnetic field corridor or clocking window ($\Delta H_{\rm clk}$) for error-free operation.

the DW nucleation can be effectively controlled by the dipole fields of an adjacent magnet (on the left side) but not vice versa. Thus, the ANC is a fundamental part of pNML, breaking the reciprocity of the dipole coupling and guaranteeing directed signal flow.

Within the model of the two magnet inverter, we can now discuss supported and prohibited switching as well as clocking to propagate information through the circuit. The stray fields from the inputs alone are insufficient to nucleate and propagate DWs through the output magnet. Therefore, an alternating/oscillating global clock-field is applied, which assists in the DW nucleation/depinning and propagates the DWs through the magnets. Figure 3.3 (a) depicts the hysteresis of the output (**O**), depending on the states (magnetization direction) of the input magnet (**I**). In the case of a parallel input, the hysteresis is shifted to smaller fields and to higher fields for an antiparallel input, respectively. In order to guarantee the error-free operation of the inverter, the amplitude of the clock field must be chosen to envelop the entire distribution of supported switching events but simultaneously evade any prohibited events. The range of possible clock-fields is described as the clocking window ($\Delta H_{\rm clk}$), it is schematically illustrated via a time versus magnetic field plot in Figure 3.3 (b). The displayed probability distribution functions underline the probabilistic nature of the switching events. To assess the achievable coupling strengths and get a realistic picture of the distance-dependent dipole fields ($H_{\rm dip}$) emanating from a nanomagnet, calculations utilizing the well known point-dipole approximation can be performed [40], [50], [70]. For that propose, numerical finite-element simulation using rectangular unit cells ($V_{\rm cell} = l_{\rm x} \cdot l_{\rm y} \cdot l_{\rm z}$) are conducted. The magnetic moment of a unit cell calculates as $\boldsymbol{m}_{\rm cell} = M_{\rm s} V_{\rm cell} \boldsymbol{e}_{\rm m}$, where magnetization vector ($\boldsymbol{e}_{\rm m}$) is confined along the Z-axis with no in-plane components ($\boldsymbol{e}_{\rm m} = \boldsymbol{e}_{\rm z}$). Furthermore, a homogeneous magnetization is assumed. Figure 3.4 (a) depcits a square magnet consisting of 200 × 200 unit cells. The magnetic field of cell $i$ can then be derived from ep. (2.16) and expressed as

$$\boldsymbol{H}_i(\boldsymbol{m}_i, \boldsymbol{r}_i) = \frac{1}{4\pi r_i^3} \left[ 3\frac{(\boldsymbol{r}_i \cdot \boldsymbol{r}_i)\boldsymbol{r}_i}{r_i^2} - \boldsymbol{m}_i \right] . \tag{3.2}$$

The superposition of all cell-fields yields the total magnetic field, it is calculated via the sum over all cells

$$\boldsymbol{H}_{\rm dip}(r) \approx \sum_i \delta \boldsymbol{H}(m_i, d_i) . \tag{3.3}$$

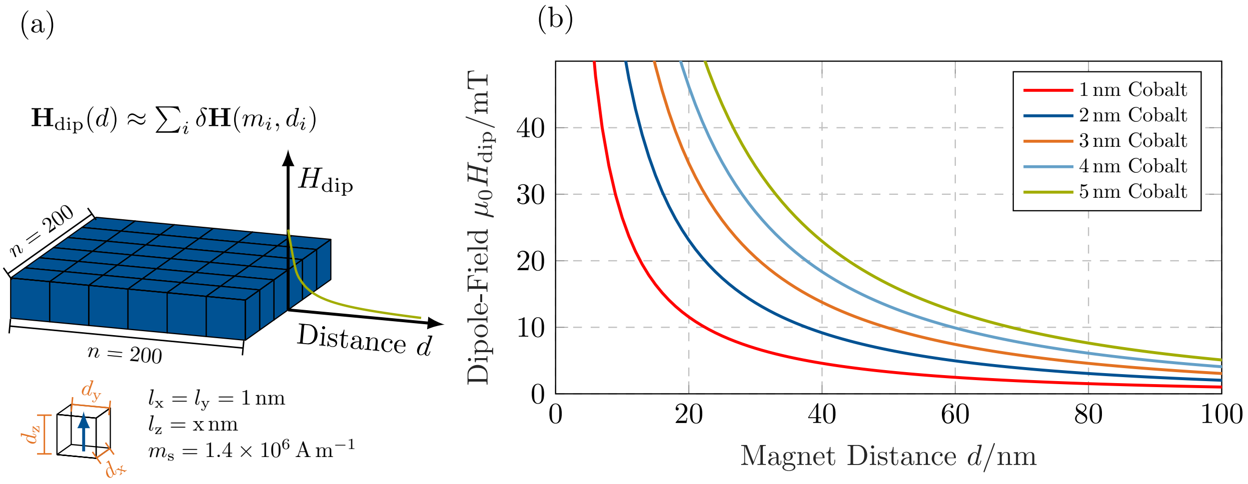

**Figure 3.4** Point-Dipole calculations of the dipole fields in close proximity to a 200 nm × 200 nm sized cobalt nanomagnet with out-of-plane magnetization. The resulting dipole fields increase linearly with the cobalt thickness (magnetic moment) but fall off $\propto \frac{1}{d^3}$. The schematic on the left describes the calculation parameter.

Figure 3.4 (b) depicts the calculated coupling fields of a 200 nm × 200 nm sized magnet with various cobalt thickness. As discussed in chapter 2, the dipole fields scale $\propto \frac{1}{d^3}$ but increase only linearly with the total magnetic moment.

### 3.1.2 Understanding and Controlling the Magnetization Reversal

The energy, or better, the magnetic field needed to switch a SD magnet can be derived from the earlier introduced *Stoner–Wohlfarth* model, in this simple approximation (at 0 K) it is equal to $\frac{2K_{\mathrm{eff}}}{\mu_0 M_s^2}$ (the anisotropy field). However, from chapter 2 we already know that the magnetization reversal in PMA magnets is not occurring via coherent rotation but is caused by domain wall (DW) nucleation at the point of lowest anisotropy and subsequent DW propagation. This circumstance results in much lower coercive fields than predicted from the intrinsic anisotropy field ($H_c \ll \frac{2K_{\mathrm{eff}}}{\mu_0 M_s^2}$). The effect is also called *Brown's* paradox [141]. The energy needed to reverse the magnetization of a magnet is, therefore, depending on its unique size and energy landscape. Furthermore, we know that DW nucleation is a probabilistic process governed by the *Arhenius-Néel* law. The probability of nucleating a DW within a certain time changes exponentially with field and temperature according to Equation (2.52). Via the *Sharrock* Equation (2.54), it is possible to assign a characteristic nucleation field ($H_{\mathrm{nuc}}$) to a specific time. However, it is crucial to understand how the SFD is widened and shifted towards higher fields as the clock frequency increases. For a better visualization Figure 3.5 depicts the modeled increase in $H_{\mathrm{nuc}}$ and distribution width ($\sigma_{\mathrm{nuc}}$) of a typical pNML nanomagnet, using experimentally determined material parameter. In pNML circuits with vast numbers of magnets, it, furthermore, becomes imperative to consider the magnet to magnet variations ($\sigma_{\mathrm{magnet}}$). These variations originate in intrinsic as well as extrinsic $K_{\mathrm{eff}}$ fluctuations. Poly-crystalline thin-films, for example, will always consist of slightly misaligned grains with different anisotropy axes. In the evaluation of pNML gates and circuits, it is, therefore, necessary to combine both SFDs for reliability calculations. As both distributions are at least in first approximation normal distributed, it is opportune to approximate the total clock frequency-dependent SFD as $\sigma_{\mathrm{tot}}^2 = \sigma_{\mathrm{nuc}}^2 + \sigma_{\mathrm{magnet}}^2$. The cumulative distribution is critical to determine the clocking window $\Delta H_{\mathrm{clk}}$ depicted in Figure 3.3 and asses the reliability of the logic gates.

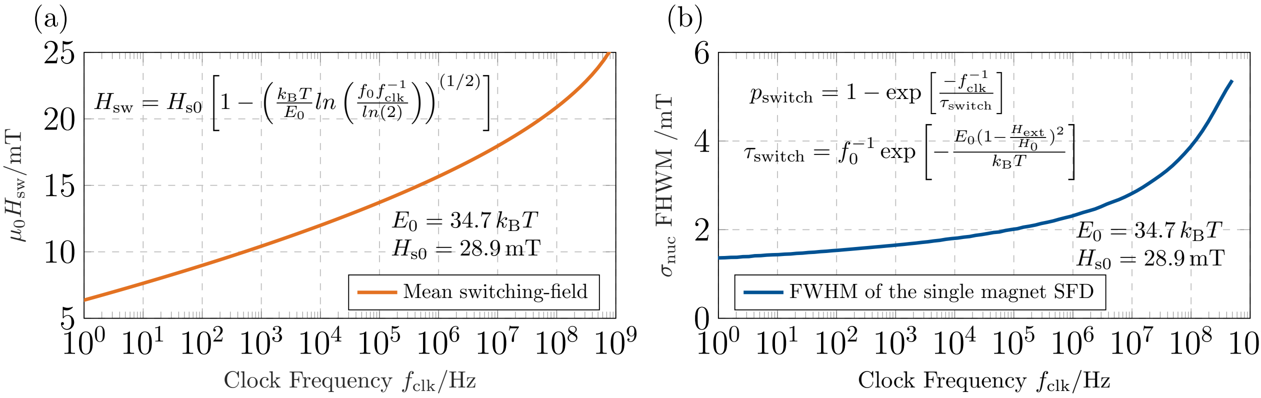

**Figure 3.5** The plot in (a) depicts the calculated mean nucleation field of a pNML nanomagnet versus the applied clock frequency $f_{\mathrm{clk}}$ at 300 K. In (b), the frequency-dependent CDF of the switching events is used to derive the width of the corresponding PDFs. The plot underlines the widening of the SFD at higher clock frequencies.

### Artificial Nucleation Center via Local Ion Irradiation

Domain wall nucleation in nanomagnets occurs at the region of lowest anisotropy, naturally determined by material defects or found at discontinuities. In structured nanomagnets, additional influences arise from edge defects introduced during fabrication. To guarantee DW nucleation, the artificial nucleation center must be the dominant anisotropy-well in the system. Although there have been different proposals on realizing suitable weak spots, ion-beam irradiation has, so far, emerged as the sole scalable means by which the anisotropy landscape can be manipulated with high spatial accuracy and at a low cost. On their way through the magnet, the ions (50 keV $\mathrm{Ga}^+$, if not stated otherwise) cause a cascade of scattering events, leading to intermixing and alloying. This is schematically illustrated by the display of a Co/Ni super-lattice before and after irradiation in Figure 3.6 (a). Even at marginal doses ($\approx 1\times10^{12}$ ions/cm$^2$), the PMA, which in metallic thin-films mainly originates from the crystal structures and interface effects, is reduced significantly. When applied locally on areas of $\approx$ 50 nm × 50 nm, a localized artificial anisotropy-well can be created. From chapter 2 we know that the required nucleation fields mainly depend on the effective anisotropy of the nucleating magnetic particle and its size ($E_0 \approx K_{\mathrm{eff}} V_{\mathrm{nuc}}$). This ANC anisotropy is defined by the ion dose and can be measured via extensive, time-resolved nucleation experiments [142], [143]. The importance of the nucleation volume $V_{\mathrm{nuc}}$ must be stressed at this point, as for nucleation to occur, its size must at least allow for the formation of one DW. For the ANC size we can, therefore, state $A_{\mathrm{ANC}} \geq V_{\mathrm{nuc}} \geq \Delta_{\mathrm{DW}}^2$. Considering solely the equation for DW nucleation, the lowest switching fields should be achieved at $K_{\mathrm{eff}} \approx 0\,\mathrm{J\,m^{-3}}$. However, we also know that the increasing anisotropy gradient created at the ANC boundary acts as a counteracting energy barrier and pinning site. Thus, the intersection between the rising depinning and falling nucleation fields will define the lowest attainable switching field. At this point, the switching mechanism changes from nucleation to depinning. This behavior can be demonstrated experimentally by sweeping the ANC ion dose and measuring the resulting coercive fields. Figure 3.6 (a) depicts the mean coercivities (measured at quasi-static fields) of Co/Ni nanomagnets plotted versus the used ANC ion dose. The error bars mark the FWHM of the respective SFDs. At low doses, the coercivity drops linearly with increasing dose, reaching a minimum at $\approx 8\times10^{12}$ ions/cm$^2$, before recovering again due to the increasing anisotropy gradient $\Delta K_{\mathrm{u}}$ between the ANC and the magnet. Following the highlighted decay trend, suggests that an OOP to IP transition ($K_{\mathrm{eff}} = 0\,\mathrm{J\,m^{-3}}$) occurs at $\approx 1.2\times10^{13}$ ions/cm$^2$. However, the anisotropy gradient continues to increase beyond this point, as the remaining $K_{\mathrm{u}}$ components continue to decay until reaching a local coercivity maximum at $\approx 2\times10^{13}$ ions/cm$^2$. Accurately describing the subsequently evolving, slightly lowered coercivity plateau at even higher doses is complicated. The most apparent effect causing an effective lowering of $\Delta K_{\mathrm{u}}$ is a widening of the anisotropy gradient up to a certain degree, together with a reduction of

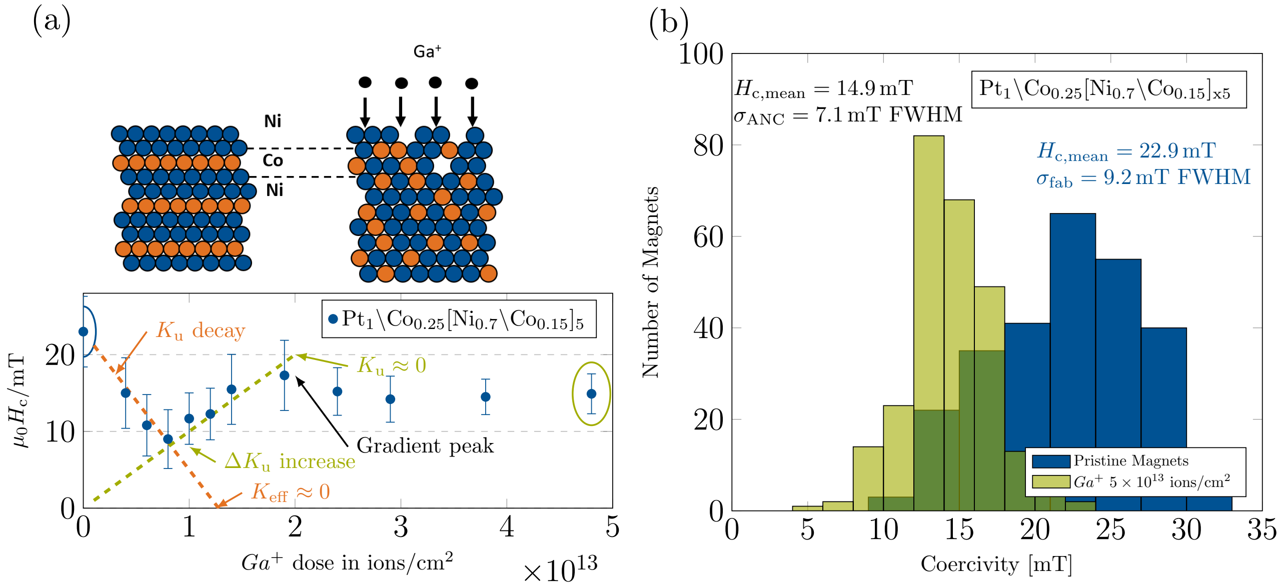

**Figure 3.6** In (a), a schematic illustration of the irradiation effects on a Co/Ni super-lattice is depicted. In (b), the mean coercivities of Co/Ni nanomagnets with a diameter of 1 µm are plotted versus the applied ANC Ga$^+$ ion dose. The error bars indicate the respective FWHM SFD. The histogram in (b) depicts the SFD of 1200 nanomagnets before and after ANC placement, highlighting the distribution shape and position change. The placed ANCs feature a size of ≈ 50 nm × 50 nm.

the magnetic moment.

Aside from controlling the nucleation position and field, the ANC also has a profound effect on the switching field distribution of the magnets. The artificially created anisotropy-well can be more consistent and less prone to fluctuations than naturally occurring defects. Figure 3.6 (a) displays, next to the mean coercivities, also the width of the attained FWHM SFDs as error bars. During the $K_u$ decay, the measured SFDs are not significantly smaller compared to the pristine magnets since the anisotropy fluctuations of the irradiated grains are still present. Only beyond the point of highest anisotropy gradient ($K_u \approx 0$) with no anisotropy remaining, a consistent and stable SFD decrease is observed. This change in shape and position of the switching field distribution is depicted in Figure 3.6 (b) in greater detail, as a histogram plot comparing the SFD of the same 1200 magnets before and after ANC placement. Without a remaining anisotropy, the only fluctuations in switching fields will arise from variations in the anisotropy gradients surrounding the ANC and in the local demagnetizing fields. Up to this point, the ANC doses for pNML were always chosen to realize the smallest possible SFD [63], [82], [142], [143].

### Clocking and DW Propagation

Up to this point, we only considered DW nucleation as part of the reversal process. However, during operation, the nucleated DWs must also propagate through the entire magnet within one clock pulse [144]. The entire reversal time will then comprise of the combined nucleation and propagation times ($t_{rev} = t_{nuc} + t_{prop}$). Figure 3.7 shows the clock-field driven operation of an inverter in detail. The logic operation takes place within the nucleation time $t_{nuc}$. Here, the dipole fields of the input magnet either increase or decrease the effective field acting on the ANC. Together with the clock pulse, the cumulative field is strong enough to nucleate DWs in the entire distribution of supported magnets (within $t_{nuc}$) without nucleating a single DW in the distribution of inhibited magnets. During the subsequent $t_{prop}$ the DWs, driven by the Zeeman energy of the clock-field, propagate through the remaining magnet. The required propagation time is defined by the DW velocity at the field strength of the clock field and the length/size of the magnet. In section 2.9.2 we already discussed the DW velocity in the flow as well as the depinning regime. Furthermore, there have been extensive studies

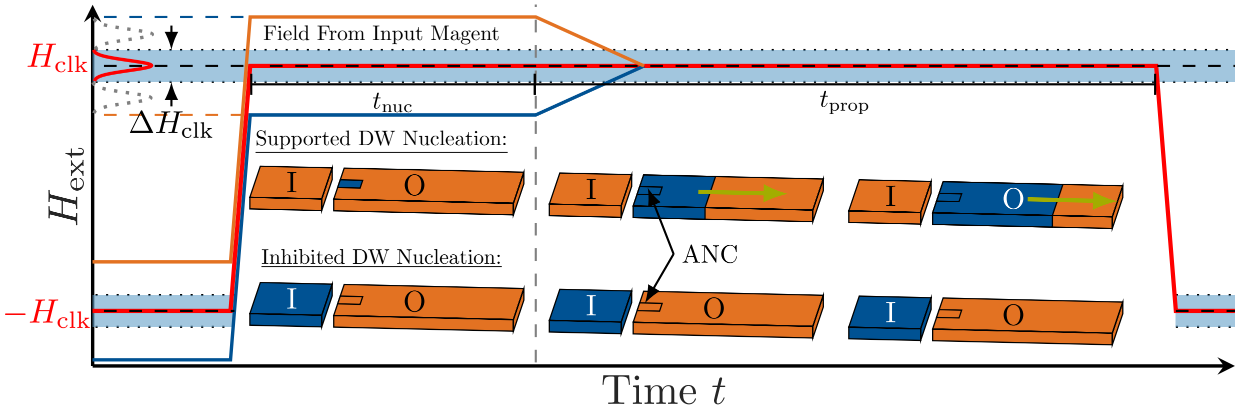

**Figure 3.7** Overview of the input dependent magnetization reversal of a pNML inverter within one positive clock phase. In case of a parallel input, the effective field acting on the ANC is increase, causing the nucleation of a domain with opposite magnetization within $t_{\mathrm{nuc}}$. In case of an anti-parallel intput, the effective field is reduced and the DW nucleation inhibited. During $t_{\mathrm{prop}}$ the created DW propagates through to remaining magnet.

on the DW propagation in thin-films and nanowires alike [125], [130], [145]. However, to assess the realistically achievable DW velocities, it is necessary to first discuss the achievable clock-fields and magnet dimensions. To allow for on-chip clocking, the fields should range not above 20 mT to 30 mT. Simultaneously, a scaled magnet should feature a width not larger than 100 nm, thus leading to a significant increase in the effective edge roughness causing increased pinning fields [146]. While operation in the flow regime would be ideal, assuming a form of depinning dominated propagation is more realistic. In the depinning regime, the DW propagation process can be seen as a series of individual probabilistic and thermally activated jumps from one pinning site to the next, driven by the external magnetic field, the locally acting demagnetizing fields, and the DW surface tension. We also know that similar to the nucleation, the time to depin follows an Arrhenius law according to Equation (2.61). Therefore, the mean DW velocity will mainly be determined by the number of pinning sites and the respective anisotropy gradients (defining the individual time to depin). This, in turn, imposes the necessity to optimize for the lowest intrinsic depinning fields possible and avoid geometrical constrictions in the layout, wherever possible. Measurements of 400 nm wide CoFeB nanowires with negligible intrinsic pinning fields yielded velocities of $\approx 20\,\mathrm{m\,s^{-1}}$ at a clock field of 20 mT [131]. The maximum attainable clock frequency for a given DW velocity can be estimated using the derived nucleation times via

$$f_{\mathrm{clk,max}} = \frac{1}{2(t_{\mathrm{nuc}} + t_{\mathrm{prop}})} \approx \frac{1}{2(t_{\mathrm{nuc}} + (l_{\mathrm{max}}/v_{\mathrm{DW}}))}\,, \tag{3.4}$$

where $l_{\mathrm{max}}$ is the length of the largest magnet in the design and $v_{\mathrm{DW}}$ is the domain wall velocity. Assuming realistic speeds of $\approx 20\,\mathrm{m\,s^{-1}}$ and magnet dimensions around of 100 nm with nucleation times $\approx$ 20 ns at the earlier mentioned 20 mT clock fields would yield a $f_{\mathrm{clk,max}} \approx 20\,\mathrm{MHz}$.

## 3.2 Logic Gates & and Interconnects

Throughout the last decade, a comprehensive family of pNML logic gates has been proposed and experimentally demonstrated. The family comprises a complete set of Boolean logic gates and includes more complex threshold gates and first binary adder circuits. Moreover, aside from pure logic gates, other vital system components like interconnects, magnetic fan-outs, and vias were shown. An overview of the demonstrated devices with the respective references is presented in Table 3.1.

**Table 3.1** Overview of the experimentally demonstrated pNML gates and interconnects. The table illustrates schematics of the most essential experimentally demonstrated pNML logic gates as well as the necessary interconnects. For detailed information on the individual devices is referred to the listed references.

| Element | Schematic Top-View | Explanation & Reference |
|---|---|---|
| Inverter/ Inverter-chain | 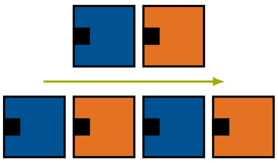 | • NOT operations<br>• Propagate information via inverter chain [61], [62], [82], [147] |
| Majority-Gate | 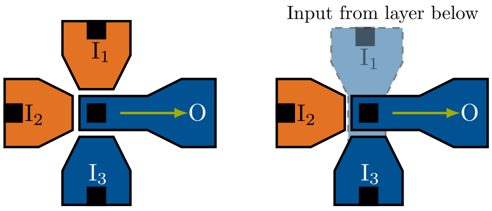 | • Runtime-configurable NAND/NOR operations<br>• 2D as well as 3D implementation [53], [64], [138] |
| 1-Bit Adder | 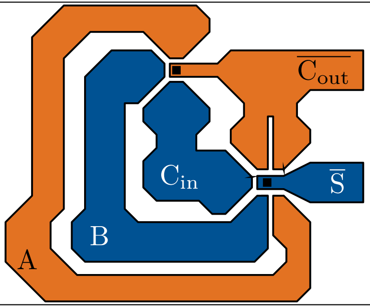 | • 1-Bit full-adder<br>• 5-input threshold gate [51], [148] |
| Domain Wall Gate | 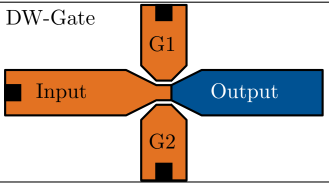 | • Domain wall gate, implemented in 2D as well as 3D [54], [149] |
| Interconnects & Vias | 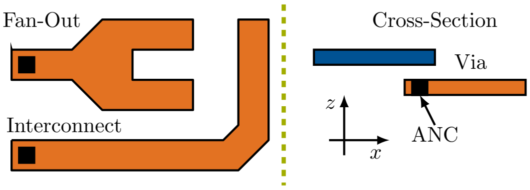 | • Signal routing<br>• Interconnects and vias [63], [138], [150], [151] |
|  |  |  |

## 3.3 Circuits and Systems

The introduced logic gates and interconnects enable the design and implementation of more complex circuits and systems. For example, within pNML, all boolean logic operations can be performed using inverters and 3-input majority gates (configured as either NAND or NOR gate). However, even more complex functionalities are possible compared to standard CMOS logic, using a direct majority gate approach with three or even five inputs per gate. An excellent example of this approach is the threshold logic-based 1-bit adder, utilizing a 5-input majority gate, presented in 2014 [51]. The adder requires only two instead of seven logic gates, thus drastically reducing the footprint and increasing the logic density [51], [148]. In order to utilize the global clock-field optimally and further increase the logic density, pNML is designed to be vertically integrated on a large scale with tens or even hundreds of functional layers connected via 3D gates or dedicates vias [52], [53], [150], [151]. As the fabrication of the thin-film magnets does not require a high thermal budget, the individual layers could be fabricated consecutively in the BEOL. For the evaluation and modeling of simple pNML circuits, a compact model based on finite element simulations was developed [137]. In order to also simulate pNML on the larger system-level, compact models were implemented in Verilog-A and can now be used in industry-standard design tools [152].

Aside from the magnetic logic domain, a pNML system also requires dedicated electrical inputs and outputs to interface with electronic systems. Although there are various physical phenomena for spin to charge conversion and vice versa, it will require extensive research to identify and integrate the technologies best-suited from efficiency, speed, and fabrication standpoints. Figure 3.8 displays a schematic overview of an exemplary pNML system with electrical as well as magnetic inputs, several layers of magnetic logic, and electrical outputs. As inputs, integrated micro-coils (potentially in combination with a soft-magnetic input) would be the most simple and mature approach [57], [58]. In contrast, technologically more complex spin-transfer-torque or spin-orbit-torque devices could potentially achieve much lower conversion losses at comparable speeds [39]. When assessing the output, aside from low-efficiency sensing coils, different magnetoresistance effects exist, which could be used to develop adequate sensors. Effects with the highest efficiencies are the giant magnetoresistance and tunneling magnetoresistance effects also found in hard-disk drive sensors or MRAM cells (TMR only)[39], [138]. However, the placement of MTJs on top of a magnetic nanowire remains a technological challenge [39], [153]. Technologically simpler though less sensitive are sensors using

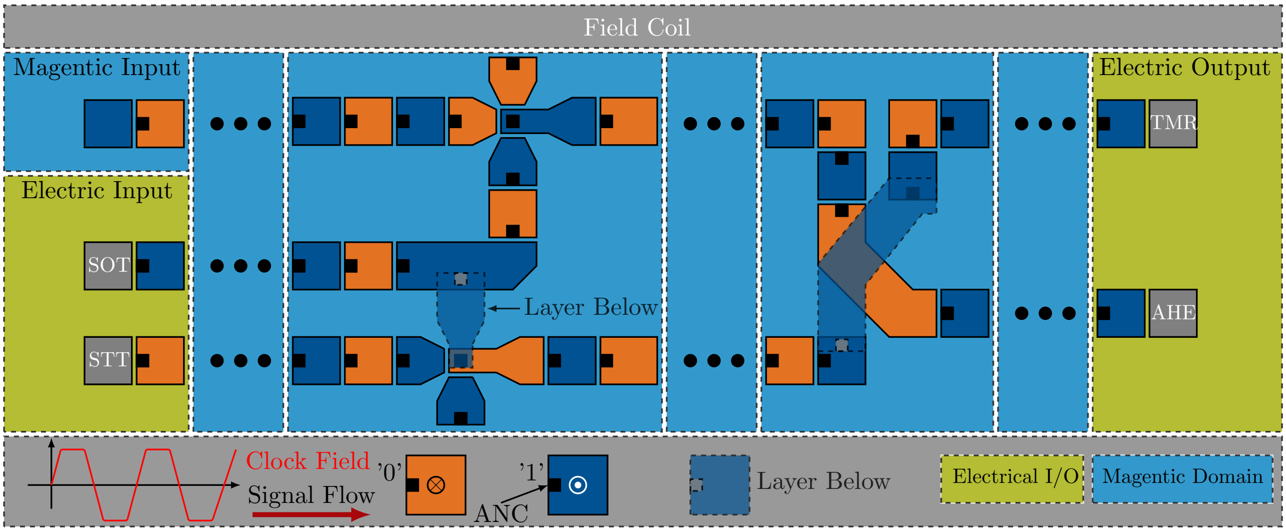

**Figure 3.8** Schematic layout of an envisioned pNML system. The data-flow driven architecture is fed by inputs from the left, processes data in the magnetic domain with 2D as well as 3D elements and presets the computed results at the output where the magnetic states are converted into a charge. The entire layout is enveloped by copper wires from the on-chip coil. Image adapted from [52].

the anomalous Hall effect [154], [155]. Utilizing the Spin-Hall magnetoresistance might also become a viable option in the future [156].

### 3.3.1 Clock-Field Generation and System Integration

Perpendicular nanomagnetic logic is built around the concept of a global bipolar clock field, driving the information flow. Complex interconnects as in CMOS designs, or multi-phasic clocking fields as in in-plane nanomagnetic logic are not required. The clock field oscillates in the easy-axis of the magnets with an amplitude equal to the mean coercive field at the respective frequency. To achieve the required field strengths ($H_{\mathrm{clk}} \approx 20\,\mathrm{mT}$) and frequencies ($f_{\mathrm{clk}} > 1\,\mathrm{MHz}$) on-chip, coils made from a copper metalization are complemented by a cladding made from soft-magnetic material (e.g. Permalloy). A schematic cross-section of the on-chip coil is shown in Figure 3.9. The achievable clock fields are thereby limited by the material parameter of the used cladding material (saturation magnetization, as well as hysteresis and Eddy current losses), and the power losses in copper metalization [56]. With this design, clock frequencies in low double-digit MHz regime at power densities $\leq 3\,\mathrm{W\,cm^{-2}}$ are realistic [56]. In order to supply the on-chip coil, adequate clock drivers and power amplifiers need to be implemented in the front-end-of-line (FEOL). For a detailed analysis of the proposed clocking scheme, it is referred to [52], [56], [157]

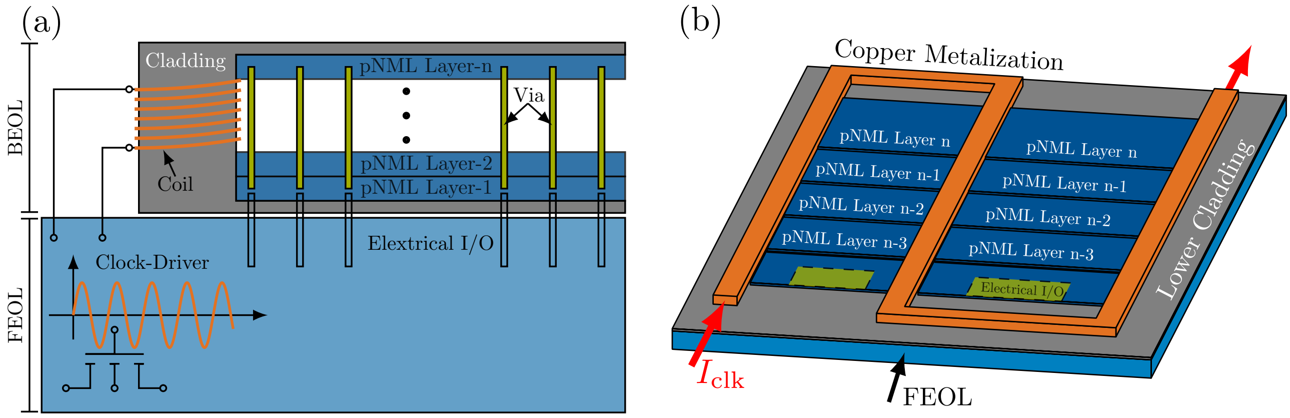

**Figure 3.9** In (a), the schematic cross-section of the envisioned global clocking scheme is illustrated. The architecture is envisioned to be implemented in the back-end of line (BEOL) on top of a CMOS front-end (similar to current MRAM designs). The stacked pNML layers are sandwiched between the on-Chip coils. For better visualization, the design is shown in 3D in figure (b). Images adapted from [52].

## 3.4 Error Rates

Since the magnetization reversal is a probabilistic process with frequency dependent distribution functions, it is necessary to carefully evaluate the error probability of pNML logic gates and estimate the necessary input coupling strengths for reliable operation. To evaluate the error probability of larger circuits or systems, complex models are necessary [137], [152]. However, for simple gates with only one output, the error probability can be approximated by simply considering the frequency dependent width of the distribution functions. For that propose, we assume a normal distribution and model the cumulative distribution function as

$$P_{\mathrm{sw}}(h_{\mathrm{dip}}) = \frac{1}{2}\left[1 + \mathrm{erf}\left(\frac{h_{\mathrm{dip}} - \mu}{\sigma\sqrt{2}}\right)\right], \tag{3.5}$$

with $h_{\mathrm{dip}}$ as the coupling field in mT, $\mu = 0$ as the mean of the switching field and $\sigma$ as the standard deviation or width of the single magnet switching field distribution (the CDF of the magnets is

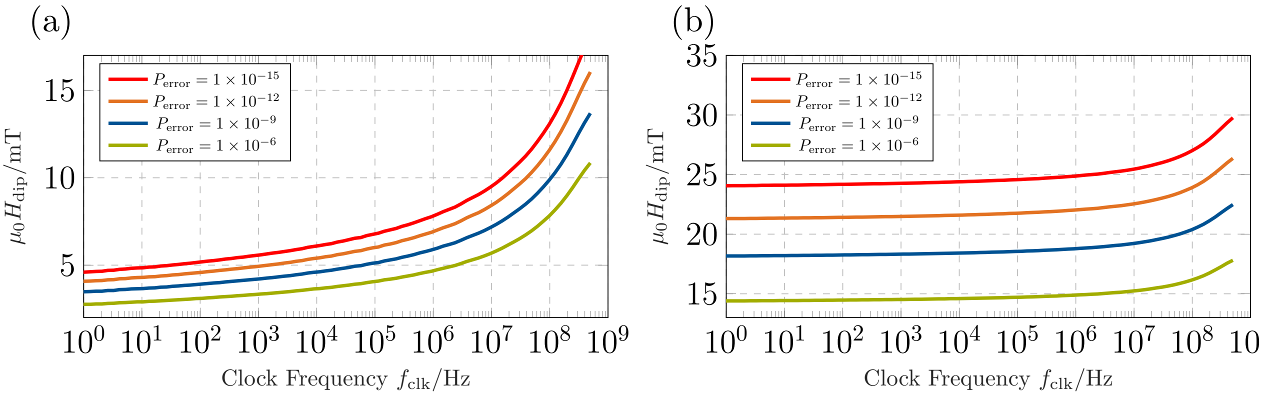

**Figure 3.10** The plot in (a) depicts the necessary input coupling fields of pNML gate to achieve certain error rates versus the applied clock frequency $f_{\text{clk}}$ at 300 K. For the calculations a nanomagnets with an energy barrier $E_0 = 35\,k_{\text{B}}T$ and a switching field at 0 K of $H_{\text{s0}} = 29$ mT is used. In (b), the calculation is expanded to account for magnet to magnet variations with a distribution width of $\sigma = 2.9$ mT.

measured via time-resolved nucleation experiments). The erf($x$) functions describes the Gauss error function. We use the same magnets, modeled for Figure 3.5 (b), depicting the frequency dependent distribution widths and solve Equation (3.5) at different frequencies for $h_{\text{c}}$ given a certain target value for $P_{\text{sw}}$. The resulting frequency dependent coupling fields for the distinct error rates ($P_{\text{error}} = 1 - P_{\text{sw}}$) are depicted in Figure 3.10 (a). The required coupling field follows the same exponential trend as the distribution widths in Figure 3.5 (b). At frequencies in the MHz regime, error rates for a single gate should be on the order of $1 \times 10^{-12}$ or smaller, thus requiring coupling fields of $\approx 10$ mT or higher. However, this estimation is not taking the magnet-to-magnet variations into account. When assuming a realistic SFD distribution as depicted in Figure 3.5 (c), the width of the CDF increases to $\sigma_{\text{tot}}^2 = \sigma_{\text{sw}}^2 + \sigma_{\text{magnet}}^2$ resulting in the significantly higher coupling fields shown in Figure 3.10 (b). This highlights the importance of controlling the SFD during magnet fabrication. Generally, it can be stated that magnets with at least a 3 nm cobalt equivalent magnetization ($M_{\text{s}} = 1.4 \times 10^6\,\text{A m}^{-1}$) are necessary for reliable operation.

## 3.5 Operating Temperatures

The temperature range of pNML systems needs to comply with the existing temperature range of CMOS systems in order to be integrable alongside the latter. Therefore, the safe operating temperatures should ideally range from −40 °C up to 100 °C.

However, up to this point, investigations into the temperature dependence of pNML were limited at best [155]. Nevertheless, the physics of temperature effects on magnets is clear, and aside from physical destruction at extreme temperatures, several other temperature-dependent effects need to be taken into consideration. The first is a temperature-induced reduction of the saturation magnetization up to the Curie temperature, where the spontaneous magnetization is lost. While the Curie temperature of thin films is significantly lower compared to bulk materials, a loss of ferromagnetic behavior is not to be expected up to temperatures above 400 °C [158], [159]. However, the saturation magnetization and thus the dipole coupling can already be reduced by values up to ≈ 10 % compared to RT at temperatures around 100 °C.

At the same time, also the PMA is reduced at higher temperatures, in turn resulting in lower DW nucleation and switching fields. Unrelated, though having the same effect, is the reduced relaxation time for domain wall nucleation and propagation at rising temperatures derived from the *Arhenius-Néel* law [160]. The combined effect is a significant reduction in the switching fields of up to 50 % (depending on the material and type of anisotropy) when heating the magnets from RT to 100 °C [155], [160]. This, on the one hand, reduces the necessary clock amplitude at elevated temperatures, causing a gain in efficiency but on the other hand, sets a minimum temperature below which the system can no longer be clocked. The temperature-dependent coercivities, furthermore, require constant temperature monitoring and adjustments of the clock amplitude to guarantee stable operation.

## 3.6 Operating Frequencies

By taking the physical limitations as well as the design goals into account, we can estimate a frequency corridor in which pNML would likely be able to operate, given arguably optimistic but nevertheless realistic material parameters and magnet sizes. This corridor is fundamentally limited in terms of clock frequencies by the attempt frequency of the used magnetic materials, which for metallic ferromagnets is $\approx 1\,\mathrm{GHz}$. The attempt frequency describes the frequency of thermal excitation attempts within the *Néel-Arrhenius* law governing the DW nucleation process [114], [161]. Although magnets can be switched at much higher frequencies, the necessary nucleation fields increase disproportionately when approaching this frequency. However, finite DW velocities will set an upper frequency significantly lower than the theoretically possible nucleation time. Assuming very high DW velocities around $100\,\mathrm{m\,s^{-1}}$ and magnet sizes not larger then $100\,\mathrm{nm}$ would according to Equation (3.4) result an upper frequency of $\approx 250\,\mathrm{MHz}$. The focus of pNML designs must, therefore, be on wide architectures utilizing the benefits 3D-integration on a massive scale can offer in order to achieve competitive computational throughputs at realistic frequencies $\leq 200\,\mathrm{MHz}$. Simulations already show that comparable computational throughputs at significantly lower power densities are conceivable [52], [56].

## 3.7 Material Systems

A variety of material systems was considered for pNML. First concepts envisioned large permalloy pillars with perpendicular-shape-anisotropy (PSA) to realize an out-of-plane easy axis. However, the first experiments were conducted using magnetic super-lattices with pronounced crystalline and interface anisotropies, namely Pt/Co multilayers. Without these robust, exchange-coupled multilayers, the design and experimental demonstration of a complete family of logic elements with associated support structures (interconnects, vias, DW-gates) would not have been possible. Its comparatively simple fabrication, together with the strong PMA and high total magnetic moments originating from both the cobalt as well as the spin-polarized platinum, made Pt/Co the ideal material for proof-of-concept studies. However, this material, together with others like Pd/Co or Au/Co were initially developed for data-storage application in magnetic hard-drives and thus are aimed at high stability, high coercivities, and thus high DW-depinning fields. However, these features are fundamentally detrimental to computation, where magnetization directions need to be reversed millions or even billions of times a second with marginal energy cost. In the following section, the materials systems, explored throughout this work are introduced and their fundamental physical properties discussed. Furthermore, other interesting material systems are introduced.

### 3.7.1 Pt/Co/HM Super-Lattices

Discovered in the late 80s, artificial Pt/Co and Pd/Co superlattices were the first systematically analyzed thin films with strong perpendicular magnetic anisotropy [162][1]. In these films, the PMA originates from the magneto-crystalline anisotropy of the fcc (111) grown cobalt, sandwiched between metals from the platinum group and the respective surface and magneto-elastic (strain) anisotropies at the upper and lower X/Co/X interfaces. In the case of Pt/Co, the lattice mismatch between both elements, grown in the (111) direction is ≈ 9 % (354 pm (Co(fcc)) vs. 406 pm(Pt)[164]), under optimal conditions, this allows for the coherent (strained) Co growth on top Pt of about one monolayer, followed by an intermediate growth region in which the lattice strain is relieved. This strain leads to a strong magneto-elastic contribution to the out-of-plane anisotropy. After a thickness of about 2-3 mono-layers additional cobalt, now grown incoherently (unstained in the (111 direction)), it no longer increases the overall effective anisotropy [90], [165], [166]. The peak in $K_{\mathrm{eff}}$, therefore, occurs near the transition between coherent/intermediate regime and the incoherent growth region ($t_{\mathrm{Co}} \approx 0.7\,\mathrm{nm}$). In order to establish a reference and measure the quality of the used fabrication equipment used throughout this work, the cobalt thickness-dependent effective anisotropy of a Pt/Co/Pt trilayer system was analyzed. Figure 3.11 displays the anisotropy evolution in absolute and thickness normalized form. The normalization allows for the easy determination of the surface ($K_{\mathrm{s}}$) as well as the volume $K_{\mathrm{v}}$ contributions to $K_{\mathrm{eff}}$ ($K_{\mathrm{eff}} = K_{\mathrm{v}} + K_{\mathrm{s}}$), via a simple linear fit. The plot furthermore underlines the transition from a coherent to incoherent cobalt growth (occurring at $t_{\mathrm{Co}} \approx 0.7\,\mathrm{nm}$). The extracted $K_{\mathrm{v}}$ and $K_{\mathrm{s}}$ components (displayed in Figure 3.11) agree well with values usually reported in literature [82], [90], [91], [165]. A general overview of different materials and their anisotropy components is depicted in Table 4.1. Considering the much smaller volume and interface contributions of (110) and (100) Co, highlights the importance of the (111) crystal structure in achieving positive $K_{\mathrm{eff}}$ values. Somewhat confusing in this context, is the fact, that $K_{\mathrm{v}}$ is still negative, however, this is due to the fact that the volume anisotropy is the sum of the magneto-crystalline and the shape anisotropy ($-\frac{1}{2}\mu_0 M_{\mathrm{s}}^2$) which for cobalt amount to $\approx -1.2\times10^6\,\mathrm{J\,m^{-3}}$. Generally speaking, the effective anisotropy is set by the cobalt thickness and the growth quality of the film. When considering single trilayer films, the OOP to

---

[1] It is worth mentioning, though, that first reports of perpendicular magnetized Pt/Co layers go back to the mid-70s [163]

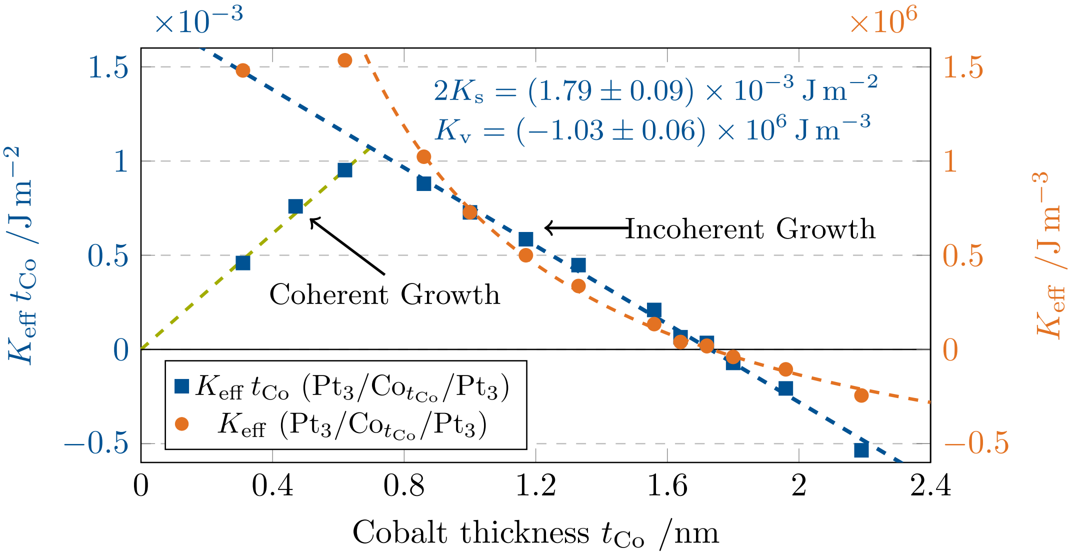

**Figure 3.11** Plot of the cobalt thickness ($t_{\mathrm{Co}}$) dependent effective anisotropy constant $K_{\mathrm{eff}}$. The plot in blue, which denotes to the left y-axis, displays the thickness normalized effective anisotropies ($K_{\mathrm{eff}}\, t_{\mathrm{Co}}$), used to extract the surface and interface component via a simple linear fit (dashed blue line). The data furthermore illustrates the two distinct growth regimes with slopes of opposing signs. As a comparison, the absolute anisotropy values are displayed to stress that $K_{\mathrm{eff}}$ is highest for a coherent growth.

**Table 3.2** Overview of typical volume and interface anisotropies of various metallic thin film systems and crystal orientations. As interface anisotropy $K_\mathrm{s}$ the mean contribution form both interfaces is listed. This can cause a wide spread of values for asymmetric systems like CoFeB/MgO.

| **Materials** | | $K_\mathrm{s}/\mathrm{J\,m^{-2}}$ | $K_\mathrm{v}/\mathrm{J\,m^{-3}}$ | **Reference** |
|---|---|---|---|---|
| Pt/Co/Pt | (111) | $\approx 0.9 \times 10^{-3}\,\mathrm{J\,m^{-2}}$ | $\approx -9 \times 10^{5}\,\mathrm{J\,m^{-3}}$ | [82], [90], [91], [165] |
| | (110) | $\approx 0.4 \times 10^{-3}\,\mathrm{J\,m^{-2}}$ | $\approx -2 \times 10^{6}\,\mathrm{J\,m^{-3}}$ | [90] |
| | (100) | $\approx 0.6 \times 10^{-3}\,\mathrm{J\,m^{-2}}$ | $\approx -6 \times 10^{6}\,\mathrm{J\,m^{-3}}$ | [90] |
| Pt/Co/Ir | (111) | $\approx 0.85 \times 10^{-3}\,\mathrm{J\,m^{-2}}$ | $\approx -1.2 \times 10^{6}\,\mathrm{J\,m^{-3}}$ | [167] |
| Ir/Co/Pt | (111) | $\approx 0.85 \times 10^{-3}\,\mathrm{J\,m^{-2}}$ | $\approx -1.2 \times 10^{6}\,\mathrm{J\,m^{-3}}$ | [167] |
| Pt/Co/Mg | (111) | $\approx 0.85 \times 10^{-3}\,\mathrm{J\,m^{-2}}$ | $\approx -1.2 \times 10^{6}\,\mathrm{J\,m^{-3}}$ | [91] |
| Pt/Co/W | (111) | $\approx 0.7 \times 10^{-3}\,\mathrm{J\,m^{-2}}$ | $\approx -0.85 \times 10^{6}\,\mathrm{J\,m^{-3}}$ | [82] |
| Co/Ni | (111) | $\approx 0.4 \times 10^{-3}\,\mathrm{J\,m^{-2}}$ | $\approx -3.9 \times 10^{5}\,\mathrm{J\,m^{-3}}$ [a] | [90], [168], [169] |
| X/Co | (111) | | $\approx -9 \times 10^{5}\,\mathrm{J\,m^{-3}}$ | [90], [169] |
| X/Ni | (111) | | $\approx -1 \times 10^{5}\,\mathrm{J\,m^{-3}}$ | [90], [170] |
| $\mathrm{Co_{20}Fe_{60}B_{20}/MgO}$ | | $0.65 - 1 \times 10^{-3}\,\mathrm{J\,m^{-2}}$ | $\approx -1 \times 10^{6}\,\mathrm{J\,m^{-3}}$ [b] | [171]–[174] |
| $\mathrm{Co_{40}Fe_{40}B_{20}/MgO}$ | | $< \mathrm{Co_{20}Fe_{60}B_{20}/MgO}$ [c] | $\approx -9.5 \times 10^{5}\,\mathrm{J\,m^{-3}}$ [b] | |
| $\mathrm{Co_{60}Fe_{20}B_{20}/MgO}$ | | $< \mathrm{Co_{20}Fe_{60}B_{20}/MgO}$ [c] | $\approx -8.7 \times 10^{5}\,\mathrm{J\,m^{-3}}$ [b] | |

[a] Measured for a $t_\mathrm{Ni}/t_\mathrm{Co}$ ratio of 2.2 and similar to the value calculated via the stoichiometry

[b] $K_\mathrm{v} \approx -\frac{1}{2}\mu_0 M_\mathrm{s}^2$, with $M_\mathrm{s}$ being calculated from the respective stoichiometry

[c] Due to the lower Fe content the CoFeB/MgO interface anisotropy is expected to be smaller

IP transition in sputtered films usually occurs at a Co thickness of $\approx 1.7\,\mathrm{nm}$ (depicted in Figure 3.11). In multilayer systems, the Co thickness is generally smaller ($< 1.5\,\mathrm{nm}$) and inversely proportional to the number of multilayers ($N$), as the crystal quality slowly degrades with the number of repetitions. The highest anisotropies are reported for compositions of one atomic layer of cobalt and two layers of platinum. Aside from the Co thickness, the most accessible parameter to adjust $K_\mathrm{eff}$ is the platinum thickness, both as seed and interlayer. The seed crystal directly affects the entire stack quality and is essential in achieving the OOP easy axis. When grown on tantalum or tungsten, the quality of the seed saturates at $\approx 3\,\mathrm{nm}$, thinner layers, directly reduce $K_\mathrm{eff}$. The Pt between the individual Co layers serves two purposes, it is vital to reestablish the (111) crystal order and simultaneously reduces the effective saturation magnetization (and thus increase $K_\mathrm{v}$) of the stack by introducing a nonmagnetic spacer layer. The spin polarization of Pt is neglected for this consideration, as the Pt layers are usually about 1 nm thick and, even if polarized, only develop a relatively small magnetic moment compared to Co. The effective saturation magnetization of the total stack can be approximated by the simple formula

$$M_\mathrm{s}^\mathrm{Pt/Co} \approx \frac{N t_\mathrm{Co} M_\mathrm{s}^\mathrm{Co}}{N t_\mathrm{Co} + (N-1) t_\mathrm{NM}}, \tag{3.6}$$

where $N$ is the number of multilayers and $t_\mathrm{NM}$ is the thickness of the nonmagnetic spacer layer (e.g., Pt, Pd). However, Equation (3.6) only yields valid results when $M_\mathrm{s}^\mathrm{Co}$ is precisely known. For Pt/Co systems with more than a monolayer of Co per layer, the intrinsic value for Co ($\approx 1.4 \times 10^6\,\mathrm{A\,m^{-1}}$) generally holds, in case of Pt/Co/HM systems, the presence of potentially very large magnetic dead layers (MDL) at the Co/HM interface complicates the use of Equation (3.6) as $M_\mathrm{s}^\mathrm{Co}$ becomes a function of $t_\mathrm{Co}$. Therefore, the saturation magnetization must be measured for a wide range of Co thicknesses. For a detailed discussion of this topic, it is referred to section 6.1. Furthermore, incorporating a different heavy metal into the Pt/Co superlattice generally increases disorder. It reduces crystal quality as most used elements exhibit larger lattice mismatches than Pt or do not feature an fcc crystal structure. This effect scales with the layer thickness and is only partially compensated by the subsequent Pt layer. However, this is not always the case, as the other platinum group metals (Ir, Pd, Ru) show very similar structures compared to Pt. Nevertheless, the increased distance between the Co layers reduces the interlayer coupling and opens the door for element-dependent RKKY or orange-peel coupling.

Nevertheless, despite the generally lower crystal quality, the cobalt thicknesses tend to increase. This appears counterintuitive only at first glance since the introduction of the HM reduces the effective saturation magnetization of the stack and enables more cobalt atoms per layer to level out the effective anisotropy. Another important but detrimental factor is the changed interface anisotropy at the upper Co/HM interface. The top interface generally contributes less to the combined anisotropy than the bottom one, as the more disordered upper Co atoms reduce the interface quality. In addition, interdiffusion and sputter damage from the heavy top metal, further degrades the interface. Depending on the platinum substitute, the resulting anisotropy can thus be smaller (W, Ir, Ru), similar (Ta, Cu), or even larger (Mg) [82], [91], [165], [167]. Another essential aspect in designing Pt/Co/HM stacks is the formation of possibly very strong interlayer couplings, originating from both the orange-peel effect as wells as RKKY coupling. By tuning the thickness of heavy metals with known RKKY interaction (e.g., Ir, Ru), it is possible to create strongly FM coupled, only weakly coupled, or even AF coupled systems. These complex interactions are usually irrelevant for Pt/Co systems as Pt mainly introduces ferromagnetic RKKY interaction, which due to the small interlayer thickness, is, generally, much larger than any orange-peel effects. Between 2015 and the early 2020s, Pt/Co/HM systems gained increased attention due to significant iDMI interactions originating from the broken inversion symmetry (different bottom and top interface). In addition, the discovery of efficient charge-to-spin conversion (Spin-Hall effect) in some of the aforementioned heavy metals (Pt, Ta, W) further drove interest in these layers.

### 3.7.2 Co/Ni Super-Lattices

PMA multilayer systems consisting of alternating layers of Cobalt and Nickel were first fabricated and characterized in the early 90s shortly after the Pt/Co and Pd/Co systems [168], [170]. Although discovered shortly after the other cobalt-based multilayer systems, the aspects of the PMA are much more plentiful and complex. Up to this date, some are still the subject of intense debates [90], [175]. A comprehensive discussion of all aspects is, therefore, beyond the scope of this work. Similar to Pt/Co and Pd/Co systems the perpendicular anisotropy in Co/Ni systems originates from a strained fcc growth on top of a Au or Pt seed and respective interface contributions, however, there are two distinct differences. First, nickel is a ferromagnet and placed directly adjacent to cobalt in the periodic-table, resulting in comparatively small interface anisotropies ($\approx 0.4 \times 10^{3}\,\mathrm{mJ\,m^{-2}}$). Second, while for the Pt/Co systems, the lattice mismatch is considered significant and every Co layer requires an new Pt sub-layer to grow in an fcc configuration, the lattice mismatch between fcc cobalt and fcc nickel is with only 0.5 % comparatively small (354 pm (Co(fcc)) vs. 352 pm(Ni(fcc))) [164]. This small mismatch enables the fcc growth of both materials without the need for nonmagnetic interlayers, given, that a seed layer enforces the initial fcc growth in (111) direction [176]. The combined effective saturation magnetization can be calculated, by adapting Equation (3.6) for a spacer with magnetic moment ($M_\mathrm{s}^\mathrm{Ni} \approx 4.9 \times 10^{5}\,\mathrm{A\,m^{-1}}$). Considering a ratio of $t_\mathrm{Ni}/t_\mathrm{Co} = 2$ for the respective thicknesses results in a combined $M_\mathrm{s}^\mathrm{Co/Ni} \approx 8 \times 10^{5}\,\mathrm{A\,m^{-1}}$. This is significantly larger compared to Pt/Co or Pt/Co/HM systems and results in different design paradigms to nevertheless achieve large anisotropies. The individual Co layers are thereby thinner than one atomic layer ($t_\mathrm{Co} \leq 0.4\,\mathrm{nm}$) and embedded in one to three atomic layers of nickel. Best results are usually achieved using $t_\mathrm{Ni}/t_\mathrm{Co}$ ratios of $\approx 2$. To elucidate these design choices, we first have to understand the crystal growth and the different anisotropy contributors. The cobalt, grown on nickel, is only strained marginally and thus features a similar volume contribution as the cobalt grown incoherently on top of platinum (this is not the case for the first Co layers grown on top of the seed layer) [169]. Nickel, aside from its small lattice mismatch, is an ideal partner for fcc cobalt, as its low saturation magnetization results in an almost insignificant volume contribution of $\approx -1 \times 10^5\,\mathrm{J\,m^{-3}}$ [90], [170]. The total Co/Ni volume anisotropy can be calculated in same manner as the saturation magnetization. Using the in Table 4.1 listed values for X/Co and X/Ni and a ratio of $t_{\mathrm{Ni}}/t_{\mathrm{Co}} = 2.2$ yields a $K_{\mathrm{v}} \approx -3.75 \times 10^5\,\mathrm{J\,m^{-3}}$, very close to the measured value of $K_{\mathrm{v}} = -3.9 \times 10^5\,\mathrm{J\,m^{-3}}$ [168]. Aside from the smaller volume contribution, the interface anisotropy is also considerably smaller than in Pt/Co/HM systems, leading to the consequence that a large number of interfaces is essential to reach substantial stack thicknesses before losing the OOP easy axis. The typical layer thicknesses, thereby, range between 2 Å to 3 Å for Co and 4 Å to 8 Å for Ni, again with a ratio of $t_{\mathrm{Ni}}/t_{\mathrm{Co}} \approx 2$ [142], [168], [170], [175]. Depending on the seed layer, this generally allows for repetition numbers between 5 and 50.

Post deposition annealing (< 300 °C) can generally be used to sharpen the interfaces and increase the PMA, although there are different and sometimes conflicting notions regarding the origins of this anisotropy increase [175], [177]. Annealing at even higher temperatures is usually considered to be detrimental, strongly increasing the pinning fields and finally causing a degradation of the stack.

### 3.7.3 CoFeB/MgO Thin Films

CoFeB is commonly used as an acronym, covering the family of cobalt-iron-boron alloys, which found adoption in MTJ and spin valves from the early 2000s onward. Their combination of low coercivities, low magnetic damping, and high spin-dependent electron scattering probabilities made them ideal for use in GMR and MTJ sensors [178]. The low coercivity results from the incorporated boron, which inhibits crystalline growth of the cobalt and iron, leading to an amorphous (ideal conditions) or at least poorly crystalline layer growth. However, out-of-plane (OOP) magnetized Ta/CoFeB/MgO thin films were first developed in 2009, independently by researchers at IBM Research and the Ohno group in Japan [173], [179]. Both were trying to optimize and improve existing in-plane magnetic tunnel junctions for storage applications and found that for CoFeB thicknesses ≤ 1.5 nm the magnetic easy-axis can point out-of-plane [180]–[182]. This discovery triggered an avalanche in research and industry alike to overcome the restrictions imposed by the shape anisotropy in in-plane magnetized devices, culminating in the development of spin-orbit-torque MRAM and scaled STT MRAMs with cell diameters below 40 nm [183]–[185]. Aside from the adoption in non-volatile memories, these films also possess many properties, making them very appealing to be considered for nanomagnetic logic. The extremely low depinning field, combined with possibly very narrow switching field distributions, promises to solve some of the most severe problems of the earlier discussed superlattices [131], [186]. To understand the exact causes for these properties, however, we first have to understand the formation of PMA in these systems.

The PMA in HM/CoFeB/MgO layers arises solely from the top and bottom interfaces, making the material system very sensitive, even to small changes or variations of the interface quality. The CoFeB/MgO interface (which usually is the top interface) can thereby be considered as the more interesting one, contributing to the combined $2K_{\mathrm{s}}$ interface anisotropy. The exact nature of the anisotropies present at the CoFeB/MgO interfaces is highly complex and, up to this date, not answered conclusively. However, in the context of this work, it is expedient to consider two key factors, namely the right oxidation states formed between the oxygen and the iron atoms at the interface (the oxygen cobalt bonds seem to play a subordinate, or even detrimental role) and the local lattice strain enforced by the crystalline MgO at the interface [187]–[190]. Very delicate, at this point, is the growth quality and stoichiometry of the MgO layer, since magnesium oxide is known to be hygroscopic and grow oxygen-rich, resulting in a potential over-oxidation of the CoFeB layer. This picture becomes even more complicated considering the typically applied post-deposition annealing, with the out-diffusion of boron, the potential crystallization of the CoFe and the inter-diffusion of the bottom interface material (usually a heavy metal) through the CoFeB layer towards the critical MgO interface [172], [191]. Aside from the CoFeB/Oxide interface, the second (usually CoFeB/Metal) interface serves two purposes, firstly it also contributes to the combined $2K_{\mathrm{s}}$ interface anisotropy, and secondly, it serves as a seed layer for the amorphous CoFeB growth and as a potential non-magnetic but metallic spacer layer, allowing for RKKY interactions between adjacent layers. The contributions from the CoFeB/Metal interface to

$2K_\mathrm{s}$ are usually considered to be subordinate since CoFeB layers sandwiched between metals generally exhibit much smaller out-of-plane anisotropies [171]. There are some notable exceptions; however, in these cases, the PMA originates also from magneto-crystalline contributions [192], [193]. The total $2K_\mathrm{s}$ anisotropy of HM/CoFeB/MgO films ranges, depending on the chosen metal and annealing temperature between $1.3\,\mathrm{mJ\,m^{-2}}$ and $2\,\mathrm{mJ\,m^{-2}}$, with the heavy metals Ta, W, and Mo reaching the highest values [171]–[174]. The influence of the interface metal on $K_\mathrm{eff}$ is, however, decisive. Many of the used materials like Ta, W, or Mo are known to develop very large magnetic dead layers (up to more than half a nm in extreme cases) and thus significantly reduce the saturation magnetization of very thin layers, causing an effective increase in $K_\mathrm{eff}$. At this point it has to be mentioned that the subject of magnetic-dead-layers and their effects on the saturation magnetization is very often handled somewhat confusing in literature since it is possible to calculate $M_\mathrm{s}$ for the nominal or the effective (nominal minus dead-layer) thickness [194]. In addition to the MDL at the interface, there are also indications that the diffused HM atoms in the CoFeB layer or at the CoFeB/MgO interface not only increase $K_\mathrm{eff}$ but also the interface anisotropy. These indications stem from experiments where a sub-mono-layer of Hf, Ta, or Mo was inserted into the CoFeB layer during sputtering, resulting in an enhanced $2K_\mathrm{s}$ interface anisotropy [194]–[196]. This not only allows for CoFeB thicknesses beyond $\approx 1.5\,\mathrm{nm}$ but also underlines the complexity of the perpendicular magnetic anisotropy in the X/CoFeB/MgO material system.

In literature, it is commonly stated that aside from the discussed interface anisotropies, the magneto-crystalline or volume anisotropy is negligible or zero (due to the amorphous nature of the film). However, such statements are somewhat misleading as they are to be interpreted, that there are no contributions aside from the always present shape anisotropy and that $K_\mathrm{v} \approx -\frac{1}{2}\mu_0 M_\mathrm{s}^2$. The volume contribution, therefore, solely depends on $M_\mathrm{s}$ which can be calculated from the respective alloy stoichiometry and the dead-layer thickness. For the most commonly used alloys, Table 4.1 illustrates the resulting approximate volume anisotropies (presuming no magnetic dead-layer). The value of $K_\mathrm{v}$ for the most frequently used $\mathrm{Co_{20}Fe_{60}B_{20}}$ alloy is comparable to that of fcc cobalt, which due to similar interface anisotropies results in similar but slightly lower transition point at $\approx 1.5\,\mathrm{nm}$ [172], [173], [195], [197]. Multilayers are, however, difficult to realize, as the MgO, an insulator, impedes the long-range RKKY interaction. Therefore, exchange coupling between layers can only occur via the non-magnetic metal in a MgO/CoFeB/X/CoFeB/MgO structure. This severely limits the total magnetic moment of the stack achievable within this material system. The necessary growth of CoFeB on top of the crystalline MgO furthermore tends to increase the DW-depinning fields, as the formations of grains is more pronounced compared to the CoFeB growth on quasi amorphous heavy metals like Ta or W (this, of course, only holds for thin metals films with thicknesses $< 5\,\mathrm{nm}$). In magnetic tunnel junctions, annealing the stacks is necessary to crystallize the CoFeB layer and achieve high TMR ratios. For logic applications, annealing would serve the sole purpose of increasing the PMA and allowing for thicker CoFeB layers. Crystallization of the CoFeB layer is thereby detrimental, as it drastically increases the DW pinning. Annealing temperatures $\leq 275\,°\mathrm{C}$ increase the PMA but only marginally affect the DW pinning, while for temperatures above $300\,°\mathrm{C}$ a strong effect on the depinning fields could be observed[2]. This seems to be a potential problem affecting the BEOL compatibility of Ta/CoFeB/MgO stacks for logic applications. However, as discussed before, there are many possible replacements for tantalum with higher thermal stabilities (e.g., W or Mo) [191], [197]–[199]. To summarize the CoFeB/MgO systems discussion, one can state that this sensitive material system features a vast parameter space. It is not without good reason that despite its sensitivity, this system is the sole material present in today's MTJs, which due to compatibility reasons, is in itself is a key argument for the usage also for logic applications. However, a potential showstopper might be the limited magnetic moment of the stacks leading to potentially insufficient coupling strengths.

---

[2] For a $\mathrm{Ta_1/CoFeB_{1.1}/MgO_1/Ta_3}$ stack annealed at 350 °C for 5 min in nitrogen atmosphere, a depinning fields increase from 0.5 mT to 14 mT was observed (measured on film-level).

### 3.7.4 Ferrimagnetic Insulators

Aside from metallic multilayers with large saturation magnetizations, there is another class of interesting magnetic materials with insulating properties. Today the most prominent group of magnetic insulators is made up of rare-earth iron garnets. These garnets are antiferromagnets with incomplete magnetic compensation, resulting in a small residual spontaneous magnetization. These so-called ferrimagnets are usually grown on single-crystal substrates and feature appealing properties for many spintronic applications [200]. The most prominent out of these garnets is the in-plane magnetized Yttrium-Iron-Garnet (YIG) which is widely used for spin-wave applications due to its unmatched damping constant of $\leq 1 \times 10^{-4}$ [200].

In particular rare-earth iron garnets, the magnetic easy-axis can also be turned out-of-plane by carefully modifying the magnetocrystalline anisotropy through magnetoelastic contributions, adding either compressive or tensile lattice strain during film growth [201]. PMA films like EuIG or DyIG feature comparatively low saturation magnetizations between $2 \times 10^4$ and $1 \times 10^5\,\mathrm{A\,m^{-1}}$ but OOP film thicknesses between 20 nm and 100 nm [201]–[203]. The low $M_\mathrm{s}$ values compared to metallic thin films could, therefore, easily be compensated by larger film thicknesses to achieve even larger magnetic moments overall.

One of the most appealing properties of these materials are the giant DW velocities in the range of $\mathrm{km\,s^{-1}}$ (close to the physical limit set by the magnon group velocity) two to three orders of magnitude larger compared to DW velocities in metallic thin films [204], [205]. Furthermore, the crystalline nature of the films should allow efficient control of the magnetic energy landscape by means of ion irradiation, in order to control domain wall nucleation (local anisotropy modification has already been shown for YIG films) [27], [206].

However, a significant disadvantage of these materials is the fact that there usually exists a huge lattice mismatch between the rare-earth iron garnets and silicon, complicating thin-film growth and potential integration. These garnets are usually grown on Gadolinium-Gallium-Garnet (GGG) single crystals or other specialized substrates. However, recent works report the growth of DyIG films with PMA on silicon substrates [203]. In the future, new classes of magnetic insulator might offer simpler integration with silicon and even higher anisotropies [207].

# 4 Fabrication Technology

The fabrication of magnetic nanostructures on silicon substrates constituted an essential part of this work. Therefore, this chapter introduces and discusses the most relevant fabrication processes used, optimized, and developed throughout the project. Readers familiar with semiconductor technology and magnetic thin-film deposition can proceed to the next chapter.

Generally speaking, the fabrication processes can be divided into three distinct categories, thin-film deposition, structuring, and ion-beam irradiation. The topic of thin-film deposition is discussed first. It covers the silicon substrate preparation (section 4.1) and subsequent sputter deposition with processes for Pt/Co/HM, Co/Ni, and CoFeB/MgO films. The different processes are thereby discussed separately (section 4.2).

Following the thin-film growth, the structuring employing deep sub-micron lithography and plasma etching is discussed in sections 4.3 and 4.4 respectively. For this purpose, a new negative tone double-resist lithography process was developed to reduce the fabrication complexity and complement established processes. The following section 4.5 covers the top power-metallization for interconnects and on-chip field coils.

The final part (section 4.6) covers the ion-beam irradiation process, introducing the used focused ion-beam microscope (FIB) and describing the procedures for ANC placement.

For the project, the cleanroom facilities and process tools of the Central Electronics and Information Technology Laboratory – ZEITlab were used for fabrication. Aside from fabrication, significant time resources were invested in maintaining and repairing the time-tested tool park and infrastructure.

Before addressing selective process steps in detail, it is imperative to mention that many of the available processes are the result of years of continuous development and optimization, which often started long before this work began. In addition, numerous researchers, technicians, and students developed and continue to maintain these processes.

## 4.1 Substrate Preparation

Silicon ⟨100⟩ wafers with a diameter of 125 mm (5") and a high n-type base doping (≈ 0.01 Ω cm) served as the substrate for all subsequent fabrication steps. The wafers featured two additional µm thick top expitaxial-layers with a dopant (phosphorous) concentration of $6 \times 10^{14}$ ions/cm$^2$ and $3 \times 10^{14}$ ions/cm$^2$ respectively. The wafers were first covered with a protective resist, before being cut into standardized 10 mm × 10 mm samples with an industrial wafer saw (Accretch-SS20). Following the segmentation, the individual dies were treated with a series of wet-chemical cleaning steps summarized under the well-known term RCA-clean. This cleaning procedure, developed by Werner Kern at the Radio-Corporation-of-America (RCA), consists of distinct steps aiming to subsequently remove particles as well as organic and ionic contaminants from the wafer surface and expose the bare silicon. After the RCA clean, a ≈ 50 nm thick thermal oxide was grown at 1000 °C in an oxygen atmosphere. This results in a well-defined, almost atomically flat surface, essential for the subsequent thin-film growth. Furthermore, the dielectric provided effective insulation between the conductive substrate and the, to be deposited, metallic thin films. The chosen oxide thickness was a trade-off between effective bulk insulation and detrimental charging effects, complicating the later ion-beam lithography and alignment process, essential for the targeted ion-irradiation of the nanostructures.
Initially, oxide thickness around ≈ 20 nm were used. However, with increasing knowledge of the magneto-optical test equipment, the oxide thicknesses were increased to reduce the reflectance in the relevant 400 nm to 600 nm range and thus increase the magneto-optical contrast [208].

## 4.2 Magnetic Thin-Film Growth

Magnetic thin films are usually grown by physical vapor deposition (PVD) techniques under high or ultra-high vacuum conditions. This is in contrast to the general trend in the semiconductor industry, moving towards highly complex chemical vapor deposition (CVD) or even atomic layer deposition (ALD) processes for ultra thin layers. The reasons for this are manifolds. The magnetic stacks usually consist of numerous different layers, each with its own requirements regarding crystallinity, interface quality, and thermal budget. The material zoo these stacks are comprised of includes next to the 3d-transition metals also many platinum group metals and other heavy metals and oxides, some of which are notoriously challenging to deposit via CVD or ALD processes [209].
Sputter deposition has, therefore, up to this point prevailed as the process of choice, combining high-quality growth with reasonable wafer throughput.

### 4.2.1 Sputter Deposition of Magnetic-Thin-Films

Historically, the development of thin films and the associated sputter processes was closely coupled to the needs of the rapidly advancing magnetic hard-drive industry for storage media and read heads alike. This became especially apparent after the discovery of the giant magnetoresistance effect in the late 80s and the emergence of PMA recording media. One of the first material systems considered for PMA recording media was a combination of atomically thin platinum and cobalt layers, which showed remarkably high PMA together with a large process window. This was one of the reasons why the first pNML implementation used Pt/Co multilayers (up to 10 layers). In this context, the wide process window must be stressed particularly, as the depositions were carried out manually using 4" Alcatel MDS 310 systems with three magnetrons, not designed for magnetic materials. However, at the start of this project, a new custom-made radio-frequency (RF) magnetron sputter tool for automated depositions became operational. This tool allowed a quick expansion in the number of material systems investigated, the most important of which are discussed in the following. The five 2" magnetrons of the sputter tool were arranged in a confocal (sputter-down) geometry, facing the center of the high-vacuum chamber. The samples were placed in the focal point of the five magnetrons with a constant distance of ≈ 20 cm between magnetrons and sample. The confocal geometry allows for uninterrupted depositions with minimal dead-times, as the samples are no longer required to move to the respective magnetrons between depositions. However, for the five magnetrons, only three RF power supplies were available at the time, two of which were hard-wired to particular magnetrons. The remaining generator was switched between the remaining three magnetrons via an RF switch. Therefore, only three materials could be deposited without powering down at least one power supply and interrupting the film growth. This introduced additional complexity and limitations, which had to be considered during process development. Before being transferred into the deposition tool, the 10 mm × 10 mm samples were annealed at 200 °C for 30 min in ambient atmosphere to desorb moisture as far as possible. Additional surface treatments inside the vaccum vessel included an UV-light shower and an ion-beam treatment using a self neutralizing anode layer ion source ($Ar^+$, 300 eV) [210]. Although we cannot provide comprehensive rule books concerning growth quality and interdependencies between the relevant process parameter for each investigated material system, we nevertheless present guidelines for the individual materials, to severe alongside the general rules for vacuum deposition [211]. Nevertheless, it has to stressed that process parameters are always tool-dependent.

### Platinum/Cobalt/Heavy-Metal Super-Lattices

The process development of the different Pt/Co/Heavy-Metal multilayers was based on the already available process knowledge obtained for Pt/Co layers in the legacy Alcatel tools. In accordance with the literature, the highest coercivities were achieved using high sputter pressures above 20 µbar while for low pressures between 2 µbar and 8 µbar low and constant coercive fields were observed [212]. Unfortunately, detailed studies on power dependence are not readily available in the literature and were not conducted. Most works only cite the rf-power but lack the necessary information to determine the power density. For the stack development, the rf-power, being closely related to plasma stability and deposition rates, was set to guarantee stable plasma conditions throughout the process and reach deposition rates $> 0.2\,\text{Å}\,\text{s}^{-1}$ to keep the number of incorporated contaminants during growth to a minimum. In order to allow for fast, uninterrupted depositions, a constant working pressure of 4 µbar was chosen, as it posed the best trade-off between coercivities and plasma stability (low anisotropies together with stable plasma conditions). Seed, stack, and capping layers were designed to consist of only three materials in total and could, therefore, be deposited uninterruptedly. For years, the quasi-standard for Pt/Co-based pNML magnets was a $Ta_2/Pt_3/[Co_{0.8}/Pt_1]_4/Pt_3$ stack, deposited via the legacy Alcatel machines. This stack featured domain sizes between 1 and 2 µm and film level coercivities around 15 mT (depending on the operator). As a rough comparison, a nominally identical stack fabricated with the automated tool features roughly ten times larger domains and doubled coercivities. Although cross-tool comparisons are always to be taken with a grain of salt, this increase in domains sizes and coercive fields suggests a significantly improved layer quality. The heavy metals most extensively studied were tungsten (W) and iridium (Ir). Both were chosen due to the reported presence of strong iDMI at the respective Co/HM interfaces. Iridium is furthermore known for its strong RKKY coupling, and it was found that the layers exhibited strong antiferromagnetic coupling at Ir thicknesses between $\approx 0.4$ nm and $\approx 0.9$ nm. However, it was also found that the introduction of tungsten heavily affects the interlayer coupling within the stack. Weak coupling between the layers with alternating signs could be observed for W thicknesses upwards of one mono-layer ($\approx 0.4$ nm) [82], [213]. A factor that should be considered in estimating the physical cobalt thickness is the sputtering damage to the cobalt layer caused by the much larger heavy metal atoms impinging on the previously deposited lighter cobalt. This damage generally ranges in the area of 1 Å [77]. Detailed deposition parameter for an exemplary $Ta_2/Pt_6/[Pt_{1.45}/Co_{1.2}/W_{0.4}]_4/Pt_3$ stack are depicted in Table 4.1. Furthermore, Figure 4.1 depicts two out-of-plane (OOP) hysteresis curves of this large anisotropy Pt/Co/W multilayer stack, next to a wide-field magneto-optical Kerr-effect image of the corresponding domain structure after easy-axis demagnetization. The first hysteresis curve is measured after demagnetization, thus allowing estimating the DW pinning fields. The second curve is recorded after saturation. Both curves are measured, utilizing the magneto-optical Kerr-effect and a de-focused laser to integrate over a larger area.

The measured coercivities and depinning fields of ≈ 30 mT suggest a film with large anisotropy and large anisotropy variations. The large anisotropy is then confirmed by the domain image in Figure 4.1 (b), showing domain sizes > 5 µm. For a better understanding of the hysteresis, it is referred to section 2.10 (multidomain magnet). The deposited Pt/Co/HM stacks are stable at room temperature, and even after several years, no degradation could be observed. It was found that annealing at temperatures > 200 °C in nitrogen atmosphere generally increases the effective anisotropy and, after longer times (> 1 h), also increases the depinning fields. However, from 350 °C onward, the continuous degradation of the stacks could be observed.

**Table 4.1** Sputter process parameter and deposition sequence of a $Ta_2/Pt_6/[Pt_{1.45}/Co_{1.2}/W_{0.4}]_4/Pt_3$ stack (nominal thicknesses given in nm). The critical Pt, Co, and W layers are deposited continuously on top of a pre-deposited Ta adhesion layer. All layers are sputtered at room temperature.

| Layer | Material | Quantity | Thickness | Pressure | Growth Rate[a] |
|---|---|---|---|---|---|
| Adhesion | Ta | 1 | 2 nm | 2 µbar | $\approx 0.5\,\text{Å}\,\text{s}^{-1}$ |
| Seed | Pt | 1 | 6 nm | 4 µbar | $\approx 0.83\,\text{Å}\,\text{s}^{-1}$ |
| Super-lattice | Co | $N = 5$ | 1.2 nm | 4 µbar | $\approx 0.4\,\text{Å}\,\text{s}^{-1}$ |
|  | W | $N = 5$ | 0.4 nm | 4 µbar | $\approx 0.23\,\text{Å}\,\text{s}^{-1}$ |
|  | Pt | $(N-1) = 4$ | 1.45 nm | 4 µbar | $\approx 0.83\,\text{Å}\,\text{s}^{-1}$ |
| Capping | Pt | 1 | 3 nm | 4 µbar | $\approx 0.83\,\text{Å}\,\text{s}^{-1}$ |

[a] A constant power density of $2\,\text{W}\,\text{cm}^{-2}$ was set for all materials

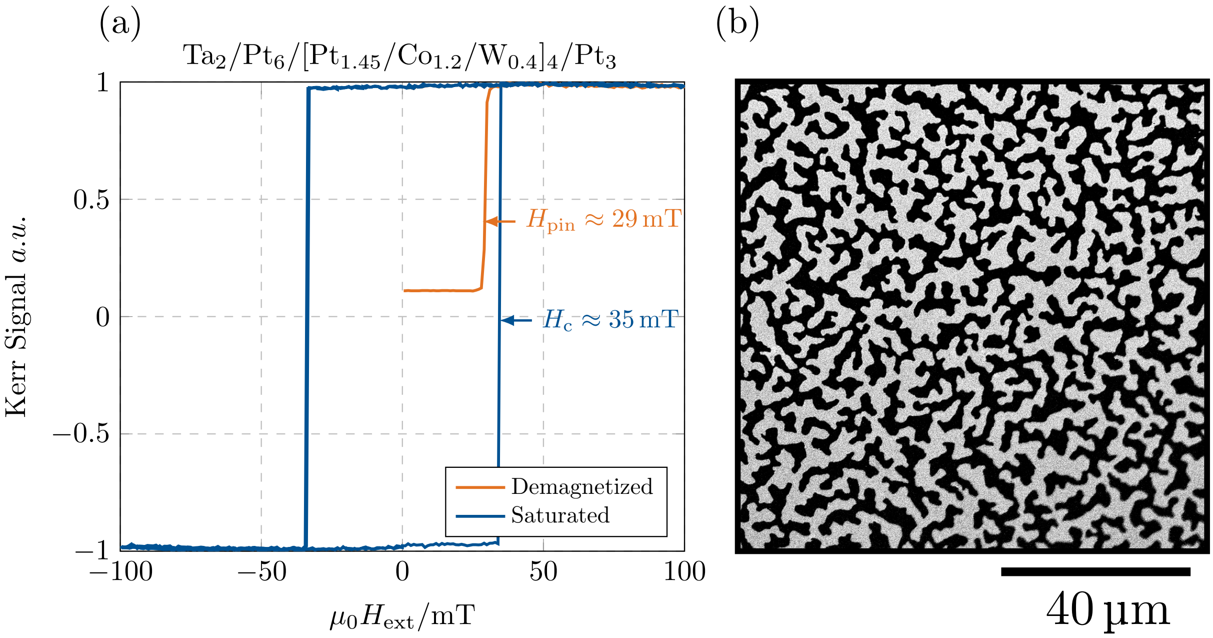

**Figure 4.1** In (a), two magnetic hysteresis curves of a pristine $Ta_2/Pt_6/[Pt_{1.45}/Co_{1.22}/W_{0.4}]_4/Pt_3$ film are displayed. In (b) a magnetic domain image of the respective film after easy-axis demagnetization is shown. High and low brightness levels indicate areas of opposing magnetization.

### Cobalt/Nickel Multilayers

Early Co/Ni processes using the legacy Alcatel tools required a thick gold (10 nm) and platinum 5 nm seed in combination with post deposition annealing 200 °C to achieve the necessary PMA [61]. With the new sputter tool and continuous, automated depositions, these extensive seed layers were no longer necessary. Without a predefined process to start, the parameter space was explored in different directions. The usage of gold as a seed layer was dropped in an early stage of development, as the resulting films exhibited large depinning fields $H_{\mathrm{depin}} \approx 20\,\mathrm{mT}$. A thin platinum seed ($t_{\mathrm{Pt}} < 1.5\,\mathrm{nm}$) grown on top of a tantalum ($t_{\mathrm{Ta}} \approx 2\,\mathrm{nm}$) adhesion layer yielded the lowest depinning fields (down to $\approx 1.5\,\mathrm{mT}$ for films with anisotropies near the easy-plane threshold) while persevering the option to scale the anisotropy via the Pt thickness effectively. Typical process parameters are listed in Table 4.2. An overview of the different Co/Ni ratios tested is provided in section 7.1, however, as a rule of thumb, we can state that a higher nickel content yields softer magnets with generally lower coercive and depinning fields [142]. This statement is naturally only valid within the single domain anisotropy corridor. In good agreement with results from literature and the theoretical discussion in section 3.7.2,

**Table 4.2** Detailed deposition parameter of $\mathrm{Ta_2/Pt_{1.35}/[Co_{0.2}/Ni_{0.4}]_6/Pt_3}$ stack. The the relevant layers (Pt, Co, and Ni) are deposited continuously onto the pre-deposited Ta seed. All films are sputtered at room temperature.

| Layer | | Quantity | Thickness | Pressure | Growth Rate[a] |
|---|---|---|---|---|---|
| Adhesion | Ta | 1 | 2 nm | 2 µbar | $\approx 0.5\,\mathrm{Å\,s^{-1}}$ |
| Seed | Pt | 1 | 1.35 nm | 4 µbar | $\approx 0.83\,\mathrm{Å\,s^{-1}}$ |
| Super-lattice | Co | N = 8 | 0.2 nm | 4 µbar | $\approx 0.4\,\mathrm{Å\,s^{-1}}$ |
| | Ni | N = 8 | 0.4 nm | 4 µbar | $\approx 0.36\,\mathrm{Å\,s^{-1}}$ |
| Capping | Pt | 1 | 3 nm | 4 µbar | $\approx 0.83\,\mathrm{Å\,s^{-1}}$ |

[a] A constant power density of $2\,\mathrm{W\,cm^{-2}}$ was chosen for all materials

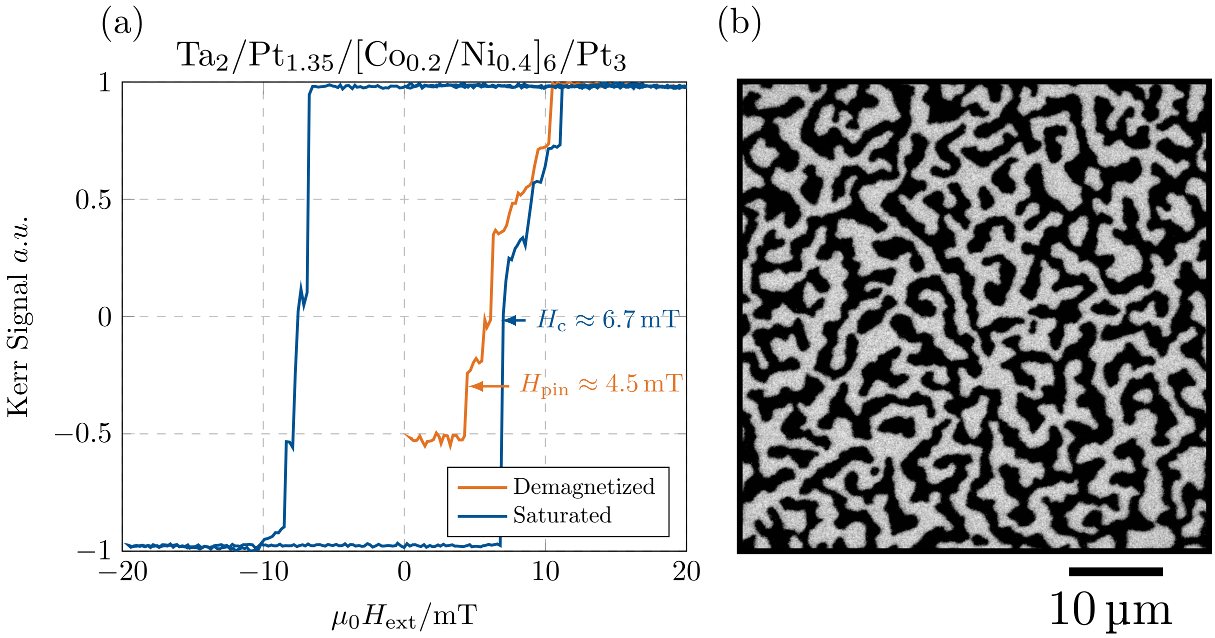

**Figure 4.2** In (a), two magnetic hysteresis curves of a pristine $\mathrm{Ta_2/Pt_{1.35}/[Co_{0.2}/Ni_{0.4}]_6/Pt_3}$ film are displayed. In (b) a magnetic domain image of the respective film after easy-axis demagnetization is shown. High and low brightness levels indicate areas of opposing magnetization.

the best trade-off between magnetization and coercivitiy was obtained for a Co/Ni ratio $t_{\mathrm{Ni}}/t_{\mathrm{Co}}$ close to 2 and a Ni thickness of one monolayer ($\approx 0.4\,\mathrm{nm}$). Furthermore, the selection of the starting layer for the Co/Ni sequence also had a strong effect on the overall anisotropy, as the Pt/Co interface yields higher surface and magneto crystalline anisotropies (see section 3.7.2).
Post deposition annealing at temperatures up to 250 °C in nitrogen as well as ambient environment was found to both increase anisotropy and depinning fields. The annealing allowed to reduce the Pt seed thickness and, in the case of a thick Ta seed, enables OOP magnetization even without a Pt seed layer. However, annealing was found to reduce the reproducibility and was therefore discarded in favor of using the Pt thickness as the main means to control the PMA. As a capping layer, a 3 nm thick platinum layer is used. The resulting stacks were stable at ambient conditions with no detectable degradation after several years. When comparing the domain images, it has to be stressed that the shown Co/Ni stack features a different anisotropy compared to the Pt/Co/W stack. Therefore, both images cannot be compared quantitatively. They instead serve the purpose of being a reference image for the listed process parameter and layer thicknesses.

### CoFeB/MgO Films

For the experiments with cobalt-iron-boron layers a sintered stoichiometrically correct CoFeB target consisting of 20 % cobalt, 60 % iron, and 20 % boron was used. This composition with high iron and boron content was chosen to achieve high interface anisotropies (from the iron-oxygen bonds), large magnetic moments, and at the same time low depinning fields (boron impedes grain formation). As discussed in section 3.7.3, the PMA in HM/CoFeB/MgO films originates solely from the two CoFeB interfaces. The CoFeB/MgO interface is crucial, as it contributes the lion-share to the total perpendicular magnetic anisotropy and, at the same time, is very sensitive to process variations. Today, the most prominent heavy-metals used in HM/CoFeB/MgO films are tantalum and tungsten, resembling the cornerstone of current MTJ-technologies for sensors and non-volatile storage devices alike. Therefore, both Ta and W were explored during process development. Although significant PMA can be achieved with both materials, Ta was chosen for further experiments due to higher as-grown coercivities and lower depinning fields. As reported in the literature, the most critical part of the deposition process was determined to be the MgO depositions. A particular problem of the MgO RF-magnetron sputter process is the very low deposition rate of $\approx 0.05\,\text{Å}\,\mathrm{s}^{-1}$ (at $2\,\mathrm{W\,cm^{-2}}$), which is roughly one order of magnitude smaller compared to metallic targets at the same power density. Furthermore, the low thermal conductivity and the brittle nature of oxide targets limit the maximum power density. The resulting very long deposition times increase the number of contaminants that can be incorporated into the layer during the layer growth. This, in turn, increases the sensitivity towards the process parameters and their fluctuations [209]. Moreover, the MgO sputter rate is known to drift during deposition, resulting in deviations between nominal and physical layer thicknesses. Initially, a nominal MgO thickness of 2 nm was chosen (a value often found in literature). However, with this thickness, no as-grown OOP easy-axis could be achieved (even of minimal CoFeB

**Table 4.3** Detailed Sputter Parameter and order of an exemplary $\mathrm{Ta_2/CoFeB_{1.1}/MgO_1/Ta_3}$ stack. All layer are deposited continuously onto the pre-deposited Ta seed. With the pressure being temporarily lowered to 1 µbar for the MgO. All films are sputtered at room temperature.

| Layer | Material | Thickness | Pressure | Growth Rate[a] |
|---|---|---|---|---|
| Adhesion & Interface Layer | Ta | 2 nm | 4 µbar | $\approx 0.45\,\text{Å}\,\mathrm{s}^{-1}$ |
| Magnetic layer | $\mathrm{Co_{20}Fe_{60}B_{20}}$ | 1.1 nm | 4 µbar | $\approx 0.28\,\text{Å}\,\mathrm{s}^{-1}$ |
| Interface Layer | MgO | 1 nm | 1 µbar | $\approx 0.05\,\text{Å}\,\mathrm{s}^{-1}$ |
| Capping | Ta | 3 nm | 4 µbar | $\approx 0.45\,\text{Å}\,\mathrm{s}^{-1}$ |

[a] A constant power density of $2\,\mathrm{W\,cm^{-2}}$ was chosen for all materials

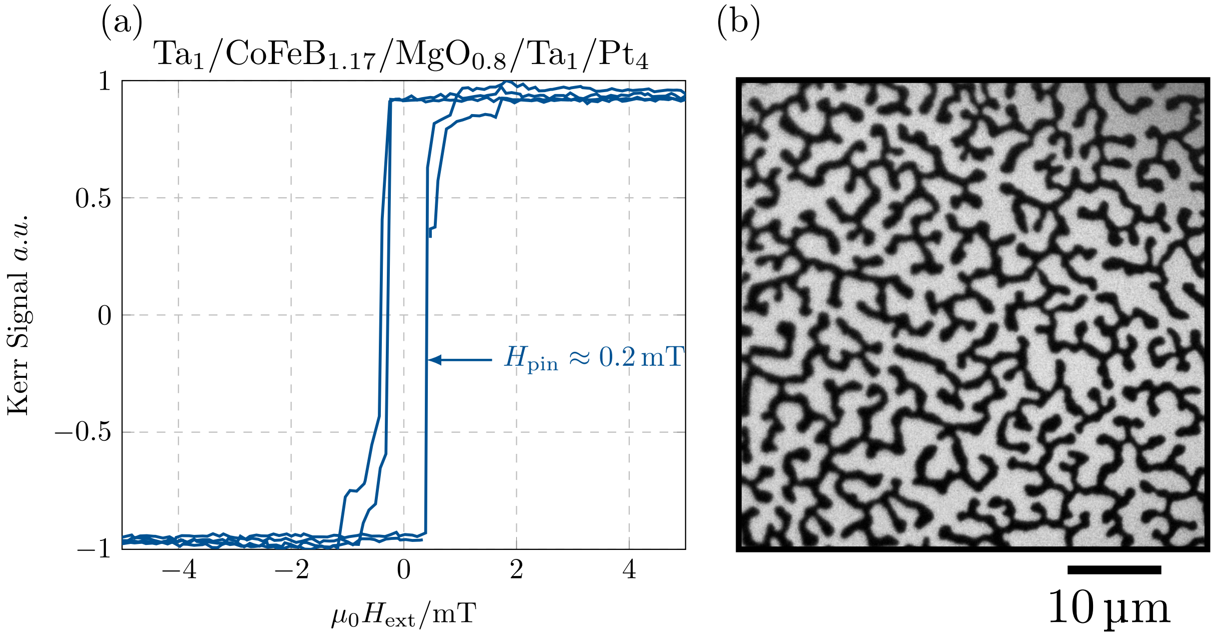

**Figure 4.3** In (a), the magnetic hysteresis curve of a pristine $Ta_1/CoFeB_{1.17}/MgO_{0.8}/Ta_1/Pt_4$ film is displayed. In (b) a magnetic domain image of the respective film after easy-axis demagnetization is shown. High and low brightness levels indicate areas of opposing magnetization.

thicknesses), and post-deposition annealing between 250 °C and 300 °C was necessary to achieve an OOP easy-axis. Large as-grown PMAs were only achieved with nominal MgO thicknesses around $\approx 1\,nm$ in combination with a very low sputter pressure of 1 µbar and a Ta or W capping layer. The reasons for this behavior could not be resolved definitively. However, a possible explanation lies in the hygroscopic nature of MgO and an oxygen-rich growth of the MgO layer, leading to reduced CoFeB/MgO interface anisotropies [187]–[190]. Furthermore, chemical reactions with the on-top deposited Ta or W could change the oxygen content a the CoFeB/MgO interface and thus modulate the interface anisotropy. An overview of the optimized process parameter is depicted in Table 4.3. The transition from out-of-plane to in-plane magnetization for pristine samples occurred at a nominal CoFeB thickness of $t_{CoFeB} = 1.2\,nm$. Although, thickness with up to $\approx 1.5\,nm$ were possible using post deposition annealing at 275 °C in nitrogen atmosphere. This maximum thicknesses is roughly comparable to literature values [172], [173], [195], [197], [199]. Annealing at temperatures above 300 °C was found to be detrimental for the PMA. The $Co_{20}Fe_{60}B_{20}$ alloy features an intrinsic saturation magnetization of $\approx 1.4 \times 10^6\,A\,m^{-1}$. However, SQUID magnetometer measurements of a $Ta_2/CoFeB_{1.0}/MgO_2/Ta_3$ revealed values of only $\approx 8.3 \times 10^5\,A\,m^{-1}$, indicating the presents of a $\approx 0.4\,nm$ thick magnetic dead layer, which is consistent with literature reports [174], [197], [199]. Compared to the Pt/Co/HM and Co/Ni, the fabricated Ta/CoFeB/MgO films feature depinning and coercive fields roughly one order of magnitude smaller. To illustrate this, Figure 4.3 (a) depicts the measured hysteresis of a pristine $Ta_1/CoFeB_{1.17}/MgO_{0.8}/Ta_1/Pt_4$ film with a coercive field of only 0.2 mT and domain sizes in the µm range (shown in Figure 4.3 (b)). Films with lower anisotropy even showed solely thermally activated DW motion at room temperature. When comparing the different domain images, it has to be stressed that the shown films feature different anisotropies. Therefore, the images cannot be compared quantitatively. Instead, they serve to be a reference image for the listed process parameter and layer thicknesses.

## 4.3 Sub-Micron FIB Lithography

The need for sub-micrometer structuring and the lack of electron-beam lithography capabilities on-site lead to the development of ion-beam lithography processes. As lithography tool, a 50 keV $Ga^+$ focused-ion-beam microscope (*Micrion 9500ex*) from 1990 is used (see Figure 4.9 for schematic illustration). The tool features stable beam currents down to 1 pA and a smallest beam diameter of $\approx 10\,\mathrm{nm}$. The beam pattern generator with blanker accepts binary bitmaps (up to $2000 \times 2000$ pixel) as input and scans the target area line-wise with a predefined dwell time per pixel (this results in a write-field spanning $20\,\mu\mathrm{m} \times 20\,\mu\mathrm{m}$ at highest resolution). This line and pixel-wise scanning will naturally result in an increased edge roughness compared to vector scan approaches. The tool was initially developed for industrial applications and, therefore, supports the Micrion direct modification description language (MDDL) for automation. The lithography resolution, aside from the sub-optimal capabilities of the pattern generator, is also reduced by a widening of the lithographic features due to scattering events, resulting in a significant undercut (when used with a positive resist). The $Ga^+$ range in typical electron beam resists is $\approx 70\,\mathrm{nm}$ thus limiting the resist to comparable thicknesses. To asses the impact of $Ga^+$ ion-beam irradiation on the respective resists, the well established SRIM/TRIM code is used for simulations[214], [215]. This thickness limitation is an important distinction compared to electron-beam lithography processes. The reliably achievable resolution of the system is mainly limited by the pattern generator and ranges around 50 nm. Resolving smaller features is still possible, though only with reduced yield rates.

### 4.3.1 Titanium Hard-Mask Process

Polymethyl methacrylate (PMMA), also known as PLEXIGLAS™, is a transparent UV-insensitive plastic, which among many other applications, is widely used as an electron beam resist. At low doses, the resist operates as a positive resist with high sensitivity (generated secondary electrons destroy the polymer chains). However, at high doses the resit changes towards a negative behavior (cross-linking of the polymer chains). For this work, PMMA (*AR-P670 Allresist GmBH*) is used in the positive regime to open the resist at the irradiated sites, followed by the deposition of a Ti hard-mask and an obligatory lift-off process to invert the lithography profiles. For better illustration, Figure 4.4 depicts the most important process steps schematically. First, the sputtered films are spin-coated with a $\approx 50\,\mathrm{nm}$ thick PMMA layer, followed by a post-exposure bake at 100 °C for 90 s. In the subsequent FIB lithography step (Figure 4.4 (b)), the layout of the magnetic structures is transferred to the resist. A dose of $\approx 3 \times 10^{12}\,\mathrm{ions/cm^2}$ or $\approx 0.5\,\mu\mathrm{C\,cm^{-2}}$ was found to yield the smallest feature sizes while only marginally affecting the sputtered films (see Appendix D1 for respective SRIM simulations). Following the irradiation, the resist is developed at room temperature in a methyl-isobutyl-ketone (MIBK) based solution for $\approx 15\,\mathrm{s}$ (*AR 600-55 Allresist GmBH*). The developer dissolves the irradiated areas, creating a pronounced undercut in the 50 nm thick resist. Adjusting the development time by a few seconds allows tuning the final feature site effectively. During the fourth step (Figure 4.4 (d)), a 3 nm to 6 nm thick Ti hard-mask is deposited onto the sample via electron-beam physical-vapor-deposition (PVD) at a base pressure $< 4 \times 10^{-7}\,\mathrm{mbar}$ ($\approx 0.5\,\text{Å}\,\mathrm{s^{-1}}$). The remaining resist is then removed via a subsequent lift-off process (Figure 4.4 (e)), using a dimethyl-sulfoxide (DSMO) solution at 70 °C in an ultrasonic cleaner. Finally, in the last step, the non-masked areas are dry etched via $Ar^+$ ion-beam milling ($E_{\mathrm{Ar}} \approx 350\,\mathrm{eV}$). For details regarding the plasma etch process it is referred to section 4.4.

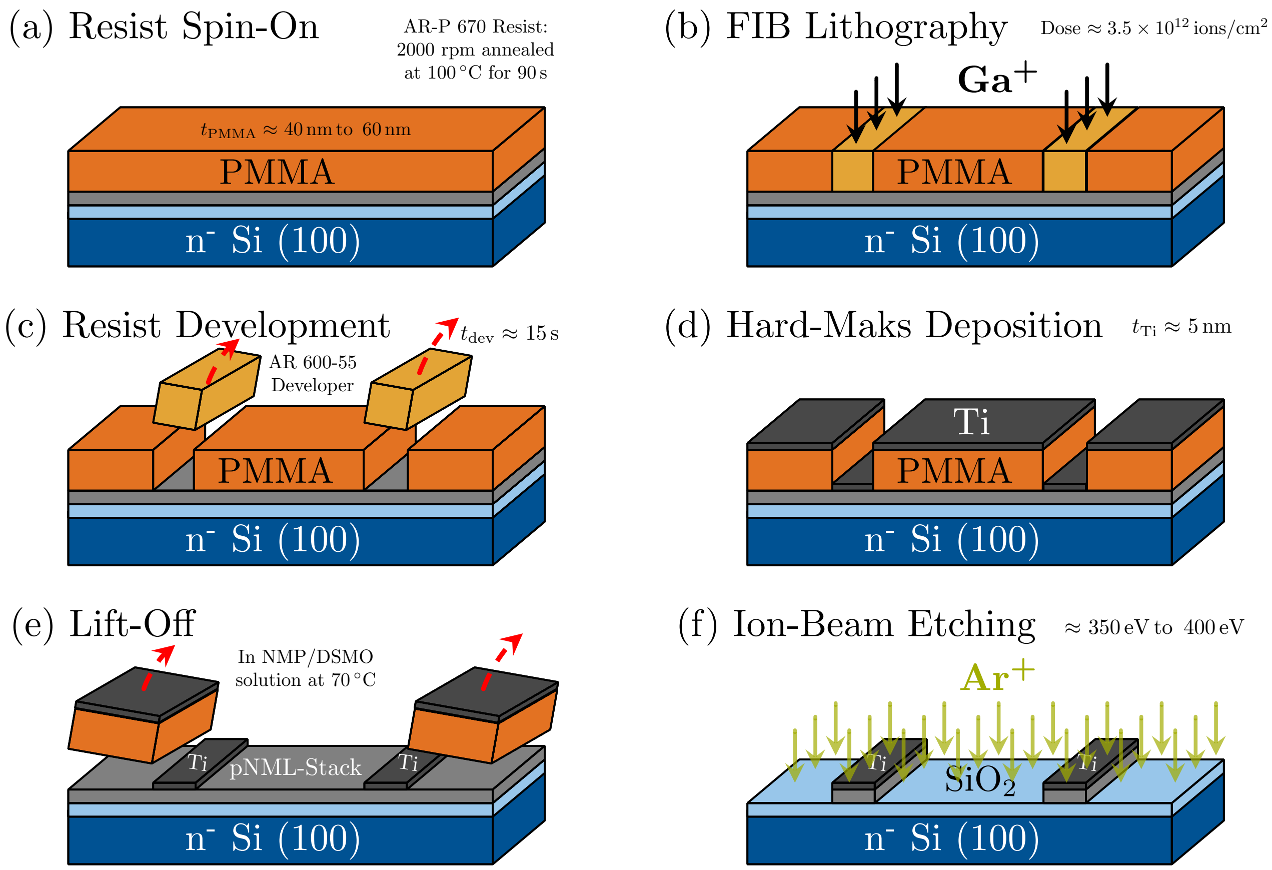

**Figure 4.4** Simplified process plan for the Ti hard-mask process, depicting the main process steps in alphabetical order. The process is used to structure the magnetic stacks deposited onto the silicon substrate during prior fabrication steps. In (a), the PMMA layer is spin-coated onto the substrate, followed by the irradiation with focused $\mathrm{Ga}^+$ ions in (b) to print the pre-designed layouts into the resist. In (c), the irradiated parts of the positive resist are developed and removed, exposing the stack. Subsequently, a nanometer-thick Ti hard-mask is deposited onto the sample via an electron-beam PVD process. The remaining resist is then lifted off in step (e) using NMP or DSMO as a solvent, leaving only the Ti hard mask behind. In the final step (f), the uncovered areas of the magnetic stack are removed via $\mathrm{Ar}^+$ ion-beam milling.

### 4.3.2 Medusa Double-Layer Process

The *Medusa* double-layer process was developed to reduce the process complexity by introducing a direct-write negative lithography process, thus removing the need for a Ti hard mask and the accompanied error-prone lift-off process. Additionally, the process aimed to provide a robust process platform for the realization of future three-dimensional structures. *Medusa* is the commercial name of a modified hydrogen silsesquioxane (HSQ) resist with increased shelf-life and stability, developed by the *Allresist GmbH*. The resist with the chemical formula $[\mathrm{HSiO}_{3/2}]_n$ is a negative e-beam resist which can be cross-linked by electron, extended UV or ion-irradiation, turning the HSQ into a stable $\mathrm{SiO}_x$ compound. During process development, both $\mathrm{Ga}^+$ and $\mathrm{He}^+$ ions were evaluated. The non-irradiated parts of the resists are susceptible to widely used tetramethylammonium hydroxide (TMAH) based developers. On the other hand, the cross-linked parts cannot be easily removed after structuring and either need to be etched (suitable plasma process or chemically via HF/NaOH) or lifted of via a solvable bottom resist. Since the selective etching of $\mathrm{SiO}_x$ against metals is complicated, the latter option was pursued for this process. In doing so, different bottom resists were evaluated before finally settling for a 50 nm thick PMMA layer, prepared identically to the one used in the PMMA hard-mask process. The entire process is again displayed schematically in Figure 4.6. After the spin-on of the PMMA and subsequent annealing, the samples were coated with an $\approx 45\,\mathrm{nm}$ thick

*Medusa* (*SX AR-N 8200*) layer, followed by a second post-exposure bake at 150 °C for 5 min. The FIB lithography was carried out identically compared to the PMMA process with a slightly increased dose of $\approx 5.5 \times 10^{12}$ ions/cm$^2$ (Figure 4.6 (b)). The Ga$^+$ ions, thereby, transfer the bulk of their energy to the *Medusa* layer and are subsequently stopped in the underlying PMMA layer (see Appendix D1 for respective SRIM simulations)). The potential for stack damage is thus further reduced. A special feature of the *Medusa* resist is the option to increase the resits sensitivity by post-exposure annealing for 10 min at 170 °C (Figure 4.6 (c)). Figure 4.5 displays the corresponding Ga$^+$ and He$^+$ dose-dependent normalized resits thicknesses after development, with and without post-exposure annealing. The sensitivity of the resist increases five-fold for the Ga$^+$ ions and roughly, by one order of magnitude in case of the 30 keV He$^+$ ions. This post-exposure anneal was essential to achieve feature sizes similar to those of the PMMA process, as the widening of the lithographic features strongly correlates with the ion dose. For the experiments with He$^+$ ions, a *Zeiss* helium ion microscope (ORION NanoFab) was used. However, due to inferior software capabilities, software bugs, and sub-optimal results, the experiments with He$^+$ ions were stopped after the initial dose and resolution studies. Following the lithography and post-expose bake, the resist was developed in a TMAH based developer (*AR 300-44*) for 90 s to 120 s (Figure 4.6 (d)). At this point, it is critical that the bottom resit is completely inert against the TMAH developer. To limit charging effects caused by the insulating PMMA, during the Ar$^+$ ion beam milling, in-situ oxygen ion-beam etching ($E_{\text{kin}} \approx 350\,\text{eV}$) is used beforehand, to remove the 50 nm thick PMMA layer (Figure 4.6 (e)). Subsequently, the magnetic stack is structured via Ar$^+$ ion beam milling ($E_{\text{Ar}} \approx 350\,\text{eV}$) using the two resists as etch mask (Figure 4.6 (f)). For details regarding the plasma etch process, it is referred to section 4.4. In the final process step, the remaining resist is removed using a chemical remover (*AR 300-76*) at 70 °C in an ultrasonic cleaner or via an oxygen plasma to ash the hydrocarbons of the remaining PMMA layer.

While the process easily fulfills the requirements regarding feature size, a distinct disadvantage compared to the Ti hard-mask is the relatively high etch-rate of the *Medusa* resist during the Ar$^+$ ion beam milling ($\approx 5\,\text{nm}\,\text{min}^{-1}$) which limits the maximum thickness of the magnetic stack. This is especially critical when using tantalum as seed or capping layer with an etch rate of only $\approx 0.3\,\text{nm}\,\text{min}^{-1}$. However, a future switch to electron beam lithography allowing for thicker resits would alleviate this constriction.

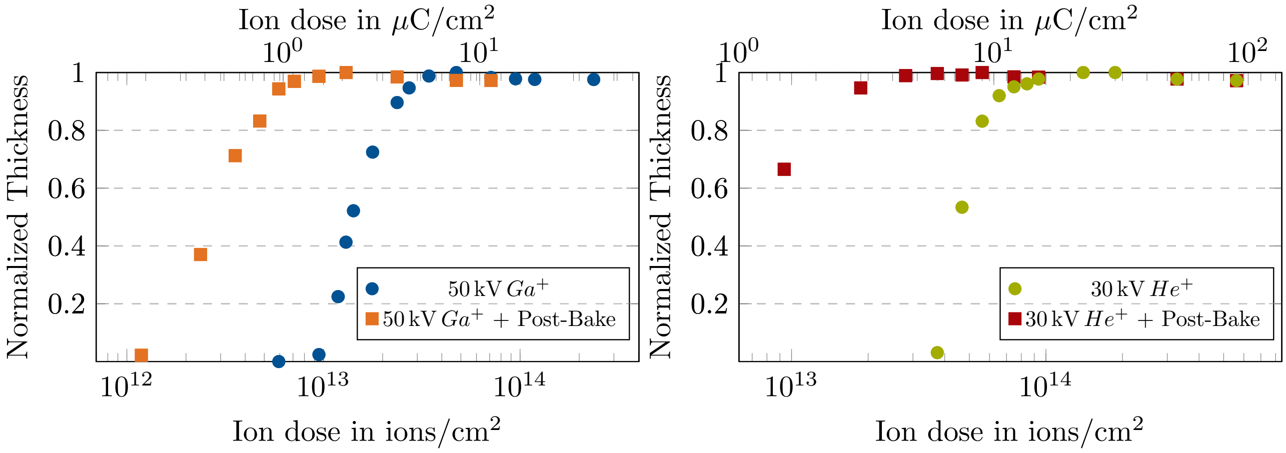

**Figure 4.5** Two plots of the ion dose dependent normalized resist thickness after development, measured via atomic-force microscopy. In plot (a) the sensitivity for Ga$^+$ ions is depicted. The process without is thereby compared to a process with post-expose bake. The same is shown in (b), however not for 50 keV Ga$^+$ ions, but for 30 keV He$^+$ ions

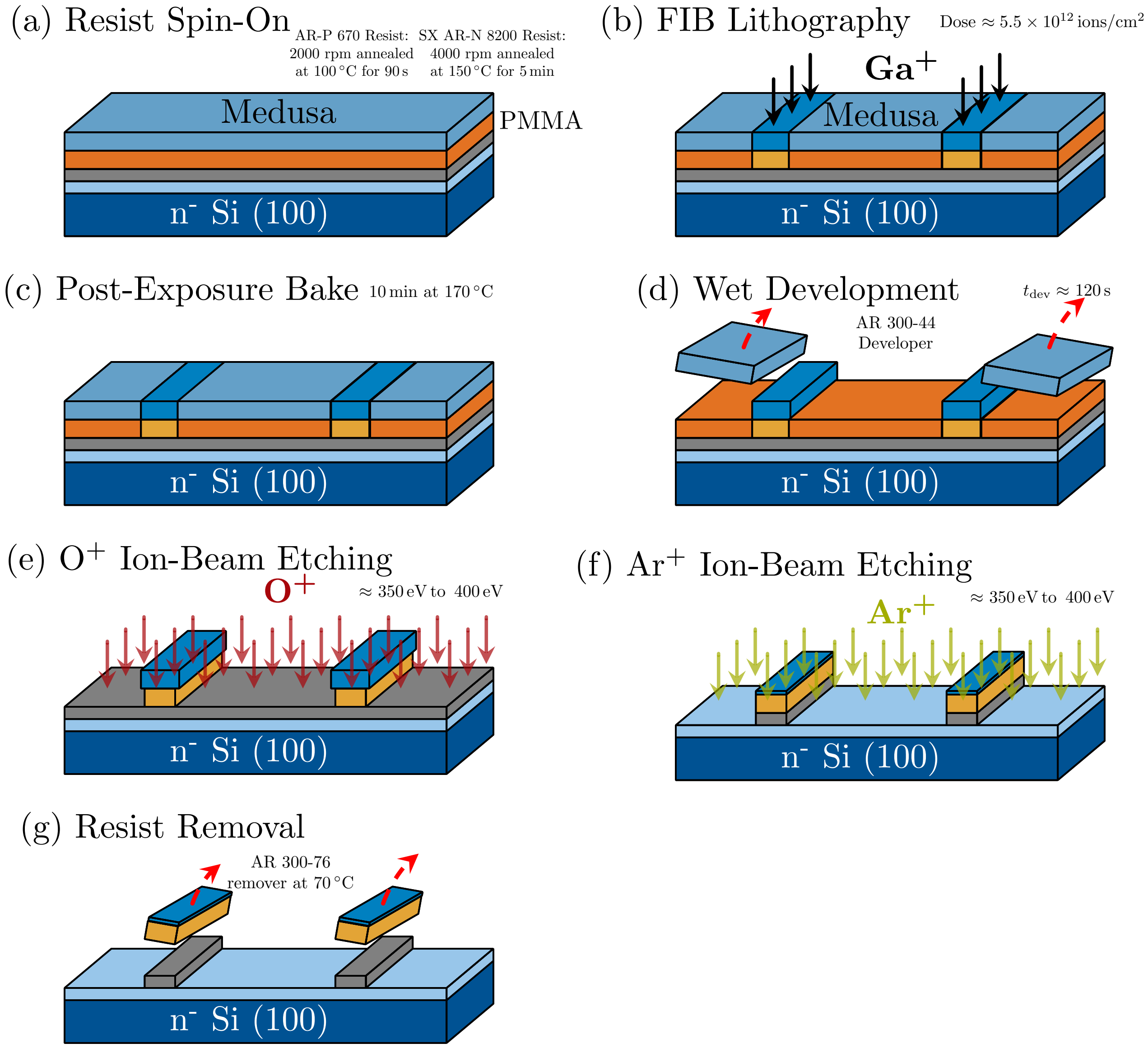

**Figure 4.6** Simplified overview of the *Medusa* double-layer process, depicting the main process steps in alphabetical order. The process is used to structure the magnetic stacks, which were deposited onto the silicon substrate during prior process steps. In (a), both resits are spin-coated onto the substrate, followed by the FIB lithography with Ga$^+$ ions in (b) to transfer the structure layouts. In (c), a post-exposure bake is performed to increase the sensitivity of the resits and improve the achievable feature size. In (d), the non-irradiated parts are developed. The developer is thereby selective and stops on the PMMA bottom resits. In (e), directed oxygen ion-beam etching is used to selectively ash the PMMA layer before the working gas is changed to Ar (f) to remove the uncovered areas via Ar$^+$ ion beam milling. In the final step, the residual resist is stripped chemically or ashed in an oxygen plasma.

## 4.4 Ion-Beam Etching

Reactive ion-beam etching (RIBE), together with $Ar^+$ ion-beam milling (IBM), is used to etch the previously masked thin film stacks as depicted in Figure 4.4 and Figure 4.6. For that purpose, a *TEPLA R.I.B.E 250* from the late 1980s is used to provide both directed $O^+$ plasma etching as well as $Ar^+$ ion beam milling capabilities. The tool features a cyclotron plasma source together with a graphite accelerator grid which increases their kinetic energy of the ions and accelerates them towards the grounded sample plate. The whole assembly is schematically illustrated in Figure 4.7. The reactants (Ar or $O_2$) can be injected directly at the site of the cyclotron source or at the sample to also realize chemically assisted ion beam milling. Custom-made copper clamps are used to hold the sample in position and mitigate plasma charging effects to enable homogeneous etching, even on top of insulating substrates. In the case of the Ti hard-mask process, $Ar^+$ ion-beam milling at $\approx 350\,\mathrm{eV}$ and a pressure of $0.5\,\mu\mathrm{bar}$ is used to etch the earlier described magnetic thin film stacks. The required etch-times are, thereby, dominated by the cumulative thickness of the Ta layers and the accompanied very low etching rates ($\approx 0.3\,\mathrm{nm\,min^{-1}}$). The deposited Ti hard-mask ($t_{\mathrm{Ti}} \approx 5\,\mathrm{nm}$) is thick enough to allow significant over-etching, thus supporting extensive stack modifications without the necessity to adjusting the etch process. However, in the case of the *Medusa* process, this no longer holds as the $Ar^+$ etch rates of the resits are significantly higher ($\approx 5\,\mathrm{nm\,min^{-1}}$). Therefore, the PMMA bottom resist is etched in an $O^+$ plasma for 15 s (Figure 4.6 (e)), before the reactant is changed to argon for the $Ar^+$ ion-beam milling. The etching time is nevertheless limited by the *Medusa* thickness, which in turn is limited by the $Ga^+$ range in the resits ($\approx 70\,\mathrm{nm}$).

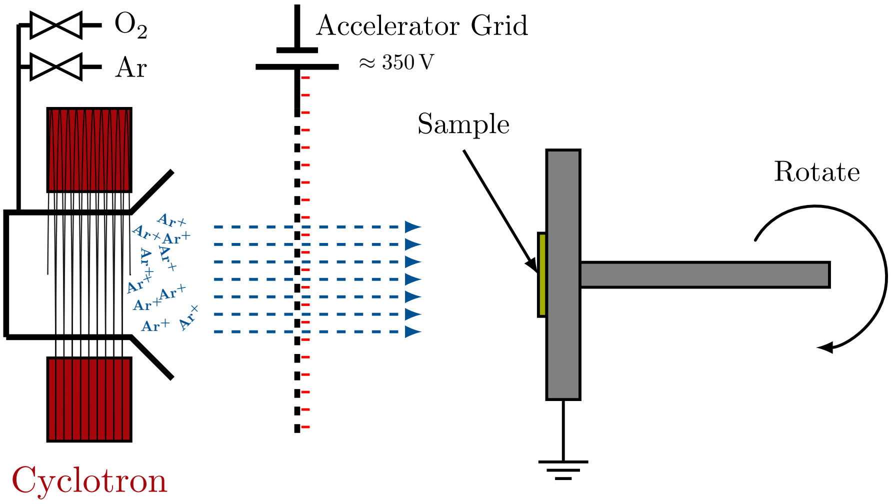

**Figure 4.7** Schematic illustration of the cyclotron plasma source, accelerator grid, and sample mount. The generated ions are being accelerated by the graphite grid and subsequently directed towards the rotating sample mount. The resulting ion energy is, thereby, set by the DC bias at the accelerator grid.

## 4.5 Metallization

After the magnetic film is structured, optical contact lithography in conjunction with a metal lift-off process is used to realize micro-meter-sized on-chip coils, and other interconnects. A sketch of the following process plan is depicted in Figure 4.8. This lift-off process for thick metal layers ($t_{\mathrm{metal}} \approx 1\,\mu\mathrm{m}$) uses a $2\,\mu\mathrm{m}$ thick negative photo-resits (maN-1420), which is exposed through a non-inverted chromium mask via a contact-aligner using an i-line ($\lambda \approx 365\,\mathrm{nm}$) UV LED. Illumination through a contact mask results in a pronounced undercut after development in a TMAH based developer (ma-D 533/S). Subsequently, the metal stack consisting of a Ti adhesion layer ($\approx 5\,\mathrm{nm}$), the main copper power metallization ($\approx 750\,\mathrm{nm}$), and a final Cr capping layer ($\approx 30\,\mathrm{nm}$), is deposited

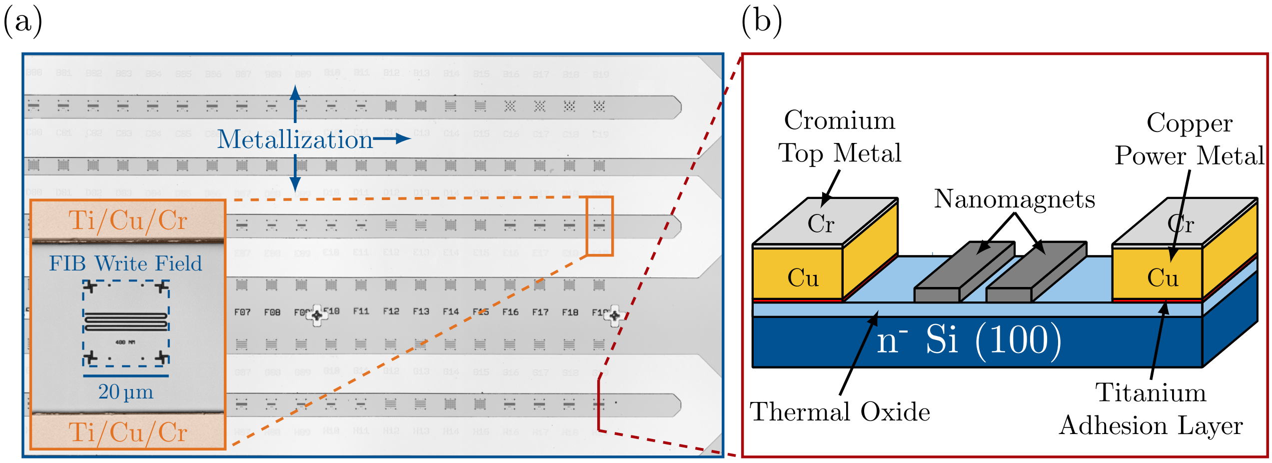

**Figure 4.8** In (a), a scanning laser microscope image of a processed sample is displayed. The image shows several lines of horizontally aligned FIB write fields spanning across 20 µm × 20 µm each, surrounded by copper metallization. In (b), a schematic cross-section of the in (a) marked area is displayed. The schematic illustrates two nanomagnets in the center on top of a thermal-oxide, flanked by the two metal lines. The metal stack consists of a titanium adhesion layer, the central copper power metal, and a top chromium layer for oxidation protection and bonding.

via electron-beam physical vapor depositions. The Cr layer is necessary to prevent the oxidation of the underlying copper and provide an adhesive surface for the subsequent wedge-bonding using aluminum bond wires. In a final step, the earlier exposed resit is lifted-off in a dimethyl sulfoxide (DSMO) or N-Methyl-2-Pyrrolidone (NMP) solution at 70 °C using an ultrasonic cleaner.

## 4.6 Localized Ion-Beam Irradiation

To enable deep sub-micron lithography and modify the energy landscape of the processed magnets with nanometer accuracy (create ANCs), the in section 4.3 introduced *Micrion 9500ex* $Ga^+$ focused ion-beam microscope is used.
The computer-controlled tool from the early 1990s uses a Gallium liquid-metal-ion-source (LMIS) and supports acceleration voltage up to 50 keV. A sketch of the the $Ga^+$ ion beam column is depicted in Figure 4.9 (a). The tool extracts a beam of $Ga^+$ ions from the LMIS by means of field evaporation from a Taylor cone that forms under the high electric fields generated by the extractor and suppressor electrodes [216]. The current of the extracted ion beam is thereby adjusted by the relative voltage difference between the extractor and suppressor. During regular operation, a $Ga^+$ current of $\approx 2\,\mu A$ is extracted, accelerated, and guided through multiple beamforming steps before being scanned across a sample. A spray aperture narrows the wide beam profile before the first electrostatic condenser lens collimates the beam in the first step. The upper octopole reduces the astigmatism of the ions before the beam hits the aperture. The variable aperture features multiple, different-sized openings to adjust the beam current across orders of magnitude. For the highest spatial resolutions, the aperture is set to reduce the beam current to $\approx 2\,pA$. Right below the aperture, a fast electrostatic blanker unit is positioned. It can divert or even cut off the beam if necessary. This blanker unit is essential to measure the beam current via a Faraday cup or to precisely control the ion dose during irradiation (cutting off the beam). The lower octopole is used to deflect and scan the beam across the sample. However, before exiting the column, the beam is focused to a spot size of $\approx 10\,nm$ by the second electrostatic lens. In order to reconstruct an image of the scanned area, a multichannel plate (MCP) is positioned next to the pole piece of the focusing lense and collects the generated secondary electrons and ions.

### Irradiation and Alignment

The effects of ion irradiation result from collisions and subsequent recoil events generated by the $Ga^+$ ions passing through the magnetic stack. The interactions with the lattice cause dislocations, vacancies, and intermixing, which in turn changes the magnetic energy landscape [63], [119], [217]. Since the ion-beam irradiation takes place after fabrication of the magnets, distinct alignment structures and procedures are necessary to achieve the necessary spatial accuracy and place the ANCs correctly (exemplary illustrated in Figure 4.9 (b)), without imaging and thus destroying the surrounding target magnets. In order to do so, a multi-step alignment process as depicted in Figure 4.9 (b) is used. After the initial rough alignment procedure, using dedicated alignment structures and large area FIB imaging (residual error $\approx$ 200 nm to 400 nm), the target area is approached.

At this position, the supposed locations of the second series of alignment structures, fabricated alongside the target magnets, are imaged with the FIB. The uncovered positions of the structures are then used to calculate precise offsets and adjust the ANC irradiation mask. Via this procedure, alignment errors in the range of a view ten nm are feasible, depending on the residual angle error and the error in estimating the final position of the alignment structures from the image. Figure 4.9 (b) illustrates this procedure graphically, showing the ANC placement for a three-input majority gate as depicted in Table. 3.1.

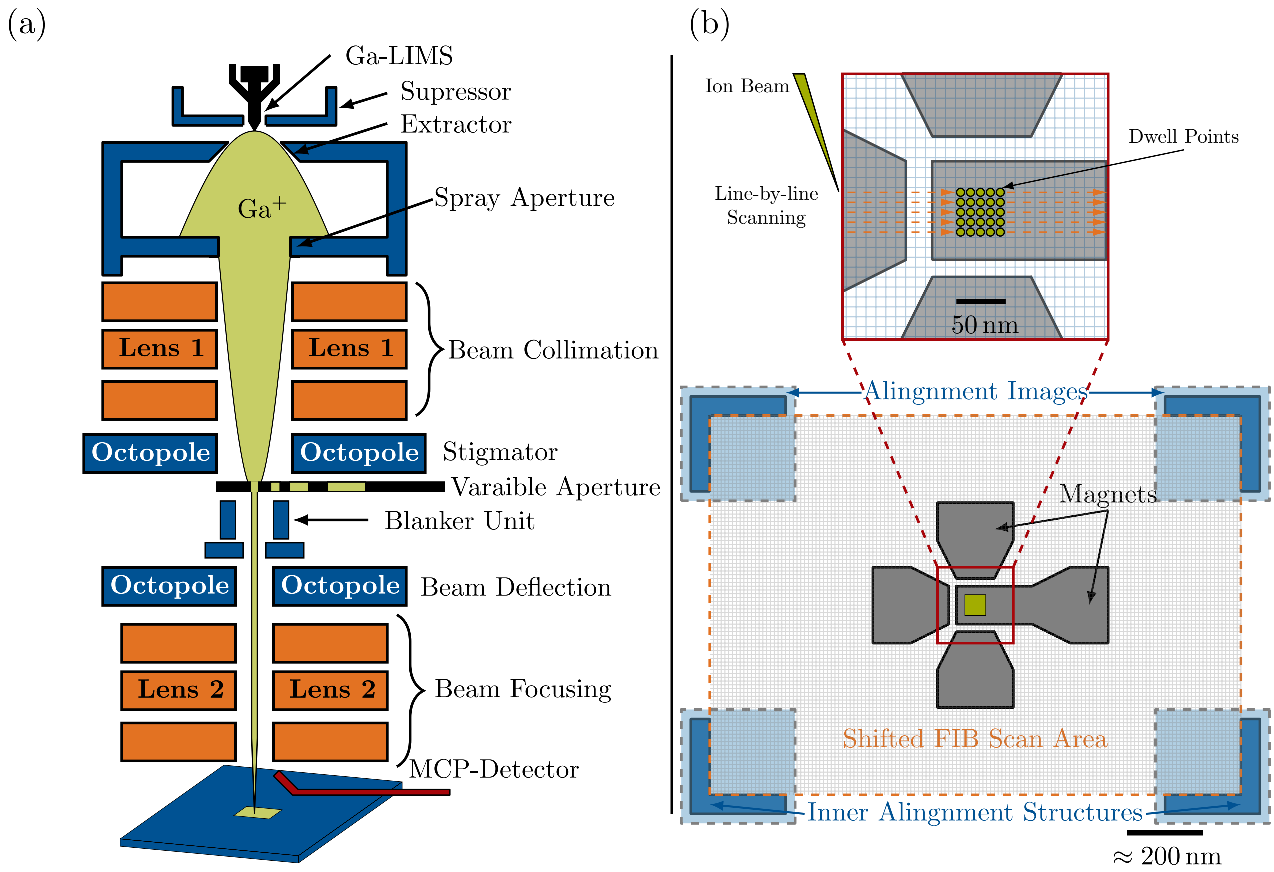

**Figure 4.9** Schematic depiction of the beam-line of a typical $Ga^+$ Focused-Ion-Beam Microscope (FIB). In (b), the alignment procedure for the ANC placements is depicted. After the target site has been approached, a picture (solely exposing the alignment structures) is taken. The target offset can now be corrected manually by adjusting the final ANC irradiation box to fit the visualized alignment structures. Image adapted from [140].

# 5 Meteorology and Methodology

This chapter provides a detailed description of the essential magnetic meteorology techniques and methods used and developed throughout this work. First, in section 5.1, the primary methods to determine intrinsic material parameters from absolute magnetometer measurements are discussed. Despite their importance, these basic methods are rarely elaborated.

The second part focuses on magneto-optical methods and tools that enable the fast and contact-less characterization of magnetic nanostructures and films. For that purpose, the magneto-optical Kerr-effect is first introduced in section 5.2, before the individual setups and techniques are discussed in detail (section 5.3). Throughout the course of this work, significant time resources were invested in the extension and optimization of the available magneto-optical setups to allow for diffraction-limited optical resolution, the parallel characterization of numerous magnets, and a semi-automatic operation of the setups. In addition, to the test setups, the concepts of the developed tests and data analyses tools are also discussed in detail.

The third part in section 5.4 introduces the used and developed magneto transport methods, building on the anomalous Hall effect (AHE) present in media with out-of-plane magnetization. These methods allow the electric characterization of thin films and electrically contacted nanostructures to measure the magnetic hysteresis or determine the magnetic anisotropy. To better understand the introduced methods, respective measurements examples are presented when necessary to complement and improve upon the provided descriptions.

## 5.1 Absolute Magnetometer

Absolute magnetometers are essential tools to measure the magnetic dipole moment of magnets and the respective field, angle, and temperature dependencies. There is a wide range of different magnetometer designs with varying degrees of complexity and sensitivity. However, the working principle of most magnetometer designs is elementary. The DUT is moved repeatedly through or along several circular pick-up coils while varying external magnetic fields or temperatures are applied. Thus, the dipole fields of the moving magnetic moments induce a current in the adjacent coils, which is proportional to the strength of the dipole field and thus the total magnetic moment of the DUT. Performing these measurements at rising or falling external magnetic fields allows measuring the absolute magnetic hysteresis of a given material. Figure 5.1 (a) displays the measured hysteresis curves of Pt/Co/W films with increasing cobalt thicknesses and an external field applied parallel to the film normal (along the magnetic easy axis). The saturated magnetic moment at high fields can then be used to calculate the (volume) saturation magnetization via

$$M_\mathrm{s} = \frac{M_\mathrm{sat}}{V_\mathrm{magnet}}\,, \tag{5.1}$$

with $V_\mathrm{magnet}$ as the volume of the magnetic layer and $M_\mathrm{sat}$ as the saturated magnetic moment. Precise knowledge of $M_\mathrm{s}$ is essential for the detection of magnetic dead layers as well as the calibration of micro-magnetic simulations. Aside from the saturation magnetization, it is also possible to extract a reasonable estimate of magnetic anisotropy energy from magnetometer measurements via the so-called "area-method" [90], [218]. Two hysteresis measurements are required for that purpose, one with the external field applied along the easy axis and one with the field along the hard axis. The area between both hysteresis curves gives the magnetic anisotropy energy of the sample. However,

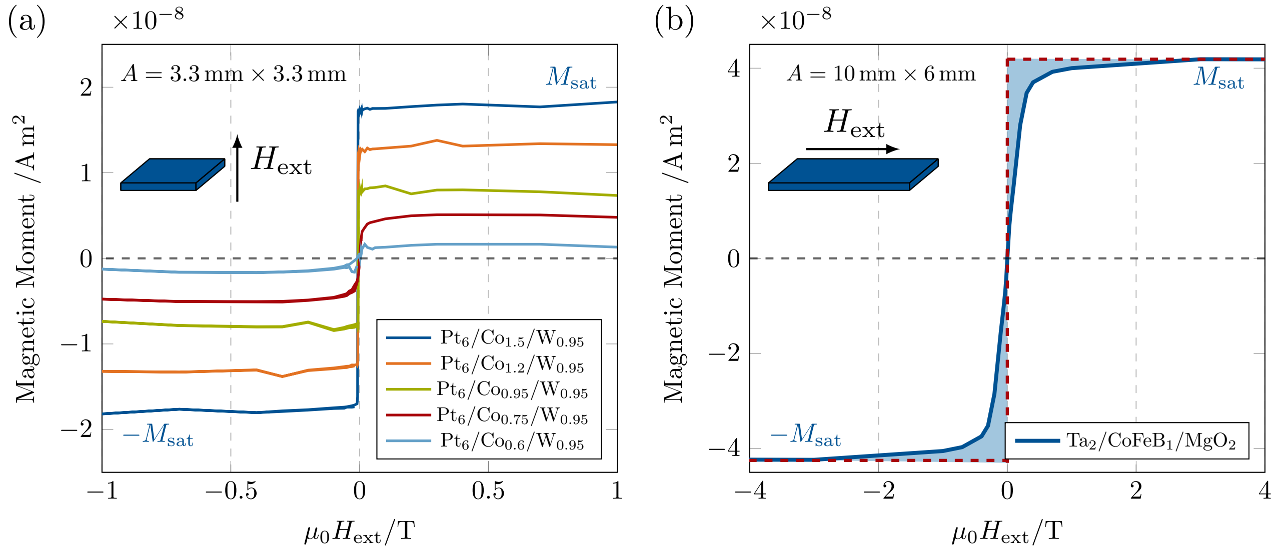

**Figure 5.1** In (a), easy-axis SQUID magnetometer loops of $Pt_6/Co_x/W_{0.95}$ films with decreasing cobalt thickness are displayed. The respective volume saturation magnetizations ($M_s$) can be calculated from the cobalt layer volume and $M_{\mathrm{sat}}$. The plot in (b) depicts a hard axis (in-plane) hysteresis loop of a $Ta_2/CoFeB_1/MgO_2$ thin film. The measurement along the hard axis allows determining the magnetic anisotropy energy via the area method [90].

in systems with pronounced PMA, the saturation field along the easy axis is $\approx 0\,\mathrm{mT}$, which allows estimating the anisotropy solely via hard-axis loops according to

$$K_{\mathrm{eff}} \approx \frac{1}{\frac{1}{2}\mu_0 M_s^2 V_{\mathrm{magnet}}} \int_{M=0}^{\pm M_{\mathrm{sat}}} H_{\mathrm{ext}}(m)\,\mathrm{d}\,m, \tag{5.2}$$

where $M_s$ is again the volume saturation magnetization (also measurable via hard axis loops) and $m$ is the measured magnetic moment as displayed in Figure 5.1 (b). For the displayed hard axis loop of a Ta/CoFeB/MgO film, $M_s$ is calculated to be $\approx 8 \times 10^5\,\mathrm{A\,m^{-1}}$ and $K_{\mathrm{eff}}$ is estimated as $\approx 1.33 \times 10^5\,\mathrm{J\,m^{-3}}$. Throughout this work, the majority of measurements were conducted using a superconducting quantum interference device (SQUID) magnetometer at the *Walther Meißner* institute in Garching, Germany. Additional measurements were performed using a vibrating sample magnetometer (VSM) at the University of Notre Dame, Indiana.

## 5.2 Magneto-Optical Characterization

Magneto-optical techniques utilize the interactions between light and the magnetization or magnetic field of a sample to probe magneto-dynamic as well magneto-static effects. They enable fast and direct characterization of magnetic structures with high spatial resolutions (only diffraction-limited) and do not require elaborate electrical connections. Magneto-optical techniques have thus become dominant tools for the characterization of magnetic micro and nano-structures in research. There are two distinct magneto-optical effects, namely the magneto-optical *Kerr*-effect (MOKE), affecting light reflected from magnetic surfaces and the *Faraday*-effect, which describes light passing through a magnetic field or material. For the characterization of non-transparent metallic structures, it was thus mainly relied on the magneto-optical *Kerr*-effect.

### 5.2.1 Magneto-optical Kerr-effect (MOKE)

The Magneto-optical Kerr-effect (MOKE) describes a polarization change when light is being reflected from a magnetic surface. It was first observed by *J. Kerr* in 1877 when he noticed a polarization change in the light, reflected from the pole of a magnet [219]. Today there are different explanation attempts for this effect, which is ultimately rooted in the spin-orbit interactions of the magnetic materials. We will attempt a vivid and macroscopic description utilizing Maxwell's equations based on a variety of sources [220]–[222]. First, we consider the polarization of an electromagnetic wave in a simplified manner, just considering the electric field. The plane wave for the electric field can be described as

$$\boldsymbol{E}(\boldsymbol{r}, t) = \boldsymbol{E}_0 \exp[\mathrm{i}(\boldsymbol{k} \cdot \boldsymbol{r} - \omega t + \varphi)] \,, \tag{5.3}$$

where $\boldsymbol{E_0}$ is the complex amplitude vector, $\boldsymbol{k}$ is the wave vector, and $\omega$, as well as $\varphi$, is the angular frequency and phase-shift, respectively. In this picture, the propagation vector $\boldsymbol{k}$ is perpendicular to the electric field $\boldsymbol{E}(\boldsymbol{r}, t)$. The polarization of the wave is determined by $\boldsymbol{E}(\boldsymbol{r}, t)$ and its oscillations on the XY-polarization plane (indicated in Figure 5.2). The polarization is often categorized into three sub-types, linear, circular, and elliptic polarization. Although, it has to be stressed that the first two are strictly speaking only special cases of elliptic polarization. In the following, we will discuss the three types in more detail, considering two plane waves in superposition, with identical frequencies and propagation vectors ($\boldsymbol{k}$).

#### Linear Polarization

Linear polarization is described as the superposition of two perpendicularly polarized waves, $\boldsymbol{E}_\mathrm{x} = \boldsymbol{E}_1 \exp[\mathrm{i}(\boldsymbol{k} \cdot \boldsymbol{r} - \omega t + \varphi_\mathrm{x})]$, and $\boldsymbol{E}_\mathrm{y} = \boldsymbol{E}_2 \exp[\mathrm{i}(\boldsymbol{k} \cdot \boldsymbol{r} - \omega t + \varphi_\mathrm{y})]$ with identical phases ($\varphi_\mathrm{x} = \varphi_\mathrm{y}$) but different amplitudes ($\boldsymbol{E}_\mathrm{x}$). In the XY-plane, this will lead to oscillations along a tilted straight line. The tilt or rotation angle $\Phi$ is, thereby, defined by the amplitudes of $\boldsymbol{E}_\mathrm{x}$ and $\boldsymbol{E}_\mathrm{y}$ according to $\tan\Phi = \frac{E_1}{E_2}$. A graphical illustration of a linear polarized wave and its oscillations in the XY-plane is depicted in Figure 5.2 (a).

#### Circular Polarization

To describe circular polarization we again consider the superposition of two perpendicularly polarized waves. However, in this case with unequal phases ($\varphi_\mathrm{x} \neq \varphi_\mathrm{y}$) but identical amplitudes ($\boldsymbol{E}_1 = \boldsymbol{E}_2$). To be more precise, the phase-shift between both waves must be equal to $\Delta\varphi = \pm\frac{\pi}{2}$ or ±90°. If these conditions are met, the electric field vector will oscillate around the propagation vector $\boldsymbol{k}$ (z-axis) like a screw thread. The sign of the phase shift, furthermore, determines the direction of this rotation, clock-wise (CW) or right handed in case of $\Delta\varphi = \frac{\pi}{2}$ and counter clock-wise (CCW) or left handed if $\Delta\varphi = -\frac{\pi}{2}$). An illustration of a circular polarized wave is depicted in Figure 5.2 (b).

#### Elliptic Polarization

Elliptic polarization describes the general case, in which neither the phases nor the amplitudes are equal ($\varphi_\mathrm{x} \neq \varphi_\mathrm{y}$, $\boldsymbol{E}_1 \neq \boldsymbol{E}_2$). Here we observe a CW or CCW rotation of the electric field vector tracing a tilted ellipse on the XY-plane as depcited in Figure 5.2 (c). The tilt or rotation angle is then determined by

$$\tan 2\Phi = \frac{2E_1E_2\cos\Delta\varphi}{E_1^2 - E_2^2} \,, \tag{5.4}$$

with $E_1$ and $E_2$ as the amplitudes of the respective perpendicularly polarized waves as well as $\Delta\varphi$ as the phase shift.

Furthermore, we can attribute a measure of the ellipticity to the polarization, thus describing the ratio between the dominant and the minor axis of the ellipse. This normalized measure, ranges

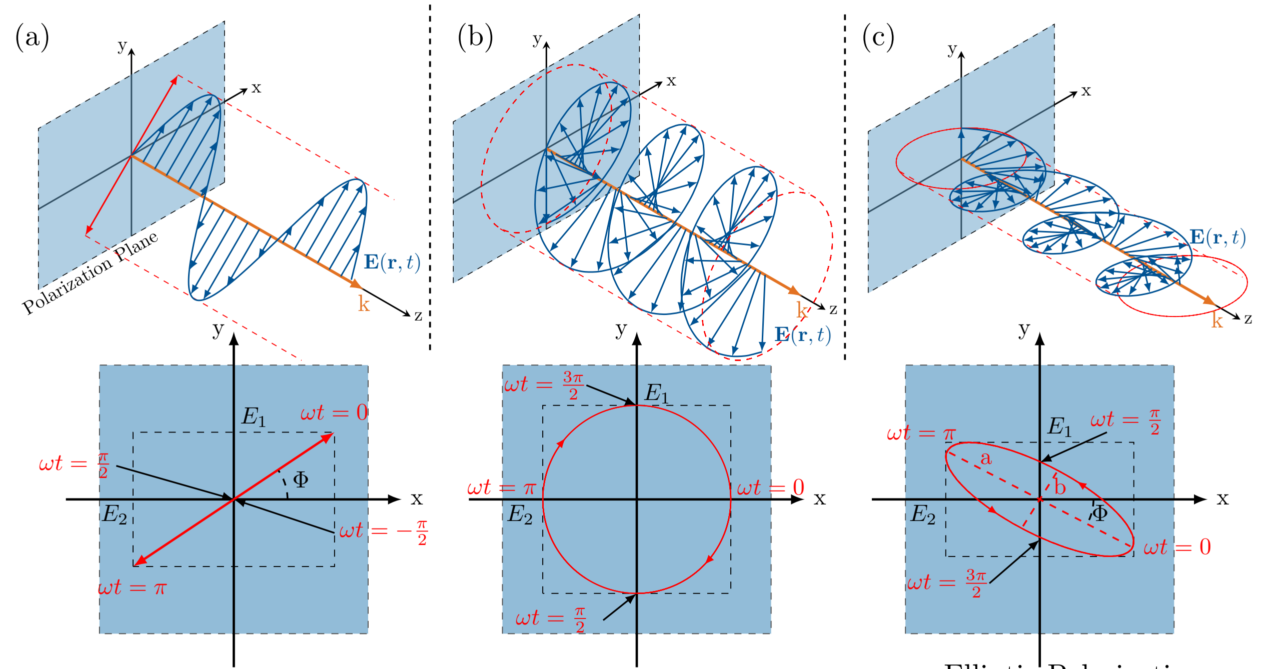

Linear Polarization

Circular Polarization

Elliptic Polarization

**Figure 5.2** Sketch of the three types of light polarization, using the electric field $\boldsymbol{E}(\boldsymbol{r},t)$ as example. In (a) linear polarization as the simplest and commonly imagined form of polarization is depicted. In (b) circular polarization with a phase shift of $\Delta\varphi = \pm\frac{\pi}{2}$ or ±90° is shown. The image in (c) displays the elliptic polarization, linear and circular polarization are only special cases of elliptic polarization.

between 0 and 1, while 0 describes circular polarized waves and 1 describes linear polarization. The ellipticity calculates as $\epsilon_{\mathrm{ell}} = \frac{a}{b}$ with $a$ and $b$ as the amplitudes of the dominant and minor axis. The graphical illustration of elliptic polarization and the respective oscillations in the xy-plane are depicted in Figure 5.2 (c).

### Interaction with magnetic surfaces

To describe the Magneto-optical Kerr-effect, we consider a linearly polarized wave as the superposition of a CW and a CCW circular polarized wave, with identical amplitudes and absolute phase shift. When interacting with a magnetic surface, the CW and CCW waves exhibit different complex reflection coefficients (affecting both amplitude and phase), depending on the magnetization direction of the magnetic surface, or better, the volume of the wave's penetration depth. This discrepancy gives rise to the so-called *Kerr*-rotation of the reflected waves if the magnetization axis is parallel to the plane of incidence [221]. Figure 5.3 (a) illustrates the *Kerr*-rotation and the transformation into an elliptically polarized wave schematically. The discrepancy of the reflection coefficients is routed in the magnetic quantum number $m$ and the magnetization-dependent occupancy of the 3d-shells. Thus, vividly speaking, CW waves can be more likely to excite electrons than CCW waves since the $+m$ states are, depending on the magnetization, more likely to be unoccupied compared to $-m$ states. This is, of course, a crudely simplified description. For a detailed explanation, it is referred to [221], [222]. Since the highest *Kerr*-rotations are obtained only when the incident light is in parallel with the magnetization axis, different measurement geometries are needed to address different magnetization vectors. The most simple and widely used configuration is the polar geometry, where the incidence angle of the light matches the surface normal (illustrated in Figure 5.3 (b)). In this configuration, however, only the out-of-plane component of the magnetization can be probed. For in-plane magnetizations, alignment is best achieved with a very shallow angle in a longitudinal

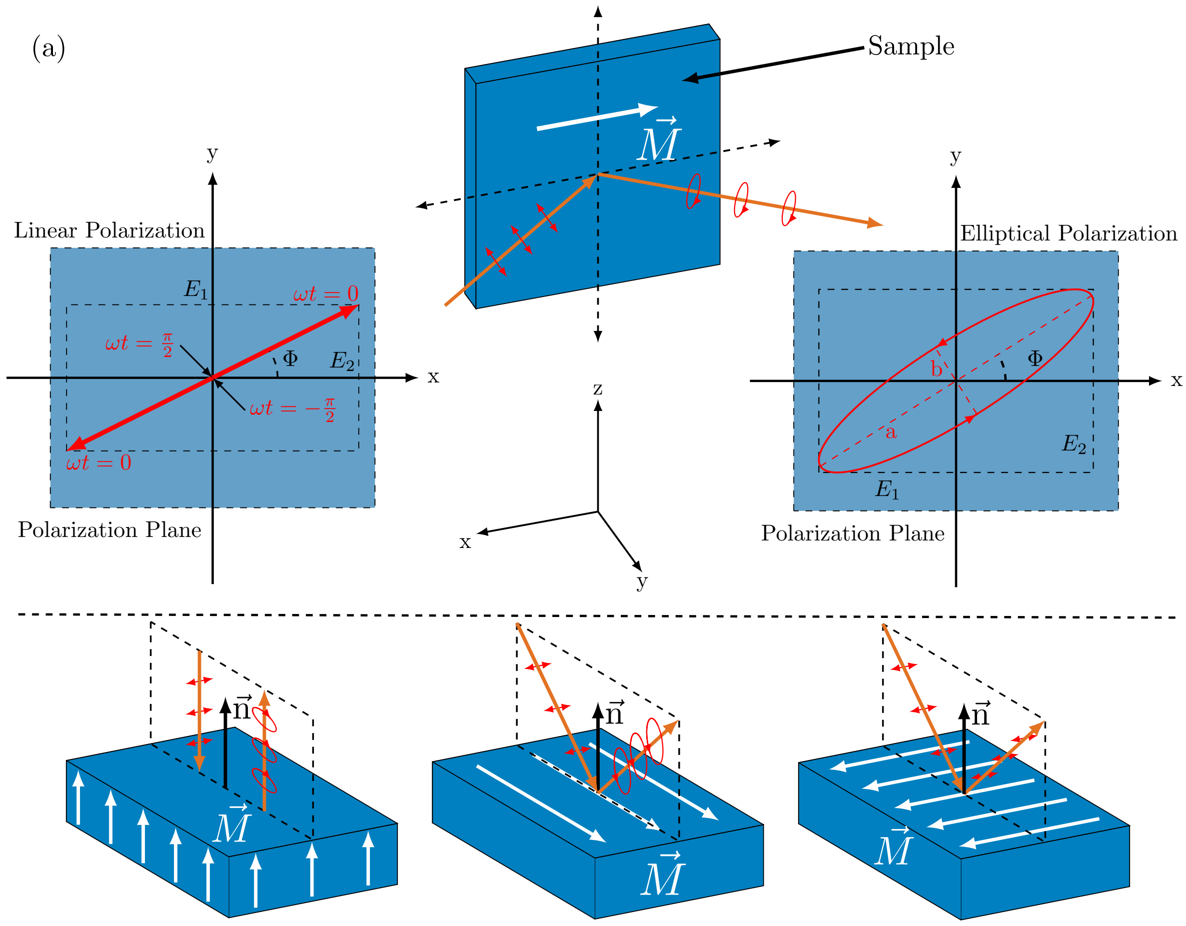

(b) Polar MOKE (c) Logitudinal MOKE (d) Transverse MOKE

**Figure 5.3** Schematic illustration of the Kerr-Effect induced transition from linear to elliptical polarization (a). Polar MOKE in (b)

configuration (Figure 5.3 (c)). In case the incident light is perpendicular to the magnetization, no *Kerr*-rotation can be observed. In this transversal geometry (Figure 5.3 (d)), however, magnetization dependent intensity changes can still be observed using perpendicularly polarized light [223], [224]. As this work focuses on out-of-plane magnetized magnets, all measurements using the magneto-optical *Kerr*-effect are done in a polar geometry.

## 5.3 Wide-Field Magneto-Optical Kerr-Effect Microscopy

As suggested by the term, wide-field magneto-optical Kerr microscopy (WMOKE) uses wide-field optical imaging of films or nanostructures to extract static information of the magnetization. For this technique, the *Köhler* illumination of a direct light microscope has to be combined with optical components necessary for polarized light microscopy (polarizer, analyzer, polarization preserving lenses, and objectives). For the in-house developed setup, a Zeiss Axio Imager 2 serves as the microscope platform. A sketch of the setup with labeled components and beam paths is displayed in Figure 5.4. The microscope uses a collimated 460 mW LED ($\lambda_{\text{peak}} = 470\,\text{nm}$) as an incoherent light source. This leads to a maximum attainable resolution of $\approx \frac{\lambda}{2} \approx 250\,\text{nm}$. For a homogeneous illumination of the sample (*Köhler* illumination), the light is first passed through a diffusor and focused onto an aperture with variable diameter. A Glan-Thompson polarizer with a high extinction ratio is used to polarize the incoming light before it is being reflected by a semi-transparent reflector towards the objective lenses. The objective focuses the light onto the sample and collects the reflected light

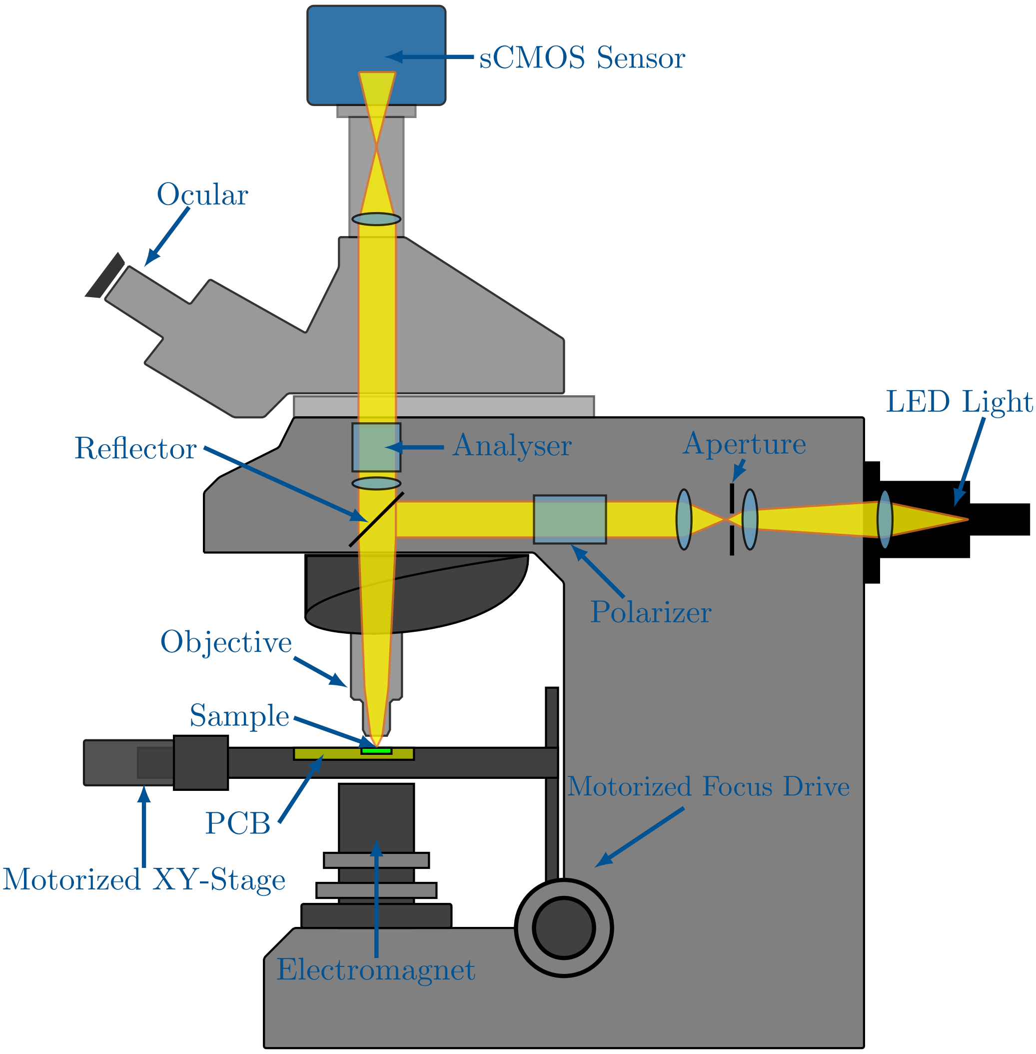

**Figure 5.4** Sketch of the wide-field magneto-optical Kerr microscopy setup, based on a *Zeiss Axio Imager 2*. The relevant setup are labeled, as are the optical components relevant for illumination and polarization contrast. The optical axis of the microscope is aligned with the center of the bottom mounted electromagnet.

with its polarization rotated either CW or CCW, depending on the magnetization direction. The reflected light is collected by the objective and passed through the semi-transparent reflector and the analyzer. The analyzer, a second Glan-Thompson polarizer, is rotated by $90° - \Phi_{Kerr}$ with respect to the initial polarizer. The effective extinction ratio of the analyzer is thus, highest for one magnetization direction and lowest for the other. The passing light is finally focused onto the active area of a cooled back-illuminated sCMOS imager (16-Bit monochrome) with a pixel size of $6.5\,\mu\text{m}^2 \times 6.5\,\mu\text{m}^2$ (pco.edge 4.2 bi). An electromagnet with a maximum OOP field of $\approx 150\,\text{mT}$ is mounted below the sample and used to change the magnetization direction of the DUT. A motorized XY-stage with sub-micron resolution, together with a focus-motor, allows for the remote and automated operation of the setup. This automation greatly reduces the mechanical noise introduced by human interaction. Therefore, all setup components (camera, focus, stage, electromagnet) and measurement routines are controlled by a central control program implemented in LabView. With this setup, magnetic thin films and nanostructures with OOP magnetization can be characterized for their quasi-static and dynamic properties.

### 5.3.1 Domain Imaging

One of the essential use cases of a WMOKE is recording domain patterns and observing domain wall movements under the influence of magnetic fields or currents. Since the optical contrast originating from the Kerr effect is usually very small compared to other optical components, direct imaging, although possible in principle, is usually disregarded in favor of more complex differential imaging techniques. For that purpose, the film is first saturated in one direction before a reference image is taken. Subsequently, DWs are nucleated and propagated before a second image is taken. The differential image is then created via simple subtraction. A series of domain patterns recorded with the WMOKE is displayed in Figure 2.12. Aside from static domain patterns, it is also possible to observe and resolve DW movements in the creep regime. Observing these movements at different external fields allows determining the intrinsic depinning fields. In the case of marginal depinning fields ($< 1\,\mathrm{mT}$) , there are even techniques to estimate the local saturation magnetization of films by measuring the domain wall compressibility [225].

### 5.3.2 Quasi-Static Measurements of Nanostructures

A single WMOKE image contains the magnetic information of every object in the image frame. This allows not only to characterize films but also large numbers of magnets simultaneously to gather statistical information effectively. In order to determine the coercivity of the observed magnets at quasi-static fields, a stair-case field ramp is applied via the electromagnet, as depicted in Figure 5.5. The DUTs are saturated in the opposite direction beforehand via a strong initial magnetic field pulse. After saturation and every subsequent field step, a new image is taken and saved for later processing. The coercive field is now determined for every DUT in the image frame from the final image series by tracking its mean pixel brightness through the field ramp.

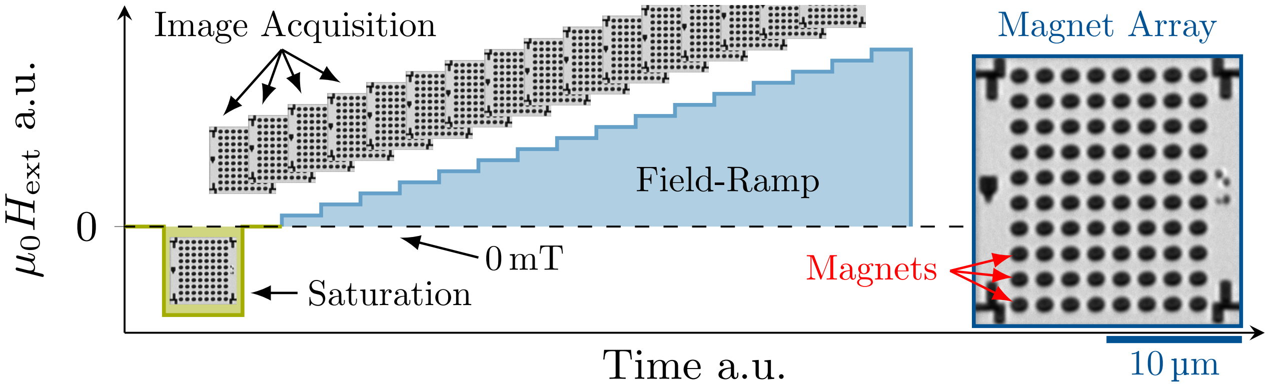

**Figure 5.5** Schematic illustration of the measurement procedure to determine the coercivity of multiple nanomagnets. The exemplary image frame in the right contains 80 magnets ($d = 1\,\mathrm{\mu m}$). The magnets are first saturated with a strong magnetic field pulse, before a stair-case field ramp in the opposing field direction is applied. Images are taken after every field-step to record changes in the magnetization of the individual magnets.

#### Data Analysis via Image Recognition and Pattern Matching

To efficiently characterize large numbers of magnets, the image and data analysis must be implemented with a high degree of automation. Therefore, the developed analysis tools make extensive use of the *National Instruments - Vision Development Module*, which provides optimized functions for image processing and pattern recognition. For the analysis, the initial image, taken after saturation, serves as a reference. In the first step, image recognition is used to find the positions of the individual magnets, record their location and label them. The result, displaying an array of labeled nanomagnets, is depicted in Figure 5.6. Subsequently, the mean pixel brightness is calculated for every magnet

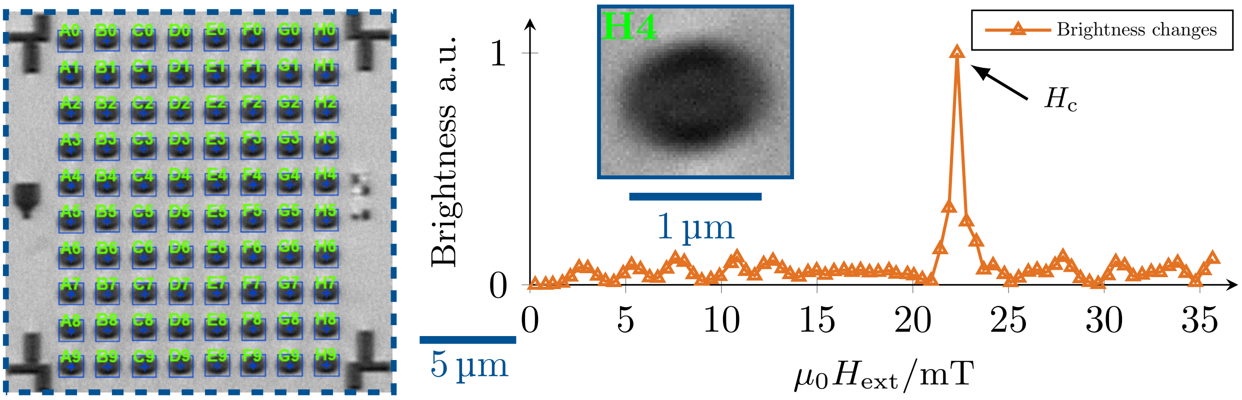

**Figure 5.6** WMOKE image of an array of Co/Ni nanomagnets on the left. For data analysis, the 80 magnets are automatically identified and labeled. In the plot on the right the normalized brightness changes of magnet H4 are plotted against the externally applied field. The peak at ≈ 22.3 mT indicates the coercive field of the magnet.

area and image. The brightness changes between the individual images are then used to determine the respective switching fields. The plot in Figure 5.6 depicts the normalized brightness changes of a single magnet (H4), selected from the array of Co/Ni nanomagnets ($\mathrm{Ta_2/Pt_{1.5}[Co_{0.2}/Ni_{0.4}]_{x8}}$) displayed on the left. The position of the brightness peak determines the respective coercive field of the magnet. It was determined that the brightness change between steps is a more robust coercivity indicator compared to the absolute brightness as the derivative is less affected by superimposed drift components. Brightness drift is, for example, caused by the external magnetic field acting on the high magnification objective (100×, NA = 0.9), resulting in a small but accumulative focus shift. An additional moving-window average filter with a window size of 2 to 4 points is applied to suppress the impact of higher (compared to the focus drift) frequency noise sources.

### 5.3.3 Time-Domain Measurements

For WMOKE imaging, the required integration times of sCMOS sensors are usually in the order of tens to hundreds of ms to obtain an adequate signal to noise ratio. These timescales effectively limit the time resolution of the technique to quasi-static imaging. However, time-domain measurements are essential to characterize domain wall nucleation and DW propagation processes at the timescales or frequencies the magnets are aimed to operate. Therefore, a differential imaging technique was implemented that probes the local magnetization before and after a magnetic-field pulse is applied, thus reviling field-induced changes in the local magnetization. However, the technique works under the assumption that the magnetization stays constant without a magnetic field, an assumption that needs to be verified carefully for any given material. The time resolution is then only limited by the length of the magnetic field pulse. After an initial saturation of the magnets with a quasi-static field pulse, the reference image is taken. Subsequently, a high amplitude µs to ns on-chip magnetic field pulse is triggered to either nucleate or depin a DW. A second (optional) propagation pulse with low amplitude (≈ 3 mT) can furthermore be generated after that via the electromagnet to ensure the complete magnetization reversal (and thus optical detection) upon a nucleation or depinning event. The second image, taken after the pulses, enables differential imaging in a later data-processing step. The procedure for a single measurement is schematically illustrated in Figure 5.7. This measurement is repeated multiple times (10 – 20×) with identical pulse parameters to assess the event (nucleation or depinning) probability at the selected field amplitude and pulse widths. This is necessary as the magnetization reversal process becomes increasingly probabilistic at short time scales. The lead use-case of this technique is the determination of the field and time-dependent nucleation probabilities of

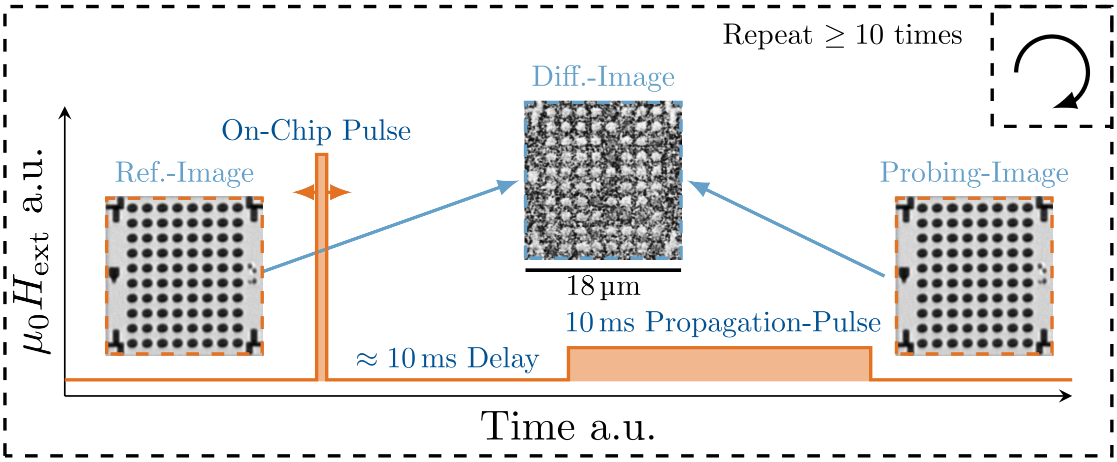

**Figure 5.7** Sketch of the measurement scheme, illustrated along a timeline. First, a reference image of an array of saturated nanomagnets is taken. Subsequently, the on-chip pulse with varying widths is triggered before a second; millisecond long pulse can be used to propagate remaining DWs and complete the reversal process. After the propagation pulse, a second image is taken to enable differential imaging.

single-domain nanomagnets. From section 2.9.1 we know that DW nucleation is a probabilistic process governed by an Arrhenius law with material-dependent cumulative distribution functions (CDF). Therefore, accurate measurements over large field and time ranges allow determining the magnetic properties of individual nanomagnets. For this purpose, however, hundreds or even thousands of the above-described measurements, conducted for different pulse amplitudes and widths, are necessary. The magnetic field is ramped to trace the individual CDFs at a given pulse width, conducting 10 to 20 measurements per field step.

The basic program structure for the analysis of time-domain measurements is similar to that for coercivity measurements via simple field ramps and has already been laid out in section 5.3.2. The major distinction is the determination of the field-dependent switching probability instead of a simple brightness change. This is done by averaging the brightness difference between the reference and the probing images at the individual field steps (pulse amplitudes). As a demonstration, the graph in Figure 5.8 displays the average brightness differences of the 20 measurements (Figure 5.7) each, plotted versus the magnetic field ($t_{\text{pulse}} = 100\,\text{ns}$) for a magnet taken from the image frame on the left. The displayed fit according to Equation (2.52) allows to better model the switching probability and

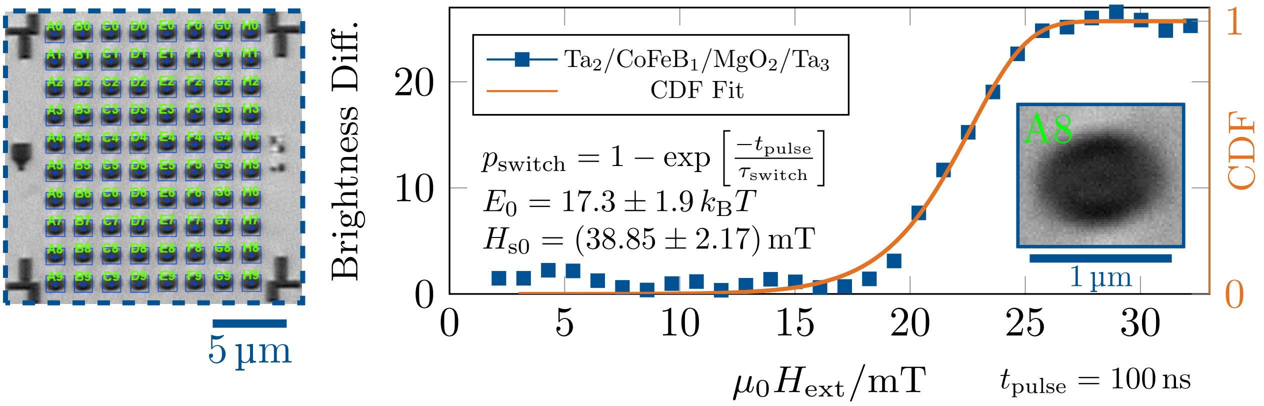

**Figure 5.8** Plot of the mean brightness differences (pixel values) and cumulative distribution function (CDF) versus the pulse amplitude. A fit to the cumulative distribution according to Equation (2.52), yields an energy barrier $E_0 \approx 17\,k_B T$ and a switching field $H_0 \approx 39\,\text{mT}$. Per data-point 20 measurements are used.

extract estimates of the switching field at 0 K ($H_{s0}$) as well as the energy barrier without field ($E_0$). Furthermore, by applying the *Sharrock* criteria ($p_{\text{switch}} = 0.5$), it is possible to ascribe a characteristic switching field to every magnet.

### Nanosecond Magnetic Field Pulses

Out-of-Plane magnetic field pulses in the µs and ns range are generated via (single winding) on-chip coils (depicted in Figure 4.8 (a)). The coils are, thereby, fabricated in a dedicated process step after the magnets, as described in section 4.5. The DUTs are placed on dedicated chip-carriers and connected to the pulser circuitry, housed by chip carrier, via aluminum wedge bonds. The whole assembly is depcited in Figure 5.9 (a). The nanosecond-pulser is implemented as a low-side switch, connecting pre-charged pulse-discharge capacitors on the high-side to ground via the on-chip coil. The low-side switch is driven by a fast gate-driver which is supplied via a software controlled Agilent 81111A pulse generator [226]. This allows for pulse widths down to ≈ 8 ns, limited by the turn-on/off time of the low-side switch. A resistive probe in parallel to the coil together with a shunt-resistor is used to measure the current flowing through the coil during the discharge. The coil current must also flow through $R_{\text{shunt}}$ (shown in Figure 5.9 (b)). The resulting voltage drop $U_{\text{shunt}}$ across the shunt resistor is subsequently divided by the 10 kΩ resistor of the restive probe and the input resistance of the oscilloscope (50 Ω). The current through the coil then ($I_{\text{coil}}$) calculates as

$$I_{\text{coil}} = \frac{U_{\text{shunt}}}{R_{\text{shunt}}} = \frac{U_{\text{measure}} \cdot \frac{1E4+50}{50}}{R_{\text{shunt}}} = \frac{21}{R_{\text{shunt}}} U_{\text{measure}} \,, \tag{5.5}$$

with $U_{\text{measure}}$ taken from the pulse plateau of respective oscilloscope traces (exemplary shown in Figure 5.10 (a)). From the current, the resulting magnetic field can be calculated using a truth Table

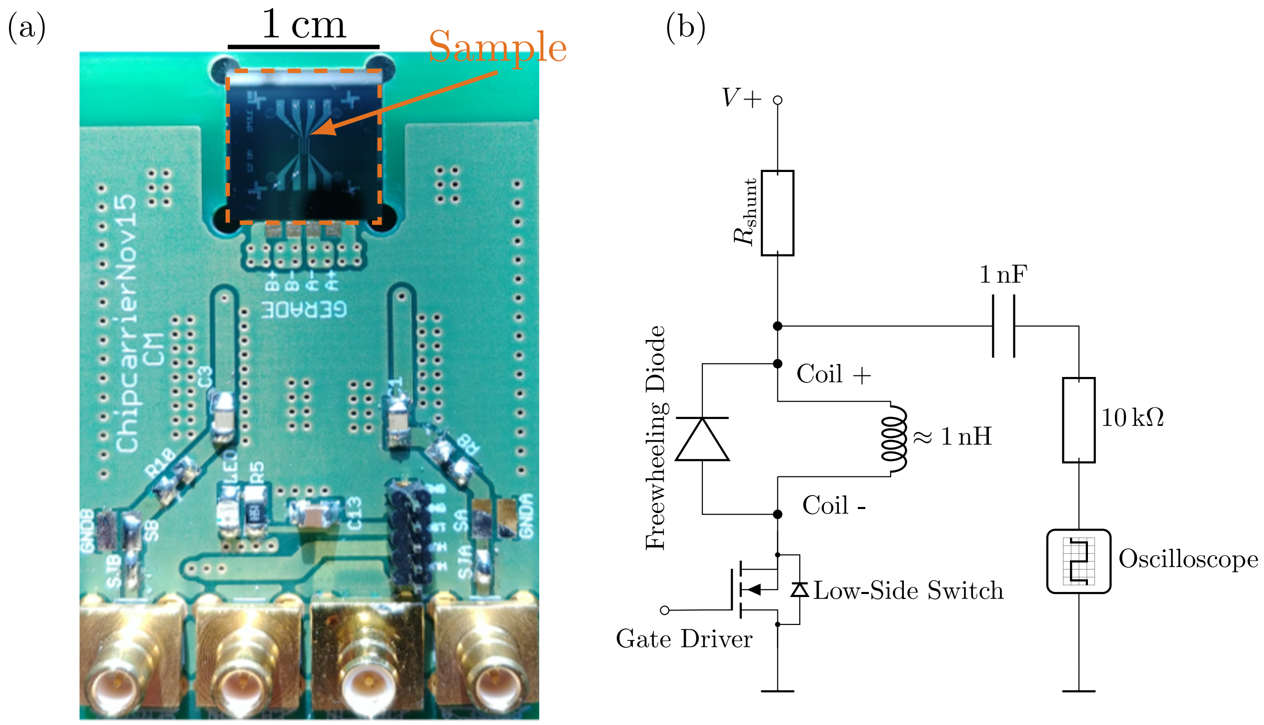

**Figure 5.9** Image of the nanosecond pulser PCB in (a), depicting a bonded sample with several on-chip coils. In (b), the circuit diagram of the pulser is shown. It depicts the on-chip coil as an inductor in the center, fed by the high voltage capacitor through the shunt resistor if the low-side switch is closed. Especially relevant is the resistive probe in parallel with the coil, which enables measuring the current through the coil accurately via the displayed resistor.

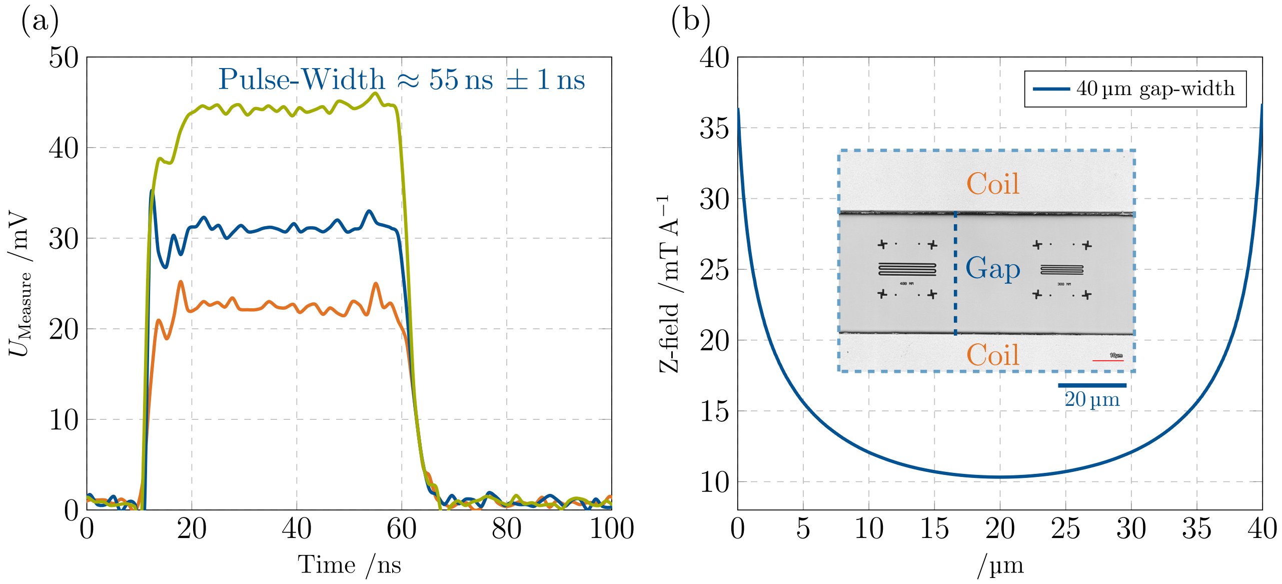

**Figure 5.10** In (a), exemplary oscilloscope traces of the resistive probe for different capacitor voltages are displayed. The pulse with is thereby set to 55 ns. In (b), the out-of-plane field components are displayed versus the respective positions within the gap of an on-chip coil with a total gap width of 40 µm (wire width = 65 µm).

obtained from finite element simulations of the coil, done with the FEMM software package.
Figure 5.10 (b) displays the respective position-dependent out-of-plane field components for a line gap of 40 µm. The inlet, displays a laser scanning microscope image of the coil lines with a magnetic nanowire placed in the center of the gap. The actual position of the magnets is determined via microscope images.

### 5.3.4 Laser Magneto-optical Kerr-effect Microscopy

In contrast to widefield imaging, the laser magneto-optical Kerr-effect microscope (LMOKE) uses the coherent light of a laser source ($\lambda_{\mathrm{laser}} \approx 600\,\mathrm{nm}$) instead of an incoherent LED to probe the magnetization and its changes on magnetic surfaces. To characterize PMA magnets, the laser is used in a polar geometry. Similarly to the WMOKE, the light is first being passed through a linear polarizer before being shaped and focused onto the surface of the DUT with varying spot sizes (ranging from ≈ 100 µm down to < 1 µm in diameter). The focusing optics subsequently capture the reflected light and pass it through the analyzer towards a differential photodetector. To suppress noise and increase the sensitivity, a lock-in amplifier in combination with a amplitude modulated laser source (kHz range) is used. Furthermore, a fast piezoelectric XY-stage allows to move the DUT and thus position the laser with high accuracy (better than 1 µm). This laser positioning, together with an electromagnet for out-of-plane and in-plane magnetic fields, allows measuring the hysteresis of films as wells as sub-µm structures alike. The exemplary hysteresis curve of the output stage of a $\mathrm{Ta_2/Pt_3/[Co_{0.2}/Ni_{0.4}]_8/Pt_3}$ inverter is displayed in Figure 5.11 (a). The penetration depth of the red laser is ≈ 10 nm in metals, which allows probing different magnetic layers and their interactions. This is best shown by the plot in Figure 5.11 (b), which shows the magnetic hysteresis of two Pt/Co layers, which are RKKY coupled via a 5 Å thick iridium layer. The layers exhibit weak antiferromagnetic coupling and an anti-parallel ground state. The piezo-stage, in addition to positioning, also allows for the fast scanning of areas up to 100 µm × 100 µm, thus enabling the recording of domain patterns with a high spatial resolution, optically limited by $\lambda_{\mathrm{laser}}$ and the used optics to ≈ 1 µm. Figure 5.12 depicts two high-resolution domain scans after out-of-plane demagnetization. The plots show the recorded, position-dependent, normalized Kerr signals and allow to separate the magnetization directions. Out of the two scans, the first, showing a stripe domain pattern with a periodicity of

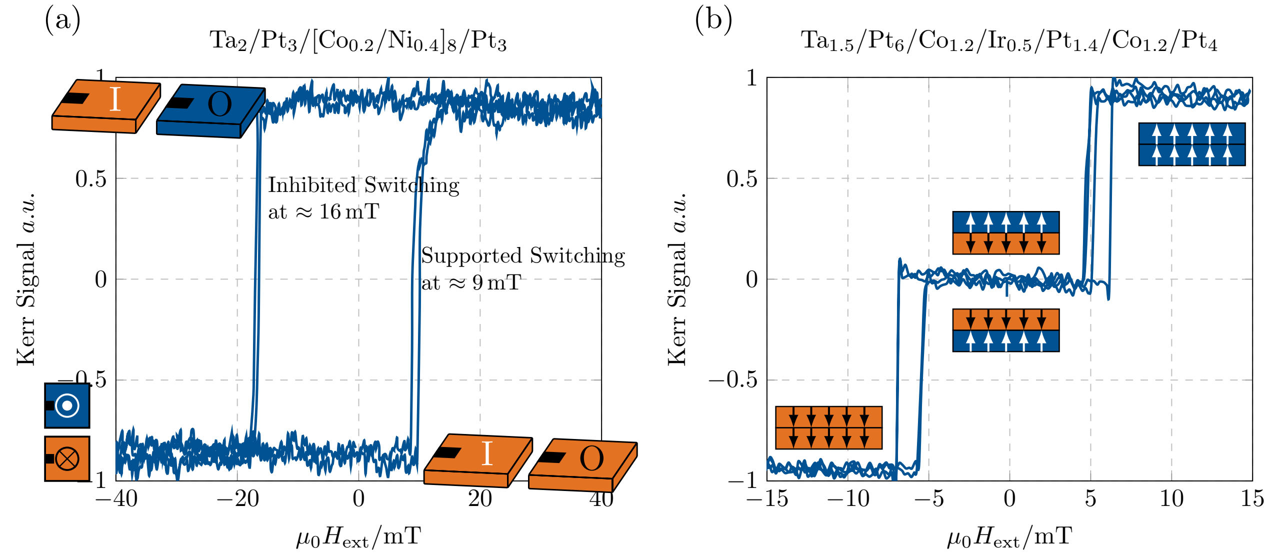

**Figure 5.11** In (a), the magnetic hysteresis of the output magnet of a pNML inverter is shown. The input magnet features a spin-down state, thus reducing the coercive field for the transition into a spin-up state. At the same time, switching into the spin-down state is impeded. In (b), the magnetic hysteresis of an antiferromagnetically coupled bi-layer is depicted. The light of the probing laser interacts with both layers allowing to resolve not only the surface magnetization.

≈ 1 µm approaches the spatial resolution limits of the setups. A WMOKE domain image of the same film ($Ta_1/MgO_2/CoFeB_{1.2}/Ta_2/Pt_4$) is depicted in Figure 2.12 (a) as comparison, highlighting the differences in spatial resolution between both methods and setups. The earlier described methods for time-domain measurements are also applicable for the LMOKE and were applied successfully even before the first WMOKE implementation [56], [227], [228]. Significant advantages of the LMOKE, thereby, are the increased signal-to-noise ratios (due to the lock-in technique) and vastly simplified data processing. However, the measurements are restricted to a single DUT (per measurement), on which the probing laser is positioned. Measuring magnet to magnet variation is thus comparatively time-consuming. For a detailed and comprehensive description of the entire setup, it is referred to [50].

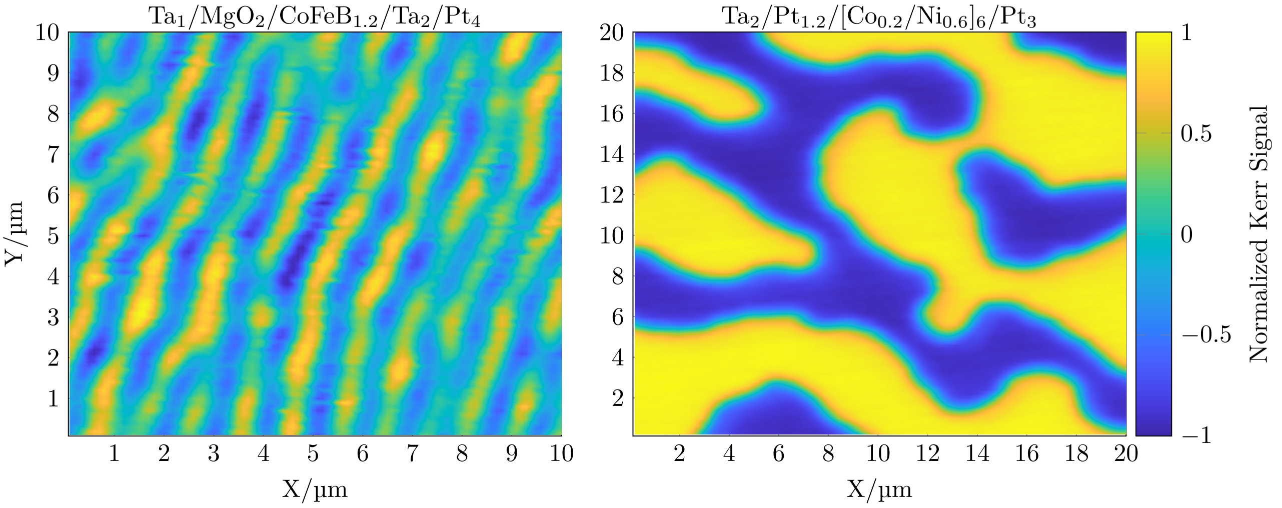

**Figure 5.12** Scanning laser MOKE images of two different thin-films after easy axis demagnetization. The image in (a) displays the stripe domain pattern of the same $Ta_1/MgO_2/CoFeB_{1.2}/Ta_2/Pt_4$ film already displayed in Figure 2.12 (a). The image in (b) depicts the larger, disordered domains of a $Ta_2/Pt_{1.2}/[Co_{0.2}/Ni_{0.6}]_6/Pt_3$ film.

## 5.4 Magnetotransport Measurements

Magnetotransport measurements summarize methods in which an electron current is used to probe the magnetic properties of a device under test. Thereby, various effects exist, which lead to changes in the apparent resistance of a magnetic material, depending on its magnetization. Notable examples of these magnetoresistive effects are the anisotropic magnetoresistance (AMR), the giant magnetoresistance (GMR), the tunnel magnetoresistance (TMR), the Spin-Hall magnetoresistance (SMR), and the anomalous Hall effect (AHE). Out of the mentioned effects, especially the AHE plays an essential role in the characterization of thin films and nanostructures with out-of-plane magnetization.

### 5.4.1 Anomalous Hall Effect Characterizations

The anomalous Hall effect (AHE), sometimes also called the extraordinary Hall effect, was first discovered by Edwin H. Hall in 1881, shortly after the ordinary Hall effect in metals and semiconductors. The AHE is restricted to magnetic materials and is usually one order of magnitude stronger than the ordinary Hall effect. The effect is ultimately routed in interactions between the orbital momenta of the conduction electrons and the magnetization (or the spins) of the localized electrons. The unpolarized current which enters the ferromagnet interacts with the local magnetization and becomes spin-polarized, with the majority of electrons aligning their spin parallel to the local magnetization. However, since the scattering at the localized electrons is spin-dependent, the conduction electrons are split and deflected in opposite directions, thus leading to charge accumulation and a potential difference perpendicular to the electron current. The effect is illustrated schematically in Figure 5.13 (b). Although discovered over one century ago, satisfying explanations for this quantum phenomenon, which cannot be described by purely classical means, have only been available for a few decades. For a comprehensive review of this effect, it is referred to [229].

However, for this work, it will suffice to use a purely phenomenological model, describing the originating voltage from both the ordinary and the anomalous Hall effect in metallic thin-film systems. The measurable voltage perpendicular to the electric field (but in-plane) calculates as

$$V_{\mathrm{Hall}} = R_{\mathrm{NHE}} B_{\mathrm{ext}} I + R_{\mathrm{AHE}} M_z I \,, \tag{5.6}$$

where $V_{\mathrm{Hall}}$ is the Hall voltage perpendicular to the applied current, $R_{\mathrm{NHE}}$ and $R_{\mathrm{AHE}}$ denote the material-dependent normal and anomalous Hall coefficients, and $M_z$ the out-of-plane component of the magnetization. The variables $B_{\mathrm{ext}}$ and $I$ describe the external magnetic field and the current through the thin film. Since the AHE voltage is directly proportional to the out-of-plane component of the magnetization, it is possible to measure its answer to externally applied fields via Hall measurements for thin-film geometries. To quantify and relate this effect, we can state that the resistance change between the two magnetization directions is in the range of a few ‰. It is therefore significantly stronger than the ordinary Hall effect but weaker than the GMR or TMR effect. While the LMOKE allows measuring the magnetic response to external magnetic fields or currents locally, the geometry of Hall measurements allows probing the magnetization over millimeter areas. One of the simplest but essential characterizations is the measurement of the magnetic hysteresis. Figure 5.13 (a) displays the hysteresis of a $\mathrm{Ta}_2/\mathrm{Pt}_3/[\mathrm{Co}_{0.2}/\mathrm{Ni}_{0.4}]_8/\mathrm{Pt}_3$ thin film. In contrast to highly localized LMOKE measurements, the AHE measurement allows resolving the start of the magnetization reversal in the depinning-regime as well as the determination of the saturation field at which the last domain wall is annihilated. To also allow for the characterization of nano-structures, lock-in techniques can be used to reach the necessary sensitivity [154].

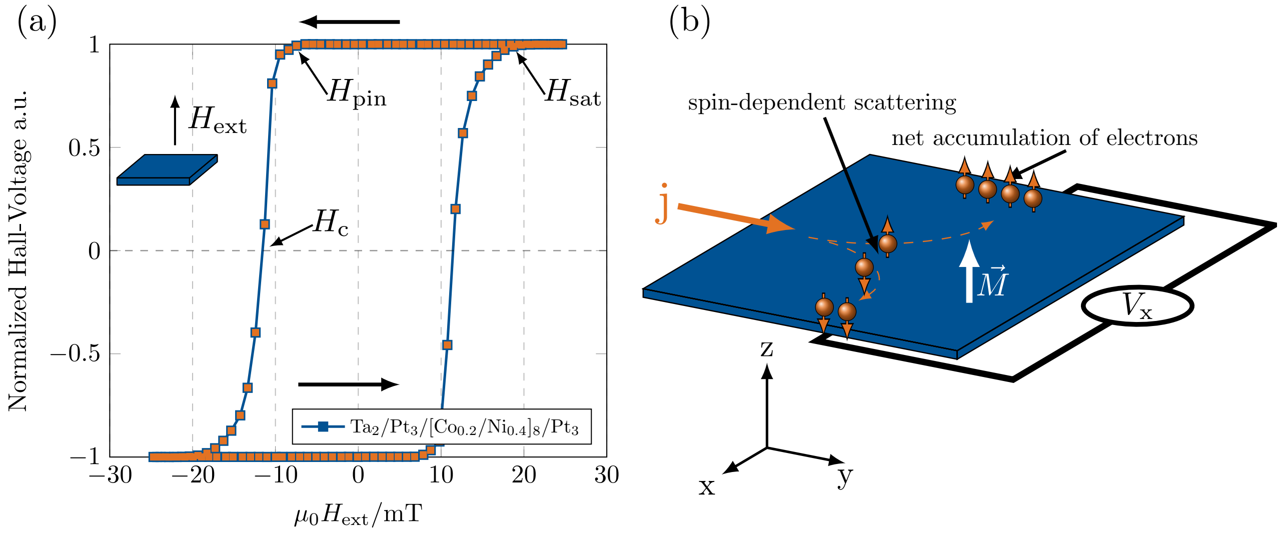

**Figure 5.13** In (a), a hysteresis curve of a $\mathrm{Ta_2/Pt_3/[Co_{0.2}/Ni_{0.4}]_8/Pt_3}$ thin film, characterized via anomalous Hall effect measurements is displayed. The measurement across a large area allows resolving the depinning field of the film. In (b), the anomalous Hall effect is depicted schematically. The electrons of the current $j$ are scattered in different directions, depending on their spin and the current magnetization of the film.

### Anisotropy Measurements

The direct relation between magnetization and AHE voltage allows to accurately determine the magnetic anisotropy of thin films, presuming the saturation magnetization is known. Two different methods were used to determine the anisotropy of magnetic thin films via AHE measurements throughout this project. Both are based on the *Stoner–Wohlfarth* model and the anisotropy-dependent tilt of the magnetization vector under the influence of strong off-axis fields. The methods, therefore, do not consider domain formation or DW-dynamics and are thus not ideally suited for measuring very small anisotropies ($K_{\mathrm{eff}} < 1 \times 10^{-4}\,\mathrm{J\,m^{-3}}$). As discussed in section 2.6, the magnetic anisotropy energy is best minimized if the magnetization is aligned with the anisotropy axis. Measuring the angle $\theta$ between the magnetization and the easy axis under the influence of an external field allows determining the anisotropy energy. The energy calculates as

$$E_{\mathrm{anis}} = -K_{\mathrm{u}} \cos^2 \theta - M_{\mathrm{s}} H_{\mathrm{ext}} \cos(\theta - \phi), \tag{5.7}$$

with, $K_{\mathrm{u}}$, $M_{\mathrm{s}}$ and $H_{\mathrm{ext}}$ as the known magnetic parameter as well as the external field. The angle between the external field and the easy axis is furthermore described by $\phi$. The angle $\theta$, necessary to determine the anisotropy, can be derived by different means. The first method used during this project was first proposed by Moon et al. and is discussed in the following [230].

### Rotation in a Constant Magnetic Field

Rotating the sample by 360° in a constant external field with high amplitude, causes the angle between the easy-axis (the sample surface normal) and the magnetization ($\theta$) to change, as the magnetization tries to follow the external field ($\phi$). The different off-axis fields tilt the magnetization and thus reduced the effective OOP component. At the same time, this out-of-plane component is monitored via the AHE effect. Figure 5.14 (a) displays this measurement procedure schematically. Subsequently, the recorded Hall voltages are normalized to determine $\cos\theta$, which describes the relative amplitude of the OOP component and thus the tilt of the magnetization. The cosine of $\theta$ is calculated as

$$\cos\theta = (V_{\mathrm{Hall}} - \frac{V_{\mathrm{min}} + V_{\mathrm{max}}}{2})/(\frac{V_{\mathrm{max}} - V_{\mathrm{min}}}{2})\,. \tag{5.8}$$

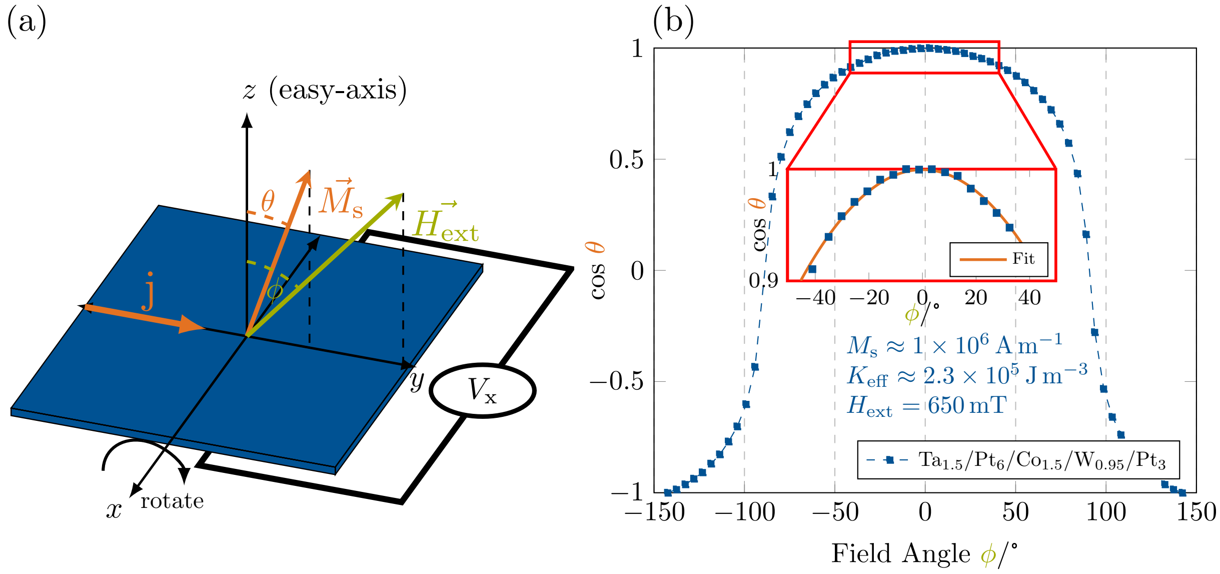

**Figure 5.14** On the left, the sketch of an AHE measurement, showing a magnetic thin-film rotating inside a constant magnetic field, is displayed. The drawn vectors depict the measurement geometry as well as the direction of the external field and magnetization in relation to the magnetic easy-axis. The plot on the right depicts $\cos\theta$ (the normalized Hall voltage) versus the field angle $\phi$. The inlet depicts a magnification of the low angle data used for the anisotropy fit (also displayed).

Via $\cos\theta$ it is now possible to approximate the anisotropy by solving Equation (5.7). By determining the zero points of the derivative and a subsequent Fourier expansion, Equation (5.7) is solved analytically (for details see [230]). Finally, for small angles ($\phi \leq 45°$) $\cos\theta$ approximates to

$$\cos\theta \approx 1 + \frac{(M_\mathrm{s}H_\mathrm{ext})^2}{2(2K_\mathrm{u} + M_\mathrm{s}H_\mathrm{ext})^2}\phi^2, \tag{5.9}$$

which allows fitting $K_\mathrm{u}$ directly, presuming that $M_\mathrm{s}$ is known. The effective anisotropy is subsequently obtained via $K_\mathrm{eff} = K_\mathrm{u} - \frac{1}{2}\mu_0 M_\mathrm{s}^2$. The measurement of a $\mathrm{Ta}_{1.5}/\mathrm{Pt}_6/\mathrm{Co}_{1.5}/\mathrm{W}_{0.95}/\mathrm{Pt}_3$ film is displayed in Figure 5.14 (b) with the fit according to Equation (5.9) displayed as inlet. The method yields good results for a wide anisotropy range but is ultimately limited by the mechanics of the setup and the contact scheme. As electrical contacts, contact springs are pressed onto the sample to provide the current and measure the resulting Hall voltage. During measurements, these contacts are prone to shift during rotation, resulting in measurement errors.

### Fixed-Angle Magnetic Field Sweeps

The second method to measure the magnetic anisotropy uses a fixed field angle $\phi$ but sweeps the external magnetic field. It was first proposed by Okamoto et al. and implemented via laser *Kerr* effect measurements [231]. Therefore, the implementation had to be adapted for the available AHE measurement equipment. The method promised to deliver a reasonable estimate of the first and second-order anisotropy terms and, furthermore, reduce measurement errors to improve the reliability of the setup. Instead of rotating the sample in a constant field (is depicted in Figure 5.14), a constant field angle ($\phi > 0°$) is chosen. The external field is subsequently swept and the Hall voltage measured. To derive the angle $\theta$ additional fields sweep are conducted at $\phi = 0°$ and $\phi = 180°$ to measure the Hall signals in saturation and calibrate the previous off-axis measurement. The deviation of the magnetization from the easy axis ($\cos\theta$) is then calculated as before, via Equation (5.8). For a comparison, we use the same $\mathrm{Ta}_{1.5}/\mathrm{Pt}_6/\mathrm{Co}_{1.5}/\mathrm{W}_{0.95}/\mathrm{Pt}_3$ stack as example. Figure 5.15 (a), therefore, depicts the resulting $\cos\theta$ for four different field angles. To obtain the anisotropy from $\cos\theta$, Okamoto et al. start from a series expansion, as discussed in section 2.4.3. They expand on Equation (5.7), also considering the second-order anisotropy term, yielding the equation

$$E_{\mathrm{tot}} = K_1 \sin^2\theta + K_2 \sin^4\theta - M_{\mathrm{s}} H_{\mathrm{ext}} \cos(\theta - \phi), \tag{5.10}$$

where $K_1$ and $K_2$ denote the first and second-order terms of the effective anisotropy. The equilibrium condition is subsequently found via the first derivative, resulting in

$$0 = (K_1 + K_2 \sin^2(\theta)) \sin(2\theta) + M_{\mathrm{s}} H_{\mathrm{ext}} \cos(\theta - \phi). \tag{5.11}$$

To allow for a numerically robust fit, Equation (5.11) is reformulated resulting in a linear problem described as

$$\frac{2K_1}{M_{\mathrm{s}}} + \frac{4K_2}{M_{\mathrm{s}}}(1 - \cos^2\theta) = H_{\mathrm{ext}} \frac{\cos\theta \sin\phi - \sin\theta \cos\phi}{\sin\theta \cos\phi} = \alpha H_{\mathrm{ext}}, \tag{5.12}$$

with $\alpha = \frac{\cos\theta \sin\phi - \sin\theta \cos\phi}{\sin\theta \cos\phi}$ [231]. With the earlier determined $\cos\theta$ it is now possible to plot Equation (5.12) directly (depicted Figure 5.15 (b)) and determine $K_1$ and $K_2$ via a simple linear fit. The anisotropy field $H_{\mathrm{k}}(\mathrm{T}) = \frac{2K_1(\mathrm{J\,m^{-3}})}{M_{\mathrm{s}}(\mathrm{A\,m^{-1}})}$ is thereby equal to the zero intercept on the y-axis. For the linear fit, it is essential to consider the limits of the *Stoner–Wohlfarth* model on which the equation is based. As with the previous method proposed by Moon et al., the measured films only behave as an ideal SW-particle up to certain angles ($\theta \leq 60°$). On the other hand, for small values of $\theta$, the small-angle approximation leads to an overestimation of measurement errors and offsets from the calibration measurements. The obtained data is, therefore, only usable within a certain angle range ($0.2 \leq (1 - \cos\theta) \leq 0.75$). Both methods yield comparable results, with differences between 10 % and 20 %. However, in direct comparison, neither of them showed clear advantages. While the method proposed by Moon et al. suffers from mechanical problems in its current configuration, it was found that the method by Okamoto et al. requires manual intervention in handling the small-angle error and choosing appropriate field angles, resulting in inconsistent results. Overall, both the rotating-field and fixed-angle methods suffer the problem that in order to be usable, prior knowledge of the saturation magnetization of the film is necessary. The saturation magnetization is usually measured with SQUID or vibrating-sample magnetometer. However, as discussed in section 5.1, it is possible

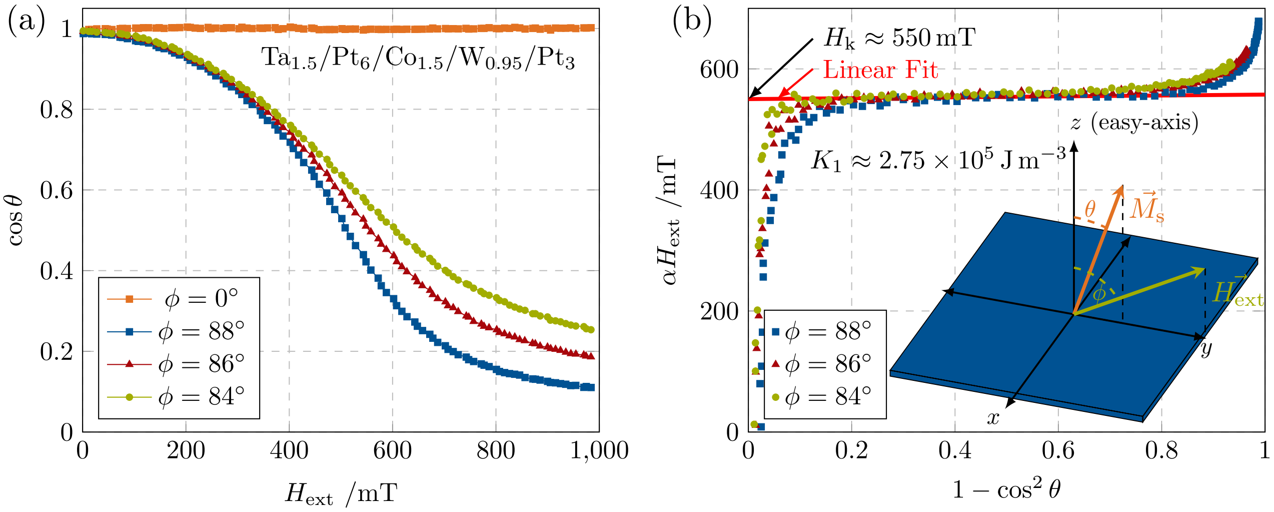

**Figure 5.15** In (a), the cosine of the magnetization angle $\theta$ is displayed as a function of the externally applied field at different angles ($\phi$). At $\phi = 0°$ or $\phi = 180°$(not displayed) the field is parallel to the easy axis of the characterized $\mathrm{Ta_{1.5}/Pt_6/Co_{1.5}/W_{0.95}/Pt_3}$ film, resulting in $\theta = 0°$ or $180°$. In (b), a plot of Equation (5.12) according to the data displayed in (a) is depicted. The red line, displays a linear fit to data points within $0.2 < (1 - \cos\theta) < 0.75$. The inlet on the lower right demonstrates the measurement configuration with different field angels $\phi$.

to derive the anisotropy directly from hard-axis magnetometer loops. Therefore, the usage of the discussed AHE methods is only merited if the material system is very well known (e.g., Pt/Co, Co/Ni).

# 6 Platinum/Cobalt/Tungsten Multilayer Systems

The work on Platinum/Cobalt/Heavy-Metal (Pt/Co/HM) systems arose as a natural consequence of the group's vast experience with Pt/Co multilayers and the integration of a new and largely untested sputtering tool into the fabrication process. Combining the new fabrication tool with a slightly modified but known material system promised to yield results within a short period of time. This strategy was backed by the at the time recent discovery of strong interfacial Dzyaloshinskii-Moriya (iDMI) interactions in Pt/Co/HM systems with broken inversion symmetry, promising higher DW velocities alongside a tendency towards *Néel*-type domain walls with higher mobility [130], [232], [233]. In these years, Pt/Co/HM multilayers drew considerable attention in the magnetism community following the discovery of iDMI stabilized Skyrmions (bubble-like spin texture with increased stability) at room temperatures and large Spin-Hall angles in particular heavy metals [234]–[236]. Two different Pt/Co/HM multilayer systems were closely investigated during that time. The first was Pt/Co/Ir, for which in 2017 Ziemys et al. demonstrated three times higher domain wall velocities by comparing nano-wires made from Pt/Co/Ir and Pt/Co multilayer stacks [145]. However, the material system systematically analyzed for use in pNML systems was Pt/Co/W. Tungsten was selected due to its strong iDMI (resulting in high DW-velocities) and large spin Hall angle, potentially allowing efficient spin-orbit-torque clocking of pNML magnets [235], [237]. The existence of strong iDMI in the sputtered Pt/Co/W films could later be confirmed, and its strength determined by Szulc et al. to be $\approx 0.8\,\mathrm{mJ\,m^{-2}}$ for a single tri-layer [213]. In 2019, Ahrens et al. [238] furthermore investigated both the Pt/Co/Ir as well as the Pt/Co/W system (even considering Pt/Co/C) in their search for stable but mobile skyrmionic spin-textures. The results of the main pNML study on Pt/Co/W were presented at the Joint European Magnetic Symposia (JEMS) in 2018 and published in 2019 [82]. The following chapter presents this work in a revised and updated form.

## 6.1 Film-Level Analysis

To assess the potential of the Pt/Co/W material system for pNML, the parameter space of the material was first explored on film level by sputtering mono and bilayers followed by higher-order stacks (N > 3). Selected stacks were subsequently processed towards adequate test structures to determine the effect of $Ga^+$ irradiation on the new material system. In the last step, the first Pt/Co/W inverters were fabricated, characterized, and assessed regarding their hysteresis. A schematic illustration of the basic stack architecture is shown in Figure 6.1.

### Perpendicular Magnetic Anisotropy

Starting from single-layers allows to assess important material parameter with reasonable effort, not feasible in higher order stack configurations. To evaluate the influence of W on $M_s$ and anisotropy, a series of increasing Co thickness within a $[Pt_{1.45}/Co_x/W_{0.95}]_1$ stack was fabricated and the results were compared with literature values of conventional Pt/Co/Pt layers. Figure 6.2 (b) depicts the derived $M_s$ values obtained from OOP SQUID magnetometer measurements in comparison to the intrinsic value of bulk Co ($\approx 1.4 \times 10^6\,\mathrm{A\,m^{-1}}$). In contrast to Pt/Co/Pt which shows a relevant increase in $M_s$ due to spin polarization of the adjacent Pt, Pt/Co/W exhibits a significant reduction for $t_{Co} < 3\,\mathrm{nm}$. The ferromagnetic behavior (hysteresis) of the stacks vanish for $t_{Co} < 0.5\,\mathrm{nm}$, which is attributed to a magnetic dead layer of roughly this magnitude. This value is also derived from the linearized $M_s$ plot indicated as inlet in Figure 6.2 (b). Possible reasons for this behavior include intermixing with tungsten as well as sputter damage caused during the tungsten deposition, thus reducing the effective Co thickness [77], [91]. Since magnetometer measurements of atomically thin layers are error-prone (potentially wrong layer thicknesses in combination with inaccuracies during sample mounting), a linear fit to the linearized $M_s$ data points is used to obtain the Co thickness-dependent $M_s$ values for the final $K_{eff}$ fit. The evolution of the Co thickness-dependent PMA also enables determining the interface and volume anisotropy components $K_s$ and $K_v$ respectively, by a fit according to the linearized equation

$$K_{eff} \cdot t_{Co} = (K_u - \frac{1}{2}\mu_0 M_s^2)t_{Co} + 2K_s = K_v\, t_{Co} + 2K_s\,, \tag{6.1}$$

where $K_u$ as the uni-axial anisotropy. For symmetric systems like Pt/Co/Pt, the contribution of each interface to $2K_s$ is expected to be similar. This, however, is not the case for systems with broken inversion symmetry, which renders a simple splitting of the $2K_s$ values invalid. The evolution of

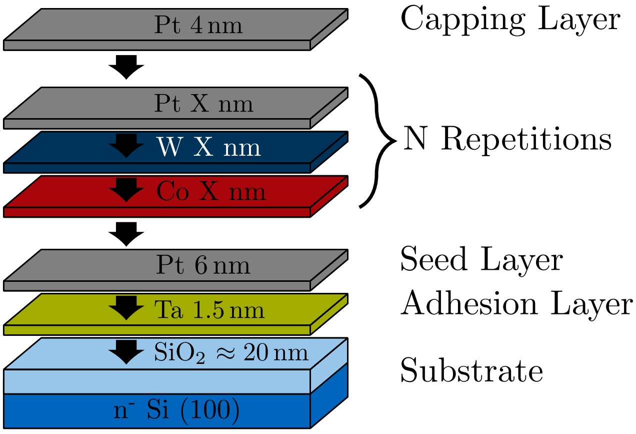

**Figure 6.1** Schematic illustration of the generalized Pt/Co/W stack architecture, showing the bulk silicon with a ≈ 20 nm thick thermal oxide layer as the primary substrate. A thin tantalum layer is used to increase the adhesion for the subsequent Pt seed layer, establishing the crystal structure for the stack growth. A variable number of Pt/Co/W trilayers is subsequently deposited before a final Pt capping layer is used to protect the stack against oxidation.

the Co thicknesses normalized $K_1$, $K_2$ values including a fit according to Equation 6.1 is depicted in Figure 6.2 (a). The effective anisotropies were thereby determined using the method proposed by Okamoto et al. introduced in section 5.4.1 [231]. For thinner Co layers ($t_{\mathrm{Co}} <\approx 1\,\mathrm{nm}$) the measured PMA of Pt/Co/W starts to deviate significantly from the initial linear trend. A relevant factor contributing to this behavior is the reduction in $M_{\mathrm{s}}$ for small $t_{\mathrm{Co}}$ values due to the large magnetic dead layer. However, the deviations are much more pronounced than can be explained by the $M_{\mathrm{s}}$ values and are best explained by a growth transition model. This model splits the layer growth into an incoherent (relaxed) region for larger Co thicknesses and a coherent region with high-strain growth conditions for thin layers [165], [239]. In case of coherent growth, $K_{\mathrm{eff}}$ increases with $t_{\mathrm{Co}}$ up to the point where the crystal starts to relax, causing relevant amounts of zero-dimensional defects (vacancies) before dislocation defects relax the lattice strain and complete the transition towards incoherent growth [239]. By only considering the incoherent growth region for the fit one can determine $2K_{\mathrm{s}}$ (summation of both interfaces) as the intersection with the y-axis and the volume anisotropy $K_{\mathrm{v}} = K_{\mathrm{u}} - \frac{1}{2}\mu_0 M_{\mathrm{s}}^2$ as the slope of the line. For Pt/Co/W this results for the first order anisotropy constants in $2K_{\mathrm{s},1} = (1.36 \pm 0.04)\,\mathrm{mJ\,m^{-2}}$ and $K_{\mathrm{v},1} = (-0.79 \pm 0.03) \times 10^9\,\mathrm{mJ\,m^{-3}}$. The fit for the second order terms converges to $2K_{\mathrm{s},2} = (-0.015 \pm 0.030)\,\mathrm{mJ\,m^{-2}}$ and $K_{\mathrm{v},2} = (0.0095 \pm 0.0190) \times 10^9\,\mathrm{mJ\,m^{-3}}$, however, with very high uncertainties. The determined surface anisotropy value, though error prone due to the limited database, is not only roughly $\approx 35\,\%$ smaller compared to Pt/Co/Pt but compared to other Pt/Co/HM systems [90], [91]. Considering the volume anisotropy, a different picture emerges. The obtained values are in line with results for (111) Pt/Co/Pt but show strong deviations compared to other Pt/Co/HM compositions usually exhibiting much lower volume anisotropies. However, a sound comparison across materials and tools requires a much broader data set, as these values are strongly dependent on the used deposition tools and parameters.

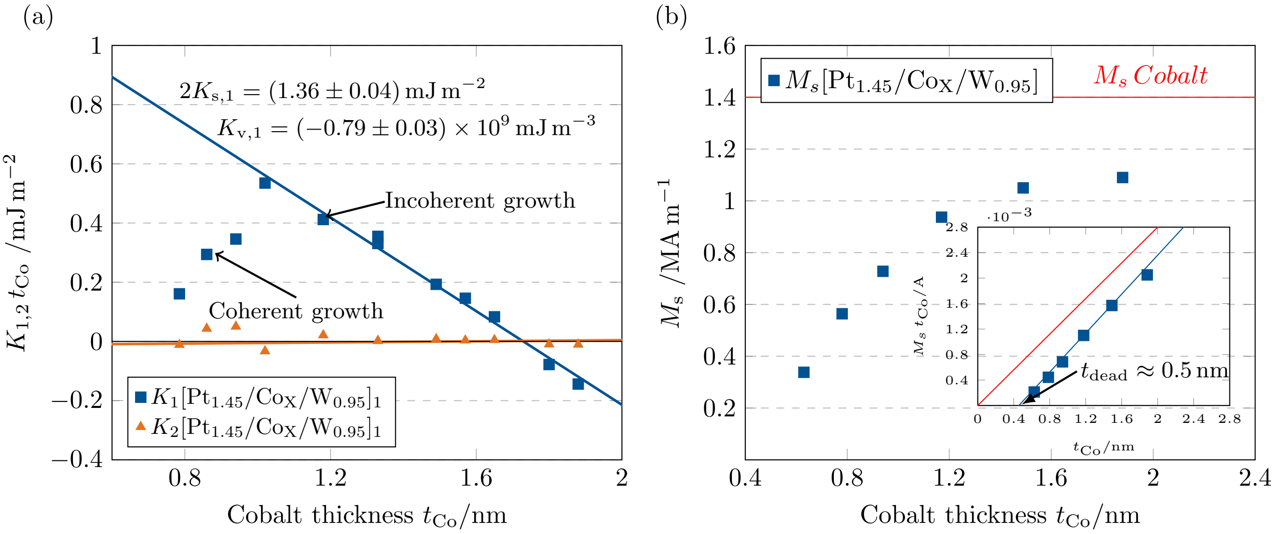

**Figure 6.2** In (a), a plot of thickness-normalized $K_{1/2}$ values for Pt/Co/W versus the respective Co thickness $t_{\mathrm{Co}}$ is shown. In (b) the evolution of the saturation magnetization with the Co thickness is plotted, including the linearization as inlet. The intrinsic values of Co are depicted as a comparison.

### Interlayer Coupling

Through the investigation of bilayers, the effect of different tungsten thicknesses on the coupling between adjacent Pt/Co layers was investigated. Therefore two series of $[Pt_{1.45}/Co_{1.22}/W_X]_2$ layers were grown and subsequently analyzed on film level via polar laser MOKE-microscopy and AHE measurements. The fabrication of both series took place six months apart to broaden the data set and assess the reproducibility and drift of the sputtering tool. Starting at $t_w \geq 0.6\,\mathrm{nm}$ ($t_w \geq 0.5\,\mathrm{nm}$ for the second series), the bilayers stop behaving like a single ferromagnet and a distinct step hysteresis behavior develops, as indicated by the inlet of Figure 6.3 (a). The step-hysteresis is a strong indicator for separately switching layers and depends on the superposition of interlayer coupling and anisotropy differences between the two Co layers. In order to separate these effects, the shifts in minor loop transitions from parallel to anti-parallel configuration and vice versa are assessed. In the case of AF coupling, the transition into the anti-parallel state is preferred compared to a favored transition into a parallel state for ferromagnetic coupling. Figure 6.3 (a) depicts the evolution of the effective interlayer coupling with increasing tungsten thicknesses. The effective coupling field rapidly decreases with increasing $t_W$. Starting from $t_w \geq 0.5\,\mathrm{nm}$ it is superposed by the anisotropy difference resulting in a two-step hysteresis. The measured interlayer coupling starts to oscillate between anti-ferromagnetic and ferromagnetic with low single-digit mT amplitudes, thus rendering a clear distinction by means of film level analysis challenging. During minor loops, a saturation of both layers cannot be guaranteed. Therefore, nucleation seeds or small domains might survive, which affects the coercivity as these domains only need to be propagated through the film. The measured coupling fields are, as a result, setting dependent and are only suited for a rough assessment. A plausible cause for this behavior would be the superposition of the oscillatory Ruderman–Kittel–Kasuya–Yosida (RKKY) coupling as well as roughness and grain-size dependent orange peel effects [108], [240]. The statistical analysis of micrometer sizes structures with varying tungsten thicknesses, required for quantitative evaluation, however, would be beyond the scope of this work. Therefore, the exact causes of the observed behavior remain unclear at this point. It is nevertheless possible to derive a qualitative picture of the $t_W$ dependent interlayer coupling of low magnitude, which is more than sufficient for evaluations

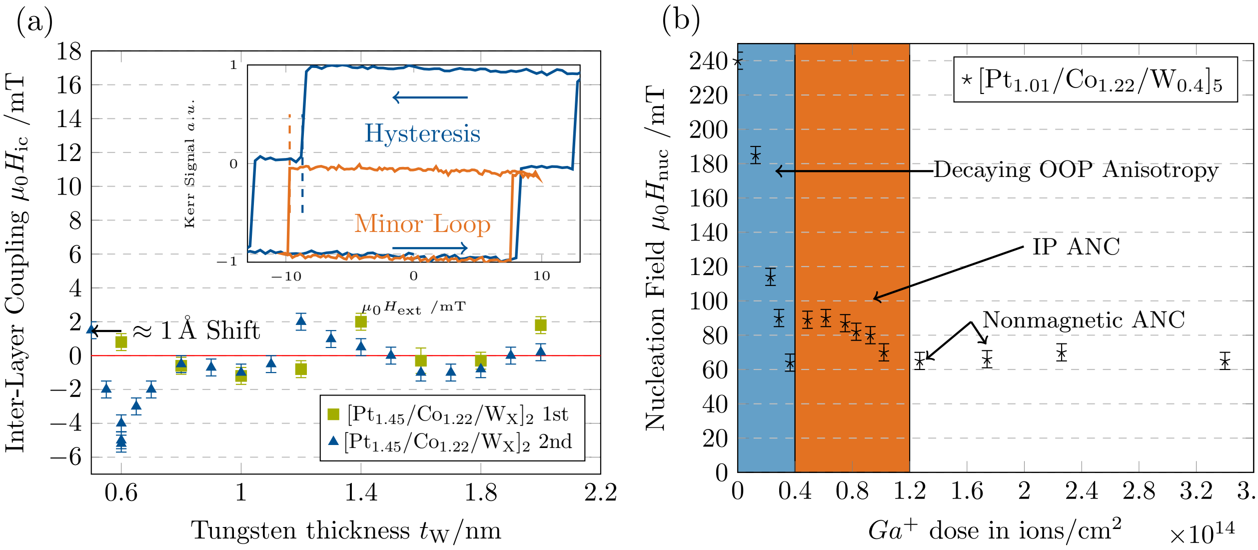

**Figure 6.3** In (a), the evolution of the interlayer coupling $\mu_0 H_{\mathrm{Ic}}$, as function of the tungsten thickness $t_W$ is shown. The plot depicts two individual sample series fabricated six months apart. An exemplary step hysteresis, including a minor loop of the "weak" layer, is presented as an inlet. The field difference between the hard and soft minor transitions indicated by the dashed lines defines the interlayer coupling. In (b), the nucleation field evolution of a $[Pt_{1.05}/Co_{1.22}/W_{0.4}]_5$ stack as function of the $Ga^+$ ion dose. Color-coded are the three distinct switching regimes caused by the transition of the ANC from out-of-plane to in-plane anisotropy and finally, the transition into a state without anisotropy.

within the framework of pNML. Large coupling fields require large net amounts of OOP magnetized Co. Thus higher-order stacks ($N > 3$) are utilized to maximize the Co amount. Building on the analysis of the mono and bilayer systems, the parameter space for 5, 6, and 7 repetition stacks was explored. For bilayer stacks, the anisotropy difference dominates the hysteresis behavior. However, for stacks of higher-order, the properties of the individual layers start to blur. The stacks behave as single ferromagnets on film level regardless of the tungsten interlayer thickness.

## 6.2 Ion-Beam Engineering

In contrast to macroscopic films, nanostructures are less affected by extrinsic defects and therefore differ significantly in their hysteresis behavior. In order to assess the stack properties on this level, a series of four Pt/Co/W stack compositions with five repetitions each were selected, further processed, analyzed, and compared to a conventional Pt/Co/Pt film processed along as reference. A repetition number of five was chosen to still enable a direct comparison with Pt/Co/Pt, which otherwise loses its single domain behavior in this configuration. The resulting structures, provided that the W thickness corresponds to weak interlayer coupling, exhibit multi-level non-deterministic switching processes in the *as-grown* state, as indicated by the hysteresis depicted in Figure 6.4 (b). Therefore, inherent layer-specific defects and thermal fluctuations dominate the magnetization reversal process. Perpendicular nanomagnetic logic achieves the necessary coercivity control by artificial nucleation centers (ANC), areas of heavily reduced anisotropy, hence areas where the DW is guaranteed to nucleate. Figure 6.4 (c) illustrates the difference in hysteresis behavior comparing a $[\mathrm{Pt}_{1.45}/\mathrm{Co}_{1.62}/\mathrm{W}_{0.95}]_5$ magnet before and after local $\mathrm{Ga}^+$ irradiation. The effect of $\mathrm{Ga}^+$ irradiation on the different stacks was evaluated by placing ANCs on rectangular test lanes $5 \times 18\,\mu\mathrm{m}$ in size. The ion dose was ramped starting from $1 \times 10^{13}$ ions/cm$^2$ and the evolution of the nucleation fields $H_{\mathrm{nuc}}$ plotted against (Figure 6.4 (a)). As discussed in section 3.1.2, the coercivity of an irradiated nanomagnet evolves with anisotropy of the ANC area. The effects of local ion irradiation on a magnet with PMA can be described by a multi-stage model [63], [119]. In the first regime, a linear decrease in coercivity can be observed as soon as the PMA of the ANC falls short of the local defect level, defining the anisotropy landscape of the magnet. The lowest nucleation fields are achieved when the effective anisotropy $K_{\mathrm{eff}}$ reaches a level where the DW nucleation energy is equal to the energy necessary to overcome the anisotropy gradient between ANC and the rest of the magnet and depin a DW. From this point on, the necessary switching fields are defined by the energy required to depin the nucleated domain wall from the ANC. A further decrease in $K_{\mathrm{eff}}$ increases the coercivity. This anisotropy gradient eventually levels out at even higher doses, and a stable switching regime emerges.

### 6.2.1 Ion-Beam Engineering in Weakly Coupled Multilayers

The nucleation fields obtained from samples with strong ferromagnetic interlayer coupling, namely $[\mathrm{Pt}_{1.45}/\mathrm{Co}_{1.22}]_5$ and $[\mathrm{Pt}_{1.05}/\mathrm{Co}_{1.22}/\mathrm{W}_{0.4}]_5$, depicted in Figure 6.4 (a) are in good accordance with the above described model and locate the point of lowest nucleation and propagation fields ($\approx 65\,\mathrm{mT}$) at $\approx 4 \times 10^{13}$ ions/cm$^2$. Results for the $[\mathrm{Pt}_{1.45}/\mathrm{Co}_{1.22}/\mathrm{W}_{0.6}]_5$ stack, however, fall out of line. In bilayer configuration, this stack composition exhibits weak antiferromagnetic interlayer coupling superposed by anisotropy differences. As the ANC equalizes the anisotropies at least locally, a reduction in step width towards uniformed switching is expected. This is clearly not the case, as the hysteresis steps (depicted in Figure 6.4 (c)), become more pronounced upon irradiation. A complete evolution of the nucleation fields is depicted in Figure 6.4 (a), with ion doses resulting in step-hysteresis behaviors or a delayed remanence field level (highlighted by tails up to their approximate remanence field level). Data taken from the weakly interlayer coupled stacks poses special interest, as not only the nucleation fields are affected by different ion doses. Depending on the stack composition and ion dose it is possible to completely suppress step-like hysteresis behavior, as illustrated by the hysteresis in Figure 6.4 (d) for the $[\mathrm{Pt}_{1.45}/\mathrm{Co}_{1.22}/\mathrm{W}_{0.95}]_5$ stack and an ion dose of $\approx 3.8 \times 10^{13}$ions/cm$^2$. A

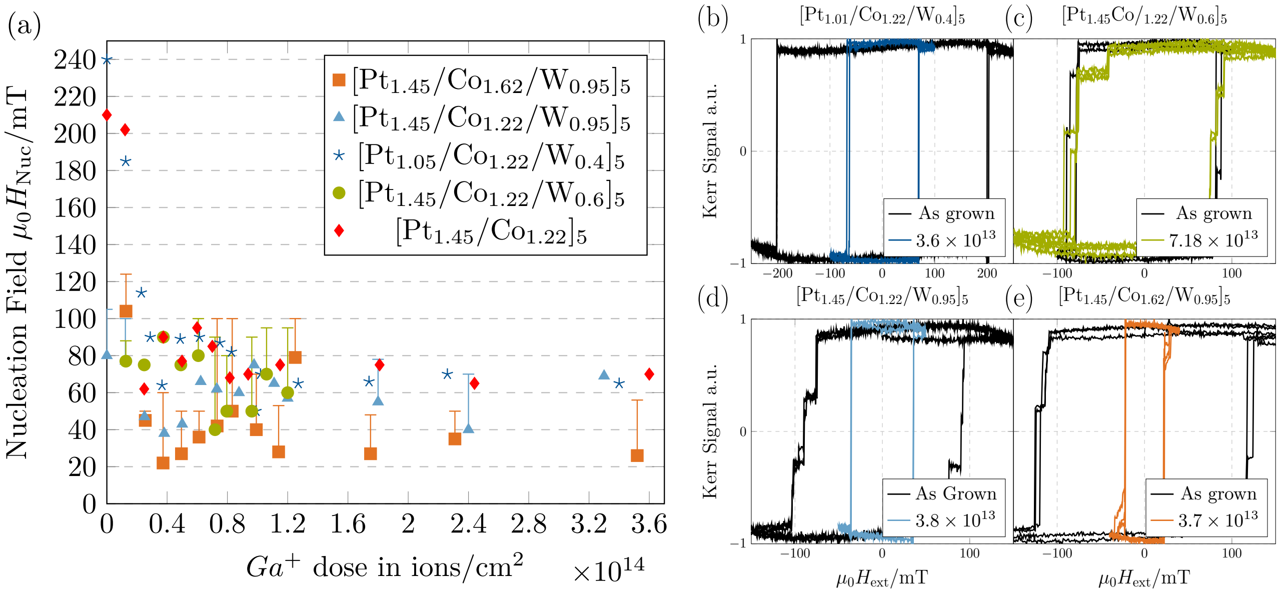

**Figure 6.4** In (a), the coercivity of varying stack compositions with and without strong interlayer coupling as a function of the Ga$^+$ dose are depicted. The irradiation area is with 50 × 50 nm constant for all samples. Step-hysteresis behaviors are highlighted by tails up to the approximate remanence field level for affected magnets. In (b), selected hysteresis plots of differently processed stacks are displayed, comparing *as-grown* behaviors with results after ANC placement.

significant reduction in nucleation fields can be attributed to weakly interlayer coupled stacks, more than halving the coercivities obtained with the reference Pt/Co/Pt stack. This might be explained by the reduced interlayer coupling acting in superposition with the demagnetization fields to achieve reduced nucleation fields. This is underlined by the fact, that the only stack with significant FM coupling [Pt$_{1.05}$/Co$_{1.22}$/W$_{0.4}$]$_5$ shows no relevant reduction in coercivity compared to Pt/Co. The evolution of $H_{\mathrm{nuc}}$ for the weakly coupled stacks also follows the above described model, featuring nucleation fields, down to ≈ 20 mT for the [Pt$_{1.45}$/Co$_{1.62}$/W$_{0.95}$]$_5$ stack. These results open the possibility not only to engineer the value of $H_{\mathrm{nuc}}$ but are also a first step towards the control of occurrence and extent of step-like hysteresis behavior in weakly coupled micro-magnetic devices.

## 6.3 Dipole Coupled Pt/Co/W Inverter

Inverter structures were fabricated alongside the test lanes and irradiated according to the above obtained optimal Ga$^+$ doses to achieve minimal coercivity fields. Figure 6.5 displays an overview of the pNML inverter working principle, which was already introduced in section 3.1.1 and is usually demonstrated using the hysteresis behavior of the output magnet. The switching field of the output is shifted depending on the magnetic state of the input. This shift is defined as two times effective coupling strength ($2 \cdot H_{\mathrm{dip}}$) and is dependent on the gap size, the magnetic moment of the stack, and the actual ANC position within the output fin. The switching field difference between the supported and suppressed case defines the clocking window $\triangle H_{\mathrm{clk}}$. Measuring the full output hysteresis for both input cases enables the characterization of the device. Figure 6.6 depicts the output hysteresis curves and characteristics of three inverters with a gap-size of ≈ 85 nm, including respective ion doses and optimal clock fields. Both the [Pt$_{1.45}$/Co$_{1.22}$/W$_{0.95}$]$_5$ as well as the [Pt$_{1.45}$/Co$_{1.22}$/W$_{0.4}$]$_5$ yield operational inverter structures, featuring reliable single-step switching, reaching remanence within the clocking window. The lowest results for the strongly FM-coupled [Pt$_{1.45}$/Co$_{1.22}$/W$_{0.4}$]$_5$ stack indicate possible clock fields of ≈ 75 mT, which is comparable to results for Pt/Co/Pt. For inverters featuring small $H_{\mathrm{Ic}}$ values, the possible clock fields show an improvement with values down to ≈ 50 mT for the [Pt$_{1.45}$/Co$_{1.22}$/W$_{0.95}$]$_5$ stack. With an even higher Co content and number of repetitions ($[\mathrm{Pt}_{1.45}/\mathrm{Co}_{1.62}/\mathrm{W}_{0.95}]_7$), the nucleation fields can even be pushed well below the 20 mT mark, as indicated by the hysteresis in Figure 6.6 (b). However, after nucleation, these stacks exhibit multi-domain formation, which must be annihilated at high energy costs, resulting in remanence field levels above 50 mT. The table in Figure 6.6 (d) illustrates a direct comparison between the three selected stacks, including the implanted ion dose and the optimal $H_{\mathrm{clk}}$ values.

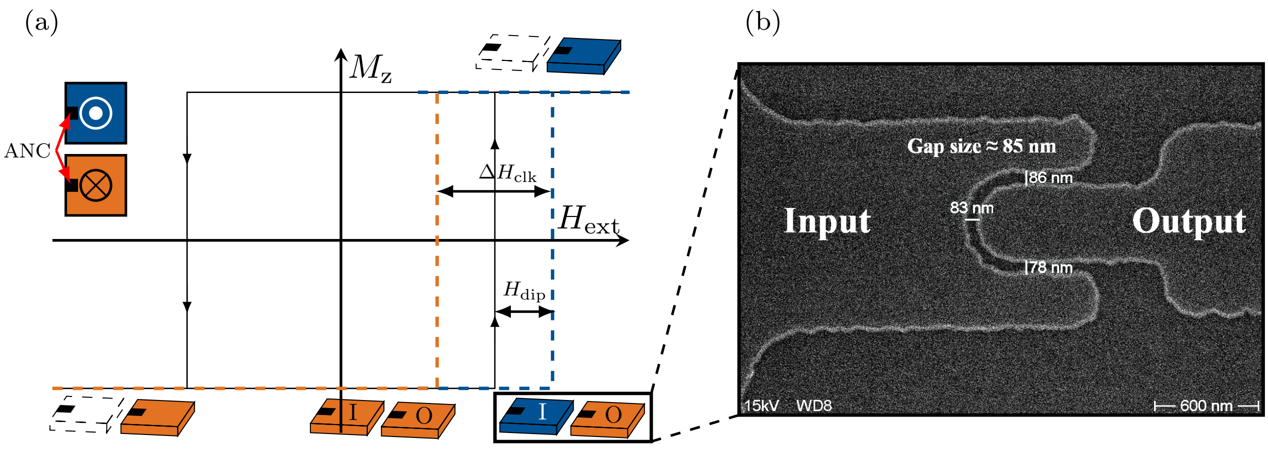

**Figure 6.5** In (a), the working principle of a pNML inverter is sketched using the possible hysteresis loops of the output magnet. Depending on the magnetization direction of the input, switching of the output is either supported (parallel configuration) or suppressed (anti-parallel configuration). The gap between both coercive fields defines the clocking window $\triangle H_{\mathrm{clk}}$. In (b), a scanning electron micrograph of a fork-inverter is displayed.

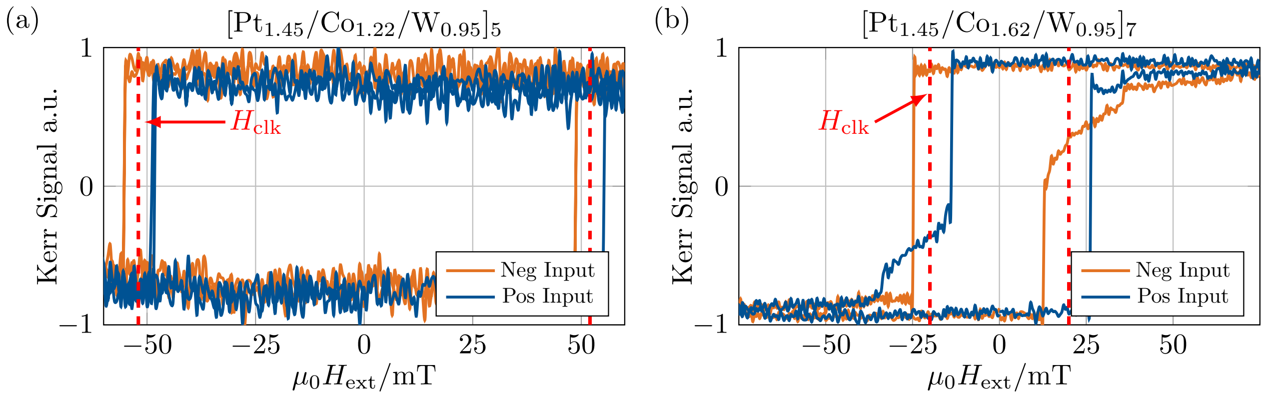

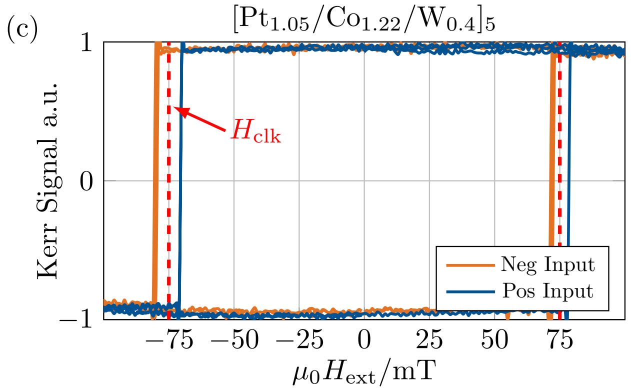

(d)

| Stack Composition | ANC Dose | $H_{\mathrm{clk}}$ | $H_{\mathrm{dip}}$ |
|---|---|---|---|
| $[\mathrm{Pt}_{1.05}/\mathrm{Co}_{1.22}/\mathrm{W}_{0.4}]_5$ | $3.8 \times 10^{13}$ ions/cm$^2$ | 75 mT | ≈ 5.5 mT |
| $[\mathrm{Pt}_{1.45}/\mathrm{Co}_{1.22}/\mathrm{W}_{0.95}]_5$ | $3.8 \times 10^{13}$ ions/cm$^2$ | 51 mT | ≈ 5.5 mT |
| $[\mathrm{Pt}_{1.45}/\mathrm{Co}_{1.62}/\mathrm{W}_{0.95}]_7$ | $3.8 \times 10^{13}$ ions/cm$^2$ | 20 mT | ≈ 9 mT |

**Figure 6.6** In (a)-(c), the hystereses of inverter output magnets are displayed. Depending on the state of the input, the output hysteresis is shifted. The dashed red lines indicate the respective clock fields at quasi-static fields. The Table in (d) depicts information regarding the used $\mathrm{Ga}^+$ dose and measured $H_{\mathrm{dip}}$ coupling fields.

## 6.4 Summary and Evaluation of the Pt/Co/W Material System

Nanomagnets made from different Pt/Co/W multilayers were evaluated as building blocks for perpendicular nanomagnetic logic. SQUID magnetometer measurements of a series of trilayer films revealed significant reductions of saturation magnetization compared to Pt/Co/Pt. This reduction is best explained by a substantial magnetic dead layer $\approx 0.5\,\text{nm}$ in size, which forms at the upper Co/W interface. The evolution of the corresponding perpendicular anisotropy showed a volume contribution comparable to Pt/Co/Pt literature values. However, the $2K_\text{s}$ surface anisotropy was found to be considerably lower, resulting in an in-plane magnetization already above $t_\text{Co} \approx 1.75\,\text{nm}$. Multilayers of Pt/Co/W exhibited weak oscillatory interlayer coupling across the Pt/W spacer which turned antiferromagnetic for the first time at $t_\text{w} \approx 0.5\,\text{nm}$ as shown by the characterized $[\text{Pt}_{1.45}/\text{Co}_{1.22}/\text{W}_\text{x}]_2$ bilayer series. This layer thickness agrees well with the typical form of RKKY coupling. However, dipole-mediated orange-peel effects cannot be excluded.

Local FIB irradiation was used to reduce the interlayer coupling effects on the switching behavior of single domain structures. Furthermore, it could be used to break the reciprocity in dipole-coupled devices. The irradiation effects on the nucleation fields and hysteresis behavior were studied for strongly as well as weakly coupled Pt/Co/W superlattices. By applying the obtained findings, Pt/Co/W based inverters could be demonstrated using both, weakly coupled ($[\text{Pt}_{1.45}/\text{Co}_{1.22}/\text{W}_{0.95}]_5$) and strongly coupled ($[\text{Pt}_{1.05}/\text{Co}_{1.22}/\text{W}_{0.4}]_5$) multilayers. Nevertheless, the achievable coercive fields show no significant reduction compared to Pt/Co/Pt magnets. Moreover, the reduced magnetic moment of the stacks reduces the effectively achievable coupling strength.

In light of the obtained findings and the fact that the oscillatory interlayer coupling raised additional questions regarding the reliability of the reversal process, it was decided not to pursue further studies involving any Pt/Co/HM system.

# 7 Cobalt/Nickel Multilayer Systems

The usage of Cobalt/Nickel multilayers in pNML devices was first proposed by Stuart Parkin during a private conversation with Markus Becherer in the late 2000s. The reasoning behind this proposal was the generally smaller damping constant of Co/Ni ($\approx 0.05$, versus $\approx 0.3$ in Pt/Co) associated with larger DW velocities [241], [242]. In addition to that, Co/Ni has several interesting and appealing properties from a design perspective. Firstly, it consists of two ferromagnetic materials, thus theoretically resulting in higher effective saturation magnetization of the stack and thus higher coupling fields between magnets. Secondly, if we consider the crystal structure of nickel, we find no clear crystalline easy axis. Therefore, the crystalline anisotropy is dominated by the crystal structure of the cobalt layers, which are grown in the (111) direction on top of platinum. Very low effective anisotropies and thus coercivities should be more easily achievable by carefully tuning stack composition (see section 3.7.2 for more information).

First attempts at using Co/Ni multilayers for pNML were carried out by Eichwald et al. in 2012, however, with mixed results at least in terms of reduced coercivities and process engineering [61]. The much higher fabrication requirements compared to Pt/Co, combined with the unsuited fabrication equipment at the time, prohibited the necessary control over the anisotropy landscape. However, this became possible with the new and automated sputtering tool, allowing for higher quality and very reproducible crystal growths. The goals of the renewed Co/Ni project were the realization of sub 20 mT clocking fields at short timescales (a precondition for on-chip clocking) and, for the first time, the collection of relevant statistical data concerning magnet to magnet variations. Furthermore, it would be necessary to validate the working principles of pNML for the case of very low intrinsic anisotropies. This would allow for the formulation of realistic coupling requirements.

The results of this project were presented by Mendisch et al. at the Joint European Magnetic Symposia and the Magnetism and Magnetic Materials Conference in 2019 and published in 2020 [142]. The following chapter presents these works in a revised and extended form incorporating additional statistical results and discussions.

## 7.1 Coercivity Behavior of Co/Ni Magnets

It is important to differentiate between the coercivities measured on film-level and those measured on µm sized single-domain structures. On film level, the magnetization reversal process is mainly carried out via domain expansion and is thus, almost exclusively dependent on the depinning and demagnetizing fields of the material. For single-domain magnets, the reversal process takes place by nucleating and subsequently propagating a DW through the structure ($t_{\text{switch}} \approx t_{\text{nuc}} + t_{\text{prop}}$). For PMA materials, it usually holds that $H_{\text{nuc}} \gg H_{\text{depin}}$, leading to nucleation rather than depinning dominated switching. To show this behavior, the coercive fields of Co/Ni stacks with different effective anisotropies are determined (via LMOKE measurements) for films as well as circular nanomagnets with a diameter of ≈ 0.8 µm. The semi-log plot in Figure 7.1 expresses this differentiation, depending on the effective anisotropy. For $K_{\text{eff}} \geq 1 \times 10^5\,\text{J}\,\text{m}^{-3}$ the coercivity discrepancies amount to more than one order of magnitude. Only for smaller values of $K_{\text{eff}}$ the coercivities start to converge, up to the point where the magnets, with or without ANC, break apart into multiple domains (e.g. the $\text{Ta}_2/\text{Pt}_1[\text{Co}_{0.15}/\text{Ni}_{0.7}]_{\text{x8}}$ stack after $\text{Ga}^+$ ion irradiation or the $\text{Ta}_{15}[\text{Co}_{0.2}/\text{Ni}_{0.4}]_{\text{x5}}$ stack). Significant is the difference in coercivity before and after introducing the ANC. This difference also scales with the anisotropy and defines the ANC process window, within which the introduced defect is the dominant one, thus determining the point of nucleation. After the extensive preliminary coercivity analysis, the best results are obtained for effective anisotropies around $0.5 \times 10^4\,\text{J}\,\text{m}^{-3}$. Higher anisotropies increase not only the coercivity of the *as-grown* magnets but also $H_c$ of the irradiated ones, due to the fact that the anisotropy gradient between the magnet and the ANC (the energy barrier that the DW needs to overcome) also increases. However, further decreasing the anisotropy rapidly closes the window in which the irradiated magnets of a given size still feature single domain behavior in the demagnetized state. However, this empirically found sweet spot is by no means universal, as it critically depends on the used materials and magnetic moment of the stack. Of the two stacks around this spot, the $\text{Ta}_2/\text{Pt}_{1.5}[\text{Co}_{0.2}/\text{Ni}_{0.4}]_{\text{x8}}$ stack showed higher ANC impacts, narrower distributions and a larger magnetic moment. It was therefore selected for further, more detailed time-resolved analyses. Figure 7.2 (a) displays the time evolution of the nucleation fields, determined via time-resolved WMOKE measurements as discussed in section 5.3.3 for an array of 40 nanomagnets. By applying

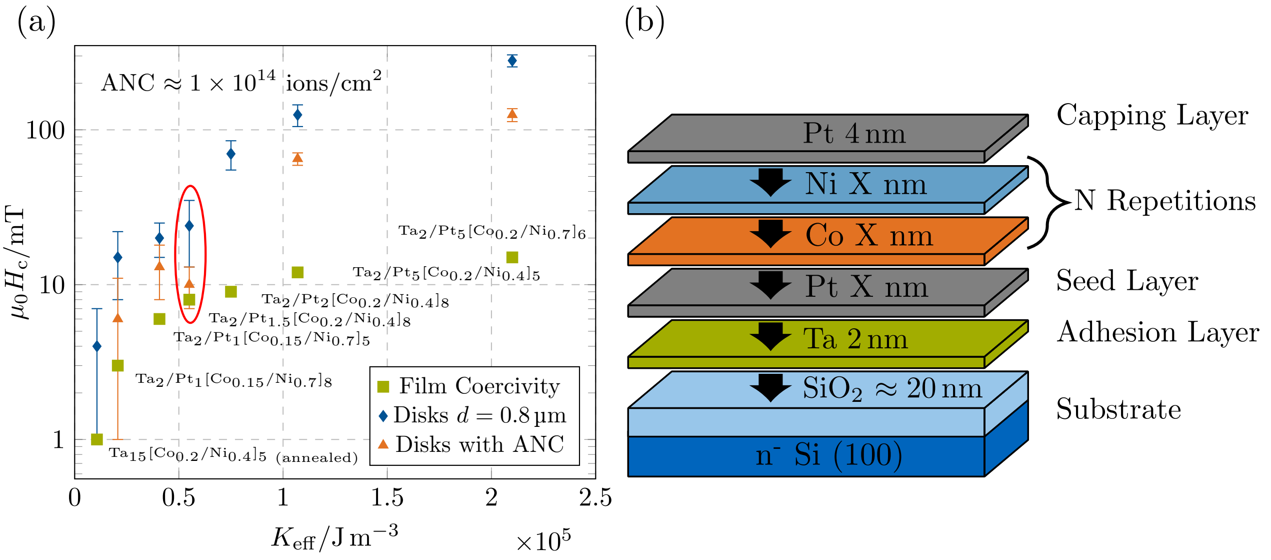

**Figure 7.1** Overview of the switching behavior of selected Co/Ni stacks with increasing $K_{\text{eff}}$. The plot underline the separation of depinning dominated coercivity from nucleation determined switching by showing the coercivity differences between films and single domain nano-structures. The $\text{Ta}_{15}[\text{Co}_{0.2}/\text{Ni}_{0.4}]_{\text{x5}}$ stack was annealed post-deposition at 225 °C for 30 min to increase the PMA. The highlighted stack was used for further experiments. The error bars indicate the respective FWHM SFDs.

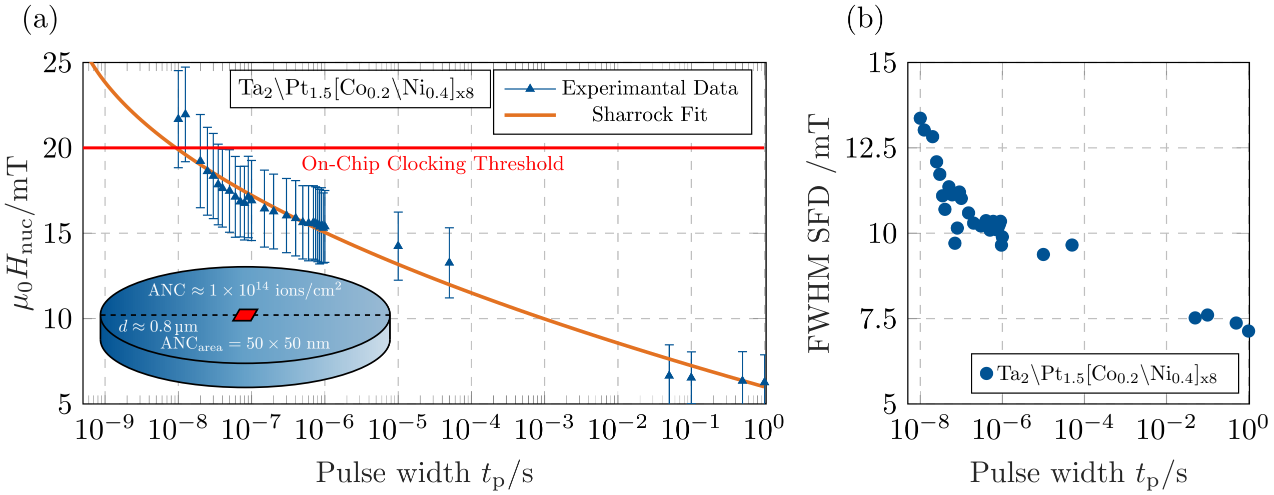

**Figure 7.2** In (a), the measured nucleation fields ($H_{\text{nuc}}$) are plotted as a function of the applied pulse width. The data is supplemented by a fit, facilitating the *Sharrock* formalism (Equation 2.54) with an attempt frequency of 1 GHz, $E_0 = 34.7\,k_{\text{B}}T$ and $H_{\text{s0}} = 28.9\,\text{mT}$. The error bars indicate the standard deviation of the 40 measured nano-disks. The inlet displays a schematic illustration of the DUT with a centered ANC. In (b), the FWHM increase of the switching field distribution is plotted against the pulse width.

the *Sharrock* criteria ($p_{\text{switch}} \geq 0.5$) we can attribute a characteristic switching field to the magnets. By fitting the identically named equation (Equation (2.54)) to the obtained time evolution we can furthermore determine the mean physical properties of the ANCs. With an attempt frequency of 1 GHz, the energy barrier $E_0$ and the anisotorpy field $H_{\text{s0}}$ converge to $E_0 = 34.7 \pm 2.1\,k_{\text{B}}T$ and $H_{\text{s0}} = (28.9 \pm 7.3)\,\text{mT}$, naturally with a high uncertainty. From the anisotropy field it is possible to calculate the effective anisotropy of the ANC area via the simple relation $H_{\text{s0}} \approx H_{\text{anis}} \approx 2K_{\text{eff}}^{\text{nuc}}/M_{\text{s}}$ [102], [111]. Assuming a saturation magnetization according to the stoichometry of the stack ($M_{\text{s}} \approx 8 \times 10^5\,\text{A}\,\text{m}^{-1}$) results in an effect anisotropy of $K_{\text{eff}}^{\text{nuc}} \approx 1.1 \times 10^4\,\text{J}\,\text{m}^{-3}$. The high ANC ion dose of the ($\approx 1 \times 10^{14}$ ions/cm$^2$) suggests an in-plane or superparamagnetic ANC. Thus, it has to be stresses, that $K_{\text{eff}}^{\text{nuc}}$ does not describe the physical anisotorpy landscape of the irradiated area but rather the effective anisotorpy of the rotating SW-particle. The anisotorpy of the ANC, in turn, allows to estimate the mean nucleation volume $V_{\text{nuc}}$ of the magnets via $E_0 \approx K_{\text{eff}}^{\text{nuc}} V_{\text{nuc}}$ [111]. The resulting nucleation volume amounts to $V_{\text{nuc}} \approx 1.24 \times 10^{-23}\,\text{m}^3$, which considering a stack thickness of $\approx 4.8\,\text{nm}$ yields a nucleation area of $A_{\text{nuc}} \approx 2.6 \times 10^{-15}\,\text{m}^2$, almost exactly matching the ANC area of $2.5 \times 10^{-15}\,\text{m}^2$ ($50 \times 50$ nm). Aside from the physical properties, the data clearly shows that while for low clock frequencies (broad pulse widths), the coercivities are well within the range for on-chip clocking, for higher frequencies ($f_{\text{clk}} > 50\,\text{MHz}$) the threshold of $\approx 20\,\text{mT}$ is increasingly exceeded. Notable is also the observed increase in FWHM switching field distribution according to Equation (2.52), recorded for the 40 magnets and displayed in Figure 7.2 (b).

## 7.2 Nucleation Centers & Switching Field Distribution

To reduce the coercivity and control the point of DW nucleation, ANCs are of vital importance for pNML operation. Ion beam irradiation has proven to be an effective way to manipulate the anisotropy of multilayer stacks with extremely high spatial resolution. It is furthermore a widely adopted technology in industry, in contrast to other proposed techniques like nano-indenting or lift-off induced anisotropy gradients [243], [244]. Figure 7.3 (a) displays the ion-dose dependent coercivity development of circular nano-disks with a diameter of 0.8 µm and an ANC area of 50×50 nm (square-shaped). The size of the ANC plays a crucial role in the behavior of the magnet. Irradiation areas smaller than the minimum nucleation volume have no measurable effect, and beyond a certain point, the magnets lose their single domain behavior. The area of 50×50 nm was chosen as it is the proposed width of the nucleation fin (magnet area affected by the input fields) of scaled logic elements and lies within the tolerated area, roughly determined for this stack to be within 20 × 20 and 100 × 100 nm. The coercivity measurements reveal a steep initial decrease of $H_{\mathrm{c,mean}}$ as the PMA decreases, followed by a local recovery associated with the easy axis of the ANC turning in-plane. At doses $> 0.3 \times 10^{14}$ ions/cm$^2$ a stable nucleation regime develops in which the DWs nucleate at the damaged edges of the ANC. This behavior is also observed in high $K_{\mathrm{eff}}$ materials like Pt/Co, thus strengthening the argument that the principles, pNML relies on, in the high $K_{\mathrm{eff}}$ regime still hold for near-threshold anisotropies [82], [119]. Figure 7.3 (b) depicts the detailed SFD data of 1260 nano-disks in the *as-grown* as well as the irradiated state ($1 \times 10^{14}$ ions/cm$^2$). Strictly speaking, the switching fields of SD magnets are not Gaussian distributed, as the magnetization reversal is a thermally assisted process governed by Arrhenius statistics. However, the model nevertheless delivers a useful approximation which is used in the following. The position and width of the corresponding distributions, not only show the in Figure 7.3 (a) displayed shift in $H_{\mathrm{c,mean}}$ (from 24 mT to 9.4 mT) but also a significant narrowing of the overall SFD (in this case, from 11.9 mT to 6.3 mT FWHM). This is presumably caused by the DW nucleation at a well-defined nucleation center rather than nucleation at random defects. Notable is the overlap between both distributions. Here the question arises whether the magnets with the lowest coercivities in the as-grown state are even affected by the irradiation. Via the in section 5.3.2 introduced methods, utilizing automatic image-recognition and tracking, it is possible to resolve this question by plotting the two coercivities for every magnet and determining the resulting coercivity change $\Delta H_{\mathrm{c}}$. This would not be possible just considering the distribution data alone. Figure 7.4 (a) depicts the corresponding individual coercivities with and without ANC plotted against each other. The plot shows, that the bulk of the coercivities is reduced to values around ≈ 9.4 mT. However, there still exist outliers, which are seemingly not or only marginally affected by the irradiation. Particularly interesting, is the irradiation impact $\Delta H_{\mathrm{c}}$ plotted against the as-grown coercivities, depicted in Figure 7.4 (b). This plot, in its essence, displays the transfer-function between the two distributions depicted in 7.3 (b). The linear slope is with ≈ 0.95 very close to 1, validating the decision to assume a normal distribution. We can furthermore attribute an impact uncertainty $\sigma_{\Delta H_{\mathrm{c}}} = (6.2 \pm 2.6)$ mT FWHM to the transfer function, by subtracting the linear slope and determining the residual uncertainty. This impact uncertainty is then approximately equal to the overall SFD

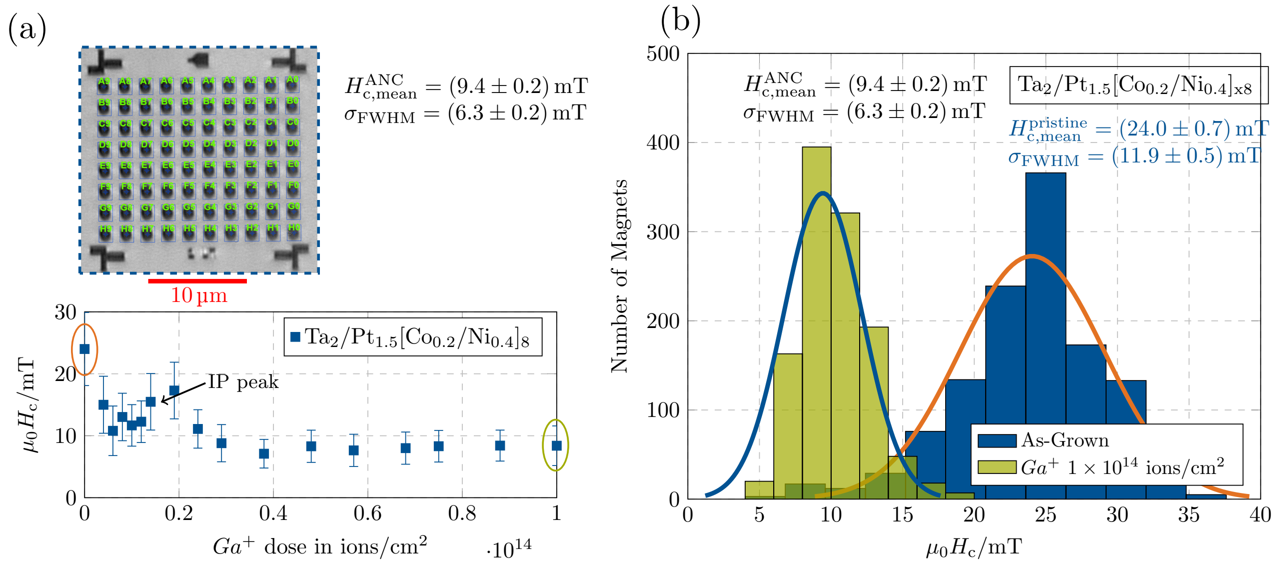

**Figure 7.3** In (a), the Ga$^+$ ion-dose dependent switching fields of circular nano-disks ($d = 0.8$ µm) with centered ANCs (50 × 50 nm) are displayed. The error bars indicate the FWHM of the probability density function based on the data of 100 magnets each. In (b), the switching field distribution histogram of 1260 nano-disks before and after irradiation with a dose of $1 \times 10^{14}$ ions/cm$^2$ is shown.

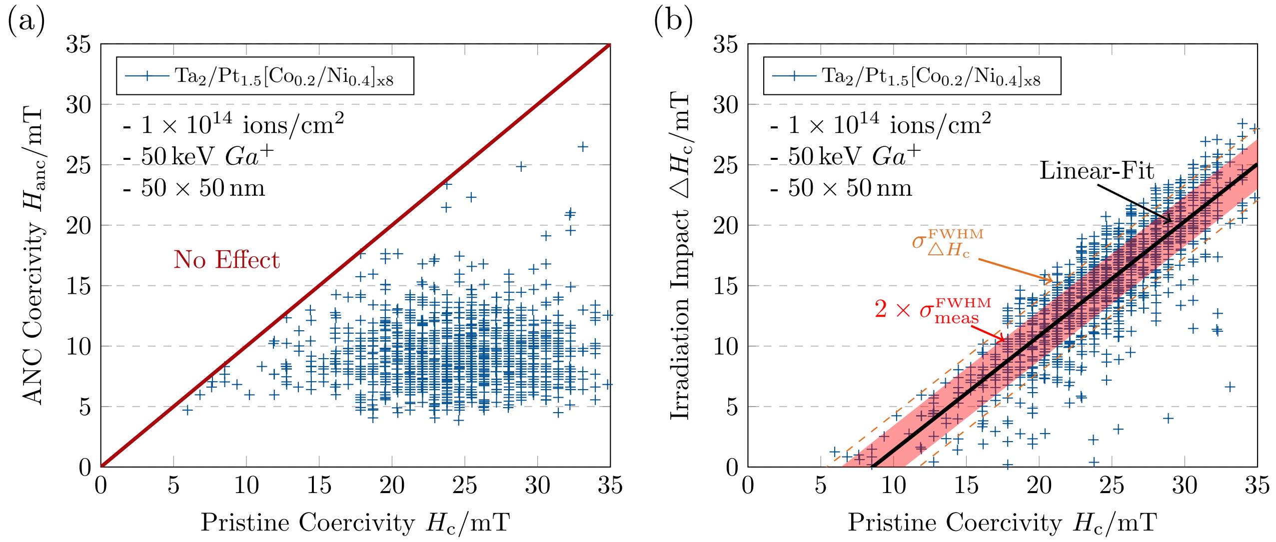

**Figure 7.4** In (a), the coercivities of the 1260 Magnets before irradiation are plotted against the respective coercivities after irradiation. The plot in (b), on the other hand, depicts the the impact of the irradiation ($\Delta H_\mathrm{c} = H_\mathrm{c}^\mathrm{pristine} - H_\mathrm{c}^\mathrm{ANC}$) versus the coercive fields of the pristine magnets.

after irradiation. The question regarding the origins of the residual coercivity variations is essential to further reduce the SFD. Again assuming validity of the Gaussian distribution model, we can use it to develop a simple phenomenological model of the irradiation impact $\Delta H_\mathrm{c}$. The model can be expressed as

$$\Delta H_\mathrm{c} \approx H_\mathrm{c}^\mathrm{pristine} - (H_\mathrm{c}^\mathrm{pristine} - (H_\mathrm{c,mean}^\mathrm{ANC} + \eta))\,, \tag{7.1}$$

with $\Delta H_\mathrm{c}$ as the irradiation effect or in other words, the reduction the coercive field. The variable $H_\mathrm{c}^\mathrm{pristine}$ denotes the mean coercivity of the pristine magnets and $\eta$ describes a probabilistic, normal distributed process $\eta \sim \mathcal{N}(\mu = 0, \sigma_{\Delta H_\mathrm{c}})$. The above described equation, models the residual distribution of the irradiated magnets as variations in the irradiation impact $\Delta H_\mathrm{c}$. In the following, we attempt to deconstruct $\sigma_{\Delta H_\mathrm{c}}$ and assess its individual contributors. To do so, we assume that all variables affecting $\sigma_{\Delta H_\mathrm{c}}$ are themselves normal distributed. This is indeed a crude approximation, however, it allows us to directly write

$$\sqrt{\sigma^2_{\Delta H_\mathrm{c}}} \approx \sqrt{2\sigma^2_{H_\mathrm{meas}} + \sigma^2_{H_\mathrm{shot}} + \sigma^2_{H_\mathrm{demag}} + \sigma^2_{H_\mathrm{anis}}} \approx 6.3\,\mathrm{mT\,FWHM}\,, \tag{7.2}$$

where $\sigma_{H_\mathrm{meas}}$ denotes the uncertainty of the WMOKE setup, experimentally determined to be ≈ 2.1 mT FWHM. The prefactor 2 applies since every magnet is probed twice to measure $\sigma_{\Delta H_\mathrm{c}}$. This measurement error naturally includes the thermal noise component at RT, therefore, it is not listed separately. The cumulative ANC impact distribution caused by $2\sigma_{H_\mathrm{meas}}$ is visualized by the red area in Figure 7.4 (b), meaning that measurement uncertainties cannot explain variations outside this red area.

The shot noise $\sigma_{H_\mathrm{shot}}$ describes contributions from possible ion-current fluctuations during irradiation. However, when comparing the ANC dose of $1 \times 10^{14}$ ions/cm$^2$ with the expected shot noise of the FIB ($< 3 \times 10^{12}$ ions/cm$^2$) we can neglect the contributions from dose variation with high confidence ($\sigma_{H_\mathrm{shot}} \approx 0$). A more complex picture emerges when analyzing the possible contributions from varying ANC positions and the resulting different demagnetizing fields ($\sigma_{H_\mathrm{demag}}$) as well as contributions from intrinsic anisotropy variations $\sigma_{H_\mathrm{anis}}$. Let us first address the SFD contributions arising from different demagnetizing fields. After irradiation, the ANC positions will vary slightly from magnet to magnet due to the limited accuracy and reproducibility of the FIB microscope and the operator. This leads, depending on the severity of these variations, to different stray fields in the ANC area and thus to different switching fields. However, cross-referencing the positional uncertainty with

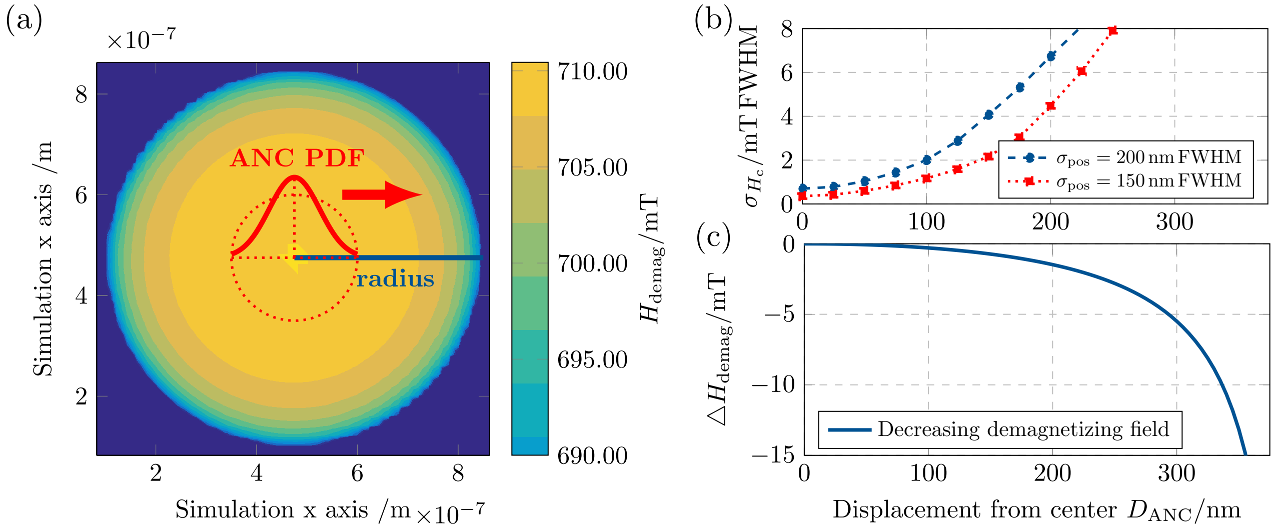

**Figure 7.5** In (a), the absolute demagnetizing fields of a $Ta_2/Pt_{1.5}/[Co_{0.2}/Ni_{0.4}]_{x8}$ nanomagnet with a diameter of 800 nm are shown as a surface plot. The demagnetizing fields are derived from point-dipole calculations using cell size of 5 nm and a saturation magnetization of $M_s \approx 8 \times 10^5\,\mathrm{A\,m^{-1}}$. In (b), the PDF position and width-dependent coercivity uncertainty are shown. Finally, in (c), the radius dependent absolute reduction in demagnetizing field $\Delta_{H_{\text{demag}}}$ is displayed.

the local demagnetizing fields derived from point-dipole calculations makes it possible to model the resulting contributions to the SFDs and give a worst-case assessment. Since the magnet and thus the demagnetizing field is circular, we use this radial symmetry to model the ANC position with a simple one-dimensional probability density function (PDF). A surface plot, showing the calculated demagnetizing fields of a Co/Ni nanomagnet ($Ta_2/Pt_{1.5}/[Co_{0.2}/Ni_{0.4}]_{x8}$) with a diameter of 800 nm is shown in Figure 7.5 (a). The used point-dipole calculations use a cell-size of 5 nm and a saturation magnetization of $M_s \approx 8 \times 10^5\,\mathrm{A\,m^{-1}}$.

The centered PDF of the ANC position is shown in red, indicating the width and the position of a potential ANC distribution. The first positional uncertainty arises from a systematic FIB alignment error during fabrication. However, since all magnets are irradiated with the same alignment, we do not need to consider this error in calculating the width of the probability density function (in first approximation only, not considering a possible angle error). The error nevertheless defines the center position of the distribution within the magnets. Figure 7.5 (c) depicts the radius-dependent absolute reduction of the demagnetizing fields from the center along the radius line drawn in Figure 7.5 (a). Considering both plots, we find that, moving outward from the center, the demagnetizing fields, up to displacements of ≈ 250 nm fall off only marginally. The second uncertainty, defining the width of the PDF, is the re-positioning error of the FIB stage, which is assumed to be between 100 nm and 200 nm FWHM. Using this data we can now calculate $\sigma_{H_{\text{demag}}}$ for probability density functions with different center positions and widths. Figure 7.5 (b) depicts the resulting $\sigma_{H_{\text{demag}}}$ values for PDFs with widths of 150 nm and 200 nm FWHM, moved outwards from the center, along the line depicted in Figure 7.5 (a). From the calculations follows, that, assuming perfect FIB alignment, the contribution of $\sigma_{H_{\text{demag}}}$ would vanish within the noise floor, set by $2\sigma_{H_{\text{meas}}}$. However, alignment error > 300 nm would on the other hand, considering the case of a 200 nm wide PDF, cause many ANCs to miss the magnet completely, something that is clearly not the case. However, this narrows $\sigma_{H_{\text{demag}}}$ down to value only between ≈ 1.5 mT and possibly ≈ 8 mT. The positional uncertainty of the ANC could, therefore, completely explain the residual SFD after irradiation or just have an insignificant effect. This is, of course, not a satisfying answer. However, we can try to narrow the range by testing the predictions that follow from assuming both extremes. Lets first assume a very large $\sigma_{H_{\text{demag}}}$. This would mean that magnets with constant demagnetizing fields should exhibit a reduced SFD after irradiation. This was tested using quasi-one-dimensional test structures (200 nm wide Co/Ni nano-wires).

The structures themselves exhibit variations in the demagnetizing fields only along their width. Irradiating 50 nm wide and 300 nm long ANCs, spanning across the entire width of the nano-wire, creates a well-defined nucleation area with high reproducibility. Nevertheless, the measured SFD of the quasi-one-dimensional magnets did not differ significantly from those measured for circular magnets on the same sample. Therefore, another approach involved the reduction of the overall ANC position uncertainty to values below ≈ 100 nm FWHM by an extensive manual on-site alignment. The irradiated circular magnets, however, showed only a marginal narrowing of the SFD, thus indicating that $\sigma_{H_\mathrm{demag}}$ in the case of the conducted study is not the dominant contribution to $\sigma_{\Delta H_\mathrm{c}}$. However, the contribution of $\sigma_{H_\mathrm{demag}}$ should increase with a wider spread of the ANC center positions. To realize this, the SFD is determined across different irradiation runs, each with a different alignment error. Despite these measures, the resulting combined SFD showed no significant increase. To summarize, there is no definitive answer regarding the significance of $\sigma_{H_\mathrm{demag}}$. Calculations predict a potentially substantial contribution. However, our experiments, designed to reveal changes in $\sigma_{H_\mathrm{demag}}$, did not reveal significant effects. This can have two causes, either the artificially introduced changes in $\sigma_{H_\mathrm{demag}}$ are too small compared to the overall $\sigma_{H_\mathrm{demag}}$, or, which is more likely, $\sigma_{H_\mathrm{demag}}$ in general plays a secondary role compared to the intrinsic anisotropy variants of the Co/Ni magnet $\sigma_{H_\mathrm{anis}}$.
The mechanisms contributing to the remaining SFD are, however, at this point not sufficiently understood and should, therefore, be the focus of future investigations. This understanding is of tremendous importance, as the SFD is the defining parameter for error-free operation and de-facto defines the coupling requirements.

## 7.3 Inverter Scaling

To validate the above-obtained findings, the output magnets of pNML fork-inverters were irradiated with a dose of $\approx 1 \times 10^{14}$ ions/cm$^2$ and the correct functionality of the devices checked accordingly. Figure 7.6 (a) illustrates the coupling strength $H_\mathrm{dip}$ of the inverters, scaling with the total gap size of the fork-input depicted in Figure 7.6 (b). The coupling strength is defined as half of the total coercivity

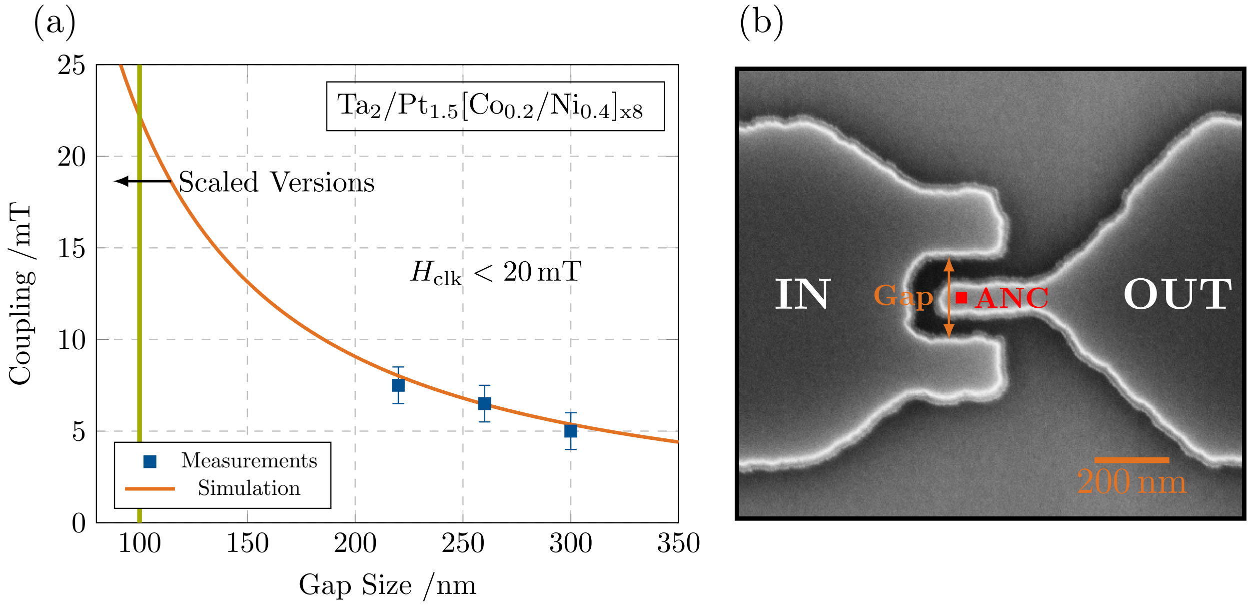

**Figure 7.6** In (a), the measured inverter coupling strength ($H_\mathrm{dip}$) is shown, plotted against the gap width of different fork structures made from a $\mathrm{Ta_2/Pt_{1.5}[Co_{0.2}/Ni_{0.4}]_{x8}}$ stack. Additionally, point-dipole simulation data is shown to depict the expected scaling behavior beyond 200 nm gap size. In (b), a scanning electron micrograph of a typical fork-inverter is displayed. The positions of in- and output are marked, respectively.

shift between a parallel and an anti-parallel input state. Point-dipole simulations, taking into account the geometry of the inverter, were conducted and are compared to the experimental data, resulting in good agreement between simulation and experiment (of course with limited significance). The fin-width of the output magnet measures 100 nm (twice the size of the ANC) to ensure a sufficiently large target area for the aligned focused ion beam. State of the art fabrication processes, however, would allow the gap-size to be pushed well below 100 nm.

## 7.4 Summary

Co/Ni multilayer stacks with near single-domain threshold anisotropies were investigated and optimized to achieve relevant clock-field reductions in operational pNML logic devices. The target of sub-threshold (20 mT) nucleation fields was met down to pulse widths of $\approx$ 20 ns translating to achievable frequencies of up to $\approx$ 50 MHz. These results were achieved by tailoring the anisotropy of the stacks to the absolute limit while preserving sufficient magnetic moments for reliable coupling. Additional investigations were made, targeting the switching field distributions of low anisotropy Co/Ni magnets. Thereby, special attention was given to the effects of local $Ga^+$ ion irradiation in these low anisotropy systems, shaping the coercivity as well as achieving significant reductions in the absolute SFD. The origins of the residual SFD after ANC irradiation could not be resolved definitively, although high intrinsic anisotropy variations were determined to be the most likely cause. The obtained findings give insight into the magnetization reversal of partially irradiated nanomagnets and mark a significant step forward in terms of coercivity reductions for pNML devices. However, the findings also underline the need for further material optimizations, targeting the significant switching field distributions.

# 8 Ta/CoFeB/MgO Trilayer Systems

Magnetic nanostructures based on Cobalt-Iron-Boron/Magnesium-oxide (CoFeB/MgO) thin films, with and without perpendicular magnetic anisotropy (PMA), already play a vital role in many emerging technologies, from magnetic tunnel-junction based sensors over non-volatile storage technologies, towards domain wall and nanomagnetic logic applications [131], [183], [245]–[247]. As already established, especially pNML necessitates precise control of the magnetic energy landscape to nucleate, propagate and pin/depin domain walls — a level of control that remains a significant challenge in CoFeB/MgO films [142], [153]. Up to this point, studies on the irradiation effects on CoFeB/MgO have mainly been restricted to film level investigations and light ($He^+$) ions [248]–[250]. In this section, we investigate the usage of heavier $Ga^+$ ions in an attempt to create artificial nucleation centers (ANC) in Ta/CoFeB/MgO nanomagnets with PMA, employing localized ion irradiation.

As a first step, the dose-dependent irradiation effects were evaluated on film level, probing material parameter, and domain configurations before the focus was shifted towards the irradiation of nanostructures and time-domain measurements. A general analysis of the coercive fields, switching field distributions, and domain wall velocities was conducted in this context. This was done before extensive time-domain studies and irradiation studies could be started.

First results, addressing the general behavior of Ta/CoFeB/MgO nanomagnets, were presented by Riente et al. at the International Magnetism and Magnetic Materials Conference in 2020 as part of a wider study analyzing the potential of Ta/CoFeB/MgO for pNML [131]. However, the main study addressing ion-beam irradiation and control over DW nucleation lasted until early 2021 and was published afterward [143]. The following chapter presents these works in a combined and revised form.

## 8.1 Areal Irradiation and Static Measurements

To understand and interpret the irradiation-dependent changes in the domain wall dynamics of nanostructures, we first analyze the irradiation effects on film level. This allows probing the essential material parameter ($M_\mathrm{s}$ and $K_\mathrm{eff}$) via comparatively simple though error-prone magnetometer measurements. The material parameters are extracted from SQUID and VSM-magnetometer loops. $K_\mathrm{eff}$ is thereby approximated from the hard-axis loops via the area method [90]. The uniaxial anisotropy constant $K_\mathrm{u}$, necessary for the micromagnetic simulations is calculated as $K_\mathrm{u} = K_\mathrm{eff} + \frac{1}{2}\mu_0 M_\mathrm{s}^2$. Figure 8.1 depicts the irradiation-induced changes in $M_\mathrm{s}$ as well as $K_\mathrm{eff}$ with increasing ion dose, determined from the magnetometer data. Similar to reports on the He$^+$ irradiation of Ta/CoFeB/MgO films, a decrease in saturation magnetization accompanied by an increase in effective anisotropy is observed [248], [249]. Figure 8.2, on the other hand, depicts the irradiation-dependent static coercivities ($H_\mathrm{c}$) of circular nano-dots ($d = 1\,\mu\mathrm{m}$) and respective (dose matched) domain images of irradiated films. The changes in the coercivities and domain sizes enable a more detailed though qualitative assessment of the shifts in the anisotropy landscape as both are closely related to $K_\mathrm{eff}$. At small film thicknesses, the domain size ($D_\mathrm{size}$) can be approximated by $D_\mathrm{size} \approx t_\mathrm{film} e^{\pi D_0 / t_\mathrm{film}}$ (where the dipolar lengths $D_0 = \frac{\pi\sqrt{A_\mathrm{ex} K_\mathrm{eff}}}{\mu_0 M_\mathrm{s}^2}$) [104], [108]. The data points in Figure 8.2 display the center of the respective switching field distribution (SFD), with the error bars indicating the full width at half maximum (FWHM). Thereby, 80 magnets are probed for each ion dose. The magnets are placed $1\,\mu\mathrm{m}$ apart to inhibit any relevant dipolar interaction between the magnets obscuring the measurements. The coercivities and domain sizes initially increase for low and medium doses but start to fall off at doses higher than $\approx 3.5 \times 10^{13}\,\mathrm{ions/cm^2}$ with the domain size dropping below the resolution limit at a dose of $\approx 8 \times 10^{13}\,\mathrm{ions/cm^2}$. The magnets also cross the single-domain threshold near this point. Although the reduced coercivities could potentially be the result of an increased defect density (this would, however, not explain the initial increase in $H_\mathrm{c}$), the shrinking domain sizes strongly indicate a loss of the perpendicular magnetic anisotropy, which leads to reduced coercivities. The decrease in both the domains sizes and coercivities strongly indicates a degradation of the PMA starting at doses $> 3.5 \times 10^{13}\,\mathrm{ions/cm^2}$. It has to be noted that the apparent decrease in $K_\mathrm{eff}$ above $\approx 3.5 \times 10^{13}\,\mathrm{ions/cm^2}$

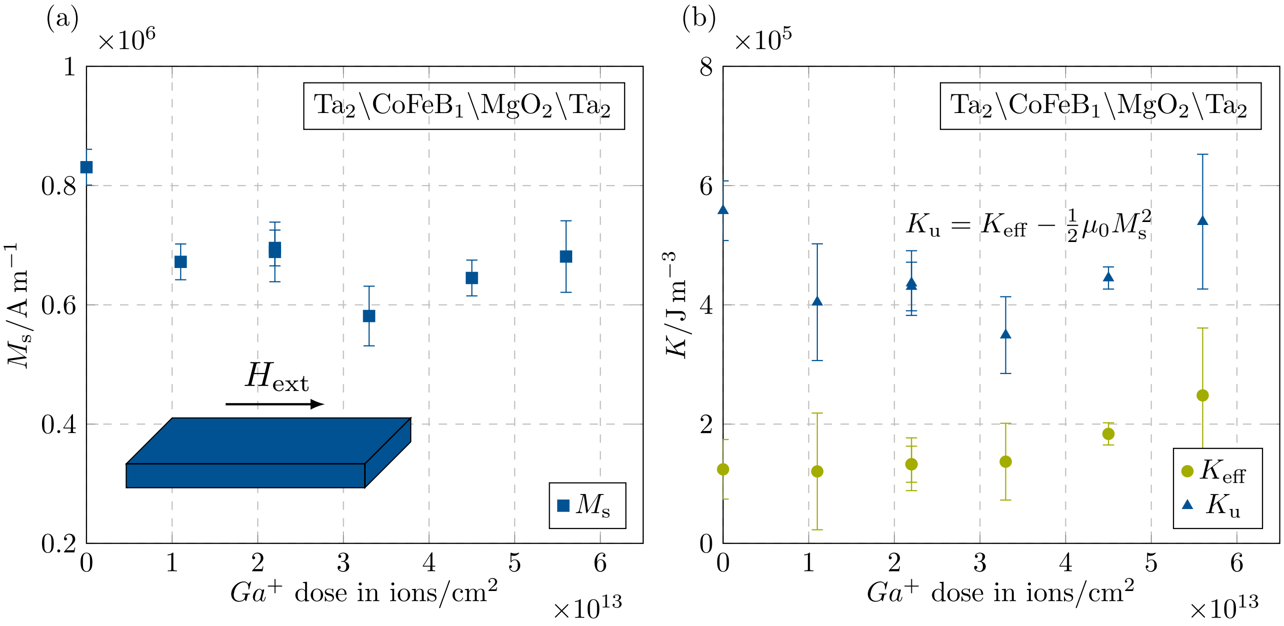

**Figure 8.1** The plot in (a), depicts the measured saturation magnetizations $M_\mathrm{s}$ of a Ta$_2$/CoFeB$_1$/MgO$_2$/Ta$_2$ repeatedly irradiated with Ga$^+$ ions. In (b), the effective anisotropy $K_\mathrm{eff}$ of the film, together with the calculated uniaxial anisotropy term $K_\mathrm{u} = K_\mathrm{eff} - \frac{1}{2}\mu_0 M_\mathrm{s}^2$ is plotted versus the applied ion dose. The anisotropies are determined from hard-axis loops via the area method (introduced in section 5.1).

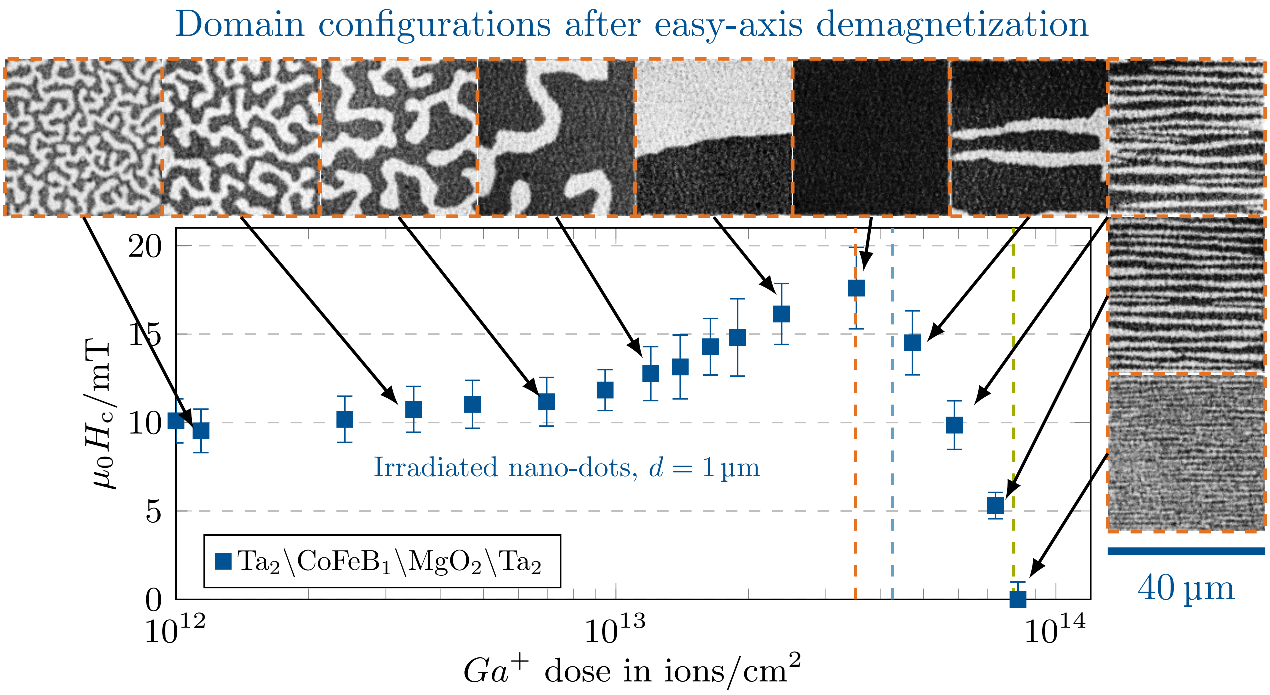

**Figure 8.2** The image shows the $Ga^+$ dose-dependent coercivity evolution of circular $Ta_2/CoFeB_1/MgO_2$ nanomagnets ($d = 1\,\mu m$). The error bars to the data points indicate the raw FWHM switching field distribution of 80 magnets each (see Appendix 9.4 for the respective histograms). The surrounding domain images display dose correlated domain patterns imaged on the same film after irradiation and easy-axis demagnetization (via a damped oscillation field). The colored dashed lines serve as markers, indicating doses used in a more detailed analysis.

could not be replicated via the corresponding magnetometer measurements. However, this fact might be explained by the macroscopic nature of the magnetometer measurements, complicating the detection of small changes in the anisotropy landscape. Explaining the non-monotonic evolution of $K_{eff}$ is difficult without a detailed stoichiometric analysis, and therefore no comprehensive explanation can be given. However, as with $He^+$ irradiation [248], [251], the behavior might be explained by the respective atomic weights of the different elements inside the stack, giving the $Ga^+$ ions a much larger probability to interact with the heavy Ta rather than with the comparatively light Fe, Co, or O atoms. Since Tantalum is known for its large magnetic dead layer in contact with ferromagnets, we assume intermixing at the Ta/CoFeB interface to be the dominant cause for the decrease in $M_s$[248], [251]. A possible explanation for the non-monotonicity in $K_{eff}$ could be that due to this reduced interaction probability, the damage to the CoFeB/MgO interface and thus $K_u$ only becomes relevant at much higher doses [248], [251]. Closely related to this is the likely accumulation of Tantalum atoms at the CoFeB/MgO interface, also strongly affecting the anisotropy [191]. An interesting observation related to the anisotropy decrease is the formation of highly ordered stripe domains at high ion doses, indicating changes in more than the primary material parameter. This is in line with reports on the increase of the interfacial Dzyaloshinskii-Moriya interaction upon the irradiation of Ta/CoFeB/MgO films [250]. Aside from irradiation-dependent coercivities and domain patterns, it is also interesting to determine the switching field distribution (SFD). As an amorphous or purely crystalline material, CoFeB should be less affected by grain-induced anisotropy variations and thus feature narrower SFDs. For the quasi-static case, the switching field distribution (SFD) is calculated from a dataset of 1600 circular $Ta_2/CoFeB_1/MgO_2$ nano-magnets ($d = 1\,\mu m$) resulting in a mean coercivity of $H_{c,mean} = (8.67 \pm 0.06)\,mT$, and a narrow FWHM SFD of only $\sigma_{FWHM} = (2.87 \pm 0.10)\,mT$. This is a significant reduction in the absolute as well as relative SFD compared to the recently evaluated low anisotropy Co/Ni multilayers [142]. The most plausible explanation for this is the amorphous

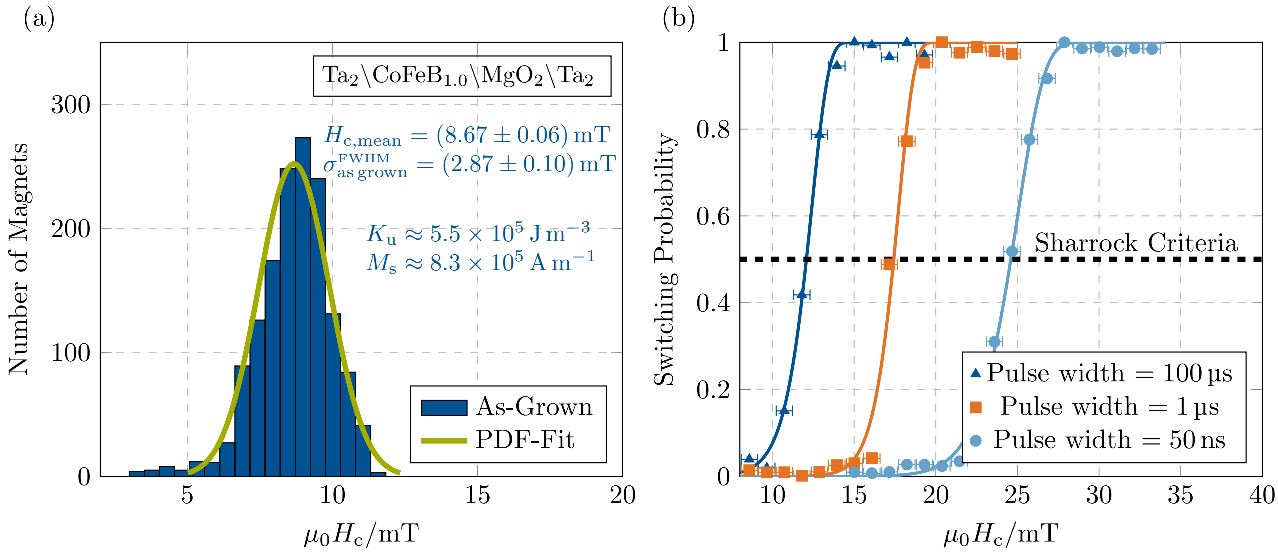

**Figure 8.3** In (a), the switching field distribution at quasi static fields of 1600 Ta/CoFeB/MgO nanomagnets with a diameter of 1 µm is shown. The distribution shows a very narrow width of $\sigma^{\mathrm{FWHM}}_{\mathrm{as\,grown}} = (2.87 \pm 0.10)\,\mathrm{mT}$ The plot in (b) depicts the measured, field-dependent, nucleation probabilities of one of the nanomagnet for different pulse widths.

structure of CoFeB layers annealed at low temperatures. However, etch-damaged induced anisotropy lowering at the edges of the magnets could also have a significant effect.

## 8.2 Controlling the Magnetization Reversal

We have already shown that the coercivities of the magnets can be effectively tailored by adjusting the ion dose. However, static measurements only provide limited insight into the reversal mechanisms and are not suited to derive relevant conclusions. Therefore, we attempt a characterization of the irradiation-dependent reversal process by probing the time-dependent magnetization reversal. For this purpose, we provide a sample base of at least 40 magnets per data point, reducing the effects of statistical outliers. Contrary to the distribution of the demagnetizing fields, DWs in CoFeB/MgO nano-magnets usually nucleate at the edges of the nanostructures due to an etch-damage-induced lowering of $K_{\mathrm{eff}}$ [252], [253]. To validate this assumption for the test structures, 20 ns long magnetic field pulses are used to nucleate DWs in circular nano-disks with a diameter of 2.5 µm with the goal to locate the nucleation sights via repeated differential WMOKE imaging. Figure 8.4 (a) shows a single WMOKE image of the domain configuration with 2 nucleation sites after a 20 ns pulse. Figure 8.4 (b) on the other hand displays the combined differential WMOKE images of ten different disks with a total of 1000 superimposed images to qualitatively show the local nucleation probability. Bright areas thereby indicate an increased DW nucleation probability. The image indicates the accumulation of nucleation events at the edges of the disks, while an inhomogeneity in the applied on-chip fields most likely explains the asymmetry towards the right side. As a sanity check, Figure 8.4 (c) depicts a combined WMOKE image without applying magnetic field pulse. The conformation of nucleation from the edges has severe implications. Instinctively, one would expect the nucleation to occur at points with strong demagnetizing fields, i.e., the center of the magnet. However, the demagnetizing fields are lowest at the edges, leading to the conclusion that the reduction in $K_{\mathrm{eff}}$ must be significantly larger than the anisotropy variations in the center of the magnets. Furthermore, the question arises, whether the DW nucleation occurs via coherent rotation according to the *Stoner–Wohlfarth* model or by depinning from an area with easy-plane anisotropy [102], [115]. This can be resolved by considering the time evolution of both processes. The rotation fields scale over time according to

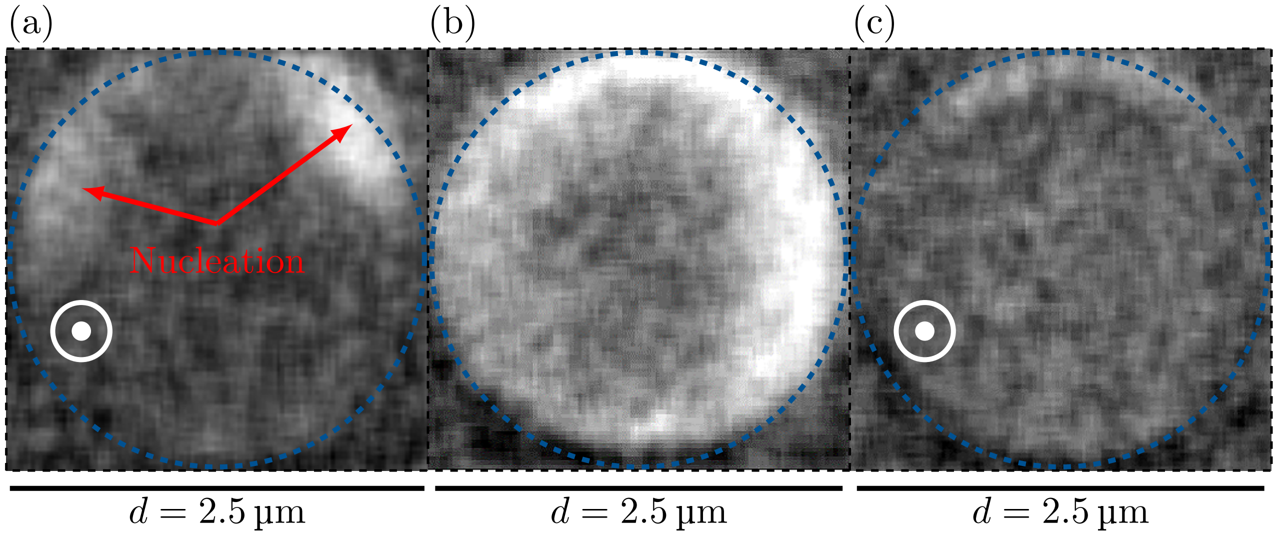

**Figure 8.4** In (a), a differential WMOKE image showing two nucleation events after a 20 ns long magnetic field pulse is depicted. The image in (b) shows 1000 superimposed differential WMOKE images of the nucleation events inside a 2.5 µm wide nano-dot. The areas of increased brightness indicate higher nucleation probabilities. Nucleation is achieved using 20 ns long pulses without consecutive propagation pulses. Finally, the image in (c) shows the WMOKE without a magnetic field pulse applied as a sanity check.

the well established *Sharrock* formalism based on an Arrhenius switching model of a *Stoner–Wohlfarth* particle and can be expressed by

$$H_{\mathrm{nuc}} = H_{\mathrm{s0}} \left\{ 1 - \left[ \frac{k_{\mathrm{B}}T}{E_0} \ln \left( \frac{f_0 t_{\mathrm{p}}}{\ln(2)} \right) \right]^{\frac{1}{2}} \right\} , \tag{8.1}$$

where $H_{\mathrm{s0}}$ is the switching field at 0 K, $f_0$ is the attempt frequency ($\approx 1 \times 10^9$ Hz), and $E_0$ is the energy barrier without applied field [102], [111], [116]. In contrast, the time necessary for a DW to overcome the anisotropy gradient and depin can be derived from the related *Néel–Brown* theory and scales according to

$$\tau = f_0^{-1} \exp \left[ \frac{M_{\mathrm{s}} V_{\mathrm{a}}}{k_{\mathrm{B}}T} (H_{\mathrm{d}} - H) \right] , \tag{8.2}$$

with $V_{\mathrm{a}}$ as the activation volume and $H_{\mathrm{d}}$ as the depinning field at 0 K [113]–[115]. By characterizing the switching fields over a wide range of different timescales (pulse widths) and comparing the evolution to the models in Equation (2.54) and Equation (8.2), it is possible to gather detailed information about the switching mechanisms. Figure 8.5 displays the pulse-width dependent nucleation fields of the circular nano-dots with a diameter of 1 µm. The measurements cover timescales ranging from the quasi-static case down to 20 ns. The data points resemble the center of the distribution, with the error bars again displaying the FWHM. The nucleation field $H_{\mathrm{nuc}}$ is furthermore defined according to the *Sharrock* formalism, as the field with a switching probability $p_{\mathrm{nuc}} \geq 50\,\%$. Figure 8.3 (b) shows a series of exemplary nucleation probability measurements for different pulse widths with the *Sharrock* criteria indicated as a dashed line. The plot furthermore depicts corresponding fits according to the Arrhenius switching model with the probability $p_{\mathrm{nuc}} = 1 - \exp(\frac{-t_{\mathrm{p}}}{\tau_{\mathrm{nuc}}})$, with $\tau_{\mathrm{nuc}}$ as the inverse of the nucleation rate [116].

### 8.2.1 Nucleation by Coherent Rotation

We first consider the pristine magnets and compare the data to the aforementioned nucleation and depinning dominated models. The nucleation fields show good agreement with the numerical

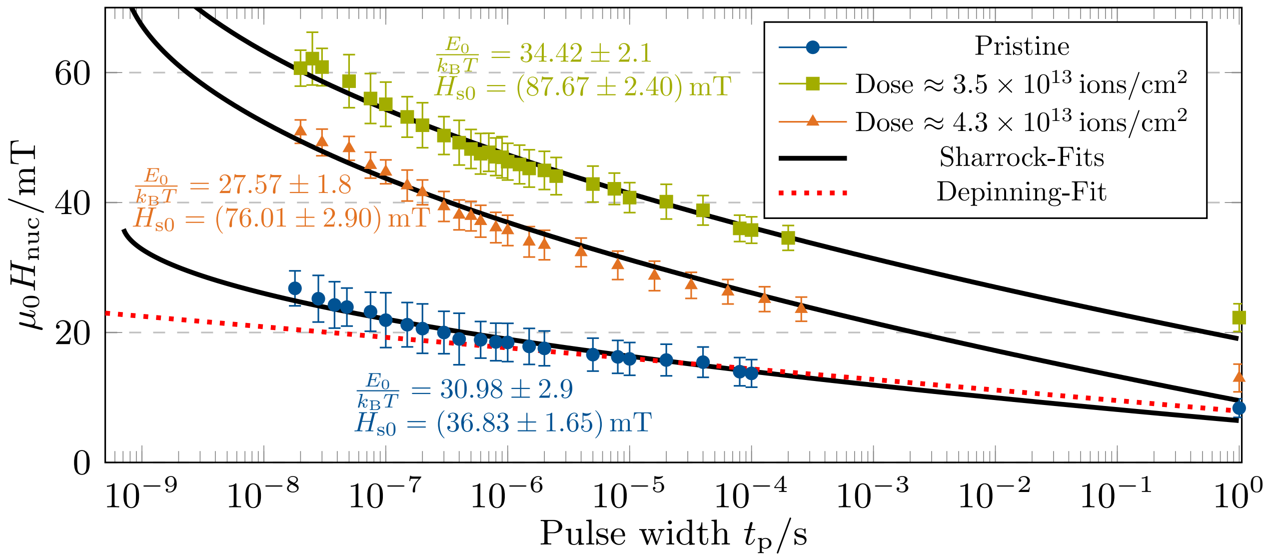

**Figure 8.5** Calculated nucleation fields ($H_{\mathrm{nuc}}$) depending on the applied pulse width. The individual data points display the center of the SFDs with the error bars displaying the FWHM. The corresponding *Sharrock* fits are illustrated as black lines. A fit, assuming depinning mediated nucleation according to Equation (8.2) for the pristine magnets, is illustrated in red.

fits according to the *Sharrock* equation, displayed as black lines; the fitting parameters converge to $H_{\mathrm{s0}} = (36.83 \pm 1.65)\,\mathrm{mT}$ and $\frac{E_0}{k_{\mathrm{B}}T} = (30.98 \pm 2.9)$. Additionally, we attempt to fit Equation (8.2) analytically by minimizing its cumulative error-function utilizing a linearized least-squares problem. However, an acceptable solution (displayed as a dotted line) is only obtained excluding pulse widths $< 1\,\mu\mathrm{s}$, thus arguing against depinning as the primary DW nucleation mechanism, at least for very short timescales. Interestingly, however, at long time scales ($> 10\,\mu\mathrm{s}$), depinning from the nucleation sites could very well be the limiting factor, thus explaining the apparent underestimation of the *Sharrock* fits at quasi-static fields. The question now arises whether $\mathrm{Ga}^+$ irradiation not only increases the effective anisotropy of the core of the disk but whether its effect on the pre-damaged edges is different. Therefore, Figure 8.5 also displays the time evolution of nano-disks homogeneously irradiated with a dose of $3.5 \times 10^{13}$ ions/cm$^2$ and $4.3 \times 10^{13}$ ions/cm$^2$. The doses are chosen to probe the peak of the static coercivity increase as well as a position within the downward slope. For better illustration, the doses are marked, in their respective colors, as dashed lines in Figure 8.2. The slopes, again, indicate nucleation by coherent rotation as the dominant mechanism. From the corresponding *Sharrock* fits, we derive the energy barriers to be $\frac{E_0}{k_{\mathrm{B}}T} = (34.42 \pm 2.1)$ and $\frac{E_0}{k_{\mathrm{B}}T} = (27.57 \pm 1.8)$, respectively. The fields at which these barriers become zero are determined to be $H_{\mathrm{s0}} = (87.67 \pm 2.40)\,\mathrm{mT}$ and $H_{\mathrm{s0}} = (76.01 \pm 2.90)\,\mathrm{mT}$. The energy barrier can be roughly modeled as $E_0 \approx K_{\mathrm{eff}}^{\mathrm{nuc}} V_{\mathrm{nuc}}$ with $V_{\mathrm{nuc}}$ as the nucleation volume and $K_{\mathrm{eff}}^{\mathrm{nuc}}$ as the anisotropy of the rotating volume or grain [111]. The nucleation field at 0 K, on the other hand, is equal to the anisotropy field $H_{\mathrm{anis}} \approx 2K_{\mathrm{eff}}^{\mathrm{nuc}}/M_{\mathrm{s}}$ [102], [111]. Assuming $M_{\mathrm{s}}$ values comparable to those measured for similar ion doses on films allows approximating the effective anisotropy and the critical size of the volume starting the magnetization reversal. Table 8.1 displays the calculated values for $K_{\mathrm{eff}}^{\mathrm{nuc}}$ and $V_{\mathrm{nuc}}$ assuming a constant saturation magnetization of $\approx 6.5 \times 10^5\,\mathrm{A\,m^{-1}}$ for the irradiated magnets. The calculated effective anisotropies of the critical volumes are roughly one order of magnitude smaller than the values obtained for the respective films. Furthermore, the irradiation-induced changes agree well with the in Figure 8.2 displayed evolution in coercivities and domain sizes. Next to $K_{\mathrm{eff}}$, it is also possible to approximate the uniaxial anisotropy components $K_{\mathrm{u}}$ of the nucleation sites and their evolution ($K_{\mathrm{u}} = K_{\mathrm{eff}} + \frac{1}{2}\mu_0 M_{\mathrm{s}}^2$). While for the pristine magnets, $K_{\mathrm{u}}$ amounts to $\approx 4.4 \times 10^5\,\mathrm{J\,m^{-3}}$ it drops to $\approx 3 \times 10^5\,\mathrm{J\,m^{-3}}$ and $\approx 2.9 \times 10^5\,\mathrm{J\,m^{-3}}$ for the irradiated magnets. This strengthens the argument of a simultaneous decrease in $M_{\mathrm{s}}$ and $K_{\mathrm{u}}$, still leading to a combined increase in $K_{\mathrm{eff}}$. Defects introduced during irradiation cannot explain

**Table 8.1** Saturation magnetization $M_s$, anisotropy of the nucleation volume $K_{\mathrm{nuc}}^{\mathrm{nuc}}$, and nucleation volume $V_{\mathrm{nuc}}$, calculated from the respective *Sharrock* fits of pristine and irradiated magnets.

| Dose in ions/cm$^2$ | $M_s$ /A m$^{-1}$ | $K_{\mathrm{eff}}^{\mathrm{nuc}}$ /J m$^{-3}$ [c] | $V_{\mathrm{nuc}}$ /m$^3$ [c] |
|---|---|---|---|
| pristine | $8.3 \times 10^5$ [a] | $1.5 \times 10^4$ | $8.4 \times 10^{-24}$ |
| $3.5 \times 10^{13}$ | $\approx 6.5 \times 10^5$ [b] | $\approx 2.9 \times 10^4$ | $\approx 5.0 \times 10^{-24}$ |
| $4.3 \times 10^{13}$ | $\approx 6.5 \times 10^5$ [b] | $\approx 2.5 \times 10^4$ | $\approx 4.6 \times 10^{-24}$ |

[a] Data taken from Figure 8.1

[b] Approximated from the magnetometer measurements in Figure 8.1

[c] $K_{\mathrm{eff}}^{\mathrm{nuc}} \approx 0.5 H_{s0} M_s$, $V_{\mathrm{nuc}} \approx E_0 / K_{\mathrm{eff}}^{\mathrm{nuc}}$

the measured increase in $K_{\mathrm{eff}}^{\mathrm{nuc}}$. The nucleation volumes, on the other hand, seemingly decrease upon irradiation, thus partially mitigating the effects of the increasing anisotropy on the nucleation fields. Assuming a square-shaped volume allows assigning a characteristic length $l_{\mathrm{nuc}}$ to the effective nucleation area ($l_{\mathrm{nuc}} = \sqrt{V_{\mathrm{nuc}}/(t_{\mathrm{film}})}$). In case of the pristine magnets, this results in a length of $\approx 92$ nm, which reduces to 71 nm and 68 nm for the irradiated magnets respectively. These sizes are interesting, as they are significantly larger than the often associated grain sizes, which in the case of the quasi amorphous Ta/CoFeB/MgO film should range around $\approx 10$ nm [253], [254]. A lower limit for the nucleation volumes will, however, be imposed by the domain wall widths $\Delta_{\mathrm{DW}}$, as the area of the nucleated volume, must at least support one DW ($V_{\mathrm{nuc}} \approx \Delta_{\mathrm{DW}}^2 \cdot t_{\mathrm{film}}$, $l_{\mathrm{nuc}} \approx \Delta_{\mathrm{DW}}$) [112]. The domain wall widths can be approximated from the anisotropy, via the relation $\Delta_{\mathrm{DW}} \approx \pi\sqrt{A_{\mathrm{ex}}/K_{\mathrm{eff}}}$, where $A_{\mathrm{ex}}$, the exchange stiffness is assumed to be $2 \times 10^{-11}$ J m$^{-2}$ for CoFeB [255]. Within the frame of the *Stoner–Wohlfarth* model, the nucleating particle has a constant anisotropy ($K_{\mathrm{eff}}^{\mathrm{nuc}}$) which would result in a DW width of $\approx 110$ nm for the pristine magnets and reduced widths of $\approx 83$ nm and $\approx 89$ nm for the irradiated magnets. These values are in good agreement with those obtained for the nucleation lengths. Attempts to directly observe the position of DW nucleation as for the pristine magnets were not successful, as the higher nucleation fields result in very high DW velocities, leading to complete reversals already within a few ns. The etch damage during patterning will induce an anisotropy drop along a gradient of typically 10 nm to 20 nm [253]. On the other hand, even inside the undamaged magnets, $\Delta_{\mathrm{DW}}$ will only decrease to values around $\approx 40$ nm (using the anisotropies measured on films). Therefore, the obtained nucleation lengths would only be off by a factor of 2 or less when considering the added influence of the edge damage. This is a reasonable result, especially when factoring in all the mentioned uncertainties.

### 8.2.2 Nucleation by Depinning

Controlling the position of DW nucleation with high spatial accuracy is an essential requirement for prospective DW applications. By targeted irradiation, the anisotropy can, in principle, be lowered locally, creating so-called artificial nucleation centers (ANC) [63]. However, the known occurrence of significant anisotropy lowering (with unknown distribution) towards the edges severely impedes efforts to create the nucleation volume with the lowest PMA reliably. However, nucleation by DW depinning from a fixed anisotropy gradient (e.g., an area with strongly reduced or easy-plane (negative) anisotropy) might offer an interesting alternative. Here, the anisotropy can be lowered by much larger extents, provided that the depinning fields fall below the intrinsic nucleation fields (via coherent rotation) [119]. Furthermore, the depinning process is governed by different time dynamics, leading to potentially lower switching fields upon approaching timescales close to $\tau_0$, which are, of course, most interesting for applications. For this purpose, ANCs with an anisotropy close to zero are placed in the center of the nanomagnets ($d = 1$ µm), employing a double-irradiation approach. First, a homogeneous background irradiation with a dose of $4.25 \times 10^{13}$ ions/cm$^2$ is used to increase $K_{\mathrm{eff}}$ beyond its peak (at $\approx 3.5 \times 10^{13}$ ions/cm$^2$). The effective anisotropy is subsequently reduced by a

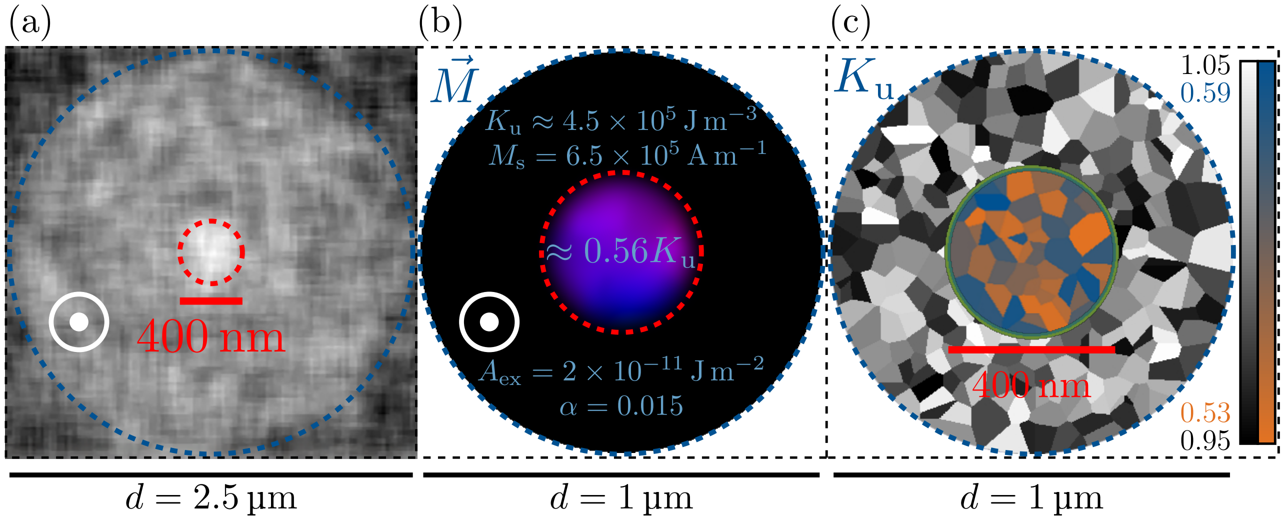

**Figure 8.6** Image (a) depicts a differential WMOKE image of a Ta/CoFeB/MgO nano-disk with a diameter of 2.5 µm. The image displays the remanent magnetization at 0 mT after saturation with 10 mT. The ANC with a diameter of ≈ 400 nm is visible at the center, with its magnetization seemingly pointing opposite to the remaining magnet. Image (b) displays the domain configuration of the respective MuMax3 model with a diameter of 1 µm in remanence. The material parameters are depicted, with special notice, given to $K_u$ inside the ANC area. Image (c) depicts the grain structure of one of the simulated samples, with the colors representing the respective anisotropies. ANC and magnet are separated by a 30 nm broad transition region (illustrated in green) with a linear anisotropy gradient. The simulated grain and mesh sizes of the dots are set to ≈ 15 nm and $2.5 \times 2.5$ nm, respectively. The simulation parameters were taken from measurements, except $\alpha$ and $A_{ex}$, which were taken from the literature [255].

second target irradiation in the center, with an additional $3.8 \times 10^{13}$ ions/cm$^2$ leading to a cumulative total dose of $\approx 8 \times 10^{13}$ ions/cm$^2$ for the ANC. For this dose, Figure 8.2 shows a coercivity of ≈ 0 mT with the magnetization effectively following the external field. The ANC position and magnetization direction in remanence is observed by differential WMOKE imaging of larger 2.5 µm wide magnets as displayed in Figure 8.6 (a). The bright spot ($d \approx 400$ nm) at the center of the circular magnet, which matches the size of the irradiated ANC area, indicates a change in the magnetization direction and thus the presence of a DW between ANC and magnet. However, it is not clear whether the magnetization of the ANC points in-plane or whether it is being aligned anti-parallel by the demagnetizing fields of the host magnet. Complementary to the experiments, a simulation model with an in-plane ANC was developed to better analyze and understand the magnetization reversal in this geometry. The model parameters are chosen to best approximate the characterized magnets. A detailed representation is depicted in Figure 8.6 (b, c). The depinning mediated magnetization reversal, starting from the DW surrounding the ANC, is analyzed by again measuring the time dependence of the switching fields. This is done for a series of magnets with centered circular ANCs (diameters ranging from $d$ = 100 nm to $d$ = 400 nm). The cumulative ion dose of all ANCs is $8 \times 10^{13}$ ions/cm$^2$ (keeping in mind the background dose of $4.25 \times 10^{13}$ ions/cm$^2$). Figure 8.7 depicts the measured nucleation fields with their corresponding fits according to Equation (8.2). The measured nucleation fields appear to agree well with the depinning model down to low µs timescales. From this point onward, $H_{nuc}$ seemingly increases drastically, reaching levels close to those of the irradiated magnets in Figure 8.5. However, a doubling of the nucleation fields within one order of magnitude (time) is hardly explainable by any reasonable depinning or rotation model. In order to explain the observed increase in $H_{nuc}$, it is necessary to consider the measurement procedure discussed in section 5.3.3. After the initial (ns-long) nucleation pulse, a secondary (ms-long) low field pulse is used to propagate the DW and ensure a complete magnetization reversal. However, the time between these two pulses allows the magnetization to relax back into the nearest local energy minimum. For a significant portion of the reversal process, this means to flip back into the initial state. We attempt to explain this

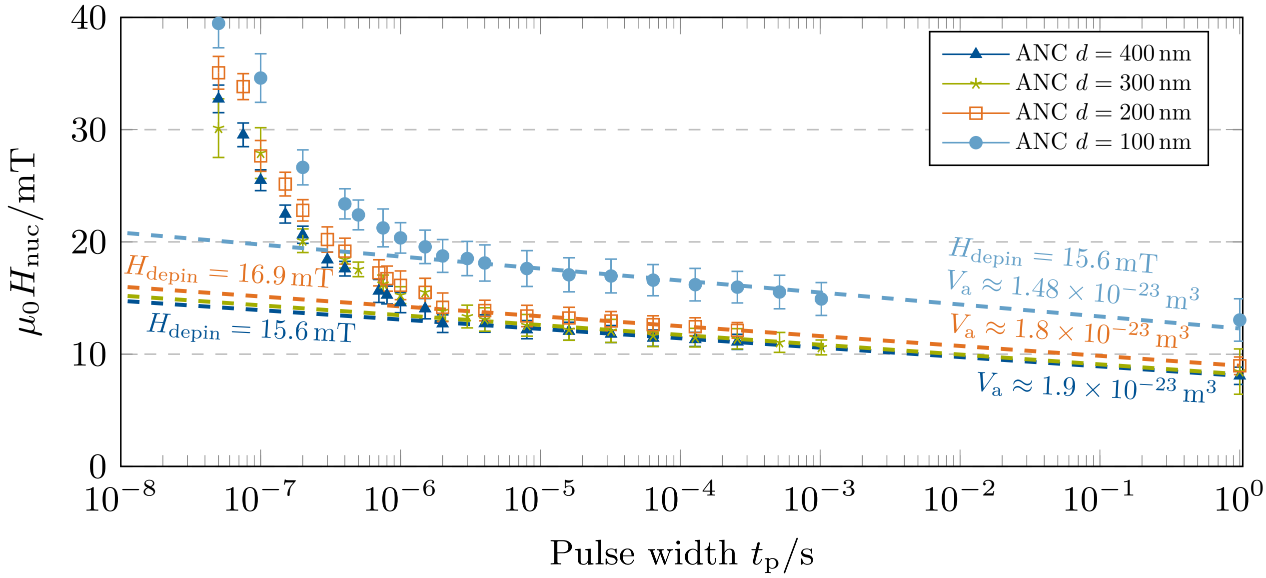

**Figure 8.7** Measured nucleation fields of double-irradiated nano-disks ($d = 1\,\mu\mathrm{m}$) as a function of the applied pulse width $t_{\mathrm{p}}$. The disks feature circular, different sized ANCs at their centers with the respective diameters given in the legend.

phenomenon by a simplified but vivid model and underline it via micro-magnetic simulations and related measurements. After the initial depinning from the ANC, the domain expansion can, in the first approximation, be modeled as the expansion of a circular bubble from the point of depinning (engulfing half of the ANC area to reduce its DW length). During this process, the system gains exchange and anisotropy energy as the DW length grows with the circumference ($\propto 2\pi r_{\mathrm{domain}}$) until reaching the edge of the magnet, where it splits into two DWs with lengths $\propto r_{\mathrm{magent}}$. The reducing demagnetizing fields do not compensate for this energy gain, as the magnet features a single-domain ground state. Without an external field, the bubble, provided it has not reached the edge, tends to collapse (it snaps back to the starting point) as the DW tries to lose energy by reducing its length. This effective force on the DW is also described as a Laplace-like pressure, reported in circular domain-structures, with a $\frac{1}{r}$ dependence [253], [256], [257]. Figure 8.8 illustrates the evolution of the total energy (without *Zeeman* terms) and respective snap-shots of the domain structure throughout the reversal process. Data and images are derived from MuMax3 micromagnetic simulations of a 1 µm nanomagnet with a centered ANC according to Figure 8.6 (b,c) [92]. The simulation parameters (listed in the plot) are thereby taken from measurements when possible to resemble the characterized magnets best and, $\alpha$ was taken from the literature [255].

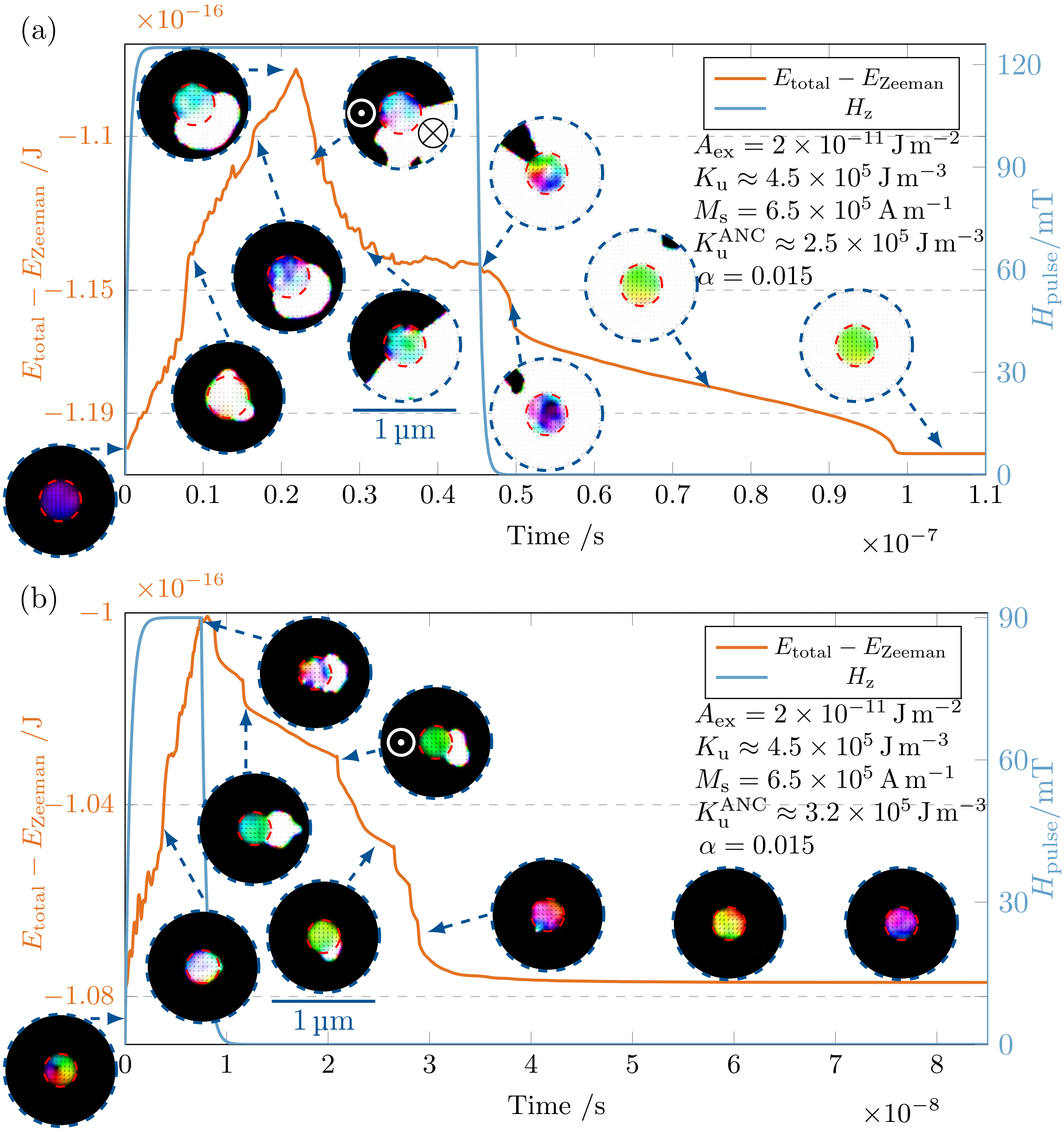

**Figure 8.8** Plots of the simulated magnetization reversal process, depicting a 1 µm circular nanomagnet with centered ANCs. The graphs displays the combined magnetic energies (excluding the *Zeeman* term) in combination with snapshots of the domain structure at relevant points. The assumed material parameters are listed in the plot. The ANC diameter is 400 nm in the case of plot (a) 300 nm in the case of (b). Please refer to Appendix 9.4 for further information about the simulations.

As described in the model above, the total energy initially increases significantly as the bubble domain expands towards the edge, reaching a tipping point before falling off, as the DW splits, reducing its length. After overcoming this energy barrier, the domain configuration can be described as quasi-stable until the propagation pulse completes the reversal process. However, if the DW does not reach the edge of the magnet within the pulse time, it implodes under the Laplace-like pressure. Such a case is depicted in Figure 8.8 for a pulse width of 7.5 ns and a field amplitude of 90 mT. In other words, Figure 8.7 displays the fields necessary to form a quasi-stable domain rather than to depin a DW. In addition to dynamic simulations, it is possible to test the model implicitly by measuring certain dependencies. By assuming the correctness of the model, larger magnets would require stronger fields to propagate the DW to the edge within the pulse duration. Figure 8.9 compares the nucleation fields of two different magnet sizes with diameters of 1 µm and 2.5 µm. For pulse-widths $t_\mathrm{p} < 200$ ns, the measured nucleation fields start to diverge, with the larger magnets requiring significantly higher field strengths for the DWs to form the necessary quasi-stable multi-domain state. However, it has to be noted that data for the 2.5 µm magnets is only available for three samples, compared to the 40 for the 1 µm magnets. Besides the dimensional scaling, it is also worth considering the timescales of a possible bubble collapse. Although it is not directly possible to observe this process via WMOKE imaging, information about the timescales at which these collapses occur can nevertheless be inferred using consecutive on-chip field pulses with varying pulse periods (dead-times between pulses). Using a fixed pulse width of 50 ns but sweeping the time between the pulses and measuring the effects on the nucleation fields, it is possible to derive upper and lower bounds for the collapse times. If the domain collapses within the time between pulses, the switching fields should be independent of the number of pulses (at least in the first approximation, not considering the higher attempt count per measurement). Starting at ≈ 1 µs a clear reduction in the measured nucleation fields is observed. At pulse periods of 200 ns (150 ns dead time), however, the measured fields are still twice as high as expected for the cumulative pulse duration of 1 µs. Only for dead-times < 50 ns, comparable nucleation fields are observed. As a sanity check, we again consider the SW-particle based rotation

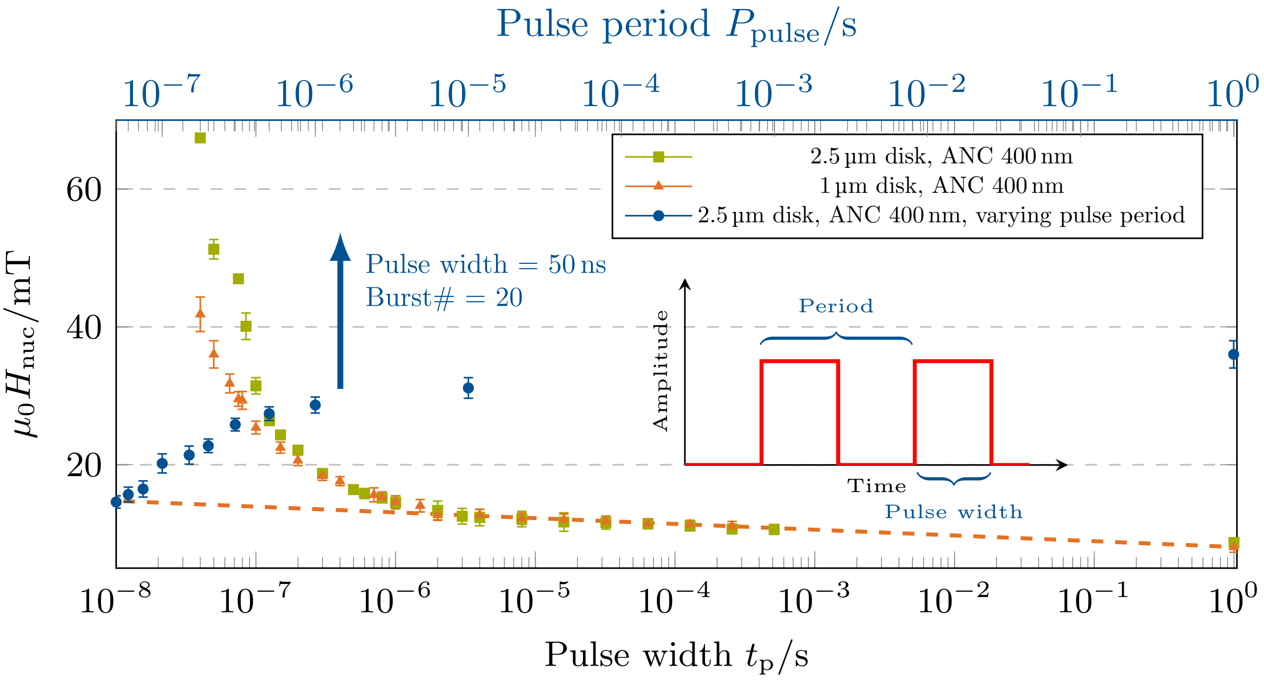

**Figure 8.9** The combined plot shows on the lower *x*-axis the nucleation fields over different pulse widths, 1 µm (orange) and 2.5 µm (green) nano-disks. The second plot, associated with the upper *x*-axis (blue), displays a sweep of the pulse period $P_\mathrm{pulse}$ and its effects on the measured nucleation fields. The cumulative pulse-width is thereby kept constant at 1 µs (Burst# = $\frac{1\,\mu\mathrm{s}}{50\,\mathrm{ns}}$).

model (for a detailed discussion, see SI). However, the time-dependent nucleation probabilities via coherent rotation are independent of the magnet size and do not scale with the pulse period. All these observations and simulations let us assume that the depinning fields scale according to Equation (8.2) even below µs pulse widths. Splitting the nucleation field measurements (displayed in Figure 8.7) at $t_p \approx 1\,\mu s$ would technically allow modeling the two slopes separately via the *Sharrock* equation. However, the presence of a DW at the ANC edge (made evident by the WMOKE image in Figure 8.6 (a)) even after initial OOP saturation plus the scaling of the nucleation fields with the ANC curvature and pulse period, let us to exclude this model. Upon analyzing the ANC size-dependent depinning fields in Figure 8.7 and Figure 8.10 , it becomes evident that the depinning process from the circular sources scales $\propto \frac{1}{d_{\text{ANC}}}$ (the curvature of the circle) and thus similar to DW depinning from a notch [121], [122], [258]. Figure 8.10 depicts both the effective activation volumes ($V_a$) and the depinning fields at 0 K versus $\frac{1}{d_{\text{ANC}}}$. $V_a$ (not to be confused with the earlier discussed nucleation volume $V_{\text{nuc}}$) is calculated from Equation (8.2), assuming $M_s \approx 6.5 \times 10^5\ \text{A m}^{-1}$ (approximated from the magnetometer data in Figure 8.1). The intrinsic depinning field $H^{\text{int}}_{\text{depin}}$ of the anisotropy gradient can be derived from the zero-intercept of the linear fit to be $H^{\text{int}}_{\text{depin}} = (13.3 \pm 2.1)\ \text{mT}$ [122]. Analyzing the evolution of the activation volume is more complicated. First of all, it is necessary to point out that the calculated absolute values strongly depend on the value of $M_s$, which is not precisely known. The sizes for $V_a$, although showing a linear $\frac{1}{d_{\text{ANC}}}$ dependence, shrink only marginally compared to the physical dimensions of the respective ANCs. To better illustrate this, we translate the activation volume into an effective ANC diameter $d^{\text{eff}}_{\text{ANC}}$, assuming a cylindrical shaped volume ($d^{\text{eff}}_{\text{ANC}} = 2\sqrt{V_a/(\pi t_{\text{film}})}$). This yields effective diameters from ≈ 140 nm to 160 nm, indicating that, especially for the larger ANCs, only a small portion takes part in the depinning process. This complies with the depinning models, predicting depinning at the area with the lowest anisotropy gradient.

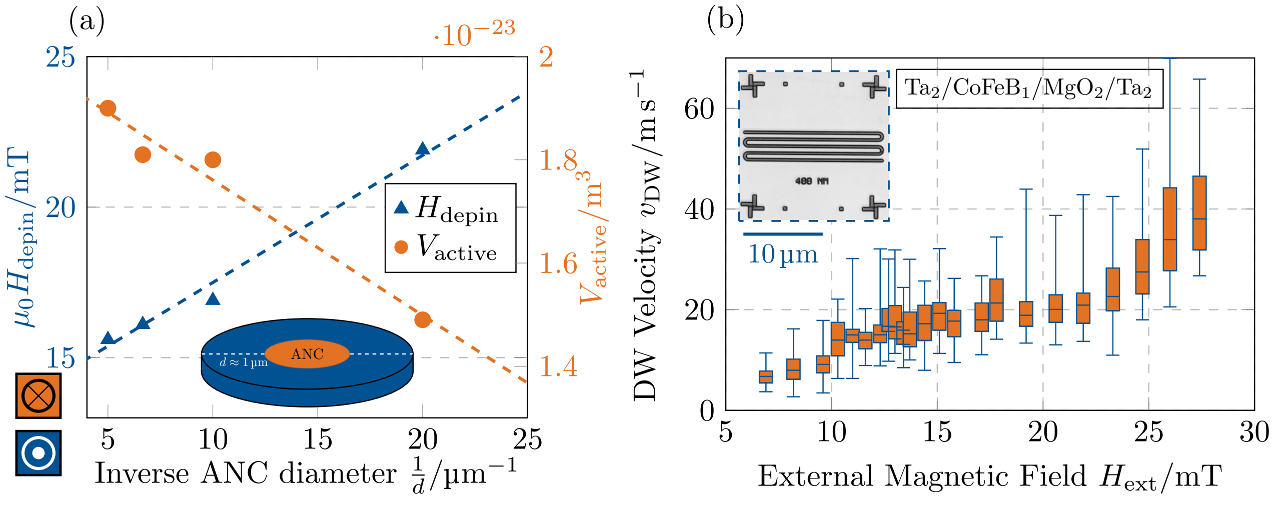

**Figure 8.10** In (a),the plot displays the depinning fields $H_{\text{depin}}$ at 0 K (on the left) together with the activation volumes $V_a$ (right) for the DW depinning process from a circular ANC, depending on the ANC curvature $\frac{1}{d_{\text{ANC}}}$. Both exhibit a linear $\frac{1}{d}$ dependence, however, with complementary slopes. The dashed lines depict the best linear fits. The inlet displays a schematic of the test structures. The plot in (b), displays a series of box plots describing the distribution of the field dependent DW velocities ($v_{\text{DW}}$) of a 400 nm wide Ta/CoFeB/MgO nanowire. Each displayed distribution consists of more than 30 measurements. The velocities are measured by propagating a DW through the nanowire via external, 25 ns long field pulses of varying field strength ($H_{\text{ext}}$).

### 8.2.3 Domain Wall Velocity

DW nucleation is only one part of the reversal process. Equally relevant is the rapid expansion and propagation of the DW through the magnet. As discussed in section 2.9.2, DW motion can, roughly speaking, be separated into two distinct domains. At low fields, domain wall depinning heavily depends on thermal activations, thus resulting in a slow probabilistic creep motion. At higher fields, however, more and more pining sites are overcome by the driving field, leading to flow-like motion, with a linear relation between $v_{\mathrm{DW}}$ and $H_{\mathrm{ext}}$. For applications, the creep regime is generally considered irrelevant, due to the low velocities $\ll 1\,\mathrm{m\,s^{-1}}$. On the other hand, pure DW flow motion is seldomly achieved in confined geometries like nanowires

In order to measure and assess the DW velocities in Ta/CoFeB/MgO nanomagnets, nucleated DWs are propagated though 400 nm wide nanowires (microscope image shown in Figure 8.10 (b)) via bursts of 25 ns long magnetic field pulses with varying amplitudes. Figure 8.10 (b) depicts the measured DW-velocity distributions as box plots for external fields up to 28 mT. In the case of quasi-static fields, the depinning fields are determined to be in the range of 0.3 mT. However, using ns-long pulses, DW movement is only observed for fields higher than $\approx 7$ mT. Furthermore, the measurements show a clear initial increase in DW-velocity, plateauing between 13 mT and 22 mT, before increasing again from 22 mT on-wards. The observed plateau may result from the decreasing velocities above the Walker-breakdown, as discussed in section 2.9.2. The Walker-breakdown, calculated to occur below 1 mT for this material system, is masked by the creep motion. The second velocity increase above 22 mT could mark the onset of flow motion. However, the wide distribution of the collected data suggests some form of intermediate flow in which large pinning sites still dominate. The data for even higher fields becomes unreliable due to the increasing amount of random nucleation events in the nanowires. For possible applications, the relevance of very high fields is, of course, limited. Considering clock fields around 20 mT and feature sizes of 400 nm, it is possible to estimate possible clock frequencies around 20 MHz.

## 8.3 Review & Assessment

Ta/CoFeB/MgO nanomagnets were examined for potential use in pNML systems. For that purpose, the effects of $\mathrm{Ga^+}$ ion irradiation were investigated in order to globally and locally modify the magnetic energy landscape as a step to control the position of DW nucleation effectively. It has been shown that $K_{\mathrm{eff}}$ initially increases upon irradiation up to doses of $3.5 \times 10^{13}$ ions/cm$^2$ followed by a steep decline, crossing the easy-plane threshold at $\approx 8 \times 10^{13}$ ions/cm$^2$. This is in stark contrast to Pt/Co/HM and Co/Ni superlattices, which show a monotonic decrease in effective anisotropy.

A nucleation field analysis of 1 µm sized nanomagnets across different timescales determined the anisotropies of the nucleation volumes to be roughly one order of magnitude smaller than the values obtained from film-level magnetometer measurements. Furthermore, control over nucleation points and fields could be achieved, employing a second focused irradiation, creating artificial regions with easy-plane magnetization, from which a DW can depin. The fields needed to depin a DW from this anisotropy gradient scale $\propto \frac{1}{d_{\mathrm{ANC}}}$.

Aside from the complex topic of artificial DW nucleation, the magnets show very low coercive and depinning fields, ideal for use in pNML circuits. Furthermore, the domain wall velocity analysis revealed significant improvements in the low field regime, compared to earlier results for Pt/Co or Pt/Co/Ir nanowires. However, these improvements are accompanied by a significant reduction of the total magnetic moment due to the limited film thickness. At this point, it is not clear whether this issue is best addressed by material engineering (e.g., CoFeB multilayers) or via gate/circuit design.

# 9 A Decade of pNML Research

From the first dipole-coupled inverters, presented by Breitkreutz et al. in 2011, perpendicular nanomagnetic logic has come a long way. An entire computing architecture was designed and developed, comprising of electrical inputs & outputs, logic gates, memory, interconnects, vias, and means for signal synchronization. All of these necessary building blocks, needed for a digital computing architecture were experimentally shown and analyzed until 2015, thus removing major obstacles for system design and modeling [137]. Majority gates, signal-crossings, and domain wall gates were even implemented in a three-dimensional design, underlining the claim of pNML as an inherently three-dimensional logic architecture capable of monolithic integration [52]–[54], [151]. Efforts addressing the problem of efficient on-chip clocking were underway by 2013, proposing on-chip coils complimented by soft magnetic claddings for clock frequencies in the MHz regime [52], [56], [157]. In this context, investigations into the time-dependent reversal mechanisms were started in 2014, targeting DW nucleation and DW propagation in magnetic multilayer. In order to build on the obtained findings, compact models were developed, allowing for higher-level system design and the integration into widely used electronic-design-automation (EDA) tools [152]. This, in turn, allowed for more realistic performance and power–delay product (PDP) estimations [50], [137].

During this initial proof-of-concept phase, Pt/Co/Pt superlattices, combining high magnetic moments with strong PMA, served as the ideal vehicle to realize demonstrators for the targeted logic functions. However, while ideal to demonstrate the working principle of logic gates, the use of Pt/Co/Pt multilayers, due to their high coercive and DW-pinning fields, impeded efforts towards the demonstration of on-chip clocking. The usage of Pt/Co/Pt thus severely hampered further developments towards system integration and the realization of on-chip demonstrators.

The search and optimization of alternative magnetic materials, in the context of the available fabrication technologies, dominated pNML research from 2017 till the end of this project in late 2020 [82], [142], [143]. In the following, we will address the different material systems individually, summarize and interpret the obtained findings and assess the necessity for future research activities. Furthermore, we will derive strategies to cope with the constraints imposed by the limitations of the evaluated metallic thin film materials. In this context, a fundamental shift in pNML architecture from planar coupling, requiring materials with large magnetic moments and complex structures, towards vertical coupling between simple, highly regular structures is proposed [131].

## 9.1 Material Systems

Throughout the course of this work, fabrication processes for three distinct magnetic thin-film systems were developed within the capabilities of the available deposition tool. The resulting films and further processed nanomagnets were characterized, and their potential as building blocks for pNML was evaluated. While initial efforts focused on improvements whit only marginal changes to the established material system, iterative learning cycles showed that entirely different materials would be necessary to address the essential topics of coercivity and switching field distribution effectively. Each new material system resembled a distinct step forward in terms of process control, characterization techniques, and magnet performance. The material systems and their development processes are summarized and evaluated in the following section.

### Pt/Co/W Superlattice

In an attempt of evolution rather than revolution, processes for Pt/Co/Ir and Pt/Co/W superlattices were developed, building on the extensive experience already gathered for Pt/Co/Pt thin-films. Pt/Co/Heavy-Metal films feature a wide process window, as the platinum seed, essential for PMA, is renewed in each iteration of the repeating tri-layer system. Pt/Co/HM was chosen due to reports of higher DW velocities associated with the net iDMI present in specific Pt/Co/HM systems [130], [259]. Significantly higher DW velocities and strong net iDMI in the developed films would later be confirmed [145], [213]. However, aside from higher DW velocities in the flow regime (in the case of Pt/Co/Ir), no substantial improvement in switching, pinning, or coupling fields could be achieved [82]. This is attributed to the polycrystalline nature of the sputtered superlattices, the large intrinsic damping constant of Pt/Co ($\approx 0.3$), and the large number of multilayers, necessary to achieve sufficient coupling (caused by the formation of significant magnetic-dead layers at the Co/HM interface) [82], [260]. The presence of potentially antiferromagnetic RKKY interaction furthermore complicated the stack design [82], [167]. In the end, all these factors led to the decision not to proceed with these material systems. However, the stack development contributed to the skyrmion research and other projects, running in parallel, at the Chair of Nano- and Quantum Sensors [213], [261].

### Co/Ni Superlattice

With the conclusions drawn from the first learning cycle involving the Pt/Co/HM films, the focus was shifted towards Co/Ni, a new materials system with supposedly lower coercive and pinning fields. It solely consists of two ferromagnets on top of an initial seed layer, thus enabling magnetic moments comparable to those of Pt/Co/HM films at only a third of the total film thickness. The reduced film thickness limits grain formation and reduces DW pinning. Furthermore, the absence of heavy metals with strong spin-orbit interactions in the stacks results in smaller damping constants ($\approx 0.05$) [262]. Although the process window of Co/Ni films is much smaller compared to Pt/Co/HM (due to the lack of a renewed seed), stack development, aiming for the smallest coercivities while preserving single-domain states, quickly yielded promising results. During the consecutive studies, a significant reduction of the switching fields could be achieved while still retaining sufficient coupling strengths [142]. Furthermore, a detailed study of the $Ga^+$ ion irradiation effects (ANC placement) on the switching fields and switching field distributions (SFD) was conducted for the first time [142]. The Co/Ni studies showed significant improvements compared to Pt/Co/HM. However, the widths of the recorded switching field distributions still reached values up to $\approx 10\,\mathrm{mT}$ FWHM, thus impeding reliable operation at the measured coupling fields. Further investigations into the cause of this large SFD revealed no conclusive results. The large SFDs could originate from the intrinsically large anisotropy variations attributed to the polycrystalline nature of the Co/Ni films. However, the uncertainty of the ANC placement might also contribute significantly to the obtained results. Naturally, the process quality of research tools is not directly comparable to the quality achievable via state-of-the-art industrial deposition tools. Nevertheless, the research into bit patterned media in the 2000s also revealed large anisotropy and switching field variations in crystalline multilayer systems [263], [264]. In this context, it has to be noted that this was the first study on the SFD of large numbers of pNML magnets. Thus, no comparable data for the previously investigated Pt/Co/Pt or Pt/Co/HM systems are available. Nevertheless, stack design and SFD data of individual magnets indicate that the distribution widths of Pt/Co based magnets are comparable if not larger [61], [147].

#### Amorphous Ta/CoFeB/MgO Films

Presuming that the intrinsic anisotropy variations of the investigated polycrystalline thin films were the main cause of the critical SFDs, together with the ongoing effort to reduce the coercive and depinning fields, led to the consideration of amorphous or poorly-crystalline thin film systems. When searching for an amorphous thin-film system with strong PMA, Cobalt-Iron-Boron (CoFeB) based tri-layers are the prime candidate since this material system is the backbone of today's GMR/TMR sensors and MRAM devices. Therefore, significant literature on the material was already available, and the integration into state-of-the-art CMOS technologies had already being started. In CoFeB alloys, the boron prevents crystal formation during sputter deposition and leads to an amorphous layer growth. In order to achieve large anisotropies, the target process used a $Co_{20}Fe_{60}B_{20}$ alloy, sandwiched between a thin tantalum seed and a magnesium-oxide capping layer. An iron-rich alloy was selected as it combines the large PMA caused by the iron-oxygen bonds with the higher magnetic moments of the iron atoms [187]–[190].
Stack development for $Co_{20}Fe_{60}B_{20}$/MgO films with out-of-plane magnetization started in late 2019. In CoFeB/MgO systems, the PMA mainly originates from the fragile metal-oxide interface, resulting in a sensitive fabrication process and a small process window. Therefore, process development became more complicated and required significant time and material resources. Initial efforts to realize OOP magnetized CoFeB layers without a MgO interface yielded no success and were quickly dropped. As the second interface, both tantalum and tungsten were successfully employed. However, as tantalum featured higher as-grown anisotropies and generally lower depinning fields, it was selected for further pNML studies. On the other hand, tungsten showed a more stable bubble phase and was therefore used for investigation into skyrmions and other spin-textures [69]. Initially, the deposition process only yielded Ta/CoFeB/MgO films with in-plane magnetization. The films needed to be annealed at temperatures between 250 °C and 300 °C after deposition to achieve an OOP magnetization. With annealing, perpendicularly magnetized CoFeB layers with thicknesses up to $\approx 1.5\,\mathrm{nm}$ could be achieved. Such thicknesses are comparable with literature results [180]–[182]. Furthermore, in a later stage, process improvements allowed for Ta/CoFeB/MgO films with an as-grown out-of-plane magnetization, up to CoFeB thicknesses of $\approx 1.2\,\mathrm{nm}$. Process and stack development saturated at this point in mid of 2020 (after the first Corona (SARS-CoV-2) wave). However, measures to stabilize the process hat to continue throughout the entire time of the project. The fabricated Ta/CoFeB/MgO nanomagnets featured, depending on the CoFeB thickness and annealing time, a coercivity between 1 mT and 15 mT as well as depinning fields in the low single-digit oersted regime [131], [143]. Measurements of field-driven DW-velocities in 400 nm wide nanowires, relieved depinning fields of only 7 mT at nanosecond long field pulses and field-less, thermally activated DW-movement at timescales above 1 ms [131]. A detailed analysis of the switching field distributions showed the desired reduction down to values below 3 mT FWHM for magnets without an artificial nucleation center [131]. However, it has to be noted that the intrinsic SFD might be masked by edge-damage induced DW-nucleation caused by plasma etching during fabrication [143]. Controlling the position of domain wall nucleation via ion-irradiation proved to be extremely difficult and complex since the $Ga^+$ ion irradiation caused an initial increase in anisotropy, with a subsequent reduction only at very high doses. This bidirectional irradiation effect turned the technique, employed for more than a decade to shape the switching behavior of magnets, on its head. Efforts to investigate and understand the reversed irradiation effects were underway by spring of 2020 and quickly yielded results. Apparently, the magnetic moment of the thin CoFeB layers is more sensitive to ion-irradiation compared to thicker superlattices, leading to a fast reduction of the saturation magnetization and thus an apparent increase in the effective

anisotropy [143]. Furthermore, the uniaxial anisotropy, heavily affected in crystalline superlattices, is more stable in the case of amorphous materials [143]. This effect impeded the a for pNML critical nucleation control via local irradiation. To nevertheless control DW-nucleation, a double-irritation technique was developed to increase the PMA of the entire magnet first and subsequently lower it in the second step by local high-dose irradiation. However, the development and implementation of this strategy to circumvent the bidirectional irradiation effects were only completed and successfully tested at the end of this project [143]. In the end, it was discovered that the bidirectional irradiation effect could also be suppressed by saturation annealing at temperatures $\geq 300\,^{\circ}\mathrm{C}$. However, annealing at such temperatures further increases the PMA, leads to crystallization of the CoFeB and thus to increased coercive and depinning fields.

Aside from the dominating (but solvable) issue of DW nucleation, CoFeB layers seem to be extremely attractive for pNML if certain obstacles can be surmounted. The main problem of CoFeB/MgO films is the comparatively low magnetic moment of the stack. With a maximum equivalent cobalt thickness of $\approx 1.5\,\mathrm{nm}$ (see section 3.7.3), a reliable operation of classic pNML gates would be challenging. CoFeB multilayer systems, on the other hand, would suffer either from a weak interlayer coupling across the insulating MgO layer or from potentially antiferromagnetic RKKY interactions across the tantalum or other heavy-metal spacer. However, asymmetric double-MgO bilayer systems have been shown to realize CoFeB thicknesses up to 2 nm [194], [195]. Nevertheless, it is not yet clear whether such bi-layer or even multilayer systems are suitable for pNML and how they would compare to Pt/Co or Co/Ni single layer systems.

## 9.2 Technology Aware Gate Designs

In the past, pNML gates were designed under the premise of high functionality and maximum achievable dipole-coupling, leading to complex geometries with up to five inputs in the same plane (see section 3.2). For the design of a pNML gate, there generally are two major factors contributing to the reliability and performance of the device. The first is the dipole-coupling between the magnets, a function of the magnetic moment, distance, and coupling area (geometry). The second is the effective DW path-length of the magnets determining the DW propagation time $t_{\mathrm{prop}}$ and thus the switching speed (see section 3.1.2). The path-length is defined by the size and shape of the magnet, also factoring in DW pinning sites like corners or notches. When envisioning pNML systems built from optimized CoFeB alloys with optimistically achievable magnetic thicknesses of $\approx 2\,\mathrm{nm}$ (cobalt equivalent), it becomes clear that any implementation will require coupling distances $< 25\,\mathrm{nm}$ to achieve the necessary coupling strengths on the order of 20 mT per input (see Figure 3.4). However, as of now, feature sizes below $\approx 50\,\mathrm{nm}$ already require complex double exposure techniques for non-trivial geometries. With magnet distances targeted around 20 nm, the fabrication of complex geometries will most likely not be viable since the deployed multi-patterning techniques impose harsh design rules, effectively limiting the available geometries to simple lines [265], [266].

Therefore, pNML systems need to be designed using highly regular structures only. This also reduces the effective DW path length, allowing for faster operation. From geometrical considerations, planar gate designs will, therefore, be limited to inverter structures and three-input majority gates as depicted in Figure 9.1 (a). However, to control the coupling distance more reliably, it might be prudent to move toward vertically coupled designs altogether and realize multiple inputs in different functional layers. Furthermore, this allows to reduce the effective coupling distance without approaching the limits lithography and increases the coupling. Vertically coupled pNML gates have already been experimentally demonstrated, though only with ferromagnetic coupling, using a single underlying input [53], [151]. Achieving antiferromagnetic coupling in a vertical geometry, necessary for a functionally complete logic architecture, requires a staggered design, as depicted in Figure 9.1 (a) and (b). Figure 9.1 (c) illustrates different coupling geometries as well the magnetic field lines emanating from the input magnet toward the output magnet and especially the ANC area. In the case of direct stacking, the field lines promote ferromagnetic alignment. However, if the input is

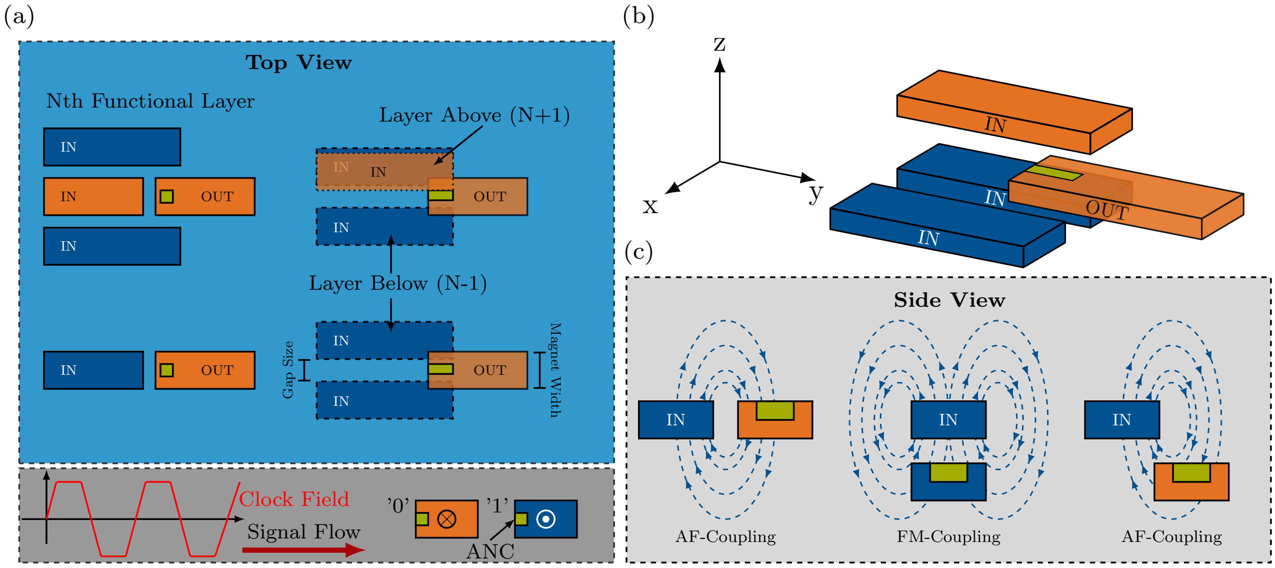

**Figure 9.1** Schematic illustration of different pNML gate designs. In (a), the top view of different planar and vertical logic gate designs is shown. The commonality between the designs is the complexity reduction in magnet geometries towards simple quasi-one-dimensional structures, best suited for advanced fabrication nodes. In (b), a three-dimensional sketch of a staggered, vertical-coupled majority gate is shown. The three inputs are placed in different functional layers with the output magnet placed between them. A top view of this gate structure is depicted in (a) on the top right. In (c), the side views of the different coupling schemes are shown, depicting the conventional planar coupling on the left and the proposed staggered vertical coupling on the right. An aligned vertical placement promoting ferromagnetic coupling is shown in the middle.

positioned with a lateral offset next to the output, the coupling can be tuned (by this offset) to promote antiferromagnetic alignment in the ANC area. In order to evaluate the potential of such designs, Riente et al. performed detailed MuMax3 simulations, analyzing the achievable coupling strengths for planar and vertical designs with two inputs [131]. For the simulations, Ta/CoFeB/MgO magnets with a CoFeB thickness of 1 nm (≈ 0.6 nm cobalt equivalent thickness) were used. The simulations of the vertical designs show that coupling fields in the range of 8 mT are achievable with two staggered inputs, using a vertical distance (filled with an inter-layer dielectric) of 10 nm and a gap size of 50 nm (using magnet with a width of 100 nm). This is a significant improvement compared to the 10 nm lateral distance, necessary to achieve the same coupling strengths with a purely planar design.

This staggered input approach is a promising addition to conventional gate designs and can help to alleviate the need for multilayers with large total magnetic moments (and the accompanying high depinning fields and low DW mobilities) in order to reach sufficient coupling strengths. However, it has to be stressed that an experimental demonstration of such a design is still lacking.

## 9.3 Limitations and Trade-Offs

In contrast to many emerging beyond CMOS technologies, there seems to be no fundamental "show-stopper" for pNML. The working principles are simple, elegant, and very robust. Furthermore, the logic family is complete, and while there are reliability risks regarding the probabilistic nature of DW nucleation and propagation, both can be addressed by material engineering, hard-axis clock field components, and circuit design (i.e., error correction) [258], [267]. While precise predictions of fundamental limitations or unavoidable trade-offs are neither possible nor advisable (one might think of the ever-present predictions of a looming end to further technology scaling), it is nevertheless necessary to formulate the thresholds and problems that, based on the knowledge of the time, limit the technology.

### Scaling

Miniaturization potential is a crucial aspect of any emerging technology. In the case of pNML, this potential is set by the physics of magnetism and the material properties of the nanomagnets. While the interacting force, the dipole-coupling, scales to ultimate dimensions, the magnets do not. Reducing the magnet size reduces the magnetic volume and thus the total magnetic moment of the particle. This can be beneficial, as the energy needed to reverse the magnetization scales with the magnetic volume. Additionally, the switching times are reduced, as the DWs need to cover less distance to complete the reversal. However, we know that the magnetization reversal is governed by the the *Arhenius-Néel* law, which defines an energy barrier dependent time between two random, thermally activated, switching events ($\tau \approx \tau_0 \exp(\frac{E_0}{k_\mathrm{B}T}) \approx (\frac{M_\mathrm{s}V}{k_\mathrm{B}T})$). Depending on anisotropy and temperature, a final magnet size exists below which the so-called relaxation time $\tau$ is smaller than the duration of one clock cycle. This superparamagnetic limit, of course, depends on multiple parameters. Nevertheless, we can provide a rough estimate for pNML magnets operating at room temperature. Assuming an anisotropy around $1 \times 10^5\,\mathrm{J\,m^{-3}}$ yields magnet sizes roughly between 20 and 30 nm.
Aside from the superparamagnetic limit, there exist other effects limiting the miniaturization. The working principle of pNML is built around the concept of DW nucleation and propagation. Furthermore, we know that there is a characteristic size or width attributed to a DW in thin films with PMA, $\Delta_\mathrm{DW} \approx \pi\sqrt{A_\mathrm{ex}/K_\mathrm{eff}} \approx 25 - 150\,\mathrm{nm}$. Below this size, the reversal process is better described by coherent rotation rather than nucleation and propagation. As the exchange stiffness $A_\mathrm{ex}$ is mostly constant for metallic thin films, $\Delta_\mathrm{DW}$ is defined by the anisotropy of the magnet or to be more precise, the anisotropy of the nucleation area ($A_\mathrm{nuc} \geq \Delta_\mathrm{DW}^2$). Since the anisotropy also defines the switching fields, a trade-off between size and energy consumption emerges. A more realistic estimate of the size limit for pNML magnets might be in the area of 50 to 100 nm. A limit that might turn out to be invalid if the working principles of pNML prove to be valid even beyond the magnet sizes governed by domain wall theory. However, at least from today's perspective, it is questionable whether reliable and nonreciprocal coupling is possible at sizes well below 100 nm.

### Clock Frequency

Another fundamental limitation of pNML, which has been mentioned multiple times throughout this work, is the comparatively slow reversal characteristic of ferromagnets, which is ultimately limited by the attempt-frequency (≈ 1 ns) [112]–[114]. This is a general problem for all emerging spintronic technologies utilizing reversing ferromagnets (e.g., NML, pNML, MESO-logic). It has to be noted, that recent advances in the area of voltage-controlled anisotropy (VCMA) might promote efficient sub-ns switching of ferromagnets[18], [19]. However, at this point, it is not conceivable how VCMA could be used for efficient clocking in pNML systems. Clock frequencies in the GHz range will, therefore, not be achievable with pNML. Furthermore, the finite DW velocity and architectural overhead put realistic operating frequencies closer to 100 MHz, presuming the problems of pinning induced low DW velocities in nanowires are successfully addressed [38]. Furthermore, as the DW velocity tends to reduce with the nanowire width, another trade-off between performance/energy consumption and magnet size emerges. Thus, at best, the clock frequencies will be about one order of magnitude lower compared to state-of-the-art CMOS designs. Competitive performances must, therefore, be achieved by wide designs and massive three-dimensional integration.

## 9.4 Final Review & Future Prospects

In summary, this work represents the first systematic investigation of different magnetic thin-film materials for use in prospective pNML systems. While in the past, pNML research investigated the fundamental principles of pNML technology, here we focused on its building blocks, the nanomagnets. Although nanomagnets with PMA have already been extensively investigated for use in MRAM cells or as an information carrier in hard-drive disks based on bit-patterned media, these use cases differ diametrically from the specific requirements of pNML. In the case of nonvolatile memory, stability and retention time are the most critical parameters as the magnets are seldomly switched, allowing for high switching energies (MRAM can be an exception). For pNML, on the other hand, fast, dynamic switching of the magnets with a minim amount of energy is the main target.

Starting from the well-tested and proven Pt/Co system, the parameter space of metallic thin film materials was explored. Promising material systems were analyzed, starting with the fundamental material parameter and culminating in the pNML specificity requirements. Throughout the course of the project, both Co/Ni as well as CoFeB/MgO thin films yielded promising results, which met the switching field requirements for integrated pNML of $\approx 20\,\mathrm{mT}$ for MHz clock frequencies. However, in the case of Co/Ni, considerable switching field distributions with widths up to $10\,\mathrm{mT}$ FWHM were observed. The definite route cause for these variations could not be determined conclusively. Although intrinsic anisotropy variations stemming from the polycrystalline nature of the material are the most sound explanation.

The amorphous CoFeB/MgO system, on the other hand, featured comparable switching fields together with drastically narrowed distribution widths ($\leq 3\,\mathrm{mT}$ FWHM). However, controlling domain wall nucleation in these magnets via ion irradiation turned out to be much more complex compared to the earlier assessed superlattices. At the same time, current CoFeB/MgO magnets do not possess the necessary magnetic moment for reliable pNML operation (even when considering the reduced SFD width), thus requiring extensive design changes towards vertically coupled devices or advance in material engineering to allow for significantly thicker CoFeB films or multilayers.

The future of pNML and associated research is unclear at this point. While this work made significant contributions to the general understanding of nanomagnets in the specific context of pNML, the obtained results do not paint a clear path forward for future research efforts. Although the works on low anisotropy Co/Ni and CoFeB/MgO pave the way for renewed device research and system development efforts, it is doubtful whether this research can be conducted successfully in a university environment without significant investment or industry partners.

In the end, pNML suffers from the dilemma that it is not at least two-orders of magnitude faster or more efficient compared to conceivable, end of the road-map CMOS designs — a dilemma which it shares with the majority of potential beyond CMOS technologies.

# Appendix A

## *Néel* and *Bloch*-Walls in In-Plane Magnetized Films

After a classification and description of energy densities and domain wall widths we can asses the total energy of *Bloch*/*Néel* walls and try to derive a trend or rule of thumb, which wall configurations are favored under what conditions. In the 60's *S. Middelhoek* developed a simple but vivid analytic model for the evolution of the total wall energy in permalloy with increasing layer thickness [268]. Before we discuss this model in more detail, it is important to stress the fact, that these models, generally speaking, should not be used to accurately calculate the domain wall configurations and widths found in experiments. They rather serve as a qualitative guide, describing the underlying physical phenomena. The model obtains the total wall energy, by simply adding up the individual stray field, exchange and anisotropy components as energy densities and finally integrating them along the wall width $\Delta_\mathrm{w}$. For a pure *Bloch* wall, the total energy amounts to

$$E_\mathrm{w}^{Bloch} \approx A(\frac{\pi^2}{\Delta_\mathrm{w}^{Bloch}})\Delta_\mathrm{w}^{Bloch} + \frac{1}{2}K_\mathrm{u}\Delta_\mathrm{w}^{Bloch} + \frac{\pi M_\mathrm{s}^2\Delta_\mathrm{w}^{Bloch}}{\Delta_\mathrm{w}^{Bloch} + t}\Delta_\mathrm{w}^{Bloch}\,, \tag{A.1}$$

and for a pure *Néel* wall respectively to

$$E_\mathrm{w}^{Néel} \approx A(\frac{\pi^2}{\Delta_\mathrm{w}^{Néel}})\Delta_\mathrm{w}^{Néel} + \frac{1}{2}K_\mathrm{u}\Delta_\mathrm{w}^{Néel} + \frac{\pi M_\mathrm{s}^2 t}{\Delta_\mathrm{w}^{Néel} + t}\Delta_\mathrm{w}^{Néel}\,. \tag{A.2}$$

By minimizing Equations A.1 and A.2 for $\Delta_\mathrm{w}$ and using it to calculate $E_\mathrm{w}$ we can derive the thickness dependent optimal solution for both, wall-widths and energies. Figure A1 depicts the results of

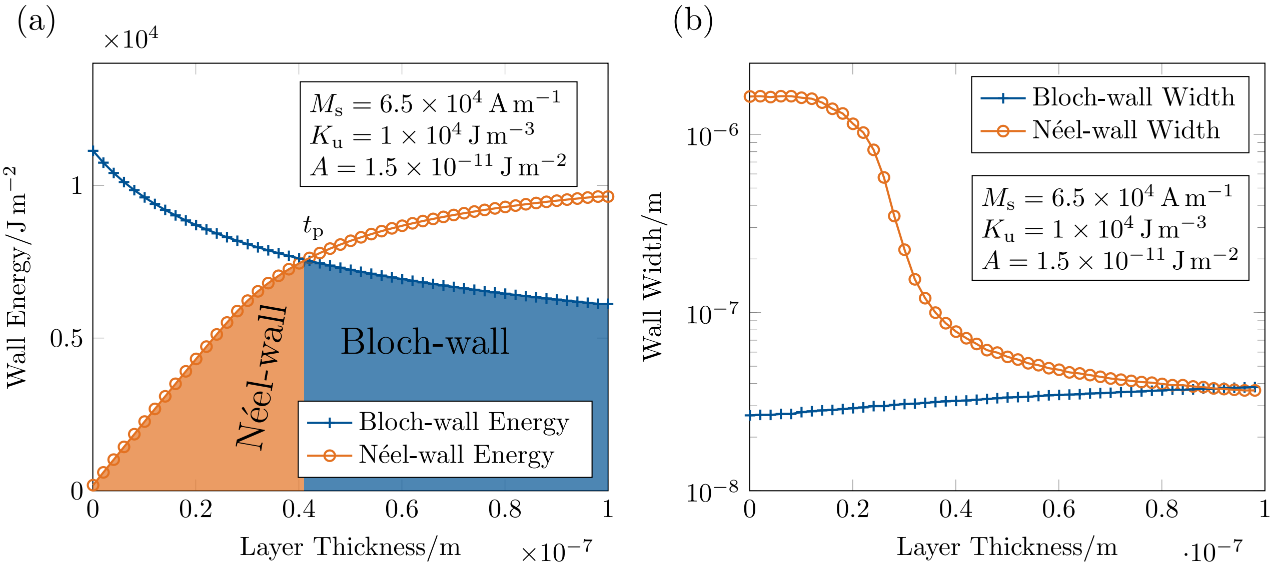

**Figure A1** Calculated domain wall energies (a) and corresponding wall-widths (b) for pure *Bloch* and *Néel* walls, depending on the magnetic layer thickness. A model according to *S. Middelhoek* is used to derive the wall energies by minimizing Equation A.1 and A.2 for $\Delta_\mathrm{w}$ and using it to calculate $E_\mathrm{w}$ [268]. The calculations are done for a soft magnetic layer with a saturation magnetization of $M_\mathrm{s} \approx 6.5 \times 10^4\,\mathrm{A\,m^{-1}}$, an uniaxial anisotropy of $K_\mathrm{u} \approx 1 \times 10^4\,\mathrm{J\,m^{-3}}$ and an exchange stiffness of $A \approx 1.5 \times 10^{-11}\,\mathrm{J\,m^{-2}}$ (values taken from [268]). All material parameter are assumed to be thickness independent.

such calculations made for a soft in-plane magnetic layer with a saturation magnetization of $M_\mathrm{s} \approx 6.5 \times 10^4\,\mathrm{A\,m^{-1}}$, an uni-axial anisotropy of $K_\mathrm{u} \approx 1 \times 10^4\,\mathrm{J\,m^{-3}}$ and an exchange stiffness of $A \approx 1.5 \times 10^{-11}\,\mathrm{J\,m^{-2}}$ (value taken from literature). When analyzing the development of the wall-energies (A1 (a)), we find opposing trends for *Néel* and *Bloch* walls with a transition from *Néel* to *Bloch*-walls at $\approx 41\,\mathrm{nm}$. When considering Equation A.2 for *Néel*-walls, we find, that upon approaching very small thicknesses ($< 40\,\mathrm{nm}$), the stray-field energy ($\mu_0 \frac{M_\mathrm{s}^2 t}{\Delta_\mathrm{w}^{N\acute{e}el} + t} \Delta_\mathrm{w}^{N\acute{e}el}$) decreases quickly, allowing for very wide domain walls, resulting in reduced total wall energies. This results in a preferred *Néel* wall configuration at thicknesses below this transition point $t_\mathrm{p}$. The position of $t_\mathrm{p}$ is now inversely proportional to $M_\mathrm{s}$ (a reduction of $M_\mathrm{s}$ by 50 % doubles $t_\mathrm{p}$) and in first approximation independent of $K_\mathrm{u}$ and $A$. We can summise, that *Néel*-walls are likeliest to be found in systems with a small saturation magnetization (not considering additional effects like iDMI, etc.). The validity of this model is however limited to films with a homogeneous stray field distribution. A more sophisticated analytical model for different nanostructures can be found in [109].

# Appendix B

## Information on the Simulation Parameter

The micromagnetic finite-difference simulations were performed using the GPU-accelerated package MuMax3 [92]. We considered a disk with a diameter of 1 µm, and film thicknesses of 1.0 nm with perpendicular magnetic anisotropy. The material parameter were taken from measurements where possible. The saturation magnetization was $M_\mathrm{s} = 8.3 \times 10^5\,\mathrm{A\,m^{-1}}$ and $M_\mathrm{s} = 6.5 \times 10^5\,\mathrm{A\,m^{-1}}$ for non-irradiated and homogeneously irradiated dots respectively. The exchange constant was always set to $A = 2 \times 10^{-11}\,\mathrm{J\,m^{-1}}$. The uniaxial anisotropy constants of the films were $K_\mathrm{u} = 5.6 \times 10^5\,\mathrm{J\,m^{-3}}$ for non-irradiated dots and $K_\mathrm{u} = 4.5 \times 10^5\,\mathrm{J\,m^{-3}}$ for homogeneously irradiated dots. The damping constant was taken from the literature [255] and set to $\alpha = 0.015$. The temperature was set to 0 K. The discretization of the sample was $2.5 \times 2.5\,\mathrm{nm}^3$. The nucleation center was modeled as a disk with a diameter ranging from 100 nm to 400 nm with a step size of 100 nm. The Zeeman field was a square wave with finite slope and a pulse width of 80 ns, it was switched off for additional 80 ns to let the dot reach a local minimum energy configuration. The value of damping parameter $\alpha$ was varied by up to 20 %, however, no significant effects could be observed.

### Multi-Domain State at Reduced Pulse Widths

The simulations shown in section 8.2.2 were also done with intermediate pulse widths, resulting in different domain configurations. Figure C1 depicts the magnetization reversal process for a pulse width of 30 ns. Here, the reduced pulse width leads to an incomplete magnetization reversal and a quasi-stable multi-domain configuration.

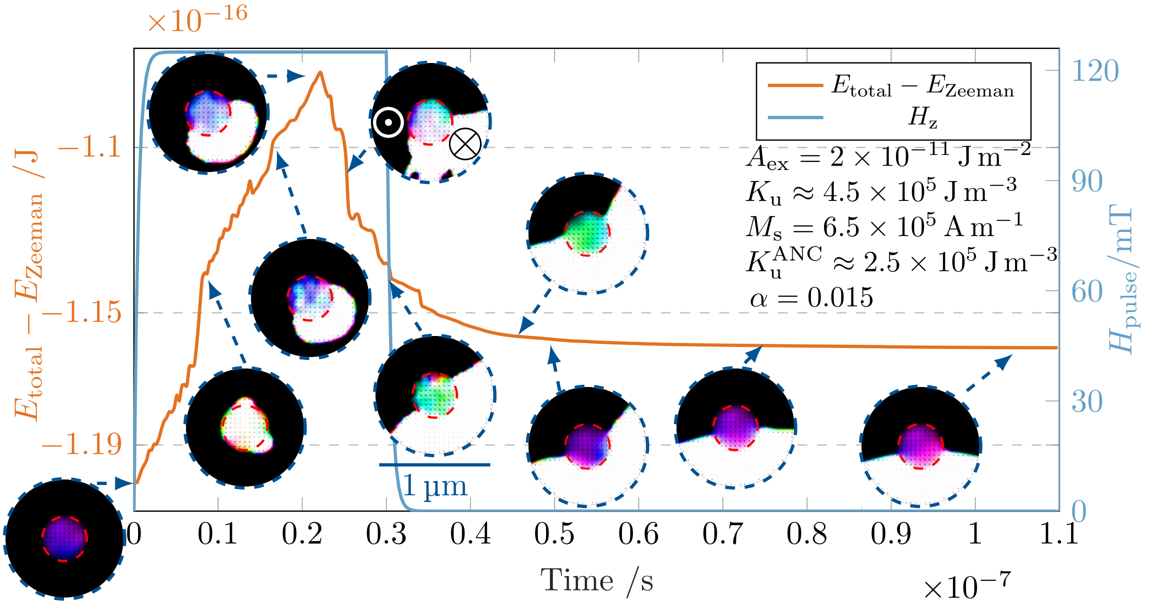

**Figure C1** Plot of the simulated magnetization reversal process, depicting a 1 µm circular nanomagnet with centered ANC ($d$ = 400 nm). The graph displays the combined magnetic energies (excluding the *Zeeman* term) in combination with snapshots of the domain structure at relevant points. The assumed material parameters are listed in the plot.

# Appendix C

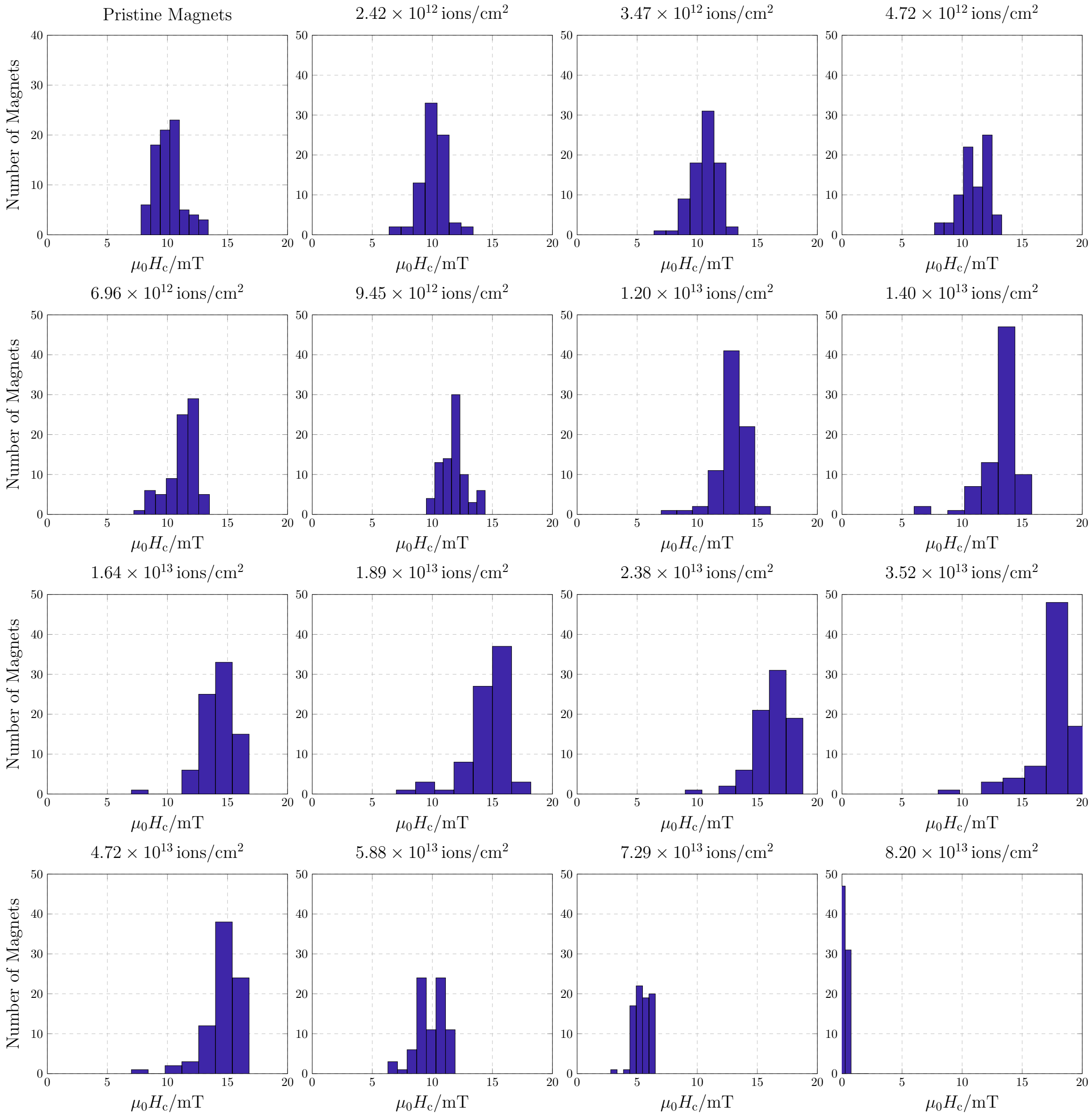

**Figure C1** Series of histograms, depicting the $Ga^+$ ion dose dependent switching field distributions of $Ta_2/CoFeB_1/MgO_2/Ta_2$ nanomagnets.

# Appendix D

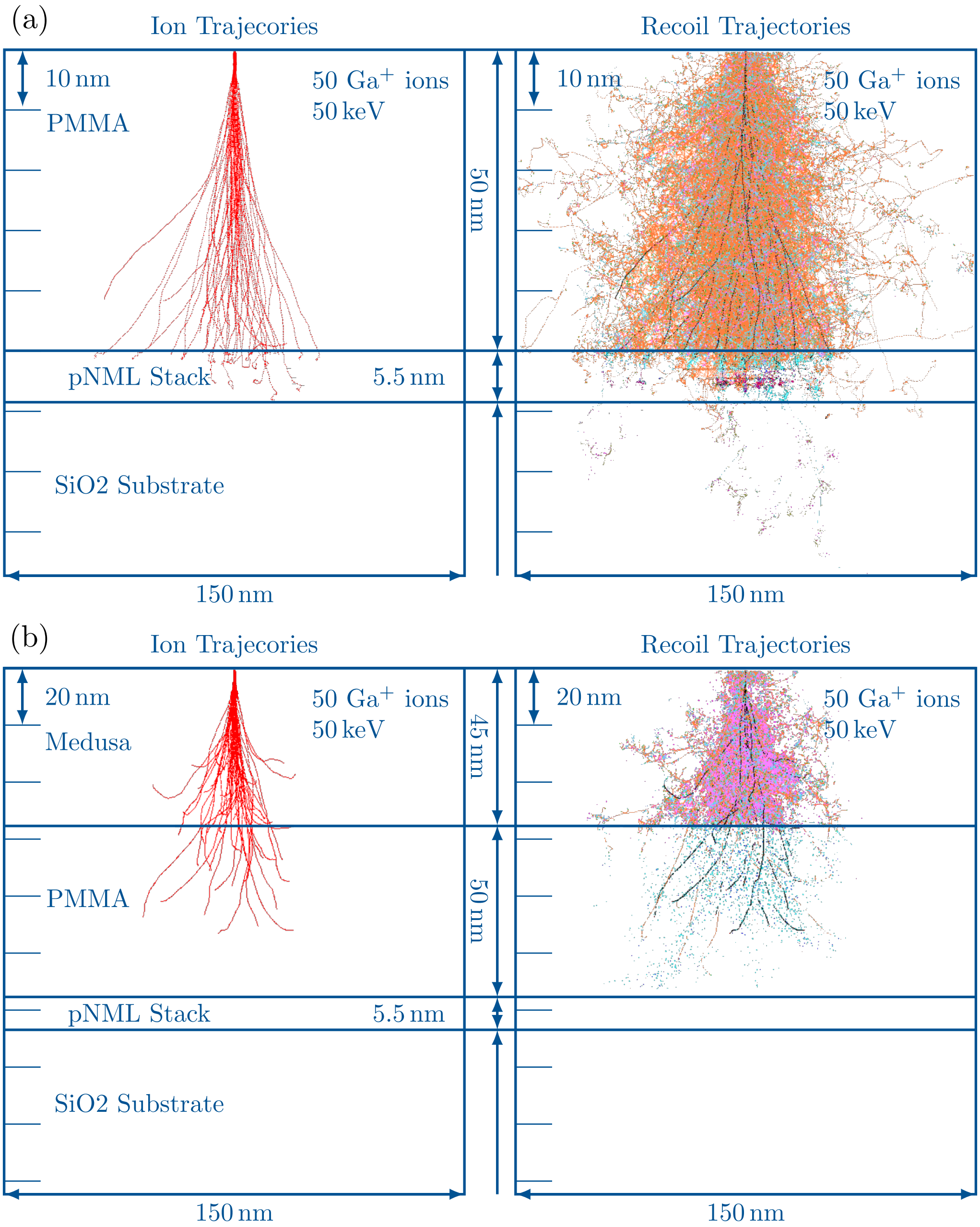

**Figure D1** SRIM simulations, showing the 50 keV Ga$^+$ ion range in PMMA and *Medusa* resists. In (a), the Ga$^+$ ion trajectories and recoil events are shown for the direct irradiation of a 50 nm thick PMMA resist on top of the pNML stack. In (b), the Ga$^+$ ion trajectories and recoil events are shown for the direct irradiation of a 45 nm thick *Medusa* (HSQ) layer on top of a 50 nm thick PMMA resists.

# Own Publications

## Journal Articles

- S. Mendisch, F. Riente, V. Ahrens, L. Gnoli, M. Haider, M. Opel, M. Kiechle, M. Ruo Roch, and M. Becherer, “Controlling domain-wall nucleation in Ta/Co-Fe-B/MgO nanomagnets via local $Ga^+$ ion irradiation”, *Phys. Rev. Applied*, vol. 16, p. 014 039, 1 2021. doi: `10.1103/PhysRevApplied.16.014039`.

- S. Mendisch, V. Ahrens, M. Kiechle, Á. Papp, and M. Becherer, “Perpendicular nanomagnetic logic based on low anisotropy Co/Ni multilayer”, *Journal of Magnetism and Magnetic Materials*, vol. 510, p. 166 626, 2020. doi: `10.1016/j.jmmm.2020.166626`.

- S. Mendisch, G. Žiemys, V. Ahrens, Á. Papp, and M. Becherer, “Pt/Co/W as a candidate for low power nanomagnetic logic”, *Journal of Magnetism and Magnetic Materials*, vol. 485, pp. 345–350, 2019. doi: `10.1016/j.jmmm.2019.03.088`.

- F. Riente, S. Mendisch, L. Gnoli, V. Ahrens, M. R. Roch, and M. Becherer, “Ta/CoFeB/MgO analysis for low power nanomagnetic devices”, *AIP Advances*, vol. 10, no. 12, p. 125 229, 2020. doi: `10.1063/9.0000013`.

- V. Ahrens, C. Kiesselbach, L. Gnoli, D. Giuliano, S. Mendisch, M. Kiechle, F. Riente, and M. Becherer, “Skyrmions under control—fib irradiation as a versatile tool for skyrmion circuits”, *Advanced Materials*, vol. 35, no. 2, p. 2 207 321, 2023. doi: `10.1002/adma.202207321`.

- V. Ahrens, S. Mendisch, W. Kaiser, M. Kiechle, S. B.-v. Gamm, and M. Becherer, “Focused ion beam irradiation for generation of skyrmionic bubble like structures”, *Journal of Magnetism and Magnetic Materials*, vol. 523, p. 167 591, doi: `10.1016/j.jmmm.2020.167591`.

- K. Szulc, S. Mendisch, M. Mruczkiewicz, F. Casoli, M. Becherer, and G. Gubbiotti, “Nonreciprocal spin-wave dynamics in Pt/Co/W/Co/Pt multilayers”, *Physical Review B*, vol. 103, no. 13, p. 134 404, 2021. doi: `10.1103/PhysRevB.103.134404`.

- G. Ziemys, V. Ahrens, S. Mendisch, G. Csaba, and M. Becherer, “Speeding up nanomagnetic logic by dmi enhanced Pt/Co/Ir films”, *AIP Advances*, vol. 8, no. 5, p. 056 310, 2018. doi: `10.1063/1.5007308`.

- L. Flacke, V. Ahrens, S. Mendisch, L. Körber, T. Böttcher, E. Meidinger, M. Yaqoob, M. Müller, L. Liensberger, A. Kákay, *et al.*, “Robust formation of nanoscale magnetic skyrmions in easy-plane anisotropy thin film multilayers with low damping”, *Physical Review B*, vol. 104, no. 10, p. L100417, 2021. doi: `10.1103/PhysRevB.104.L100417`.

- M. Kiechle, A. Papp, S. Mendisch, V. Ahrens, M. Golibrzuch, G. H. Bernstein, W. Porod, G. Csaba, and M. Becherer, “Spin-Wave Optics in YIG Realized by Ion-Beam Irradiation”, *Small*, p. 2 207 293, 2023. doi: `10.1002/smll.202207293`.

- Á. Papp, M. Kiechle, S. Mendisch, V. Ahrens, L. Sahin, L. Seitner, W. Porod, G. Csaba, and M. Becherer, “Experimental demonstration of a concave grating for spin waves in the Rowland arrangement”, *Scientific Reports*, vol. 11, no. 1, pp. 1–8, 2021. doi: `10.1038/s41598-021-93700-z`.

- T. L. Maier, M. Golibrzuch, S. Mendisch, W. Schindler, M. Becherer, and K. Krischer, “Lateral silicon oxide/gold interfaces enhance the rate of electrochemical hydrogen evolution reaction in alkaline media”, *The Journal of chemical physics*, vol. 152, no. 15, p. 154 705, 2020. DOI: `10.1063/5.0003295`.
- V. Ahrens, L. Gnoli, D. Giuliano, S. Mendisch, M. Kiechle, F. Riente, and M. Becherer, “Skyrmion velocities in fib irradiated w/cofeb/mgo thin films”, *AIP Advances*, vol. 12, no. 3, p. 035 325, 2022. DOI: `10.1063/9.0000287`.

## Relevant Conference Presentations

- S. Mendisch, G. Žiemys, V. Ahrens, Á. Papp, and M. Becherer, “Pt/Co/W as a candidate for low power nanomagnetic logic”, in *Joint European Magnetic Symposia , Talk A-1256, 2018-09*, Mainz Germany, Sep. 2018.
- S. Mendisch, V. Ahrens, M. Kiechle, A. Papp, and M. Becherer, “Perpendicular Nanomagnetic Logic Based on Ultra-low Anisotropy Co/Ni Multilayers”, in *Joint European Magnetic Symposia , Talk O82, 2019-09*, Uppsala Sweden, Aug. 2019.
- S. Mendisch, M. Kiechle, V. Ahrens, A. Papp, and M. Becherer, “Ion-Beam Controlled Switching Field Distributions in the Low Coercivity Regime”, in *Conference on Magnetism and Magnetic Materials , Poster GP-02, 2019-11*, Las Vegas US, Nov. 2019.

# Bibliography

[1] R. Allenspach, M. Stampanoni, and A. Bischof, "Magnetic domains in thin epitaxial Co/Au (111) films", *Physical Review Letters*, vol. 65, no. 26, p. 3344, 1990. DOI: 10.1103/PhysRevLett.65.3344.

[2] G. Binasch, P. Grünberg, F. Saurenbach, and W. Zinn, "Enhanced magnetoresistance in layered magnetic structures with antiferromagnetic interlayer exchange", *Physical review B*, vol. 39, no. 7, p. 4828, 1989. DOI: 10.1103/PhysRevB.39.4828.

[3] M. N. Baibich, J. M. Broto, A. Fert, F. N. Van Dau, F. Petroff, P. Etienne, G. Creuzet, A. Friederich, and J. Chazelas, "Giant magnetoresistance of (001) Fe/(001) Cr magnetic superlattices", *Physical review letters*, vol. 61, no. 21, p. 2472, 1988. DOI: 10.1103/PhysRevLett.61.2472.

[4] W. N. Papian, "The MIT magnetic-core memory", in *Papers and discussions presented at the Dec. 8-10, 1953, eastern joint AIEE-IRE computer conference: information processing systems—reliability and requirements*, 1953, pp. 37–42. DOI: 10.1145/1434878.1434888.

[5] J. P. Eckert Jr, J. R. Weiner, H. F. Welsh, and H. F. Mitchell, "The UNIVAC system", in *Papers and discussions presented at the Dec. 10-12, 1951, joint AIEE-IRE computer conference: Review of electronic digital computers*, 1951, pp. 6–16. DOI: 10.1145/1434770.1434772.

[6] W. Beausoleil, D. Brown, and B. Phelps, "Magnetic bubble memory organization", *IBM Journal of Research and Development*, vol. 16, no. 6, pp. 587–591, 1972. DOI: 10.1147/rd.166.0587.

[7] H. Washburn and P. Silverman, "A multiplexed 4 Mbit bubble memory device", *IEEE journal of solid-state circuits*, vol. 18, no. 5, pp. 567–571, 1983. DOI: 10.1109/JSSC.1983.1051995.

[8] T. C. Chen and H. Chang, "Magnetic bubble memory and logic", in *Advances in Computers*, vol. 17, Elsevier, 1978, pp. 223–282. DOI: 10.1016/S0065-2458(08)60393-9.

[9] R. Sandfort and E. Burke, "Logic functions for magnetic bubble devices", *IEEE Transactions on Magnetics*, vol. 7, no. 3, pp. 358–360, 1971. DOI: 10.1109/TMAG.1971.1067089.

[10] N. Z. Haron and S. Hamdioui, "Why is CMOS scaling coming to an END?", in *2008 3rd International Design and Test Workshop*, IEEE, 2008, pp. 98–103. DOI: 10.1109/IDT.2008.4802475.

[11] T. Skotnicki, J. A. Hutchby, T.-J. King, H.-S. Wong, and F. Boeuf, "The end of cmos scaling: Toward the introduction of new materials and structural changes to improve mosfet performance", *IEEE Circuits and Devices Magazine*, vol. 21, no. 1, pp. 16–26, 2005. DOI: 10.1109/MCD.2005.1388765.

[12] "Counting Down to the End of Moore's Law", *The New York Times*, 2009. [Online]. Available: https://bits.blogs.nytimes.com/2009/05/22/counting-down-to-the-end-of-moores-law.

[13] "International Roadmap for Devices and Systems (IRDS): BEYOND CMOS Chapter", 2021. [Online]. Available: irds.ieee.org.

[14] R. P. Feynman, "There's plenty of room at the bottom", *Journal of microelectromechanical systems*, vol. 1, no. 1, pp. 60–66, 1992. DOI: 10.1109/84.128057.

[15] M. T. Bohr and I. A. Young, "CMOS scaling trends and beyond", *IEEE Micro*, vol. 37, no. 6, pp. 20–29, 2017. DOI: 10.1109/MM.2017.4241347.

[16] W. Scotten, “Economics in the 3D Era”, *ICKnowledge*, 2020. [Online]. Available: `https://semiwiki.com/wp-content/uploads/2020/03/Lithovision-2020.pdf`.

[17] “Technology and Cost Trends at Advanced Nodes”, *ICKnowledge*, 2021. [Online]. Available: `www.icknowledge.com/index.html`.

[18] Y. C. Wu, “High Speed MRAM with Voltage Control of Magnetic Anisotropy (VCMA) Effect”, Ph.D. dissertation, 2021. [Online]. Available: `https://lirias.kuleuven.be/3363743?limo=0`.

[19] Y. Wu, W. Kim, K. Garello, F. Yasin, G. Jayakumar, S. Couet, R. Carpenter, S. Kundu, S. Rao, D. Crotti, *et al.*, “Deterministic and field-free voltage-controlled MRAM for high performance and low power applications”, in *2020 IEEE Symposium on VLSI Technology*, IEEE, 2020, pp. 1–2. DOI: `10.1109/VLSITechnology18217.2020.9265057`.

[20] S. S. Parkin, M. Hayashi, and L. Thomas, “Magnetic domain-wall racetrack memory”, *Science*, vol. 320, no. 5873, pp. 190–194, 2008. DOI: `10.1126/science.1145799`.

[21] R. Bläsing, A. A. Khan, P. C. Filippou, C. Garg, F. Hameed, J. Castrillon, and S. S. Parkin, “Magnetic racetrack memory: From physics to the cusp of applications within a decade”, *Proceedings of the IEEE*, vol. 108, no. 8, pp. 1303–1321, 2020. DOI: `10.1109/JPROC.2020.2975719`.

[22] N. Sharma, J. Bird, C. Binek, P. Dowben, D. Nikonov, and A. Marshall, “Evolving magneto-electric device technologies”, *Semiconductor Science and Technology*, vol. 35, no. 7, p. 073 001, 2020. DOI: `10.1088/1361-6641/ab8438`.

[23] S. Manipatruni, D. E. Nikonov, C.-C. Lin, T. A. Gosavi, H. Liu, B. Prasad, Y.-L. Huang, E. Bonturim, R. Ramesh, and I. A. Young, “Scalable energy-efficient magnetoelectric spin-orbit logic”, *Nature*, vol. 565, no. 7737, pp. 35–42, 2019. DOI: `10.1038/s41586-018-0770-2`.

[24] A. Chumak, P. Kabos, M. Wu, C. Abert, C. Adelmann, A. Adeyeye, J. Åkerman, F. Aliev, A. Anane, A. Awad, *et al.*, “Roadmap on spin-wave computing concepts”, *IEEE Transactions on Quantum Engineering*, 2021. DOI: `10.48550/arXiv.2111.00365`.

[25] G. Csaba, Á. Papp, and W. Porod, “Perspectives of using spin waves for computing and signal processing”, *Physics Letters A*, vol. 381, no. 17, pp. 1471–1476, 2017. DOI: `10.1016/j.physleta.2017.02.042`.

[26] Á. Papp, W. Porod, Á. I. Csurgay, and G. Csaba, “Nanoscale spectrum analyzer based on spin-wave interference”, *Scientific reports*, vol. 7, no. 1, pp. 1–9, 2017. DOI: `10.1038/s41598-017-09485-7`.

[27] Á. Papp, M. Kiechle, S. Mendisch, V. Ahrens, L. Sahin, L. Seitner, W. Porod, G. Csaba, and M. Becherer, “Experimental demonstration of a concave grating for spin waves in the Rowland arrangement”, *Scientific Reports*, vol. 11, no. 1, pp. 1–8, 2021. DOI: `10.1038/s41598-021-93700-z`.

[28] A. Papp, G. Csaba, and W. Porod, “Characterization of nonlinear spin-wave interference by reservoir-computing metrics”, *Applied Physics Letters*, vol. 119, no. 11, p. 112 403, 2021. DOI: `10.1063/5.0048982`.

[29] D. A. Connelly, G. Csaba, H. R. O. Aquino, G. H. Bernstein, A. Orlov, W. Porod, and J. Chisum, “Efficient electromagnetic transducers for spin-wave devices”, *Scientific Reports*, vol. 11, no. 1, pp. 1–14, 2021. DOI: `10.1038/s41598-021-97627-3`.

[30] S. Breitkreutz-von Gamm, A. Papp, E. Egel, C. Meier, C. Yilmaz, L. Heiss, W. Porod, and G. Csaba, “Design of on-chip readout circuitry for spin-wave devices”, *IEEE Magnetics Letters*, vol. 8, pp. 1–4, 2016. DOI: `10.1109/LMAG.2016.2618779`.

[31] E. Egel, G. Csaba, A. Dietz, S. Breitkreutz-von Gamm, J. Russer, P. Russer, F. Kreupl, and M. Becherer, “Design of a 40-nm CMOS integrated on-chip oscilloscope for 5-50 GHz spin wave characterization”, *AIP Advances*, vol. 8, no. 5, p. 056 001, 2018. DOI: `10.1063/1.5007435`.

[32] D. Smith, “A magnetic shift register employing controlled domain wall motion”, *IEEE Transactions on Magnetics*, vol. 1, no. 4, pp. 281–284, 1965. DOI: `0.1109/TMAG.1965.1062979`.

[33] R. Spain and H. Jauvtis, “Controlled domain tip propagation. Part I and II”, *Journal of Applied Physics*, vol. 37, no. 7, pp. 2572–2593, 1966. DOI: `10.1063/1.1782087`.

[34] R. Spain and M. Marino, “Magnetic film domain-wall motion devices”, *IEEE Transactions on Magnetics*, vol. 6, no. 3, pp. 451–463, 1970. DOI: `10.1109/TMAG.1970.1066853`.

[35] R. Spain, “Domain tip propagation logic”, *IEEE Transactions on Magnetics*, vol. 2, no. 3, pp. 347–351, 1966. DOI: `10.1109/TMAG.1966.1065929`.

[36] D. Allwood, G. Xiong, M. Cooke, C. Faulkner, D. Atkinson, N. Vernier, and R. Cowburn, “Submicrometer ferromagnetic NOT gate and shift register”, *Science*, vol. 296, no. 5575, pp. 2003–2006, 2002. DOI: `10.1126/science.1070595`.

[37] Z. Luo, A. Hrabec, T. P. Dao, G. Sala, S. Finizio, J. Feng, S. Mayr, J. Raabe, P. Gambardella, and L. J. Heyderman, “Current-driven magnetic domain-wall logic”, *Nature*, vol. 579, no. 7798, pp. 214–218, 2020. DOI: `10.1038/s41586-020-2061-y`.

[38] E. Raymenants, D. Wan, S. Couet, L. Souriau, A. Thiam, D. Tsvetanova, Y. Canvel, I. Asselberghs, M. Heyns, D. E. Nikonov, *et al.*, “All-electrical control of scaled spin logic devices based on domain wall motion”, in *2020 IEEE International Electron Devices Meeting (IEDM)*, IEEE, 2020, pp. 21–5. DOI: `10.1109/IEDM13553.2020.9372127`.

[39] E. Raymenants, O. Bultynck, D. Wan, T. Devolder, K. Garello, L. Souriau, A. Thiam, D. Tsvetanova, Y. Canvel, D. Nikonov, *et al.*, “Nanoscale domain wall devices with magnetic tunnel junction read and write”, *Nature Electronics*, vol. 4, no. 6, pp. 392–398, 2021. DOI: `10.1038/s41928-021-00593-x`.

[40] G. Csaba, A. Imre, G. H. Bernstein, W. Porod, and V. Metlushko, “Nanocomputing by field-coupled nanomagnets”, *IEEE Transactions on Nanotechnology*, vol. 1, no. 4, pp. 209–213, 2002. DOI: `10.1109/TNANO.2002.807380`.

[41] G. Csaba, *Computing with field-coupled nanomagnets*. University of Notre Dame, 2003. [Online]. Available: `https://ui.adsabs.harvard.edu/abs/2003PhDT........24C`.

[42] A. Imre, G. Csaba, L. Ji, A. Orlov, G. Bernstein, and W. Porod, “Majority logic gate for magnetic quantum-dot cellular automata”, *Science*, vol. 311, no. 5758, pp. 205–208, 2006. DOI: `10.1126/science.1120506`.

[43] I. Hänninen, H. Lu, E. Blair, C. Lent, and G. Snider, “Field-Coupled Nanocomputing: Paradigms, Progress, and Perspectives”, 2014. DOI: `10.1007/978-3-662-43722-3`.

[44] G. Csaba, P. Lugli, and W. Porod, “Power dissipation in nanomagnetic logic devices”, in *4th IEEE Conference on Nanotechnology, 2004.*, IEEE, 2004, pp. 346–348. DOI: `10.1109/NANO.2004.1392346`.

[45] G. Csaba, P. Lugli, A. Csurgay, and W. Porod, “Simulation of power gain and dissipation in field-coupled nanomagnets”, *Journal of Computational Electronics*, vol. 4, no. 1, pp. 105–110, 2005. DOI: `10.1007/s10825-005-7118-5`.

[46] E. Varga, M. T. Niemier, G. Csaba, G. H. Bernstein, and W. Porod, “Experimental realization of a nanomagnet full adder using slanted-edge magnets”, *IEEE transactions on magnetics*, vol. 49, no. 7, pp. 4452–4455, 2013. DOI: `10.1109/TMAG.2013.2249576`.

[47] M. Parish and M. Forshaw, “Physical constraints on magnetic quantum cellular automata”, *Applied Physics Letters*, vol. 83, no. 10, pp. 2046–2048, 2003. DOI: `10.1063/1.1608492`.

[48] E. Varga, G. Csaba, G. Bernstein, and W. Porod, “Implementation of a nanomagnetic full adder circuit”, in *2011 11th IEEE International Conference on Nanotechnology*, IEEE, 2011, pp. 1244–1247. DOI: `10.1109/NANO.2011.6144445`.

[49] M. T. Alam, S. J. Kurtz, M. A. J. Siddiq, M. T. Niemier, G. H. Bernstein, X. S. Hu, and W. Porod, "On-chip clocking of nanomagnet logic lines and gates", *IEEE Transactions on Nanotechnology*, vol. 11, no. 2, pp. 273–286, 2011. DOI: `10.1109/TNANO.2011.2169983`.

[50] S. Breitkreutz-von Gamm, "Perpendicular Nanomagnetic Logic: Digital Logic Circuits from Field-coupled Magnets", Ph.D. dissertation, Universitätsbibliothek der TU München, 2015. [Online]. Available: `https://mediatum.ub.tum.de/1293292`.

[51] S. Breitkreutz, I. Eichwald, J. Kiermaier, A. Papp, G. Csaba, M. Niemier, W. Porod, D. Schmitt-Landsiedel, and M. Becherer, "1-bit full adder in perpendicular nanomagnetic logic using a novel 5-input majority gate", in *EPJ web of conferences*, EDP Sciences, vol. 75, 2014, p. 05 001. DOI: `10.1051/epjconf/20147505001`.

[52] M. Becherer, S. B.-v. Gamm, I. Eichwald, G. Žiemys, J. Kiermaier, G. Csaba, and D. Schmitt-Landsiedel, "A monolithic 3D integrated nanomagnetic co-processing unit", *Solid-State Electronics*, vol. 115, pp. 74–80, 2016. DOI: `10.1016/j.sse.2015.08.004`.

[53] I. Eichwald, S. Breitkreutz, G. Ziemys, G. Csaba, W. Porod, and M. Becherer, "Majority logic gate for 3D magnetic computing", *Nanotechnology*, vol. 25, no. 33, p. 335 202, 2014. DOI: `10.1088/0957-4484/25/33/335202`.

[54] S. Breitkreutz, I. Eichwald, G. Ziemys, G. Hiblot, G. Csaba, D. Schmitt-Landsiedel, and M. Becherer, "Towards nonvolatile magnetic crossbar arrays: A three-dimensional-integrated field-coupled domain wall gate with perpendicular anisotropy", *Journal of Applied Physics*, vol. 117, no. 17, p. 17D507, 2015. DOI: `10.1063/1.4913729`.

[55] F. Riente, G. Ziemys, G. Turvani, D. Schmitt-Landsiedel, S. B.-v. Gamm, and M. Graziano, "Towards logic-in-memory circuits using 3d-integrated nanomagnetic logic", in *2016 IEEE International Conference on Rebooting Computing (ICRC)*, IEEE, 2016, pp. 1–8. DOI: `10.1109/ICRC.2016.7738700`.

[56] M. Becherer, J. Kiermaier, S. Breitkreutz, I. Eichwald, G. Žiemys, G. Csaba, and D. Schmitt-Landsiedel, "Towards on-chip clocking of perpendicular nanomagnetic logic", *Solid-State Electronics*, vol. 102, pp. 46–51, 2014. DOI: `10.1016/j.sse.2014.06.012`.

[57] J. Kiermaier, S. Breitkreutz, I. Eichwald, X. Ju, G. Csaba, D. Schmitt-Landsiedel, and M. Becherer, "Programmable input for nanomagnetic logic devices", in *EPJ Web of Conferences*, EDP Sciences, vol. 40, 2013, p. 16 007. DOI: `10.1051/epjconf/20134016007`.

[58] J. Kiermaier, S. Breitkreutz, G. Csaba, D. Schmitt-Landsiedel, and M. Becherer, "Electrical input structures for nanomagnetic logic devices", *Journal of Applied Physics*, vol. 111, no. 7, 07E341, 2012. DOI: `10.1063/1.3678584`.

[59] J. Kiermaier, S. Breitkreutz, X. Ju, G. Csaba, D. Schmitt-Landsiedel, and M. Becherer, "Field-coupled computing: Investigating the properties of ferromagnetic nanodots", *Solid-state electronics*, vol. 65, pp. 240–245, 2011. DOI: `10.1016/j.sse.2011.06.027`.

[60] R. Waser, "Nanoelectronics and Information Technology, 2nd", *Nanoelectronics and Information Technology*, p. 995, 2005. DOI: `10.1109/ICRC.2016.7738700`.

[61] I. Eichwald, A. Bartel, J. Kiermaier, S. Breitkreutz, G. Csaba, D. Schmitt-Landsiedel, and M. Becherer, "Nanomagnetic logic: Error-free, directed signal transmission by an inverter chain", *IEEE Transactions on Magnetics*, vol. 48, no. 11, pp. 4332–4335, 2012. DOI: `10.1109/TMAG.2012.2196030`.

[62] J. Kiermaier, S. Breitkreutz, I. Eichwald, M. Engelstädter, X. Ju, G. Csaba, D. Schmitt-Landsiedel, and M. Becherer, "Information transport in field-coupled nanomagnetic logic devices", *Journal of Applied Physics*, vol. 113, no. 17, 17B902, 2013. DOI: `10.1063/1.4794184`.

[63] S. Breitkreutz, J. Kiermaier, S. Vijay Karthik, G. Csaba, D. Schmitt-Landsiedel, and M. Becherer, "Controlled reversal of Co/Pt dots for nanomagnetic logic applications", *Journal of Applied Physics*, vol. 111, no. 7, 07A715, 2012. DOI: `10.1063/1.3675171`.

[64] S. Breitkreutz, J. Kiermaier, I. Eichwald, X. Ju, G. Csaba, D. Schmitt-Landsiedel, and M. Becherer, “Majority gate for nanomagnetic logic with perpendicular magnetic anisotropy”, *IEEE Transactions on Magnetics*, vol. 48, no. 11, pp. 4336–4339, 2012. DOI: `10.1109/TMAG.2012.2197184`.

[65] Y. Seon, J. Chang, C. Yoo, and J. Jeon, “Device and circuit exploration of multi-nanosheet transistor for sub-3 nm technology node”, *Electronics*, vol. 10, no. 2, p. 180, 2021. DOI: `10.3390/electronics10020180`.

[66] C. Pan, P. Raghavan, D. Yakimets, P. Debacker, F. Catthoor, N. Collaert, Z. Tokei, D. Verkest, A. V.-Y. Thean, and A. Naeemi, “Technology/system codesign and benchmarking for lateral and vertical gaa nanowire fets at 5-nm technology node”, *IEEE Transactions on Electron Devices*, vol. 62, no. 10, pp. 3125–3132, 2015. DOI: `10.1109/TED.2015.2461457`.

[67] Q. Xie, X. Lin, Y. Wang, S. Chen, M. J. Dousti, and M. Pedram, “Performance comparisons between 7-nm finfet and conventional bulk cmos standard cell libraries”, *IEEE Transactions on Circuits and Systems II: Express Briefs*, vol. 62, no. 8, pp. 761–765, 2015. DOI: `10.1109/TCSII.2015.2391632`.

[68] T. L. Maier, M. Golibrzuch, S. Mendisch, W. Schindler, M. Becherer, and K. Krischer, “Lateral silicon oxide/gold interfaces enhance the rate of electrochemical hydrogen evolution reaction in alkaline media”, *The Journal of chemical physics*, vol. 152, no. 15, p. 154 705, 2020. DOI: `10.1063/5.0003295`.

[69] V. Ahrens, L. Gnoli, D. Giuliano, S. Mendisch, M. Kiechle, F. Riente, and M. Becherer, “Skyrmion velocities in fib irradiated w/cofeb/mgo thin films”, *AIP Advances*, vol. 12, no. 3, p. 035 325, 2022. DOI: `10.1063/9.0000287`.

[70] J. M. Coey, *Magnetism and magnetic materials*. Cambridge university press, 2010. DOI: `10.1017/CBO9780511845000`.

[71] L. Bergmann, C. Schaefer, and S. Blügel, *Lehrbuch der Experimentalphysik 6. Festkörper*. Walter de Gruyter, 2005, vol. 6, ISBN: 978-3110174854.

[72] A. Einstein and W. De Haas, “Experimental proof of the existence of Ampère’s molecular currents”, in *Proc. KNAW*, vol. 181, 1915, p. 696.

[73] M. Getzlaff, *Fundamentals of magnetism*. Springer Science & Business Media, 2007. DOI: `10.1007/978-3-540-31152-2`.

[74] W. Shockley, “The quantum physics of solids, i the energies of electrons in crystals”, *The Bell System Technical Journal*, vol. 18, no. 4, pp. 645–723, 1939. DOI: `10.1002/j.1538-7305.1939.tb00821.x`.

[75] A. P. Guimarães and A. P. Guimaraes, *Principles of nanomagnetism*. Springer, 2009, vol. 7. DOI: `10.1007/978-3-642-01482-6`.

[76] J.-Y. Choi, H. Jun, K. Ashiba, J.-U. Baek, T.-H. Shim, and J.-G. Park, “Double pinned perpendicular-magnetic-tunnel-junction spin-valve providing multi-level resistance states”, *Scientific reports*, vol. 9, no. 1, pp. 1–9, 2019. DOI: `10.1038/s41598-019-48311-0`.

[77] J. Swerts, S. Mertens, T. Lin, S. Couet, Y. Tomczak, K. Sankaran, G. Pourtois, W. Kim, J. Meersschaut, L. Souriau, *et al.*, “BEOL compatible high tunnel magneto resistance perpendicular magnetic tunnel junctions using a sacrificial Mg layer as CoFeB free layer cap”, *Applied Physics Letters*, vol. 106, no. 26, p. 262 407, 2015. DOI: `10.1063/1.4923420`.

[78] M.-H. Nguyen, D. Ralph, and R. Buhrman, “Spin torque study of the spin hall conductivity and spin diffusion length in platinum thin films with varying resistivity”, *Physical review letters*, vol. 116, no. 12, p. 126 601, 2016. DOI: `10.1103/PhysRevLett.116.126601`.

[79] P. Hadley, “Lecture notes on molecular and solid state physics”, [Online]. Available: `http://lamp.tu-graz.ac.at/~hadley/ss1/skriptum/outline.php`.

[80] B. Dieny, I. L. Prejbeanu, K. Garello, P. Gambardella, P. Freitas, R. Lehndorff, W. Raberg, U. Ebels, S. O. Demokritov, J. Akerman, *et al.*, "Opportunities and challenges for spintronics in the microelectronics industry", *Nature Electronics*, vol. 3, no. 8, pp. 446–459, 2020. DOI: `10.1038/s41928-020-0461-5`.

[81] A. Khvalkovskiy, D. Apalkov, S. Watts, R. Chepulskii, R. Beach, A. Ong, X. Tang, A. Driskill-Smith, W. Butler, P. Visscher, *et al.*, "Basic principles of stt-mram cell operation in memory arrays", *Journal of Physics D: Applied Physics*, vol. 46, no. 7, p. 074 001, 2013. DOI: `10.1088/0022-3727/46/7/074001`.

[82] S. Mendisch, G. Žiemys, V. Ahrens, Á. Papp, and M. Becherer, "Pt/Co/W as a candidate for low power nanomagnetic logic", *Journal of Magnetism and Magnetic Materials*, vol. 485, pp. 345–350, 2019. DOI: `10.1016/j.jmmm.2019.03.088`.

[83] M. Kuepferling, A. Casiraghi, G. Soares, G. Durin, F. Garcia-Sanchez, L. Chen, C. H. Back, C. H. Marrows, S. Tacchi, and G. Carlotti, "Measuring interfacial Dzyaloshinskii-Moriya interaction in ultra thin films", *arXiv*, 2020. DOI: `10.48550/arXiv.2009.11830`.

[84] F. Hellman, A. Hoffmann, Y. Tserkovnyak, G. S. Beach, E. E. Fullerton, C. Leighton, A. H. MacDonald, D. C. Ralph, D. A. Arena, H. A. Dürr, *et al.*, "Interface-induced phenomena in magnetism", *Reviews of modern physics*, vol. 89, no. 2, p. 025 006, 2017. DOI: `10.1103/RevModPhys.89.025006`.

[85] T. Dohi, R. M. Reeve, and M. Kläui, "Thin film skyrmionics", *Annual Review of Condensed Matter Physics*, vol. 13, 2021. DOI: `10.1146/annurev-conmatphys-031620-110344`.

[86] A. Malozemoff and J. Slonczewski, *Magnetic domain walls in bubble materials: advances in materials and device research*. Academic press, 2016, vol. 1, ISBN: 9781483214764.

[87] A. Aharoni, "Demagnetizing factors for rectangular ferromagnetic prisms", *Journal of applied physics*, vol. 83, no. 6, pp. 3432–3434, 1998. DOI: `10.1063/1.367113`.

[88] J. Osborn, "Demagnetizing factors of the general ellipsoid", *Physical review*, vol. 67, no. 11-12, p. 351, 1945. DOI: `10.1103/PhysRev.67.351`.

[89] A. Mougin, M. Cormier, J. Adam, P. Metaxas, and J. Ferré, "Domain wall mobility, stability and walker breakdown in magnetic nanowires", *EPL (Europhysics Letters)*, vol. 78, no. 5, p. 57 007, 2007. DOI: `10.1209/0295-5075/78/57007`.

[90] M. Johnson, P. Bloemen, F. Den Broeder, and J. De Vries, "Magnetic anisotropy in metallic multilayers", *Reports on Progress in Physics*, vol. 59, no. 11, p. 1409, 1996. DOI: `10.1088/0034-4885/59/11/002`.

[91] S. Bandiera, R. Sousa, B. Rodmacq, and B. Dieny, "Asymmetric interfacial perpendicular magnetic anisotropy in Pt/Co/Pt trilayers", *IEEE Magnetics Letters*, vol. 2, pp. 3 000 504–3 000 504, 2011. DOI: `10.1109/LMAG.2011.2174032`.

[92] A. Vansteenkiste, J. Leliaert, M. Dvornik, M. Helsen, F. Garcia-Sanchez, and B. Van Waeyenberge, "The design and verification of MuMax3", *AIP Advances*, vol. 4, no. 10, p. 107 133, 2014. DOI: `10.1063/1.4899186`.

[93] "The Object Oriented MicroMagnetic Framework (OOMMF)", 1998. [Online]. Available: `http://math.nist.gov/oommf/`.

[94] T. L. Gilbert, "A phenomenological theory of damping in ferromagnetic materials", *IEEE transactions on magnetics*, vol. 40, no. 6, pp. 3443–3449, 2004. DOI: `10.1109/TMAG.2004.836740`.

[95] L. Landau and E. Lifshitz, "On the theory of the dispersion of magnetic permeability in ferromagnetic bodies", in *Perspectives in Theoretical Physics*, Elsevier, 1992, pp. 51–65. DOI: `10.1016/B978-0-08-036364-6.50008-9`.

[96] M. Lakshmanan, "The fascinating world of the Landau–Lifshitz–Gilbert equation: an overview", *Philosophical Transactions of the Royal Society A: Mathematical, Physical and Engineering Sciences*, vol. 369, no. 1939, pp. 1280–1300, 2011. DOI: 10.1098/rsta.2010.0319.

[97] T. Gilbert and J. Kelly, "Anomalous rotational damping in ferromagnetic sheets", in *Conf. Magnetism and Magnetic Materials, Pittsburgh, PA*, 1955, pp. 253–263.

[98] J. C. Slonczewski, "Current-driven excitation of magnetic multilayers", *Journal of Magnetism and Magnetic Materials*, vol. 159, no. 1-2, pp. L1–L7, 1996. DOI: 10.1016/0304-8853(96)00062-5.

[99] A. Thiaville, Y. Nakatani, J. Miltat, and Y. Suzuki, "Micromagnetic understanding of current-driven domain wall motion in patterned nanowires", *EPL (Europhysics Letters)*, vol. 69, no. 6, p. 990, 2005. DOI: 10.1209/epl/i2004-10452-6.

[100] J. Leliaert, J. Mulkers, J. De Clercq, A. Coene, M. Dvornik, and B. Van Waeyenberge, "Adaptively time stepping the stochastic Landau-Lifshitz-Gilbert equation at nonzero temperature: Implementation and validation in MuMax3", *Aip Advances*, vol. 7, no. 12, p. 125 010, 2017. DOI: 10.1063/1.5003957.

[101] J. Leliaert and J. Mulkers, "Tomorrow's micromagnetic simulations", *Journal of Applied Physics*, vol. 125, no. 18, p. 180 901, 2019. DOI: 10.1063/1.5093730.

[102] E. C. Stoner and E. Wohlfarth, "A mechanism of magnetic hysteresis in heterogeneous alloys", *Philosophical Transactions of the Royal Society of London. Series A, Mathematical and Physical Sciences*, vol. 240, no. 826, pp. 599–642, 1948. DOI: 10.1098/rsta.1948.0007.

[103] C. Tannous and J. Gieraltowski, "The Stoner–Wohlfarth model of ferromagnetism", *European journal of physics*, vol. 29, no. 3, p. 475, 2008. DOI: 10.1088/0143-0807/29/3/008.

[104] B. Kaplan and G. Gehring, "The domain structure in ultrathin magnetic films", *Journal of Magnetism and Magnetic Materials*, vol. 128, no. 1-2, pp. 111–116, 1993. DOI: 10.1016/0304-8853(93)90863-W.

[105] B. Kaplan, "Ferromagnetic stripe domains in ultrathin films", *Journal of magnetism and magnetic materials*, vol. 288, pp. 178–182, 2005. DOI: 10.1016/j.jmmm.2004.08.034.

[106] B. Kaplan, "Domain morphology in ultrathin ferromagnetic films with perpendicular magnetization", *Journal of magnetism and magnetic materials*, vol. 298, no. 2, pp. 135–138, 2006. DOI: 10.1016/j.jmmm.2005.03.092.

[107] A. Sukstanskii and K. Primak, "Domain structure in an ultrathin ferromagnetic film", *Journal of magnetism and magnetic materials*, vol. 169, no. 1-2, pp. 31–38, 1997. DOI: 10.1016/S0304-8853(96)00729-9.

[108] O. Hellwig, A. Berger, J. B. Kortright, and E. E. Fullerton, "Domain structure and magnetization reversal of antiferromagnetically coupled perpendicular anisotropy films", *Journal of Magnetism and Magnetic Materials*, vol. 319, no. 1-2, pp. 13–55, 2007. DOI: 10.1016/j.jmmm.2007.04.035.

[109] M. DeJong and K. Livesey, "Analytic theory for the switch from bloch to néel domain wall in nanowires with perpendicular anisotropy", *Physical Review B*, vol. 92, no. 21, p. 214 420, 2015. DOI: 10.1103/PhysRevB.92.214420.

[110] M. DeJong and K. Livesey, "Domain walls in finite-width nanowires with interfacial dzyaloshinskii-moriya interaction", *Physical Review B*, vol. 95, no. 5, p. 054 424, 2017. DOI: 10.1103/PhysRevB.95.054424.

[111] M. P. Sharrock, "Measurement and interpretation of magnetic time effects in recording media", *IEEE Transactions on Magnetics*, vol. 35, no. 6, pp. 4414–4422, 1999. DOI: 10.1109/20.809133.

[112] J. Vogel, J. Moritz, and O. Fruchart, "Nucleation of magnetisation reversal, from nanoparticles to bulk materials", *Comptes Rendus Physique*, vol. 7, no. 9-10, pp. 977–987, 2006. DOI: 10.1016/j.crhy.2006.10.011.

[113] W. F. Brown Jr, "Thermal fluctuations of a single-domain particle", *Physical Review*, vol. 130, no. 5, p. 1677, 1963. DOI: `10.1103/PhysRev.130.1677`.

[114] L. Néel, "Théorie du traînage magnétique des ferromagnétiques en grains fins avec application aux terres cuites", *Annales de géophysique*, vol. 5, pp. 99–136, 1949. [Online]. Available: `https://hal.archives-ouvertes.fr/hal-03070532`.

[115] S.-B. Choe, D.-H. Kim, K.-S. Ryu, H.-S. Lee, and S.-C. Shin, "Direct observation of Barkhausen effect in strip-patterned ferromagnetic Co/Pd multilayer films", *Journal of applied physics*, vol. 99, no. 10, p. 103 902, 2006. DOI: `10.1063/1.2199978`.

[116] W. Wernsdorfer, E. B. Orozco, K. Hasselbach, A. Benoit, B. Barbara, N. Demoncy, A. Loiseau, H. Pascard, and D. Mailly, "Experimental evidence of the néel-brown model of magnetization reversal", *Physical Review Letters*, vol. 78, no. 9, p. 1791, 1997. DOI: `10.1103/PhysRevLett.78.1791`.

[117] M. Sharrock, "Time dependence of switching fields in magnetic recording media", *Journal of Applied Physics*, vol. 76, no. 10, pp. 6413–6418, 1994. DOI: `10.1063/1.358282`.

[118] T. Gerhardt, A. Drews, and G. Meier, "Controlled pinning and depinning of domain walls in nanowires with perpendicular magnetic anisotropy", *Journal of Physics: Condensed Matter*, vol. 24, no. 2, p. 024 208, 2011. DOI: `10.1088/0953-8984/24/2/024208`.

[119] J. H. Franken, M. Hoeijmakers, R. Lavrijsen, and H. J. Swagten, "Domain-wall pinning by local control of anisotropy in Pt/Co/Pt strips", *Journal of Physics: Condensed Matter*, vol. 24, no. 2, p. 024 216, 2011. DOI: `10.1088/0953-8984/24/2/024216`.

[120] R. Lavrijsen, J. Franken, J. Kohlhepp, H. Swagten, and B. Koopmans, "Controlled domain-wall injection in perpendicularly magnetized strips", *Applied Physics Letters*, vol. 96, no. 22, p. 222 502, 2010. DOI: `10.1063/1.3432703`.

[121] K.-J. Kim and S.-B. Choe, "Analytic theory of wall configuration and depinning mechanism in magnetic nanostructure with perpendicular magnetic anisotropy", *Journal of Magnetism and Magnetic Materials*, vol. 321, no. 14, pp. 2197–2199, 2009. DOI: `10.1016/j.jmmm.2009.01.031`.

[122] K.-J. Kim, G.-H. Gim, J.-C. Lee, S.-M. Ahn, K.-S. Lee, Y. J. Cho, C.-W. Lee, S. Seo, K.-H. Shin, and S.-B. Choe, "Depinning field at notches of ferromagnetic nanowires with perpendicular magnetic anisotropy", *IEEE Transactions on Magnetics*, vol. 45, no. 10, pp. 4056–4058, 2009. DOI: `10.1109/TMAG.2009.2024893`.

[123] A. Himeno, S. Kasai, and T. Ono, "Depinning fields of a magnetic domain wall from asymmetric notches", *Journal of applied physics*, vol. 99, no. 8, 08G304, 2006. DOI: `10.1063/1.2167327`.

[124] S. Breitkreutz, I. Eichwald, J. Kiermaier, G. Hiblot, G. Csaba, W. Porod, D. Schmitt-Landsiedel, and M. Becherer, "Controlled domain wall pinning in nanowires with perpendicular magnetic anisotropy by localized fringing fields", *Journal of Applied Physics*, vol. 115, no. 17, p. 17D506, 2014. DOI: `10.1063/1.4864737`.

[125] P. Metaxas, J. Jamet, A. Mougin, M. Cormier, J. Ferré, V. Baltz, B. Rodmacq, B. Dieny, and R. Stamps, "Creep and flow regimes of magnetic domain-wall motion in ultrathin Pt/Co/Pt films with perpendicular anisotropy", *Physical review letters*, vol. 99, no. 21, p. 217 208, 2007. DOI: `10.1103/PhysRevLett.99.217208`.

[126] G. S. Beach, C. Nistor, C. Knutson, M. Tsoi, and J. L. Erskine, "Dynamics of field-driven domain-wall propagation in ferromagnetic nanowires", *Nature materials*, vol. 4, no. 10, pp. 741–744, 2005. DOI: `10.1038/nmat1477`.

[127] J. Hütner, T. Herranen, and L. Laurson, "Multistep Bloch-line-mediated Walker breakdown in ferromagnetic strips", *Physical Review B*, vol. 99, no. 17, p. 174 427, 2019. DOI: `10.1103/PhysRevB.99.174427`.

[128] P. Chauve, T. Giamarchi, and P. Le Doussal, "Creep and depinning in disordered media", *Physical Review B*, vol. 62, no. 10, p. 6241, 2000. DOI: 10.1103/PhysRevB.62.6241.

[129] P. Lendecke, R. Eiselt, G. Meier, and U. Merkt, "Temperature dependence of domain-wall depinning fields in constricted Permalloy nanowires", *Journal of Applied Physics*, vol. 103, no. 7, p. 073 909, 2008. DOI: 10.1063/1.2903932.

[130] T. H. Pham, J. Vogel, J. Sampaio, M. Vaňatka, J.-C. Rojas-Sánchez, M. Bonfim, D. Chaves, F. Choueikani, P. Ohresser, E. Otero, *et al.*, "Very large domain wall velocities in Pt/Co/GdOx and Pt/Co/Gd trilayers with Dzyaloshinskii-Moriya interaction", *EPL (Europhysics Letters)*, vol. 113, no. 6, p. 67 001, 2016. DOI: 10.1209/0295-5075/113/67001.

[131] F. Riente, S. Mendisch, L. Gnoli, V. Ahrens, M. R. Roch, and M. Becherer, "Ta/CoFeB/MgO analysis for low power nanomagnetic devices", *AIP Advances*, vol. 10, no. 12, p. 125 229, 2020. DOI: 10.1063/9.0000013.

[132] J. Shibata, G. Tatara, and H. Kohno, "A brief review of field-and current-driven domain-wall motion", *Journal of Physics D: Applied Physics*, vol. 44, no. 38, p. 384 004, 2011. DOI: 10.1088/0022-3727/44/38/384004.

[133] I. Lemesh and G. S. Beach, "Walker breakdown with a twist: Dynamics of multilayer domain walls and skyrmions driven by spin-orbit torque", *Physical Review Applied*, vol. 12, no. 4, p. 044 031, 2019. DOI: 10.1103/PhysRevApplied.12.044031.

[134] A. Kirilyuk, J. Ferré, V. Grolier, J. Jamet, and D. Renard, "Magnetization reversal in ultrathin ferromagnetic films with perpendicular anisotropy", *Journal of magnetism and magnetic materials*, vol. 171, no. 1-2, pp. 45–63, 1997. DOI: 10.1016/S0304-8853(96)00744-5.

[135] A. Himeno, T. Okuno, T. Ono, K. Mibu, S. Nasu, and T. Shinjo, "Temperature dependence of depinning fields in submicron magnetic wires with an artificial neck", *Journal of magnetism and magnetic materials*, vol. 286, pp. 167–170, 2005. DOI: 10.1016/j.jmmm.2004.09.023.

[136] H.-S. P. Wong, C.-S. Lee, J. Luo, and C.-H. Wang, "CMOS Technology Scaling Trend", 2020. [Online]. Available: https://nano.stanford.edu/cmos-technology-scaling-trend.

[137] S. B.-v. Gamm, G. Ziemys, I. Eichwald, D. Schmitt-Landsiedel, M. Becherer, G. Csaba, G. H. Bernstein, and W. Porod, "Device-level compact modeling of perpendicular nanomagnetic logic for benchmarking purposes", in *Nanotechnology (IEEE-NANO), 2015 IEEE 15th International Conference on*, IEEE, 2015, pp. 1033–1036. DOI: 10.1109/NANO.2015.7388796.

[138] I. Eichwald, "Perpendicular nanomagnetic logic: Three-dimensional devices for non-volatile field-coupled computing", Ph.D. dissertation, Technische Universität München, 2016. [Online]. Available: http://mediatum.ub.tum.de/?id=1277422.

[139] J. Kiermaier, "Integrated Nanomagnetic Logic System in Perpendicular Magnetic Media", Ph.D. dissertation, Technische Universität München, 2014. [Online]. Available: https://mediatum.ub.tum.de/1206044.

[140] M. Becherer, "Nanomagnetic Logic in Focused Ion Beam Engineered Co/Pt Multilayer Films", Ph.D. dissertation, Technische Universität München, 2011. [Online]. Available: https://mediatum.ub.tum.de/1116274.

[141] W. F. Brown Jr, "The fundamental theorem of the theory of fine ferromagnetic particles", *Annals of the New York Academy of Sciences*, vol. 147, no. 12, pp. 463–488, 1969. DOI: 10.1111/j.1749-6632.1969.tb41269.x.

[142] S. Mendisch, V. Ahrens, M. Kiechle, Á. Papp, and M. Becherer, "Perpendicular nanomagnetic logic based on low anisotropy Co/Ni multilayer", *Journal of Magnetism and Magnetic Materials*, vol. 510, p. 166 626, 2020. DOI: 10.1016/j.jmmm.2020.166626.

[143] S. Mendisch, F. Riente, V. Ahrens, L. Gnoli, M. Haider, M. Opel, M. Kiechle, M. Ruo Roch, and M. Becherer, “Controlling domain-wall nucleation in Ta/Co-Fe-B/MgO nanomagnets via local $Ga^+$ ion irradiation”, *Phys. Rev. Applied*, vol. 16, p. 014 039, 1 2021. DOI: 10.1103/PhysRevApplied.16.014039.

[144] G. Ziemys, G. Csaba, and M. Becherer, “On the discrimination between nucleation and propagation in nanomagnetic logic devices”, *AIP Advances*, vol. 8, no. 5, p. 056 003, 2018. DOI: 10.1063/1.5006935.

[145] G. Ziemys, V. Ahrens, S. Mendisch, G. Csaba, and M. Becherer, “Speeding up nanomagnetic logic by dmi enhanced Pt/Co/Ir films”, *AIP Advances*, vol. 8, no. 5, p. 056 310, 2018. DOI: 10.1063/1.5007308.

[146] S. Dutta, S. A. Siddiqui, J. A. Currivan-Incorvia, C. A. Ross, and M. A. Baldo, “Micromagnetic modeling of domain wall motion in sub-100-nm-wide wires with individual and periodic edge defects”, *AIP Advances*, vol. 5, no. 12, p. 127 206, 2015. DOI: 10.1063/1.4937557.

[147] S. Breitkreutz, J. Kiermaier, X. Ju, G. Csaba, D. Schmitt-Landsiedel, and M. Becherer, “Nanomagnetic logic: Demonstration of directed signal flow for field-coupled computing devices”, in *2011 Proceedings of the European Solid-State Device Research Conference (ESSDERC)*, IEEE, 2011, pp. 323–326. DOI: 10.1109/ESSDERC.2011.6044169.

[148] S. Breitkreutz, J. Kiermaier, I. Eichwald, C. Hildbrand, G. Csaba, D. Schmitt-Landsiedel, and M. Becherer, “Experimental demonstration of a 1-bit full adder in perpendicular nanomagnetic logic”, *IEEE Transactions on Magnetics*, vol. 49, no. 7, pp. 4464–4467, 2013. DOI: 10.1109/TMAG.2013.2243704.

[149] S. Breitkreutz, G. Ziemys, I. Eichwald, J. Kiermaier, G. Csaba, W. Porod, D. Schmitt-Landsiedel, and M. Becherer, “Domain wall gate for magnetic logic and memory applications with perpendicular anisotropy”, in *Electron Devices Meeting (IEDM), 2013 IEEE International*, IEEE, 2013, pp. 22–4. DOI: 10.1109/IEDM.2013.6724684.

[150] I. Eichwald, J. Kiermaier, S. Breitkreutz, J. Wu, G. Csaba, D. Schmitt-Landsiedel, and M. Becherer, “Towards a signal crossing in double-layer nanomagnetic logic”, *IEEE Transactions on Magnetics*, vol. 49, no. 7, pp. 4468–4471, 2013. DOI: 10.1109/TMAG.2013.2238898.

[151] I. Eichwald, S. Breitkreutz, J. Kiermaier, G. Csaba, D. Schmitt-Landsiedel, and M. Becherer, “Signal crossing in perpendicular nanomagnetic logic”, *Journal of Applied Physics*, vol. 115, no. 17, 17E510, 2014. DOI: 10.1063/1.4863810.

[152] G. Žiemys, A. Giebfried, M. Becherer, I. Eichwald, D. Schmitt-Landsiedel, and S. B.-v. Gamm, “Modeling and simulation of nanomagnetic logic with Cadence Cirtuoso using Verilog-A”, *Solid-State Electronics*, vol. 125, pp. 247–253, 2016. DOI: 10.1016/j.sse.2016.05.013.

[153] M. Manfrini, A. Vaysset, D. Wan, E. Raymenants, J. Swerts, S. Rao, O. Zografos, L. Souriau, K. B. Gavan, N. Rassoul, *et al.*, “Interconnected magnetic tunnel junctions for spin-logic applications”, *AIP Advances*, vol. 8, no. 5, p. 055 921, 2018. DOI: 10.1063/1.5007622.

[154] M. Becherer, J. Kiermaier, S. Breitkreutz, G. Csaba, X. Ju, J. Rezgani, T. Kießling, C. Yilmaz, P. Osswald, P. Lugli, *et al.*, “On-chip Extraordinary Hall-effect sensors for characterization of nanomagnetic logic devices”, *Solid-State Electronics*, vol. 54, no. 9, pp. 1027–1032, 2010. DOI: 10.1016/j.sse.2010.04.011.

[155] J. Kiermaier, S. Breitkreutz, X. Ju, G. Csaba, D. Schmitt-Landsiedel, and M. Becherer, “Ultra-low volume ferromagnetic nanodots for field-coupled computing devices”, in *2010 Proceedings of the European Solid State Device Research Conference*, IEEE, 2010, pp. 214–217. DOI: 10.1109/ESSDERC.2010.5618385.

[156] Y. Xu, Y. Yang, H. Xie, and Y. Wu, “Spin hall magnetoresistance sensor using auxpt1- x as the spin-orbit torque biasing layer”, *Applied Physics Letters*, vol. 115, no. 18, p. 182 406, 2019. DOI: 10.1063/1.5127838.

[157] M. Becherer, J. Kiermaier, S. Breitkreutz, I. Eichwald, G. Csaba, and D. Schmitt-Landsiedel, "Nanomagnetic logic clocked in the Mhz regime", in *2013 Proceedings of the European Solid-State Device Research Conference (ESSDERC)*, IEEE, 2013, pp. 276–279. DOI: `10.1109/ESSDERC.2013.6818872`.

[158] K.-M. Lee, J. W. Choi, J. Sok, and B.-C. Min, "Temperature dependence of the interfacial magnetic anisotropy in w/cofeb/mgo", *AIP Advances*, vol. 7, no. 6, p. 065 107, 2017. DOI: `10.1063/1.4985720`.

[159] H. Sato, P. Chureemart, F. Matsukura, R. Chantrell, H. Ohno, and R. Evans, "Temperature-dependent properties of cofeb/mgo thin films: Experiments versus simulations", *Physical Review B*, vol. 98, no. 21, p. 214 428, 2018. DOI: `10.1103/PhysRevB.98.214428`.

[160] K. Narayanapillai, X. Qiu, J. Rhensius, and H. Yang, "Thermally assisted domain wall nucleation in perpendicular anisotropy trilayer nanowires", *Journal of Physics D: Applied Physics*, vol. 47, no. 10, p. 105 005, 2014. DOI: `10.1088/0022-3727/47/10/105005`.

[161] W. F. Brown Jr, "Relaxational behavior of fine magnetic particles", *Journal of Applied physics*, vol. 30, no. 4, S130–S132, 1959. DOI: `10.1063/1.2185851`.

[162] P. Carcia, "Perpendicular magnetic anisotropy in Pd/Co and Pt/Co thin-film layered structures", *Journal of applied physics*, vol. 63, no. 10, pp. 5066–5073, 1988. DOI: `10.1063/1.340404`.

[163] D. Treves, J. Jacobs, and E. Sawatzky, "Platinum-cobalt films for digital magneto-optic recording", *Journal of Applied Physics*, vol. 46, no. 6, pp. 2760–2765, 1975. DOI: `10.1063/1.321953`.

[164] C. Vaz, J. Bland, and G. Lauhoff, "Magnetism in ultrathin film structures", *Reports on Progress in Physics*, vol. 71, no. 5, p. 056 501, 2008. DOI: `10.1088/0034-4885/71/5/056501`.

[165] P. Chowdhury, P. Kulkarni, M. Krishnan, H. C. Barshilia, A. Sagdeo, S. Rai, G. Lodha, and D. Sridhara Rao, "Effect of coherent to incoherent structural transition on magnetic anisotropy in Co/Pt multilayers", *Journal of Applied Physics*, vol. 112, no. 2, p. 023 912, 2012. DOI: `10.1063/1.4739284`.

[166] C.-J. Lin, G. Gorman, C. Lee, R. Farrow, E. Marinero, H. Do, H. Notarys, and C. Chien, "Magnetic and structural properties of Co/Pt multilayers", *Journal of Magnetism and Magnetic Materials*, vol. 93, pp. 194–206, 1991. DOI: `10.1016/0304-8853(91)90329-9`.

[167] M. Gabor, T. Petrisor Jr, R. Mos, M. Nasui, C. Tiusan, and T. Petrisor, "Interlayer exchange coupling in perpendicularly magnetized Pt/Co/Ir/Co/Pt structures", *Journal of Physics D: Applied Physics*, vol. 50, no. 46, p. 465 004, 2017. DOI: `10.1088/1361-6463/aa8ece`.

[168] G. Daalderop, P. Kelly, and F. Den Broeder, "Prediction and confirmation of perpendicular magnetic anisotropy in Co/Ni multilayers", *Physical review letters*, vol. 68, no. 5, p. 682, 1992. DOI: `10.1103/PhysRevLett.68.682`.

[169] M. Johnson, J. De Vries, N. McGee, J. Aan de Stegge, and F. Den Broeder, "Orientational dependence of the interface magnetic anisotropy in epitaxial Ni/Co/Ni sandwiches", *Physical review letters*, vol. 69, no. 24, p. 3575, 1992. DOI: `10.1103/PhysRevLett.69.3575`.

[170] P. Bloemen, W. De Jonge, and F. Den Broeder, "Magnetic anisotropies in Co/Ni (111) multilayers", *Journal of applied physics*, vol. 72, no. 10, pp. 4840–4844, 1992. DOI: `10.1063/1.352048`.

[171] Y. Yan, X. Lu, B. Liu, X. Zhang, X. Zheng, H. Meng, W. Liu, J. Wang, I. G. Will, J. Wu, *et al.*, "Element-specific spin and orbital moments and perpendicular magnetic anisotropy in Ta/CoFeB/MgOstructures", *Journal of Applied Physics*, vol. 127, no. 6, p. 063 903, 2020. DOI: `10.1063/1.5129489`.

[172] T. Liu, Y. Zhang, J. Cai, and H. Pan, "Thermally robust Mo/CoFeB/MgO trilayers with strong perpendicular magnetic anisotropy", *Scientific reports*, vol. 4, no. 1, pp. 1–6, 2014. DOI: `10.1038/srep05895`.

[173] S. Ikeda, K. Miura, H. Yamamoto, K. Mizunuma, H. Gan, M. Endo, S. Kanai, J. Hayakawa, F. Matsukura, and H. Ohno, "A perpendicular-anisotropy CoFeB–MgO magnetic tunnel junction", *Nature materials*, vol. 9, no. 9, pp. 721–724, 2010. DOI: `10.1038/nmat2804`.

[174] D. M. Lattery, D. Zhang, J. Zhu, X. Hang, J.-P. Wang, and X. Wang, "Low Gilbert damping constant in perpendicularly magnetized W/CoFeB/MgO films with high thermal stability", *Scientific reports*, vol. 8, no. 1, pp. 1–9, 2018. DOI: `10.1038/s41598-018-31642-9`.

[175] M. Arora, R. Hübner, D. Suess, B. Heinrich, and E. Girt, "Origin of perpendicular magnetic anisotropy in Co/Ni multilayers", *Physical Review B*, vol. 96, no. 2, p. 024 401, 2017. DOI: `10.1103/PhysRevB.96.024401`.

[176] A. Al Subhi and R. Sbiaa, "Control of magnetization reversal and domain structure in (Co/Ni) multilayers", *Journal of Magnetism and Magnetic Materials*, vol. 489, p. 165 460, 2019. DOI: `10.1016/j.jmmm.2019.165460`.

[177] E. Liu, J. Swerts, T. Devolder, S. Couet, S. Mertens, T. Lin, V. Spampinato, A. Franquet, T. Conard, S. Van Elshocht, *et al.*, "Seed layer impact on structural and magnetic properties of [Co/Ni] multilayers with perpendicular magnetic anisotropy", *Journal of Applied Physics*, vol. 121, no. 4, p. 043 905, 2017. DOI: `10.1063/1.4974885`.

[178] M. Fujita, K. Yamano, A. Maeda, T. Tanuma, and M. Kume, "Exchange coupling in spin-valve structures containing amorphous CoFeB", *Journal of applied physics*, vol. 81, no. 8, pp. 4909–4911, 1997. DOI: `10.1063/1.364816`.

[179] D. Worledge, G. Hu, D. W. Abraham, P. Trouilloud, and S. Brown, "Development of perpendicularly magnetized Ta | CoFeB | MgO-based tunnel junctions at IBM", *Journal of Applied Physics*, vol. 115, no. 17, p. 172 601, 2014. DOI: `10.1063/1.4870169`.

[180] A. Kaidatzis, C. Bran, V. Psycharis, M. Vázquez, J. M. Garcıa-Martın, and D. Niarchos, "Tailoring the magnetic anisotropy of CoFeB/Mgo stacks onto W with a Ta buffer layer", *Applied Physics Letters*, vol. 106, no. 26, p. 262 401, 2015. DOI: `10.1063/1.4923272`.

[181] J. Sinha, M. Hayashi, A. J. Kellock, S. Fukami, M. Yamanouchi, H. Sato, S. Ikeda, S. Mitani, S.-h. Yang, S. S. Parkin, *et al.*, "Enhanced interface perpendicular magnetic anisotropy in Ta | CoFeB | Mgo using nitrogen doped Ta underlayers", *Applied Physics Letters*, vol. 102, no. 24, p. 242 405, 2013. DOI: `10.1063/1.4811269`.

[182] J. Sinha, M. Gruber, M. Kodzuka, T. Ohkubo, S. Mitani, K. Hono, and M. Hayashi, "Influence of boron diffusion on the perpendicular magnetic anisotropy in Ta | CoFeB | Mgo ultrathin films", *Journal of Applied Physics*, vol. 117, no. 4, p. 043 913, 2015. DOI: `10.1063/1.4906096`.

[183] K. Garello, F. Yasin, S. Couet, L. Souriau, J. Swerts, S. Rao, S. Van Beek, W. Kim, E. Liu, S. Kundu, *et al.*, "SOT-MRAM 300mm integration for low power and ultrafast embedded memories", in *IEEE Symposium on VLSI Circuits*, IEEE, 2018, pp. 81–82. DOI: `10.1109/VLSIC.2018.8502269`.

[184] M. Gupta, M. Perumkunnil, K. Garello, S. Rao, F. Yasin, G. Kar, and A. Furnémont, "High-density SOT-MRAM technology and design specifications for the embedded domain at 5nm node", in *IEEE International Electron Devices Meeting (IEDM)*, IEEE, 2020, pp. 24–5. DOI: `10.1109/IEDM13553.2020.9372068`.

[185] D. Edelstein, M. Rizzolo, D. Sil, A. Dutta, J. DeBrosse, M. Wordeman, A. Arceo, I. Chu, J. Demarest, E. Edwards, *et al.*, "A 14 nm Embedded STT-MRAM CMOS Technology", in *2020 IEEE International Electron Devices Meeting (IEDM)*, IEEE, 2020, pp. 11–5. DOI: `10.1109/IEDM13553.2020.9371922`.

[186] C. Burrowes, N. Vernier, J.-P. Adam, L. Herrera Diez, K. Garcia, I. Barisic, G. Agnus, S. Eimer, J.-V. Kim, T. Devolder, *et al.*, "Low depinning fields in Ta-CoFeB-MgO ultrathin films with perpendicular magnetic anisotropy", *Applied Physics Letters*, vol. 103, no. 18, p. 182 401, 2013. DOI: `10.1063/1.4826439`.

[187] Z.-P. Li, S. Li, Y. Zheng, J. Fang, L. Chen, L. Hong, and H. Wang, "The study of origin of interfacial perpendicular magnetic anisotropy in ultra-thin CoFeB layer on the top of MgO based magnetic tunnel junction", *Applied Physics Letters*, vol. 109, no. 18, p. 182 403, 2016. DOI: 10.1063/1.4966891.

[188] S. Peng, M. Wang, H. Yang, L. Zeng, J. Nan, J. Zhou, Y. Zhang, A. Hallal, M. Chshiev, K. L. Wang, *et al.*, "Origin of interfacial perpendicular magnetic anisotropy in MgO/CoFeB/metallic capping layer structures", *Scientific reports*, vol. 5, no. 1, pp. 1–6, 2015. DOI: 10.1038/srep18173.

[189] S. Kanai, M. Tsujikawa, Y. Miura, M. Shirai, F. Matsukura, and H. Ohno, "Magnetic anisotropy in Ta/CoFeB/MgO investigated by x-ray magnetic circular dichroism and first-principles calculation", *Applied Physics Letters*, vol. 105, no. 22, p. 222 409, 2014. DOI: 10.1063/1.4903296.

[190] L. Vojáček, F. Ibrahim, A. Hallal, B. Dieny, and M. Chshiev, "Giant perpendicular magnetic anisotropy enhancement in MgO-based magnetic tunnel junction by using Co/Fe composite layer", *Physical Review Applied*, vol. 15, no. 2, p. 024 017, 2021. DOI: 10.1103/PhysRevApplied.15.024017.

[191] N. Miyakawa, D. Worledge, and K. Kita, "Impact of ta diffusion on the perpendicular magnetic anisotropy of Ta/CoFeB/MgO", *IEEE Magnetics Letters*, vol. 4, pp. 1 000 104–1 000 104, 2013. DOI: 10.1109/LMAG.2013.2240266.

[192] R. Lavrijsen, "Another spin in the wall: Domain wall dynamics in perpendicularly magnetized devices", 2011. DOI: 10.6100/IR693486.

[193] R. Lavrijsen, A. Fernández-Pacheco, D. Petit, R. Mansell, J. Lee, and R. Cowburn, "Tuning the interlayer exchange coupling between single perpendicularly magnetized CoFeB layers", *Applied Physics Letters*, vol. 100, no. 5, p. 052 411, 2012. DOI: 10.1063/1.3682103.

[194] H. Cheng, J. Chen, S. Peng, B. Zhang, Z. Wang, D. Zhu, K. Shi, S. Eimer, X. Wang, Z. Guo, *et al.*, "Giant Perpendicular Magnetic Anisotropy in Mo-Based Double-Interface Free Layer Structure for Advanced Magnetic Tunnel Junctions", *Advanced Electronic Materials*, vol. 6, no. 8, p. 2 000 271, 2020. DOI: 10.1002/aelm.202000271.

[195] T. Liu, J. Cai, and L. Sun, "Large enhanced perpendicular magnetic anisotropy in CoFeB/MgO system with the typical Ta buffer replaced by an Hf layer", *Aip Advances*, vol. 2, no. 3, p. 032 151, 2012. DOI: 10.1063/1.4748337.

[196] V. Naik, H. Meng, and R. Sbiaa, "Thick cofeb with perpendicular magnetic anisotropy in cofeb-mgo based magnetic tunnel junction", *Aip Advances*, vol. 2, no. 4, p. 042 182, 2012. DOI: 10.1063/1.4771996.

[197] K. Watanabe, S. Fukami, H. Sato, S. Ikeda, F. Matsukura, and H. Ohno, "Annealing temperature dependence of magnetic properties of CoFeB/MgO stacks on different buffer layers", *Japanese Journal of Applied Physics*, vol. 56, no. 8, 0802B2, 2017. DOI: 10.7567/JJAP.56.0802B2.

[198] G.-G. An, J.-B. Lee, S.-M. Yang, J.-H. Kim, W.-S. Chung, and J.-P. Hong, "Highly stable perpendicular magnetic anisotropies of CoFeB/MgO frames employing W buffer and capping layers", *Acta Materialia*, vol. 87, pp. 259–265, 2015. DOI: 10.1016/j.actamat.2015.01.022.

[199] N. Sato, R. M. White, and S. X. Wang, "Effect of annealing on exchange stiffness of ultrathin CoFeB film with perpendicular magnetic anisotropy", *Applied Physics Letters*, vol. 108, no. 15, p. 152 405, 2016. DOI: 10.1063/1.4945039.

[200] A. Serga, A. Chumak, and B. Hillebrands, "Yig magnonics", *Journal of Physics D: Applied Physics*, vol. 43, no. 26, p. 264 002, 2010. DOI: 10.1088/0022-3727/43/26/264002.

[201] S. M. Zanjani and M. C. Onbaşlı, "Predicting new iron garnet thin films with perpendicular magnetic anisotropy", *Journal of Magnetism and Magnetic Materials*, vol. 499, p. 166 108, 2020. DOI: 10.1016/j.jmmm.2019.166108.

[202] V. H. Ortiz, M. Aldosary, J. Li, Y. Xu, M. I. Lohmann, P. Sellappan, Y. Kodera, J. E. Garay, and J. Shi, “Systematic control of strain-induced perpendicular magnetic anisotropy in epitaxial europium and terbium iron garnet thin films”, *APL Materials*, vol. 6, no. 12, p. 121 113, 2018. DOI: `10.1063/1.5078645`.

[203] J. J. Bauer, E. R. Rosenberg, S. Kundu, K. A. Mkhoyan, P. Quarterman, A. J. Grutter, B. J. Kirby, J. A. Borchers, and C. A. Ross, “Dysprosium iron garnet thin films with perpendicular magnetic anisotropy on silicon”, *Advanced Electronic Materials*, vol. 6, no. 1, p. 1 900 820, 2020. DOI: `10.1002/aelm.201900820`.

[204] L. Caretta, S.-H. Oh, T. Fakhrul, D.-K. Lee, B. H. Lee, S. K. Kim, C. A. Ross, K.-J. Lee, and G. S. Beach, “Relativistic kinematics of a magnetic soliton”, *Science*, vol. 370, no. 6523, pp. 1438–1442, 2020. DOI: `10.1126/science.aba5555`.

[205] C. O. Avci, E. Rosenberg, L. Caretta, F. Büttner, M. Mann, C. Marcus, D. Bono, C. A. Ross, and G. S. Beach, “Interface-driven chiral magnetism and current-driven domain walls in insulating magnetic garnets”, *Nature nanotechnology*, vol. 14, no. 6, pp. 561–566, 2019. DOI: `10.1038/s41565-019-0421-2`.

[206] W. Ruane, S. White, J. Brangham, K. Meng, D. Pelekhov, F. Yang, and P. Hammel, “Controlling and patterning the effective magnetization in y3fe5o12 thin films using ion irradiation”, *AIP Advances*, vol. 8, no. 5, p. 056 007, 2018. DOI: `10.1063/1.5007058`.

[207] S. Emori and P. Li, “Ferrimagnetic insulators for spintronics: Beyond garnets”, *Journal of Applied Physics*, vol. 129, no. 2, p. 020 901, 2021. DOI: `10.1063/5.0033259`.

[208] D. Kim, Y.-W. Oh, J. U. Kim, S. Lee, A. Baucour, J. Shin, K.-J. Kim, B.-G. Park, and M.-K. Seo, “Extreme anti-reflection enhanced magneto-optic Kerr effect microscopy”, *Nature communications*, vol. 11, no. 1, pp. 1–8, 2020. DOI: `10.1038/s41467-020-19724-7`.

[209] H. C. Knoops, T. Faraz, K. Arts, and W. M. Kessels, “Status and prospects of plasma-assisted atomic layer deposition”, *Journal of Vacuum Science & Technology A: Vacuum, Surfaces, and Films*, vol. 37, no. 3, p. 030 902, 2019. DOI: `10.1116/1.5088582`.

[210] V. Dudnikov and A. Westner, “Ion source with closed drift anode layer plasma acceleration”, *Review of scientific instruments*, vol. 73, no. 2, pp. 729–731, 2002. DOI: `10.1063/1.1431703`.

[211] D. M. Mattox, *Handbook of physical vapor deposition (PVD) processing*. William Andrew, 2010, ISBN: 0471491101. DOI: `10.1016/B978-0-8155-2037-5.00016-2`.

[212] S. Hashimoto, Y. Ochiai, and K. Aso, “Perpendicular magnetic anisotropy and magnetostriction of sputtered Co/Pd and Co/Pt multilayered films”, *Journal of applied physics*, vol. 66, no. 10, pp. 4909–4916, 1989. DOI: `10.1063/1.343760`.

[213] K. Szulc, S. Mendisch, M. Mruczkiewicz, F. Casoli, M. Becherer, and G. Gubbiotti, “Nonreciprocal spin-wave dynamics in Pt/Co/W/Co/Pt multilayers”, *Physical Review B*, vol. 103, no. 13, p. 134 404, 2021. DOI: `10.1103/PhysRevB.103.134404`.

[214] J. F. Ziegler and J. P. Biersack, *The stopping and range of ions in matter*. Springer, 1985, pp. 93–129. DOI: `10.1007/978-1-4615-8103-1_3`.

[215] J. F. Ziegler, “The stopping and range of ions in matter”, DOI: `http://www.srim.org/`.

[216] G. Mair, “Emission from liquid metal ion sources”, *Nuclear Instruments and Methods*, vol. 172, no. 3, pp. 567–576, 1980. DOI: `10.1016/0029-554X(80)90350-X`.

[217] J. Fassbender, D. Ravelosona, and Y. Samson, “Tailoring magnetism by light-ion irradiation”, *Journal of Physics D: Applied Physics*, vol. 37, no. 16, R179, 2004. DOI: `10.1088/0022-3727/37/16/r01`.

[218] L. Flacke, V. Ahrens, S. Mendisch, L. Körber, T. Böttcher, E. Meidinger, M. Yaqoob, M. Müller, L. Liensberger, A. Kákay, *et al.*, "Robust formation of nanoscale magnetic skyrmions in easy-plane anisotropy thin film multilayers with low damping", *Physical Review B*, vol. 104, no. 10, p. L100417, 2021. DOI: `10.1103/PhysRevB.104.L100417`.

[219] J. Kerr, "XLIII. On rotation of the plane of polarization by reflection from the pole of a magnet", *The London, Edinburgh, and Dublin Philosophical Magazine and Journal of Science*, vol. 3, no. 19, pp. 321–343, 1877. DOI: `10.1080/14786447708639245`.

[220] J. F. Cochran and B. Heinrich, *Applications of Maxwell's Equations (Cochran and Heinrich)*, [Online; accessed 2022-04-02], Jun. 2021. [Online]. Available: `https://phys.libretexts.org/@go/page/22709`.

[221] G. W. Fernando, "Probing Layered Systems: A Brief Guide to Experimental Techniques", in *Handbook of Metal Physics*, vol. 4, Elsevier, 2008, pp. 111–130. DOI: `10.1016/S1570-002X(07)00005-5`.

[222] P. M. Oppeneer, "Theory of the magneto-optical kerr effect in ferromagnetic compounds", Ph.D. dissertation, 2000. DOI: `10.13140/2.1.3171.4083`.

[223] D. Allwood, P. Seem, S. Basu, P. Fry, U. Gibson, and R. Cowburn, "Over 40% transverse Kerr effect from Ni 80 Fe 20", *Applied Physics Letters*, vol. 92, no. 7, p. 072 503, 2008. DOI: `10.1063/1.2884332`.

[224] C. Dehesa-Martınez, L. Blanco-Gutierrez, M. Vélez, J. Diaz, L. Alvarez-Prado, and J. Alameda, "Magneto-optical transverse Kerr effect in multilayers", *Physical Review B*, vol. 64, no. 2, p. 024 417, 2001. DOI: `10.1103/PhysRevB.64.024417`.

[225] N. Vernier, J.-P. Adam, S. Eimer, G. Agnus, T. Devolder, T. Hauet, B. Ocker, F. Garcia, and D. Ravelosona, "Measurement of magnetization using domain compressibility in CoFeB films with perpendicular anisotropy", *Applied Physics Letters*, vol. 104, no. 12, p. 122 404, 2014. DOI: `10.1063/1.4869482`.

[226] C. Mattersdorfer, "High Current Nanopulser", 2015.

[227] S. Breitkreutz, A. Fischer, S. Kaffah, S. Weigl, I. Eichwald, G. Ziemys, D. Schmitt-Landsiedel, and M. Becherer, "Time-dependent domain wall nucleation probability in field-coupled nanomagnets with perpendicular anisotropy", *Journal of Applied Physics*, vol. 117, no. 17, 17B503, 2015. DOI: `10.1063/1.4906440`.

[228] G. Ziemys, C. Trummer, S. B.-v. Gamm, I. Eichwald, D. Schmitt-Landsiedel, and M. Becherer, "Characterization of the magnetization reversal of perpendicular Nanomagnetic Logic clocked in the ns-range", *AIP Advances*, vol. 6, no. 5, p. 056 404, 2016. DOI: `10.1063/1.4944336`.

[229] N. Nagaosa, J. Sinova, S. Onoda, A. H. MacDonald, and N. P. Ong, "Anomalous hall effect", *Reviews of modern physics*, vol. 82, no. 2, p. 1539, 2010. DOI: `10.1103/RevModPhys.82.1539`.

[230] K.-W. Moon, J.-C. Lee, S.-B. Choe, and K.-H. Shin, "Determination of perpendicular magnetic anisotropy in ultrathin ferromagnetic films by extraordinary hall voltage measurement", *Review of Scientific Instruments*, vol. 80, no. 11, p. 113 904, 2009. DOI: `10.1063/1.3262635`.

[231] S. Okamoto, K. Nishiyama, O. Kitakami, and Y. Shimada, "Enhancement of magnetic surface anisotropy of Pd/Co/Pd trilayers by the addition of sm", *Journal of Applied Physics*, vol. 90, no. 8, pp. 4085–4088, 2001. DOI: `10.1063/1.1405817`.

[232] A. Hrabec, N. Porter, A. Wells, M. Benitez, G. Burnell, S. McVitie, D. McGrouther, T. Moore, and C. Marrows, "Measuring and tailoring the dzyaloshinskii-moriya interaction in perpendicularly magnetized thin films", *Physical Review B*, vol. 90, no. 2, p. 020 402, 2014. DOI: `10.1103/PhysRevB.90.020402`.

[233] G. J. Vida, E. Simon, L. Rózsa, K. Palotás, and L. Szunyogh, "Domain-wall profiles in Co/Ir n/Pt (111) ultrathin films: Influence of the Dzyaloshinskii-Moriya interaction", *Physical Review B*, vol. 94, no. 21, p. 214 422, 2016. DOI: `10.1103/PhysRevB.94.214422`.

[234] C. Moreau-Luchaire, C. Moutafis, N. Reyren, J. Sampaio, N. Van Horne, C. Vaz, K. Bouzehouane, K. Garcia, C. Deranlot, P. Warnicke, *et al.*, “Skyrmions at room temperature: From magnetic thin films to magnetic multilayers”, *arXiv preprint arXiv:1502.07853*, 2015. DOI: 10.1038/nnano.2015.313.

[235] C.-F. Pai, L. Liu, Y. Li, H. Tseng, D. Ralph, and R. Buhrman, “Spin transfer torque devices utilizing the giant spin Hall effect of tungsten”, *Applied Physics Letters*, vol. 101, no. 12, p. 122 404, 2012. DOI: 10.1063/1.4753947.

[236] Q. Hao, W. Chen, and G. Xiao, “Beta ($\beta$) tungsten thin films: Structure, electron transport, and giant spin hall effect”, *Applied Physics Letters*, vol. 106, no. 18, p. 182 403, 2015. DOI: 10.1063/1.4919867.

[237] D. Bhowmik, L. You, and S. Salahuddin, “Spin Hall effect clocking of nanomagnetic logic without a magnetic field”, *Nature nanotechnology*, vol. 9, no. 1, pp. 59–63, 2014. DOI: 10.1038/nnano.2013.241.

[238] V. Ahrens, S. Mendisch, W. Kaiser, M. Kiechle, S. B.-v. Gamm, and M. Becherer, “Focused ion beam irradiation for generation of skyrmionic bubble like structures”, *Journal of Magnetism and Magnetic Materials*, vol. 523, p. 167 591, DOI: 10.1016/j.jmmm.2020.167591.

[239] C. Canedy, X. Li, and G. Xiao, “Large magnetic moment enhancement and extraordinary hall effect in Co/Pt superlattices”, *Physical Review B*, vol. 62, no. 1, p. 508, 2000. DOI: 10.1103/PhysRevB.62.508.

[240] J. Moritz, F. Garcia, J. Toussaint, B. Dieny, and J. Nozieres, “Orange peel coupling in multilayers with perpendicular magnetic anisotropy: Application to (Co/Pt)-based exchange-biased spin-valves”, *EPL (Europhysics Letters)*, vol. 65, no. 1, p. 123, 2004. DOI: 10.1209/epl/i2003-10063-9.

[241] K. Yamada, J.-P. Jamet, Y. Nakatani, A. Mougin, A. Thiaville, T. Ono, and J. Ferré, “Influence of instabilities on high-field magnetic domain wall velocity in (co/ni) nanostrips”, *Applied Physics Express*, vol. 4, no. 11, p. 113 001, 2011. DOI: 10.1016/j.jmmm.2007.07.032.

[242] K.-S. Ryu, L. Thomas, S.-H. Yang, and S. S. Parkin, “Current induced tilting of domain walls in high velocity motion along perpendicularly magnetized micron-sized Co/Ni/Co racetracks”, *Applied Physics Express*, vol. 5, no. 9, p. 093 006, 2012. DOI: 10.1143/APEX.5.093006.

[243] W. Kaiser, M. Kiechle, G. Žiemys, D. Schmitt-Landsiedel, and S. B.-v. Gamm, “Micromagnetic simulation of nanomagnets with geometry-tuned domain wall nucleation”, in *Journal of Physics: Conference Series*, IOP Publishing, vol. 903, 2017, p. 012 052. DOI: 10.1088/1742-6596/903/1/012052.

[244] J. Kimling, T. Gerhardt, A. Kobs, A. Vogel, S. Wintz, M.-Y. Im, P. Fischer, H. Peter Oepen, U. Merkt, and G. Meier, “Tuning of the nucleation field in nanowires with perpendicular magnetic anisotropy”, *Journal of Applied Physics*, vol. 113, no. 16, p. 163 902, 2013. DOI: 10.1063/1.4802687.

[245] K. Garello, F. Yasin, H. Hody, S. Couet, L. Souriau, S. Sharifi, J. Swerts, R. Carpenter, S. Rao, W. Kim, *et al.*, “Manufacturable 300mm platform solution for field-free switching SOT-MRAM”, in *Symposium on VLSI Circuits*, IEEE, 2019, T194–T195. DOI: 10.23919/VLSIC.2019.8778100.

[246] S. Sakhare, M. Perumkunnil, T. H. Bao, S. Rao, W. Kim, D. Crotti, F. Yasin, S. Couet, J. Swerts, S. Kundu, *et al.*, “Enablement of STT-MRAM as last level cache for the high performance computing domain at the 5nm node”, in *2018 IEEE International Electron Devices Meeting (IEDM)*, IEEE, 2018, pp. 18–3. DOI: 10.1109/IEDM.2018.8614637.

[247] F. Xie, R. Weiss, and R. Weigel, “Hysteresis compensation based on controlled current pulses for magnetoresistive sensors”, *IEEE Transactions on Industrial Electronics*, vol. 62, no. 12, pp. 7804–7809, 2015. DOI: 10.1109/TIE.2015.2458958.

[248] T. Devolder, I. Barisic, S. Eimer, K. Garcia, J.-P. Adam, B. Ockert, and D. Ravelosona, "Irradiation-induced tailoring of the magnetism of CoFeB/MgO ultrathin films", *Journal of Applied Physics*, vol. 113, no. 20, p. 203 912, 2013. DOI: 10.1063/1.4808102.

[249] L. Herrera Diez, F. Garcıa-Sánchez, J.-P. Adam, T. Devolder, S. Eimer, M. El Hadri, A. Lamperti, R. Mantovan, B. Ocker, and D. Ravelosona, "Controlling magnetic domain wall motion in the creep regime in He+-irradiated CoFeB/MgO films with perpendicular anisotropy", *Applied Physics Letters*, vol. 107, no. 3, p. 032 401, 2015. DOI: 10.1063/1.4927204.

[250] L. H. Diez, M. Voto, A. Casiraghi, M. Belmeguenai, Y. Roussigné, G. Durin, A. Lamperti, R. Mantovan, V. Sluka, V. Jeudy, *et al.*, "Enhancement of the Dzyaloshinskii-Moriya interaction and domain wall velocity through interface intermixing in Ta/CoFeB/MgO", *Physical Review B*, vol. 99, no. 5, p. 054 431, 2019. DOI: 10.1103/PhysRevB.99.054431.

[251] H. T. Nembach, E. Jué, K. Poetzger, J. Fassbender, T. J. Silva, and J. M. Shaw, "Tuning of the dzyaloshinskii-moriya interaction by $He^+$ ion irradiation", *arXiv:2008.06762*, 2020. DOI: 10.48550/arXiv.2008.06762.

[252] X. Zhang, N. Vernier, W. Zhao, L. Vila, and D. Ravelosona, "Extrinsic pinning of magnetic domain walls in CoFeB-MgO nanowires with perpendicular anisotropy", *AIP Advances*, vol. 8, no. 5, p. 056 307, 2018. DOI: 10.1063/1.5006302.

[253] Y. Zhang, X. Zhang, N. Vernier, Z. Zhang, G. Agnus, J.-R. Coudevylle, X. Lin, Y. Zhang, Y.-G. Zhang, W. Zhao, *et al.*, "Domain-Wall Motion Driven by Laplace Pressure in Co- Fe- B/MgO Nanodots with Perpendicular Anisotropy", *Physical Review Applied*, vol. 9, no. 6, p. 064 027, 2018. DOI: 10.1103/PhysRevApplied.9.064027.

[254] Y.-T. Chen and C. Chang, "Effect of grain size on magnetic and nanomechanical properties of co60fe20b20 thin films", *Journal of Alloys and Compounds*, vol. 498, no. 2, pp. 113–117, 2010. DOI: 10.1016/j.jallcom.2010.03.141.

[255] R. Tomasello, E. Martinez, R. Zivieri, L. Torres, M. Carpentieri, and G. Finocchio, "A strategy for the design of skyrmion racetrack memories", *Scientific Reports*, vol. 4, no. 1, p. 6784, 2014. DOI: 10.1038/srep06784.

[256] K.-W. Moon, J.-C. Lee, S.-G. Je, K.-S. Lee, K.-H. Shin, and S.-B. Choe, "Long-range domain wall tension in Pt/Co/Pt films with perpendicular magnetic anisotropy", *Applied Physics Express*, vol. 4, no. 4, p. 043 004, 2011. DOI: 10.1143/APEX.4.043004.

[257] X. Zhang, N. Vernier, W. Zhao, H. Yu, L. Vila, Y. Zhang, and D. Ravelosona, "Direct observation of domain-wall surface tension by deflating or inflating a magnetic bubble", *Physical Review Applied*, vol. 9, no. 2, p. 024 032, 2018. DOI: 10.1103/PhysRevApplied.9.024032.

[258] J. J. Goertz, G. Ziemys, I. Eichwald, M. Becherer, H. J. Swagten, and S. Breitkreutz-v. Gamm, "Domain wall depinning from notches using combined in-and out-of-plane magnetic fields", *AIP Advances*, vol. 6, no. 5, p. 056 407, 2016. DOI: 10.1063/1.4944698.

[259] A. Thiaville, S. Rohart, É. Jué, V. Cros, and A. Fert, "Dynamics of Dzyaloshinskii domain walls in ultrathin magnetic films", *EPL (Europhysics Letters)*, vol. 100, no. 5, p. 57 002, 2012. DOI: 10.1209/0295-5075/100/57002.

[260] B. Zhang, A. Cao, J. Qiao, M. Tang, K. Cao, X. Zhao, S. Eimer, Z. Si, N. Lei, Z. Wang, *et al.*, "Influence of heavy metal materials on magnetic properties of Pt/Co/Heavy metal tri-layered structures", *Applied Physics Letters*, vol. 110, no. 1, p. 012 405, 2017. DOI: 10.1063/1.4973477.

[261] V. Ahrens, S. Mendisch, W. Kaiser, M. Kiechle, S. B.-v. Gamm, and M. Becherer, "Focused ion beam irradiation for generation of skyrmionic bubble like structures", *Journal of Magnetism and Magnetic Materials*, vol. 523, p. 167 591, 2021. DOI: 10.1016/j.jmmm.2020.167591.

[262] M. Tang, W. Li, Y. Ren, Z. Zhang, S. Lou, and Q. Jin, "Magnetic damping and perpendicular magnetic anisotropy in pd-buffered [co/ni] 5 and [ni/co] 5 multilayers", *RSC advances*, vol. 7, no. 9, pp. 5315–5321, 2017. DOI: 10.1039/C6RA26087J.

[263] J. M. Shaw, H. T. Nembach, and T. J. Silva, "Roughness induced magnetic inhomogeneity in Co/Ni multilayers: Ferromagnetic resonance and switching properties in nanostructures", *Journal of Applied Physics*, vol. 108, no. 9, p. 093 922, 2010. DOI: 10.1063/1.3506688.

[264] T. Hauet, O. Hellwig, S.-H. Park, C. Beigne, E. Dobisz, B. Terris, and D. Ravelosona, "Influence of ion irradiation on switching field and switching field distribution in arrays of Co/Pd-based bit pattern media", *Applied Physics Letters*, vol. 98, no. 17, p. 172 506, 2011. DOI: 10.1063/1.3581896.

[265] E. Sicard and L. Trojman, "Introducing 5-nm finfet technology in microwind", 2021. [Online]. Available: https://hal.archives-ouvertes.fr/hal-03254444/.

[266] E. Sicard, L. Trojman, and I. l. M. Vanves, "Introducing 3-nm nano-sheet fet technology in microwind", 2021. [Online]. Available: https://hal.archives-ouvertes.fr/hal-03377556/document.

[267] J. Crop, E. Krimer, N. Moezzi-Madani, R. Pawlowski, T. Ruggeri, P. Chiang, and M. Erez, "Error detection and recovery techniques for variation-aware cmos computing: A comprehensive review", *Journal of Low Power Electronics and Applications*, vol. 1, no. 3, pp. 334–356, 2011. DOI: 10.3390/jlpea1030334.

[268] S. Middelhoek, "Domain walls in thin Ni–Fe films", *Journal of Applied Physics*, vol. 34, no. 4, pp. 1054–1059, 1963. DOI: 10.1063/1.1729367.

[269] M. Becherer, S. Breitkreutz, I. Eichwald, G. Ziemys, J. Kiermaier, G. Csaba, and D. Schmitt-Landsiedel, "Low-power 3D integrated ferromagnetic computing", in *Ultimate Integration on Silicon (EUROSOI-ULIS), 2015 Joint International EUROSOI Workshop and International Conference on*, IEEE, 2015, pp. 121–124. DOI: 10.1109/ULIS.2015.7063788.

[270] D. Carlton, B. Lambson, A. Scholl, A. Young, P. Ashby, S. Dhuey, and J. Bokor, "Investigation of defects and errors in nanomagnetic logic circuits", *IEEE Transactions on Nanotechnology*, vol. 11, no. 4, pp. 760–762, 2012. DOI: 10.1109/TNANO.2012.2196445.

[271] M. Niemier, M. Alam, X. S. Hu, G. Bernstein, W. Porod, M. Putney, and J. DeAngelis, "Clocking structures and power analysis for nanomagnet-based logic devices", in *Proceedings of the 2007 international symposium on Low power electronics and design*, ACM, 2007, pp. 26–31. DOI: 10.1145/1283780.1283787.

[272] Y. Yafet and E. Gyorgy, "Ferromagnetic strip domains in an atomic monolayer", *Physical Review B*, vol. 38, no. 13, p. 9145, 1988. DOI: 10.1103/PhysRevB.38.9145.

[273] A. MacIsaac, J. Whitehead, M. Robinson, and K. De'Bell, "Striped phases in two-dimensional dipolar ferromagnets", *Physical Review B*, vol. 51, no. 22, p. 16 033, 1995. DOI: 10.1103/PhysRevB.51.16033.

[274] Z. Málek and V. Kambersk, "On the theory of the domain structure of thin films of magnetically uni-axial materials", *Cechoslovackij fiziceskij zurnal*, vol. 8, no. 4, pp. 416–421, 1958. DOI: 10.1007/BF01612066.

[275] W. F. Brown, *Magnetostatic principles in ferromagnetism*. North-Holland Publishing Company, 1962, vol. 1.

[276] M. Kuznetsov, O. Udalov, and A. Fraerman, "Anisotropy of Neel "orange-peel" coupling in magnetic multilayers", *Journal of Magnetism and Magnetic Materials*, vol. 474, pp. 104–106, 2019. DOI: 10.1016/j.jmmm.2018.10.115.

[277] J. Fassbender and J. McCord, "Magnetic patterning by means of ion irradiation and implantation", *Journal of Magnetism and Magnetic Materials*, vol. 320, no. 3-4, pp. 579–596, 2008. DOI: 10.1016/j.jmmm.2007.07.032.

[278] M. Mansuripur, *The physical principles of magneto-optical recording*. Cambridge University Press, 1998. DOI: 10.1017/CBO9780511622472.

[279] G. Ziemys, S. Breitkreutz-v. Gamm, G. Csaba, D. Schmitt-Landsiedel, and M. Becherer, “Experiment-based thermal micromagnetic simulations of the magnetization reversal for ns-range clocked nanomagnetic logic”, *AIP Advances*, vol. 7, no. 5, p. 056 625, 2017. DOI: `10.1063/1.4974021`.

[280] A. Thiaville, J. Garcıa, and J. Miltat, “Domain wall dynamics in nanowires”, *Journal of Magnetism and Magnetic Materials*, vol. 242, pp. 1061–1063, 2002. DOI: `10.1016/S0304-8853(01)01353-1`.

[281] S. Klingler, P. Pirro, T. Brächer, B. Leven, B. Hillebrands, and A. V. Chumak, “Design of a spin-wave majority gate employing mode selection”, *Applied Physics Letters*, vol. 105, no. 15, p. 152 410, 2014. DOI: `10.1063/1.4898042`.

[282] “What’s After CMOS?”, *Semiengineering.com*, 2014. [Online]. Available: `https://semiengine%5C-ering.com/whats-after-cmos/`.

[283] J. Ding, C. Liu, Y. Zhang, U. Erugu, Z. Quan, R. Yu, E. McCollum, S. Mo, S. Yang, H. Ding, *et al.*, “Nanometer-thick yttrium iron garnet films with perpendicular anisotropy and low damping”, *Physical Review Applied*, vol. 14, no. 1, p. 014 017, 2020. DOI: `10.1103/PhysRevApplied.14.014017`.

# Acknowledgments

Dear interested reader, thank you for reading (parts of) this work. In this last chapter, I want to express my gratitude to the people who crossed my path throughout the time of this project.

Foremost, I would like to thank my supervisor, PD Dr. habil. Markus Becherer for putting his trust in me and offering me the opportunity to return to university after my Master Thesis. Without any prior experience in the field of magnetism, I must have been a risky choice. However, due to his expertise and passion for lab work, I quickly caught up with the topic and successfully navigated the first, arguably chaotic year of the project. His excitement for research and unmatched passion for teaching inspired not only me to join his group. The numerous discussions on the latest measurement results, interesting papers, or university politics over one or two cups of coffee will remain one of the defining aspects of this time.

Next, I would like to thank Gražvydas Žiemys, Valentin Ahrens, and Martina Kiechle, my immediate colleagues in Munich who worked in the field of magnetism, alongside, next, or sometimes against me. Together, we formed a small but effective group, working on related research topics. Gražvy, our intense discussions and arguments started back in 2017 and will probably continue throughout our joined time at IFX. Valentin, your composure in difficult situations and fine humor influenced and enriched my daily work. Thank you for that. Martina, during our joined projects, we were not always on the same page. However, these situations made me reflect and improve upon myself, and I would like to thank you for that.

In addition to my immediate colleagues working in the field of magnetism, I would also like to thank Josef Mock and Matthias Golibrzuch. You had the privilege or misfortune to work at the Garching Campus. Sometimes it must not have been easy for you and your topics in a group so heavily focused on magnetism.

Today, close collaboration between universities and research groups is existential. Therefore, I want to express my appreciation to the researchers we shared a close collaboration. First, I would like to mention Fabrizio Riente and Luca Gnoli from the Politecnico di Torino, who worked with us during the difficult time of the pandemic and made invaluable contributions to our joint projects. Their enthusiasm and dedication pushed every member of the group.

The same goes for Luis Flacke from the Walther-Meissner-Institut, with whom we worked on a fascinating project and shared many stimulating discussions. Significant contributions were also made by Ádám Papp, who, during his stays in Munich, first argued for a new research project at the chair and subsequently helped to launch and run it.

This work builds on the prior works of numerous Ph.D., Master's, and Bachelor's students. I especially want to thank my direct predecessors Markus Becherer, Stephan Breitkreutz-v Gamm, Josef Kiermeier, Irina Eichwald, and Gražvydas Žiemys. They conceived pNML, developed fabrication processes, and set up vital measurement equipment. Without their work, this project would not have been possible. I would also like to thank my Bachelor's and Master's students for their contributions, and I hope they experienced me to be a capable and fair supervisor.

It is also necessary to acknowledge the invaluable contributions from the people who helped us in keeping the museum, which we called clean-room, running. They maintained and repaired equipment and still found the time to work on improvements or develop new fabrication processes. First I would like to mention the current and former permanent ZEITlab staff, Rainer Emling, Annika Kwiatkowski, Rosemarie Mittermeier and Silke Boche. However, I would also like to thank Prof. Dr. Franz Kreupl, Maximilian Stelzer, and Moritz Jung, who, like us, spent countless hours repairing and maintaining our shared equipment. Furthermore, I want to thank the work-shop staff, Wolfgang Pielock and Karl Demmel, for their support in providing high precision components for fabrication

tools and measurement equipment alike. On the administrative side, I want to thank Kathrin Blahetek and Susanne Maier, who absorbed most of the administrative overhead one has the pleasure to be confronted with at a "leading" German university.
Special thanks go to Michael Haider, whom I liberated from his solitude by moving into his office and staying there for three years. Although not working in the field of magnetism, Michael became the ideal colleague, sharing my passion for technology and political discussions. Our office quickly emerged as the cornerstone of scientific and non-scientific interdepartmental collaboration at our institute. Michael, thank you for the numerous entertaining side-projects and the exciting bug-hunt. Furthermore, I would also like to thank my mentor and Master thesis supervisor Thomas Ganka for his valuable input and many off-topic discussion about silicon photomultiplier.
At this point, I am obligated to mention the technical program committee and all participants of the International Conferences on Mostly Scientific Topics (ICMST). Named sponsors of theses distinguished events were Michael Haider Waldemar Kaiser Michael Rinderle Tim Albes Valentin Ahrens Martina Kiechle Mark Schmidt Annika Kwiatkowski, Maximilian Stelzer Johannes Popp Michael Riesch, Lukas Seitner Jesus Abundis Patino, Gražvydas Žiemys, Marius Loch, Andreas Albrecht, Marco Bobinger, Florin Loghin, Amir Fallahpour, to name a few.
A Ph.D. is about more than ones own research project. It is also about collaboration and the exchange of ideas across different disciplines and cultures. During my three and a half years, I had the pleasure of meeting, discussing, and working with outstanding researchers and extraordinary personalities from all over the world. This privilege should be recognized and valued, and I will be forever grateful for this opportunity.

Finally, I would like to thank my family and friends for their support throughout the last years. Thank you for putting up with me being late, not available, or too consumed by my work.